Structured Wavefunctions for Precision Quantum Metrology

by

Connor Kapahi

A thesis
presented to the University of Waterloo
in fulfillment of the
thesis requirement for the degree of
Doctor of Philosophy
in
Physics - Quantum Information

Waterloo, Ontario, Canada, 2025

© Connor Kapahi 2025

Examining Committee Membership

The following served on the Examining Committee for this thesis. The decision of the Examining Committee is by majority vote.

External Examiner:	Valery Nesvizhevsky Senior Researcher, European Centre for Neutron Research, Institut Laue-Langevin
Supervisor:	Dmitry Pushin Associate Professor, Dept. of Physics, University of Waterloo
Co-Supervisor:	David G. Cory Professor, Dept. of Chemistry, University of Waterloo
Internal-External Member:	Jonathan Baugh Professor, Dept. of Chemistry, University of Waterloo
Internal Member:	Kevin J. Resch Professor, Dept. of Physics, University of Waterloo
Internal Member:	Bradley Hauer Assistant Professor, Dept. of Electrical and Computer Engineering, University of Waterloo

Author's Declaration

This thesis consists of material all of which I authored or co-authored: see Statement of Contributions included in the thesis. This is a true copy of the thesis, including any required final revisions, as accepted by my examiners.

I understand that my thesis may be made electronically available to the public.

Statement of Contributions

Connor Kapahi is the sole author for chapters 1 and 5, which were written under the supervision of Dr. Dmitry Pushin and were not written for publication. This thesis contains six manuscripts written for publication. Each section that consists of manuscript pages is noted with a summary of contributions.

This research was funded primarily through Transformative Quantum Technologies (TQT) and the Canada First Research Excellence Fund, with Dr. David Cory, Dr. Dmitry Pushin, and Dr. Ben Thompson as primary investigators. Neutron experiments conducted at the National Institute of Standards and Technology (NIST) Center for Neutron Research (NCNR), made possible by the US Department of Energy, Office of Nuclear Physics, under Interagency Agreement 89243019SSC000025.

Exceptions to sole authorship of material in this thesis are as follows:

Research in Chapter 2

For the publication entitled "High-Transmission Neutron Optical Devices Utilizing Micro-Machined Structures" [1]: The triangular array of refractive prisms was fabricated at the TQT facilities at the University of Waterloo by Ivar Taminiau. Neutron measurements were conducted at the BT-5 instrument at the NCNR. Initial experiments were conducted by Markus Bleuel, Dr. Dmitry Pushin, and Dr. Michael Huber. Follow-up measurements were conducted by Markus Bleuel and Dr. Melissa Henderson. Data analysis was primarily conducted by Connor Kapahi, Dr. Benjamin Heacock, and Dr. Dmitry Pushin, with contributions from all authors. Connor Kapahi wrote the draft manuscript, to which all co-authors contributed.

Research in Chapter 3

For the publication entitled "Human psychophysical discrimination of spatially dependent Pancharatnam–Berry phases in optical spin-orbit states" [2]: The apparatus used to generate entoptic patterns in participants was designed and built by Connor Kapahi and Dr. Dusan Sarenac. The psychophysical procedure to determine the visibility of entoptic patterns was designed by Dr. Andrew Silva and Dr. Ben Thompson. Experiments with participants were conducted by Connor Kapahi and Dusan Sarenac. Patient data was analyzed by Dr. Andrew Silva. Dr. Dusan Sarenac and Connor Kapahi prepared the draft manuscript, to which all co-authors contributed.

For the publication entitled "Direct discrimination of structured light by humans" [3]: The apparatus used to generate entoptic patterns was designed and built by Connor Kapahi and Dr. Dusan Sarenac. The psychophysical procedure to determine the visibility of entoptic patterns was designed by Dr. Andrew Silva and Dr. Ben Thompson. Experiments with participants were conducted by Connor Kapahi and Dusan Sarenac. Patient data was analyzed by Dr. Andrew Silva. Dr. Dusan Sarenac and Connor Kapahi prepared the draft manuscript, to which all co-authors contributed.

For the publication entitled "Measuring the visual angle of polarization-related entoptic phenomena using structured light" [4]: The apparatus used to generate entoptic patterns was designed by Connor Kapahi and Dr. Dusan Sarenac. The psychophysical procedure to determine the size of entoptic patterns was designed by Connor Kapahi, Dr. Andrew Silva, and Dr. Ben Thompson. The device and driver software were built by Connor Kapahi. Experiments with participants were conducted by Connor Kapahi, Dr. Mukhit Kulmaganbetov, Dr. Melanie Mungalsingh, and Taranjit Singh. Patient data was analyzed by Connor Kapahi. Connor Kapahi and Dr. Andrew Silva prepared the draft manuscript, to which all co-authors contributed.

For the publication entitled "Generation and detection of spin-orbit coupled neutron beams" [5]: The design to generate neutron orbital angular momentum states was developed by Dr. Dusan Sarenac, Dr. Dmitry Pushin, and Dr. David Cory. The triangular coils were designed by Connor Kapahi and fabricated by Dr. Kirill Zhernenkov and Ivar Taminiau. Neutron measurements were conducted by Connor Kapahi, Dr. Wangchun Chen, and Dr. Michael Huber. Data was analyzed by Connor Kapahi. Dr. Dusan Sarenac and Connor Kapahi prepared the draft manuscript, to which all co-authors contributed. The work utilized facilities supported, in part, by the National Science Foundation under Agreement DMR-150824

Research in Chapter 4

For the manuscript pre-print entitled "Design and Monte Carlo Simulation of a Phase Grating Moiré Neutron Interferometer to Measure the Gravitational Constant": The proposed experiment was conceptualized by Dr. Dmitry Pushin, Dr. Dusan Sarenac, Dr. David Cory, and Dr. Benjamin Heacock. The path-integral model of the phase grating moiré interferometer was developed by Connor Kapahi, Roger Serrat, Dr. Dmitry Pushin, Dr. Benjamin Heacock, Dr. Dusan Sarenac, and Dr. Michael Huber. Connor Kapahi prepared the draft manuscript, to which all co-authors contributed.

Abstract

In this thesis, several projects from biomedical optics measurements of the retina to precision gravimetric designs with neutron interferometers are presented, united by the common theme of applied quantum information techniques to develop next-generation precision metrological instruments. In particular, we introduce theoretical tools for analyzing neutron optical experiments and highlight parallels between neutron and light optics. These tools are applied to a new neutron prism design, demonstrating significantly higher transmission than traditional designs. Designs for devices applying these techniques, including a neutron Fresnel prism, spectrum analyzer, and spin collimator, are discussed. Potential advantages in neutron flux and spectrum resolution are quantified for these designs. The isometry between neutron spin and the polarization of light is exploited to validate the neutron spin collimator experimentally. Applications of structured states of light and experiments applying spin-orbit states to create patterns in the human visual system are described. Results demonstrate an increase in the perceived extent of these patterns, from 3° for Haidinger's Brush to 10° for a spin-orbit state. Work demonstrating a new method of generating a lattice of spin-orbit states in light is applied to neutron optics. Throughout the preceding experiments, methods of modeling neutron optics experiments with light and a semi-classical path-integral approximation have been developed. These methods are then applied to design an experiment that measures the gravitational constant using a neutron interferometer. A three-phase grating moiré interferometer (3-PGMI) design is first tested with infrared light. The deflection caused by a wafer sample is measured with the 3-PGMI and found to match direct measurements. The path-integral model is then applied to determine the uncertainty in the gravitational constant that can be achieved with a near-term measurement with a neutron 3-PGMI. An experiment to measure the gravitational constant is described, with an uncertainty budget, resulting in a measurement to 150 ppm. Potential corrections to previous experiments measuring the gravitational constant, due to lunar gravitational forces are quantified. Future applications of the tools and techniques described in this thesis are then discussed.

Acknowledgments

While it's impossible to accurately list everyone who impacted my life leading up to this work, I will do my best. Here at the University of Waterloo, I've been fortunate to work with dozens of excellent people who impacted me professionally and personally. None of the work in this thesis would have been possible without the support of my supervisor, Dr. Dmitry Pushin, and my co-supervisor, Dr. David Cory. Their continued advice, guidance, and support, even as our work followed a remarkably different path from its conception, cannot be overstated. My journey here was particularly impacted by Dr. Dusan Sarenac, whose guidance from the day I started as a undergraduate researcher made my graduate studies possible, and from whom I learned so much. I was lucky working on interdisciplinary research in the vision sciences, to be guided by Dr. Ben Thompson, whose work ethic and mentorship was an exceptional example of how to lead a team. The team from Waterloo and Hong Kong, namely Dr. Andrew Silva, Dr. Mukhit Kulmaganbetov, Dr. Melanie Mungalsingh, and Taranjit Singh were instrumental in the success of our work and truly friends to me, personally. Our collaborators at NIST in Gaithersburg have been instrumental in my research from before I started graduate school, and my time here would not have been the same without the professional and personal support of Dr. Michael Huber, Dr. Benjamin Heacock, Markus Bleuel, Shannon Watson, and Dr. Wangchun Chen. At RAC2, I've had the support of unbelievably talented staff including Ivar Taminiau, Alex Mitrovic, Sara Clark, and Sarah Wang. The friendship of colleagues at RAC, including Dr. Michael Reimer and Christine Dietrich was so valuable to me in some of the hardest times of my research. Within our group, I've been fortunate to work with so many fabulous researchers who have become valued friends. From the undergraduates we've worked with, including Timothy Khoo, Alex Obray, and Davis Garrad, to my fellow graduate students, Liuhe Wang, and Iman Salehi, I'm continually amazed by the talent that has come through our group. To the colleagues who kept me sane during the most difficult parts of my research, Dr. Lane Gunderman, Vinodh Raj Rajagopal Muthu, Dr. George Nichols, Dr. Melissa Henderson, Kent Ueno, Peter Sprenger, and Owen Lailey, I cannot thank you enough for your friendship.

Going back to my time at Queen's University, the friendships that have persisted over these long years are something that I cherish. Today, I still rely on the support of my housemates, Chris Anderson, Matt Clark, and Kiarash Kashanian, to my friends Michael Grotsky and Dr. Lemonte Alie-Lamarche. I'm also lucky to remain in touch with my fellow Engineering Physics survivors, Peter Carniglia, Chris Valentine, Jason Lockhart, Derek Grossman, Dr. Erin Broatch, Dr. Kier Darling, and Dr. Fiona Burns. Despite the distance back to Vancouver, I am fortunate to still be in touch with people that have

been friends for over 20 years now, Patrick Ross and Oliver Bibby. Reflecting on our time at St. George's School, I have to make special mention of Ed and Dannette Mortimer, who were so instrumental in my life back to grade 2. Since moving to Ontario, I've been so lucky to be welcomed by my "adoptive" family, Paul, Nancy, Tia, Will and Katie, and Lizabee. Along with the people who've been with us since 39th Street, Shel, Jill, and Jaime, who have become family. My siblings, Emily and Samantha, and my parents Naveen and Shelagh, and my grandparents Tilak and Rani, made me the person I am today, the work that sits here now would not have been possible without them. In the last 10 years, I have changed so much for the better, and that is all because of Lizabee, the love of my life. "If I have seen further it is by standing on the shoulders of giants", that is not only true scientifically but also personally.

Dedication

To Elizabeth.

Table of Contents

Examining Committee ii

Author's Declaration iii

Statement of Contributions iv

Abstract vi

Acknowledgments vii

Dedication ix

List of Figures xiv

List of Tables xvii

Quote xviii

1 Introduction 1

1.1 Thesis outline 1

1.2 Neutrons as probes 2

1.2.1 Neutron Interferometry 3

1.3 Neutron Optics 4

1.3.1 General Neutron Potentials . . . 4
1.3.2 Magnetic Potentials . . . 7
1.3.3 Gravitational Potentials . . . 9
1.3.4 Other Potentials . . . 10
1.3.5 Neutron Coherence . . . 11
1.4 Neutrons, light, and other matter-waves . . . 14
1.4.1 Structured States . . . 14
1.4.2 Phase Grating Interferometry . . . 15
1.4.3 Modeling neutron phase grating interferometers . . . 18
1.5 Measuring the Gravitational Constant . . . 19

2 Applications of Prism Potentials **21**
2.1 Triangular Arrays of Refractive Prisms . . . 21
2.1.1 Introduction . . . 22
2.1.2 Materials and Methods . . . 23
2.1.3 Results . . . 28
2.1.4 Discussion . . . 30
2.1.5 Applications . . . 33
2.2 Spin-based collimator . . . 35
2.2.1 Prism Potential Phase . . . 36
2.2.2 Neutron Approximation . . . 38
2.2.3 Light Approximation . . . 39
2.2.4 Experiment . . . 40
2.3 Next Steps . . . 40

3 Orbital Angular Momentum States **45**
3.1 Non-Separable States . . . 45
3.2 Human Discrimination of Spin-Orbit states . . . 50

3.2.1 Introduction . . . 51
3.2.2 Results . . . 57
3.2.3 Discussion . . . 57
3.2.4 Supplementary Material . . . 58
3.3 Human Discrimination of Structured States . . . 67
3.3.1 Introduction . . . 67
3.3.2 Setup and Stimuli . . . 76
3.3.3 Participants . . . 77
3.3.4 Psychophysical Procedure . . . 79
3.4 Measuring the visual angle of entoptic phenomena . . . 80
3.4.1 Introduction . . . 80
3.4.2 Theory . . . 81
3.4.3 Empirical Experiment . . . 85
3.4.4 Results . . . 87
3.4.5 Discussion . . . 89
3.4.6 Appendix . . . 89
3.5 Outlook on Biological Applications of Structured States . . . 94
3.6 Neutron OAM States . . . 94
3.6.1 Introduction . . . 96
3.6.2 Methods . . . 97
3.6.3 Results and Discussion . . . 100
3.6.4 Conclusion . . . 105
3.7 Outlook on Structured Neutron States . . . 106

4 Phase Grating Interferometry **107**
4.1 Modeling neutron PGMI with light . . . 107
4.2 Modeling the PGMI . . . 112
4.2.1 Modeling Gravitational Potentials . . . 112

4.3 Measuring the Gravitational Constant with a neutron PGMI 115
4.4 Introduction 116
4.5 Phase Grating Moiré Interferometer Model 117
4.6 Measuring G 120
4.7 Proposed Experiment 123
4.8 Uncertainties 125
4.8.1 Phase Correction Uncertainty 126
4.8.2 Source-Mass Phase Uncertainty 129
4.8.3 Statistical Uncertainty 131
4.9 Conclusion 132
4.10 Model Validation 133
4.11 Gravitational Potential of a Right Rectangular Prism 135
4.12 Phase Fit Statistics 135
4.13 Implementation 137

5 Outlook **141**
5.1 Structured States of Light 141
5.1.1 Biological Applications 141
5.1.2 Quantum Information Transmission 142
5.2 Neutrons as probes 142
5.2.1 Structured Neutron States 143
5.2.2 Next Generation Neutron Interferometers 143

References **145**

List of Figures

1.1 Schematic of neutron interferometer from the "COW" experiment 9

1.2 Schematic of prism pairs used to measure vertical neutron coherence and resulting neutron counts 13

1.3 Illustration of coordinates and displacement vectors used in Eqn. Eqn. (1.42). 16

1.4 Interference pattern from sodium atom interferometer 17

2.1 Images of aluminum prisms used to make the TARP, with data on surface quality 25

2.2 Microscope image of assembled TARP device with quantification of prism spacing 26

2.3 Schematic of USANS experiment used to measure beam deflection from the TARP, with relevent neutron ray angles labeled 27

2.4 Results from USANS experiment with TARP 30

2.5 Quality factor of TARP for different materials, with comparisons to other devices 32

2.6 Schematic of neutron Fresnel lens using TARP-like prisms 34

2.7 Angle and path labels for neutron trajectory in prism potential 36

2.8 Schematic of two-prism spin collimator with resulting neutron flux 37

2.9 Intensity images from polarization collimator with red light 41

2.10 Comparison of normalized intensity from experiment with theory 42

2.11 Schematic of four prism spin collimator with calculated flux results. 43

2.12 Simulation of VCN interferometer contrast using spin collimator to filter paths 43

3.1 Visualization of participant procedure in LOV prism entoptic pattern experiment . . . 52
3.2 Schematic of apparatus in LOV prism perception experiment . . . 54
3.3 Participant results in LOV prism perception experiment . . . 55
3.4 Simulated and measured intensity with LOV prisms . . . 60
3.5 Polarized images of states seen by participants in LOV prism perception study 63
3.6 Reconstruction of polarization topology from LOV prism perception study 64
3.7 Representation of state seen by participant, with schematic of macular structure . . . 69
3.8 Schematic of apparatus used in spin-orbit perception study . . . 71
3.9 Participant results from spin-orbit perception study . . . 74
3.10 Polarized images of states used in spin-orbit perception study . . . 78
3.11 Simulated entoptic pattern and apparatus from visual-angle perception study 82
3.12 Example staircase results from visual angle perception study . . . 86
3.13 Threshold results from participants in visual angle perception study . . . 87
3.14 Retinal images from participant in visual angle perception study . . . 88
3.15 Image of assembled triangular coil and magnetic field measurement results 95
3.16 Magnetic field results from triangular coil, with μ-metal guide tube . . . 96
3.17 Apparatus used in neutron LOV prism experiment . . . 98
3.18 Simulated and observed polarized intensity in neutron LOV prism experiment 99
3.19 Simulation of distortion in intensity due to stray magnetic fields . . . 102
3.20 Simulated and observed polarized intensity with prism translation . . . 103
3.21 Azimuthal intensity measured in neutron LOV prism experiment . . . 104

4.1 Schematic of beamline used to test PGMI with NIR light . . . 108
4.2 Intensity measured with NIR-PGMI and interference fringe carpet . . . 109
4.3 Beam deflection image with map of displacement and orientation across sample wafer . . . 110
4.4 Horizontal beam deflection measured directly with NIR camera . . . 111

4.5 Neutron count measurement with grating translation 114
4.6 Measured values of G from CODATA 2022, with our proposed experiment errorbar 118
4.7 Schematic of interfering paths in 3-PGMI 119
4.8 Schematic of apparatus proposed to measure G with a neutron 3-PGMI . . 124
4.9 Statistical uncertainty in 3-PGMI measurement with beam-time 127
4.10 Neutron intensity measured with VCN interferometer with grating rotation, with simulated intensity line 133
4.11 Measured contrast values from PGMI experiments with simulated results . 134

List of Tables

4.1 Measured beam deflection from NIR-PGMI and direct measurements . . . 112

4.2 Parameters for the experiment proposed in Sec. 4.7 with absolute uncertainties to 1σ (68 % confidence). The distances to each grating from the camera and source slit are each measured with the same absolute uncertainty as the grating separations. Source mass displacements (Δx, Δy, Δz) are given to the surface of the source mass. Parameters are grouped by relevance to subsections in Sec. 4.8. 129

4.3 Uncertainty budget for the 3-PGMI measurement proposed using a rectangular source mass. The methods used to calculate the uncertainty of each parameter are described in Sec. 4.8, with values listed in this table to two significant digits. Statistical uncertainty of 131.1 ppm is the result of 240 d of total experiment time consisting of two 120 d beam time runs for a null and source mass experiment. 130

"Our future discoveries must be looked for in the sixth place of decimals."

— Albert A. Michelson

Chapter 1

Introduction

1.1 Thesis outline

The focus of this thesis is to present the context and results of several experiments, utilizing both neutron matter-waves and light-waves, which each explore the ability of structured states to improve optical device design or precision measurement techniques. This thesis builds on the work of many other students and colleagues. To name a few, this work most closely builds upon the work of Dusan Sarenac [6] describing the lattice of optical vortex (LOV) prisms and phase grating moiré interferometer (PGMI) devices, and Benjamin Heacock's thesis [7] expanding the analysis of the PGMI to include diffraction from realistic grating profiles. The Ph.D. thesis of my supervisor, Dmitry Pushin, also set the foundation for much of the work in this thesis, describing the neutron wavefunction inside a perfect-crystal neutron interferometer (NI). The structure of this thesis will build towards an experimental design to measure Newton's Constant of Gravitation (G) with a neutron three-grating PGMI, highlighting experimental results as they contribute towards that result. Building toward that proposed experiment are several chapters that lay foundation and highlight notable results developed in the course of that research in the following order:

1. A mathematical description of neutrons as quantum probes is introduced, and the advantages of neutrons over other tools are highlighted. Those tools are applied to several potentials, the coherence properties of neutrons are discussed, and analogies between neutron matter-wave and optical light-waves are illustrated.

2. Analogies from optics are applied to design a neutron Fresnel prism. The fabrication of this design is described and experimental results are analyzed. An extension of

this design towards a Fresnel lens is outlined and potential applications for these devices are shown. Prism potentials are further exploited to create a collimation device, described theoretically with neutrons and experimentally with light.

3. The utility of the orbital angular momentum (OAM) degree-of-freedom is discussed and several experiments leveraging OAM in both neutrons and light waves are highlighted. Future applications for these states are described and significant developments in the generation and application of OAM states are shown.

4. A new path-integral model of the neutron PGMI is outlined and validated. Simulation results are compared to previous experiments and other models. An experiment to measure G to 150 ppm precision is proposed and the uncertainty budget quantified. Future experimental sites for the PGMI are evaluated and precision measurements beyond gravitational forces are described.

5. Potential applications for the devices and techniques described in this thesis are highlighted and new fields of research arising from these results are indicated.

1.2 Neutrons as probes

Neutrons possess several properties that make them valuable probes for both material science and fundamental physics. Their neutral electric charge allows neutrons to deeply penetrate materials, making them unparalleled probes of bulk effects like phonon interactions and internal magnetic fields [8, 9]. Neutron imaging methods are widely used across a range of material science applications, from real-time analysis of lithium-ion batteries [10], to non-destructive measurement of historical artifacts [11], and imaging the interface between human bone and metal implants [12]. Recently, neutron scattering tomography has been used extensively to measure the internal dynamics of topological skyrmions, illuminating the effect of inhomogeneities on the structure of "tubes" formed by the magnetic structure of skyrmions within a millimeter-scale sample [13]. Interferometry has a long history at the forefront of metrology, dating back to the foundations of relativity and the experiments of Michelson and Morley [14, 15]. In 1962, neutron self-interference was first demonstrated using two glass prisms to recombine a diverging neutron beam [16]. This arrangement was limited to fairly small neutron path separation and produced very low neutron fluence due to the requirement of narrow slits at the interferometer input. More damaging was the loss of neutron coherence properties due to the introduction of a phase-shifting material into the beam [17].

1.2.1 Neutron Interferometry

In 1974, a new NI design, adapted from perfect crystal interferometers originally developed for X-rays, was successfully tested [18]. Broadly, these designs utilize dynamical diffraction to create two coherent paths from an incident mono-energetic neutron beam, separated by Bragg angles of up to 45° [19, 20, 21, 22, 23]. This design allowed for two coherent neutron paths to be separated by centimeters, and enabled a wealth of quantum mechanical experiments in the 20$^{\text{th}}$ century. Single-crystal NIs were used in the first observation of gravitational effects on a quantum particle [24] and the first measurement of the 4π symmetry of spin-$\frac{1}{2}$ particles [25]. Modern precision metrology takes advantage of modern NI advancements [26], placing limits on the interaction strength of potential dark energy chameleon fields [27] and searching for short-range corrections to Newtonian gravity [28].

A significant challenge in applying neutron techniques to metrology remains the low fluence of neutron sources compared to X-ray synchrotron sources [29]. Even with nuclear reactors tuned for research purposes, like the National Institute of Standards and Technology (NIST) Center for Neutron Research (NCNR) reactor, neutron flux at a small angle neutron scattering (SANS) instrument of $6 \times 10^6\,\text{cm}^{-2}\,\text{s}^{-1}$, is typical [30]. With this challenge, neutron optical devices (i.e. lenses and mirrors) that are both effective and high-transmission are critical; however, a neutron's ability to penetrate into the bulk of materials now poses a new challenge. The refractive power of neutron-matter interactions scales with neutron wavelength λ as $\sim 1 - 10^{-6}\,\text{Å}^{-2} \cdot \lambda$, limiting the focal length of simple lenses to $\sim 100\,\text{m}$ [31]. Despite the achievements of single-crystal NIs, their requirement of precisely aligned crystal planes has historically limited designs to length scales of $\approx 10\,\text{cm}$. With few exceptions, single-crystal interferometers must be machined from a single-crystal ingot, which limits the size of single-crystal NIs [32]. Single-crystal interferometers split a neutron beam via Bragg diffraction, limiting the range of incident neutron angles that the interferometer can accept to the Darwin width ($\Theta_D \approx 4.4\,\mu\text{rad}$ and the acceptable wavelength spread to $\Delta\lambda/\bar{\lambda} \approx 1\%$ [8, 33]. The result of these limitations, it that neutron counts from a single crystal interferometer are on the order of $1\,\text{s}^{-1} - 10\,\text{s}^{-1}$. Around the turn of the millennium, a new interferometer configuration using phase gratings interferometers was limited in length only by the experimental reality that slow neutrons "fall already appreciably in the gravitational field of the earth (5 cm over 4 m)" [34]. This design expanded the acceptable wavelength spread of $\Delta\lambda/\bar{\lambda} \approx 22\%$ and accepted a beam with a divergence angle $\approx 1\,\text{mrad}$; however, the design also required very cold neutrons, which again limited the count rate at the detector to $1\,\text{s}^{-1}$ [35].

Recently, a new phase grating interferometer design, called the phase-grating moiré interferometer interferometer (PGMI), was designed for X-rays and later demonstrated

with neutrons [36, 37, 38]. The PGMI is a polychromatic interferometer, generating high-contrast interference fringes for a wide-spectrum neutron beam and enabling metrological experiments with NIs to unprecedented precision. Regardless of the neutron imaging or interferometry technique applied, we can approach the study of these techniques, and therefore the underlying materials or potentials, with relatively simple neutron optics.

1.3 Neutron Optics

Shortly after the discovery of neutrons by Chadwick [39], W.M. Elsasser suggested that neutron motion could be determined by quantum mechanics [40]. The Schrödinger Equation and Maxwell's equations are fundamentally wave equations, leading to analogous behavior between neutrons and light. In 1945, during the Manhattan Project, researchers noted that the CP-3 reactor studied by Enrico Fermi could be used to study the refraction, reflection, and diffraction of neutrons with materials, stating the reactor was "well suited to the study of *neutron optics*" [41]. From this perspective, a neutron is a matter wave with wavelength λ, given by the de Broglie relation [42]

$$\lambda = \frac{h}{|\mathbf{p}|}, \tag{1.1}$$

where $\mathbf{p}$ is the momentum of the neutron and h is Plank's constant. This relation can equivalently be expressed as $\mathbf{p} = \hbar\mathbf{k}$, where the wave vector $|\mathbf{k}| = \frac{2\pi}{\lambda}$, and $\hbar$ is the reduced Plank constant. As the velocity of neutrons $v \ll c$ for terrestrial sources, the neutron wave-function $\Psi(\mathbf{r}, t)$ is described by the solution to the non-relativistic time-dependent Schrödinger equation (TDSE),

$$-\frac{\hbar^2}{2m_N}\nabla^2\Psi(\mathbf{r}, t) + U(\mathbf{r}, t)\Psi(\mathbf{r}, t) = i\hbar\frac{\partial\Psi(\mathbf{r}, t)}{\partial t}, \tag{1.2}$$

where the neutron mass $m_N = 1.674 \times 10^{-27}\,\mathrm{kg}$, and $U(\mathbf{r}, t)$ describes the potential a neutron traverses.

1.3.1 General Neutron Potentials

Solving the Schrödinger equation for a generalized, realistic potential that describes a material or external force in an experiment is rarely possible analytically and is computationally

expensive numerically. With light, this problem is solved by describing potentials through an index of refraction and applying a geometrical optics model [43]. We can apply the same concept to neutrons. For a neutron with energy $E = \hbar\omega$ in a potential, the wave function is described by

$$\Psi(\mathbf{r}, t) = \psi(\mathbf{r})e^{-i\omega t}, \tag{1.3}$$

where ψ is the solution to the time-independent Schrödinger equation (TISE),

$$-\frac{\hbar^2}{2m_N}\nabla^2\psi(\mathbf{r}) + U(\mathbf{r})\psi(\mathbf{r}) = E\psi(\mathbf{r}). \tag{1.4}$$

This still leaves us with the problem of solving a linear differential equation, which is, in general, difficult. We can arrive at a solution by applying the Wentzel–Kramers–Brillouin (WKB) approximation [44], first assuming a solution in terms of another function $S(\mathbf{r})$,

$$\psi(\mathbf{r}) = e^{iS(\mathbf{r})/\hbar}, \tag{1.5}$$

substituting this into the TISE leaves

$$i\hbar\nabla^2 S - (\nabla S)^2 = 2m_N[U(\mathbf{r}) - E]. \tag{1.6}$$

The approximation is to expand S as a power-series in $\hbar$ and keep only terms to the first order,

$$S(\mathbf{r}) = S_0(\mathbf{r}) + \hbar S_1(\mathbf{r}) + \mathcal{O}(\hbar^2). \tag{1.7}$$

This approximation is called semi-classical and, before moving further, we can see the motivation for this nomenclature by looking at the solution to the TISE to the zeroth-order in S. Taking the partial derivative with respect to $\hbar$ yields two equations,

$$\begin{aligned} \nabla^2 S &= 0 \\ (\nabla S_0)^2 &= 2m_N[E - U(\mathbf{r})], \end{aligned} \tag{1.8}$$

the latter should be recognized as the Hamilton-Jacobi equation, with S_0 as the classical action [45]. Taking terms to the *first-order* in $\hbar$ is therefore called semi-classical. Retaining the first order, we reduce the TISE to

$$(\nabla S_0)^2 + 2\hbar\nabla S_0 \cdot \nabla S_1 - i\hbar\nabla^2 S_0 = 2m_N\left[E - U(\mathbf{r})\right], \tag{1.9}$$

which, again taking the partial derivative with respect to $\hbar$, yields

$$(\nabla S_0)^2 = 2m_N\left[E - U(\mathbf{r})\right] = p^2(\mathbf{r}) \tag{1.10}$$

$$2\nabla S_0 \cdot \nabla S_1 = i\nabla^2 S_0. \tag{1.11}$$

The above equations can be solved to find

$$\nabla S_0 = \pm\mathbf{p}(\mathbf{r}) \implies S_0(\mathbf{r}) = \pm\int_{\mathbf{r}_0}^{\mathbf{r}} \mathbf{p}(\mathbf{r}') \cdot d\mathbf{r}', \tag{1.12}$$

$$\nabla S_1 = \frac{i\,\nabla^2 S_0}{2\,\nabla S_0} = \frac{i}{2}\frac{(\pm\nabla\mathbf{p}(\mathbf{r}))}{(\pm\mathbf{p}(\mathbf{r}))} = \frac{i\,\nabla\mathbf{p}}{2\,\mathbf{p}} \tag{1.13}$$

$$iS_1(x) = -\frac{1}{2}\ln\mathbf{p}(\mathbf{r}) + C', \tag{1.14}$$

where C' is a constant. These can then be combined with our definition of ψ to show

$$\psi(\mathbf{r}) = \exp\left[\frac{i}{\hbar}\left(S_0 + \hbar S_1 + \mathcal{O}(\hbar^2)\right)\right] \simeq \exp\left[\frac{i}{\hbar}S_0\right]\exp[iS_1] \tag{1.15}$$

$$\psi(\mathbf{r}) = \exp\left[\pm\frac{i}{\hbar}\int_{\mathbf{r}_0}^{\mathbf{r}} \mathbf{p}(\mathbf{r}')\ \cdot d\mathbf{r}'\right]\exp\left[-\frac{1}{2}\log\mathbf{p}(\mathbf{r}) + C'\right] \tag{1.16}$$

$$\psi(\mathbf{r}) = \frac{A}{\sqrt{\mathbf{p}(\mathbf{r})}}\exp\left[\pm\frac{i}{\hbar}\int_{\mathbf{r}_0}^{\mathbf{r}} \mathbf{p}(\mathbf{r}')\ \cdot d\mathbf{r}'\right], \tag{1.17}$$

where A is a constant amplitude. The WKB approximation allows us to compute the effect of a slow-varying potential on a neutron wave function by computing its amplitude A, defined by initial conditions, and momentum $p(\mathbf{r})$ along the classically allowed neutron trajectory.

The de Broglie relation shows that we can, instead of computing the path-integral of the momentum in Eqn. (1.17), compute the path integral of the neutron wave-vector. Plugging de Broglie into the definition of local momentum,

$$\mathbf{p}^2(\mathbf{r}) = \hbar^2\mathbf{k}^2(\mathbf{r}) = 2m_N[E - U(\mathbf{r})], \tag{1.18}$$

we can compute the index of refraction $n(\mathbf{r})$ in a general potential,

$$n(\mathbf{r}) = \frac{|\mathbf{k}(\mathbf{r})|}{|\mathbf{k}_0|} = \left[1 - \frac{U(\mathbf{r})}{E}\right]^{1/2}, \tag{1.19}$$

where $\mathbf{k}_0$ is the neutron wave-vector in zero potential. Alternatively, we can compute the neutron's wave-vector in a potential with

$$|\mathbf{k}| = |\mathbf{k}_0|\sqrt{1 - \frac{2m_N U}{\hbar|\mathbf{k}_0|^2}}. \tag{1.20}$$

We now have the tools, with Eqn. (1.17) and Eqn. (1.20), to compute the phase difference, $\Delta\gamma$, between interfering paths in an interferometer by integrating along the closed-loop, $\mathcal{L}$, of the interfering paths,

$$\Delta\gamma = \oint_{\mathcal{L}} \mathbf{k}(s) \cdot d\mathbf{s}. \tag{1.21}$$

For the potentials in this work the neutron energy $E \gg U$. The phase accumulated along the classically allowed trajectory through a potential is therefore

$$\Delta\gamma \approx \oint_{\mathcal{L}} |\mathbf{k}_0| \ |d\mathbf{s}| + \frac{m_N}{\hbar|\mathbf{k}_0|^2} \oint_{\mathcal{L}} U(s) \ |\mathbf{k}_0| \ |d\mathbf{s}| + \mathcal{O}\left(U(s)^2\right). \tag{1.22}$$

1.3.2 Magnetic Potentials

Magnetic fields act on a neutron's spin degree of freedom with the potential

$$\mathcal{U}_{mag} = -\mu\sigma \cdot \mathbf{B} \tag{1.23}$$

where σ is the Pauli vector, μ is the neutron magnetic dipole moment, and B is the applied magnetic field vector. Choosing the direction of this magnetic field as our quantization axis, the two states of our neutron spin are eigenstates of the magnetic field Hamiltonian.

Following the prescription of Section 1.3.1, we can calculate the index of refraction for each eigenstate, aligned and anti-aligned to the magnetic field, with

$$n_{\uparrow/\downarrow} = \sqrt{1 \ {}^{+}\!/_{-} \ \frac{2m_N\mu B}{\hbar^2\mathbf{k}_0^2}} \tag{1.24}$$

$$\approx 1 \ {}^{+}\!/_{-} \ \frac{m_N\mu B}{\hbar^2\mathbf{k}_0^2}, \tag{1.25}$$

where the approximation holds for neutron kinetic energies of interest in this thesis, between 8 meV and 40 meV], and magnetic potential energies of ≈ 0.04 meV for field strengths of 300 G. Leaning on the analogy between light-waves and matter-waves, Eqn. (1.25) with the elementary physics of Snell's Law shows that these eigenstates of a neutron will following different trajectories within the magnetic potential. An obvious quantity to calculate is the accumulated phase between spin-eigenstates as a neutron traverses a magnetic field region. Allowing each eigenstate a distinct trajectory $T_{\uparrow/\downarrow}$, the phase difference between these states is

$$\begin{aligned}\Delta\gamma &= \int_{T_\uparrow} \mathbf{k}_\uparrow \cdot d\mathbf{s} - \int_{T_\downarrow} \mathbf{k}_\downarrow \cdot d\mathbf{s} \\ &= \int_{T_\uparrow} n_\uparrow(\mathbf{s}) \ \mathbf{k}_0 \cdot d\mathbf{s} - \int_{T_\downarrow} n_\downarrow(\mathbf{s}) \ \mathbf{k}_0 \cdot d\mathbf{s}.\end{aligned} \tag{1.26}$$

For the case of a neutron following a path of length L in a uniform magnetic field $\mathbf{B} = B\hat{y}$, where the neutron path deviation due to the field is negligible, this phase reduces to

$$\Delta\gamma = |\mathbf{k}_0|(n_\uparrow - n_\downarrow)L \tag{1.27}$$

$$\approx -\frac{2m_N\mu B}{\hbar^2|\mathbf{k}_0|}L, \tag{1.28}$$

which equals the Larmor precession angle.

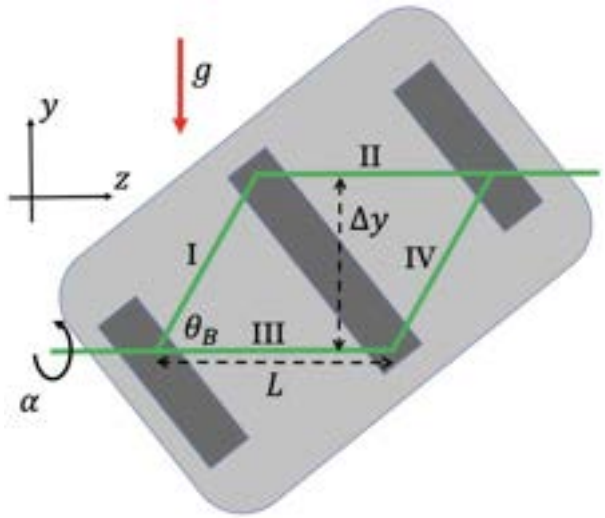


Figure 1.1: Schematic of the single-crystal interferometer used in [24]. By rotating the interferometer about the incident beam-axis by an angle α, a potential difference between paths II and III is induced.

1.3.3 Gravitational Potentials

Of particular interest in this thesis is the propagation of neutrons within gravitational potentials. The foundational work on this topic was published by Colella, Overhauser, and Werner (COW) in 1975, where the quantum mechanical phase shift caused by a gravitational field was first measured [24]. In that work, a perfect-crystal NI was rotated about in incident neutron beam to create a gravitational potential difference between neutron paths. The framework described in Section 1.3.1, combined with the Hamiltonian for Earth's local gravitational potential,

$$\mathcal{U}_g = m_N \mathbf{g} \cdot \mathbf{r}, \tag{1.29}$$

where $\mathbf{g}$ is the Earth's gravitational field vector, allows us to compute the phase shift as a function of interferometer rotation. The schematic in Figure 1.1 shows four path segments which, for the length scales in [24], are approximately straight lines. In the coordinate system of Figure 1.1, the gravitational potential only depends on the y-coordinate. As the path segments I and IV have equal y-coordinates, the phase accumulated by a neutron is equal. Therefore, only path segments II and III contribute to the phase measured by the interferometer.

With an incident neutron beam propagating in the z-direction, the phase shift measured by the NI will be

$$\Delta\gamma_g = \int_{II} \mathbf{k}\cdot d\mathbf{s} - \int_{III} \mathbf{k}\cdot d\mathbf{s} \tag{1.30}$$

$$= |\mathbf{k}_0|\left(1+\frac{2m_N^2 g}{\hbar^2\mathbf{k}_0^2}[\Delta y + y_0]L\right) - |\mathbf{k}_0|\left(1+\frac{2m_N^2 g}{\hbar^2\mathbf{k}_0^2}y_0 L\right) \tag{1.31}$$

$$= \frac{2m_N^2 g}{\hbar^2|\mathbf{k}_0|}\Delta y L. \tag{1.32}$$

In the original COW experiment, the calculated phase shift from Eqn. (1.32) was $\Delta\gamma_{g,\text{ theory}} = 59.6\sin\alpha$, while the measured phase shift, $\Delta\gamma_{g,\text{ exp.}} = 54.3\sin\alpha$. Including additional phase shifts induced by the bending of the silicon crystal as the interferometer is rotated and the Sagnac effect reduced the discrepancy between $\Delta\gamma_{g,\text{ theory}}$ and $\Delta\gamma_{g,\text{ exp.}}$ to 0.8% [46]. Subsequent X-ray measurements and modeling attributed this remaining discrepancy to crystallographic imperfections in realistic crystal NIs [47, 48]. In the 50 years since the original COW experiment, the perfect-crystal interferometer has not been used to perform precision measurements of the gravitational constant. This is, in large part, due to the limited fluence of single-crystal NIs.

1.3.4 Other Potentials

The other potentials of interest in this work include the effects of propagation through ambient air, bulk material, and the effects of Earth's rotation. The interaction of a neutron with matter is dominated by the nuclear-nuclear interaction [8].

For a non-magnetic material, this gives an effective optical potential for the material [43]

$$\mathcal{U}_{opt} = \frac{2\pi\hbar^2}{m_N} b_c N, \tag{1.33}$$

where b_c is the coherent scattering length, and N is the number density of the material [49]. Of interest in any experiment where the interferometer moves or changes orientation is non-inertial effects arising from the rotation of the Earth, commonly called the Sagnac Effect. The effective potential term in the Hamiltonian of a neutron within a reference frame rotating with an angular velocity $\boldsymbol{\Omega}$ is

$$\mathcal{U}_S = -\boldsymbol{\Omega} \cdot (\mathbf{r}_E \times \mathbf{p}), \tag{1.34}$$

where the coordinate $\mathbf{r}_E$ has its origin about the Earth's center of mass [50]. Finally, we consider a neutron traveling through ambient air which, near standard temperature and pressure, can be considered an ideal gas mixture [51]. Much like a solid material, we apply the Fermi pseudo-potential to the nucleus of atoms within the gas. This produces an optical potential, where we now need to consider multiple atoms,

$$U_A = \frac{2\pi\hbar^2}{m_N} \sum_i b_{ci} N_i, \tag{1.35}$$

where we are now summing over different atoms in the gas, each with coherent scattering length b_{ci}, and number density N_i.

1.3.5 Neutron Coherence

In describing the phase difference between interfering paths in Eqn. (1.22), the closed loop $\mathcal{L}$ implicitly implied that interfering neutron paths overlapped perfectly in space and time. To properly consider this, we must discuss neutron coherence properties, which in turn requires some conceptual idea of how to represent the *particle* nature of a neutron. Throughout neutron physics is "the pervasive conceptual idea of a wave-packet" [8] which describes a neutron wavefunction as a superposition of plane waves with a Gaussian probability destiny function in each spatial dimension and a group velocity v_0 (and associated wavevector $\mathbf{k}_0$). Following the solution of Darwin for an unbound electron assumed initially to be a Gaussian wave-packet [52], a neutron wavefunction in one-dimension of space is

$$\psi(z, t=0) = \exp\left[-\frac{1}{2\sigma^2}(z - z_0)^2 + ik(z - z_0)\right], \tag{1.36}$$

where the complex part is chosen such that the wavefunction has an initial momentum $p = \hbar k$. This solution to the free electron, or equivalently the free neutron, as a function of time is

$$\psi(z,t) = \frac{\sigma}{\sqrt{\sigma^2 + i\frac{ht}{2\pi m_N}}} \exp\left[-\frac{1}{2}\frac{(z - z_0 - vt)^2}{\sigma^2 + i\frac{ht}{2\pi m_N}} + i\frac{2\pi}{h} m_N v \left(z - z_0 - \frac{1}{2}vt\right)\right]. \tag{1.37}$$

After propagating for a time t, the standard deviation of $|\psi(z,t)|^2$, for the above free neutron is

$$[\sigma(t)]^2 = [\sigma(t=0)]^2 + \left[\frac{\hbar t}{2m_N\sigma(t=0)}\right]^2, \tag{1.38}$$

suggesting we can say that the neutron should have a longitudinal coherence length related to the above standard deviation.

Experimentally, single-crystal NIs have often been used to measure the coherence length of a neutron in each dimension. In 1983, Kaiser, Werner, and George reported the first experimental measurement of a coherence length, namely the longitudinal (propagation axis) coherence length [53]. In this experiment, a material is placed into one arm of the NI such that the material surfaces are parallel to the lattice planes of the silicon crystal. Kaiser et al. claimed that this measurement was "the first experiment in which the detailed longitudinal shape of a neutron wave packet was observed". A similar experiment, by Clothier et al. [54], measured contrast in their interferometer drop to zero with samples that retard a neutron by $\approx 150\,\text{Å}$. While these may appear to be direct measurements of the longitudinal extent of our wave packet, there is a different explanation for this drop in contrast. The delay Δ_z of the neutron matter-wave caused by a material of thickness D, is given by

$$\Delta_z = \frac{\lambda^2 N b_c}{2\pi} D, \tag{1.39}$$

which shows that the phase shift $\mathbf{k}\cdot\Delta$ is wavelength dependent. In an experiment, where the resulting interference pattern is the result of averaging over a wavelength distribution, we would expect the contrast to drop as a result of *dephasing*. Therefore, we must distinguish between coherence lengths, which may result from experimental parameters and dephasing effects, and the size of a neutron wave packet. Clothier et al. demonstrated exactly this by recovering contrast in their NI by adding a material that produces an equal and opposite delay of the neutron wave-packet in the same arm as the material that originally killed contrast [54]. Further experiments have recovered interference fringes using a chopper, to time-bin wavelengths of a neutron beam [55] and analyzer crystals [56].

The transverse properties of neutron coherence, both in the diffraction plane of the interferometer (typically "horizontal") and perpendicular to this and the propagation axis (called "vertical"), have also been explored through neutron interferometry. In the case of vertical coherence, two pairs of prisms are placed in each arm of a single-crystal NI

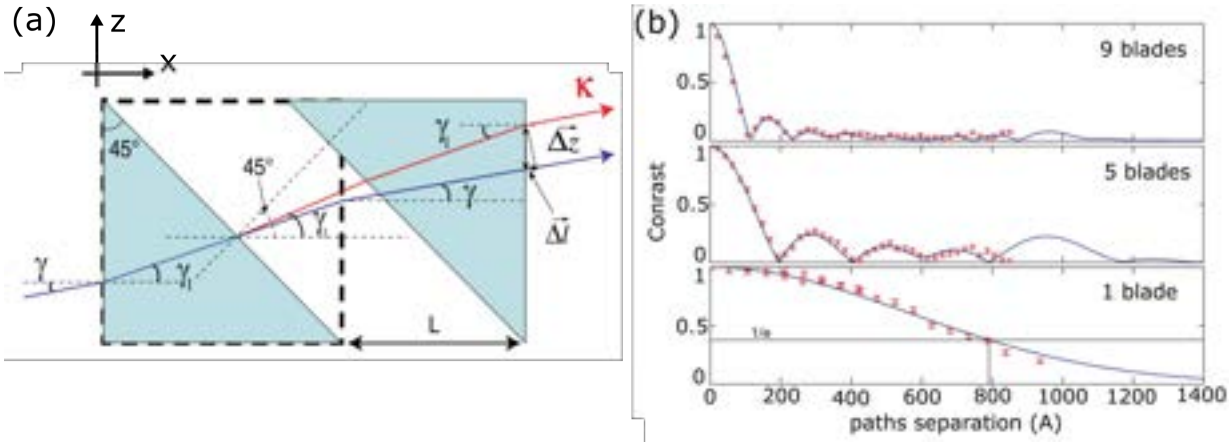


Figure 1.2: (a) Schematic of the complimentary prism pairs used to create a vertical shift in a neutron beam. Prisms joined, with $L = 0$, compensate for the material phase shift of separated prisms, isolating the effect of vertical displacements. (b) Measured contrast from single-crystal NI with different vertical momentum distributions on the incident neutron beam. The introduction of more blade to the vertical monochromator allows for a wider distribution of momentum in the vertical direction, causing a reduction in the vertical coherence length as measured by the NI. Figure reproduced from [57].

[57]. All four of these wedges had a wedge angle of 45° and identical dimensions, allowing them to fit together and act only to add a phase. Separating these complimentary prism pairs, shown in Figure 1.2(a), by a distance L has two effects: a neutron path will be displaced in the vertical direction by Δy, and the propagation distance from the source to detector will be increased by Δz. Using these displacements, the intensity at the detector can be computed with an incoherent sum over plane waves. Pushin et al. performed three measurements of contrast with varying L and showed that contrast loss depended on the vertical monochromator configuration [57]. Equation 7 of [57] shows that this change in the vertical monochromator alters the distribution of momentum in the neutron beam, but not the wavefunction of the neutron itself. This suggests that the coherence length in the vertical direction was a property of the neutron beam and not an intrinsic property describing the "size" of a neutron.

As was the case in both longitudinal and vertical coherence, transverse coherence was also found to depend on properties extrinsic to the neutron. In the transverse case, a phase shifting aluminum slab was placed in a neutron beam; however, unlike the longitudinal case, the face of the phase shifter is parallel to the reflecting lattice planes. This orientation of the aluminum slab produces a wavelength independent phase shift while also shifting the

neutron beam in the horizontal direction. As this phase shift is wavelength independent and because a single-crystal NI accepts a narrow range of neutron momentum in the horizontal direction, the reduction in contrast observed by Rauch et al. was attributed "mainly caused by the beam attenuation and the roughness of the sample surfaces"[58]. Diffraction via a Bragg prism was latter used to generate an extremely collimated neutron beam, enabling a measurement of transverse coherence lengths up to 175 µm [59]. These experiments contradict the model of a single neutron as a traveling wave-packet, that a neutron has some intrinsic length-scales over which it is *allowed* to interact. Instead, these experiments suggest that coherence length depends on extrinsic experimental parameters, like wavelength distribution. This is the description suggested by Werner and Rauch, that "coherence cannot be destroyed by any Hamiltonian interaction, but only by stochastic and dissipative effects which are related to a transition from a quantum to a classical world" [8].

1.4 Neutrons, light, and other matter-waves

While photons are massless spin-1 particles, several isometries between the properties of photons and neutrons enable the testing and validation of neutron devices and experiments with light. First, a photon can only occupy the ± 1 spin states, meaning both neutron spin and the polarization of light are described by states in $\mathcal{C}^2$, which can then be mapped onto a $3D$ unit sphere as the Block sphere or Poincaré sphere, respectively. We can model the effect of magnetic fields on neutrons using birefringent materials with light. Experiments originally conducted with visible light and birefringent crystals enabled the development of the LOV prisms, a series of birefringent prisms that produce a lattice of orbital angular momentum states [60]. Applying our isomorphism outlined in Section 1.3.2, a series of triangular coils, creating prism-shaped regions of uniform magnetic fields, will generate a similar lattice of orbital angular momentum states from neutrons. These similarities allow developments in optics to be translated into neutron optics, while leveraging the high fluence of laser sources in the development of new neutron optical devices.

1.4.1 Structured States

Two degrees of freedom are of particular interest in describing structured states of light and matter waves: spatial phase profile and spin. The spatial profile of light or matter-waves is simply the amplitude and phase of a wave, which typically varies across the profile of a beam [61]. Of particular interest in this thesis are states possessing orbital

angular momentum (OAM), most often represented as Laguerre–Gaussian modes. Formal mathematical descriptions of these states will be expanded upon, but the core of the OAM degree of freedom can be seen through an analogy with linear momentum. For light, described by some electromagnetic field, $\mathbf{E} = |\mathbf{E}|e^{-i\Phi}$, the momentum of that field is a vector field given by

$$\mathbf{k} = \nabla\Phi, \tag{1.40}$$

which can be written either in Cartesian coordinates, giving the linear momentum in each spatial direction, or in cylindrical coordinates

$$\mathbf{k} = \frac{\partial\Phi}{\partial\rho}\hat{\rho} + \frac{1}{\rho}\frac{\partial\Phi}{\partial\varphi}\hat{\varphi} + \frac{\partial\Phi}{\partial z}\hat{z}, \tag{1.41}$$

where z is the propagation axis, ρ is the radial coordinate, and φ is the azimuthal angle. The azimuthal component of momentum, $\frac{\partial\Phi}{\partial\varphi}$, is what we call OAM. OAM states have been generated for a wide range of waves, including light [62], electrons [63], and neutrons [64], with applications in a wide range of fields from optical trapping, and high-bandwidth communication [65, 66, 67, 68], to quantum information processing [69, 70]. In Section 3, we will explore applications for structured states where OAM is coupled to the spin degree of freedom and demonstrate how magnetic potentials can be exploited to generate these states in neutrons.

1.4.2 Phase Grating Interferometry

In highlighting the historical utility of neutrons as probes, we touched on several NI designs, from the original bi-prism experiment [16], to the single-crystal NI [18], and modern PGMI [38]. Throughout the history of NI development, advancements in other fields of interferometry have been adapted and applied to neutron optics. The original single-crystal NI was adapted from X-ray interferometer designs [71], while the PGMI was first described and demonstrated with visible and X-ray sources [36]. In that work, the two-grating PGMI was modeled with the Fresnel-Kirchhoff diffraction integral, where the scalar field V across a 1-dimensional detector is

$$V(y_c) \propto \int\int \frac{1}{|\mathbf{r}_0||\mathbf{r}_1||\mathbf{r}_2|} \exp[i\mathbf{k}\cdot(\mathbf{r}_0+\mathbf{r}_1+\mathbf{r}_2)]T_1(y_1)T_2(y_2)dy_1dy_2, \tag{1.42}$$

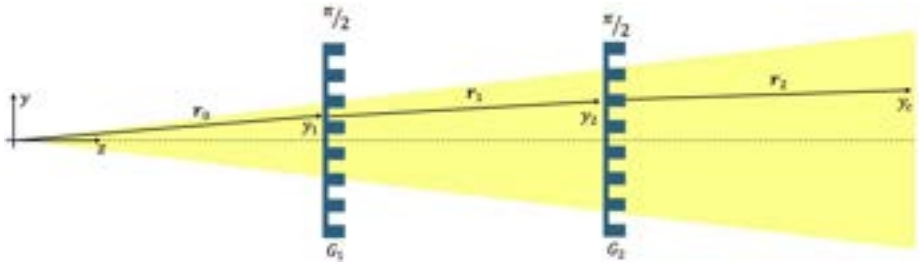


Figure 1.3: Illustration of coordinates and displacement vectors used in Eqn. (1.42).

where T_1 and T_2 are t transmission functions, y_1, y_2, and y_c are the coordinates in the planes of grating 1 (G_1), grating 2 (G_2) and the camera, respectively, and r_0, r_1, r_2 are the successive spacings between the source, y_1, y_2, and y_c, illustrated in Figure 1.3. The Appendix of [36] applies this model, considering the source as a superposition of point sources, to show that an interference pattern is visible at the camera due to the interference of a diffraction order (e.g. the wave generated by the n^{th} order of G_1 and the m^{th} order of G_2), with neighboring orders (e.g. the $(n+1)^{th}$ order of G_1 and the $(m-1)^{th}$ order of G_2). This is captured in Eqn. 7 of [36], where a wavelength independent phase gradient in y arises from Eqn. (1.42). The three-grating PGMI is then modeled by recognizing that there exists an "echo-plane" after the second grating, where the wave amplitude of the beam is a Fourier image of G_1 [72]. Interference for the 3-PGMI can then understood to occur between the Fourier image of G_1 at this "echo-plane" and grating 3 (G_3). This model has been expanded to neutrons in the cone-beam model of the PGMI, that convolves the momentum distribution of a neutron beam by a propagation kernel and the Fourier transform of the transmission functions of objects [73]. While powerful tools for a variety of samples, these models capture interactions (with samples, gratings, or any potential) through transmission functions, like those in Eqn. (1.42). Applying this to potentials like those of a gravitational source mass, requires applying a series of these transmission functions that each describe the spatially dependent potential at subsequent spatial planes. This is computationally ineffective for the potential of a macroscopic source mass and suggests that a new approach to understanding the PGMI is required.

The WKB approximation and path-integral framework provides a basis to model for the PGMI, but made no mention of the effect of a polychromatic beam nor described how to incorporate a wavelength distribution into the model. Looking to the intertwined heritage of NIs with interferometry with other particles, we can turn to atom interferometry, namely work that built towards an experimental determination of G [74]. The first experimental demonstration of an interferometer for atoms utilized an apparatus remark-

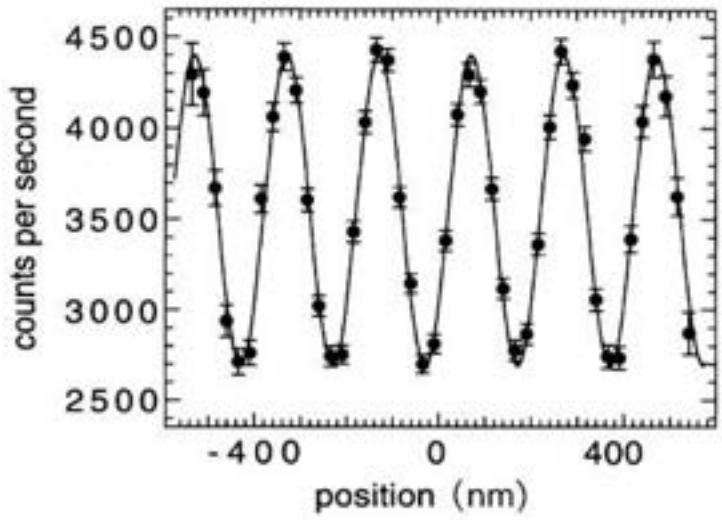


Figure 1.4: Measured interference pattern from sodium atom interferometer. Figure reproduced from [76].

ably similar to the 3-PGMI, where three gratings are used to generate interference in a beam of sodium atoms [75]. Later experiments, designed to measure the electric polarizability of sodium atoms, modeled the wavefunction, following the WKB approximation, as $\psi_{\mathrm{Na}}(x) \propto e^{i\int k(x)dx}$, just as we did in Section 1.3.1 [76]. As is the case with the neutron PGMI, the atom interferometer in [76] is polychromatic, necessitating an average over atom/neutron wavelengths. In both neutron PGMI and atom interferometry experiments, the phase of the sinusoidal interference pattern seen at the camera is used to extract information about the sample or potential in question. Figure 1.4 shows the interference fringe from the sodium atom interferometer in [76]. The effect of the Stark potential used in that experiment is the translation of the interference fringe in Fig. 1.4 by a phase $\Delta\phi_{\mathrm{Stark}}$.

The measured phase shift in that experiment included atoms with a range of velocities. Extracting the electric polarizability of sodium therefore requires an incoherent average over the interference patterns of each wavelength. This amounts to an integral over cosines of similar periods, which produces a sinusoidal pattern that is, up to a scaling factor,

$$1 + \mathcal{C}_{\mathrm{avg}} \cos\left(\frac{2\pi}{P_f} y + \Delta\phi_{\mathrm{avg}}\right) = \int_0^\infty P(\lambda)\left[1 + \mathcal{C}_\lambda \cos\left(\frac{2\pi}{P_f} y + \Delta\phi_\lambda\right)\right] d\lambda, \tag{1.43}$$

where the phase ϕ_i, and fringe contrast $\mathcal{C}_i$, are associated either with a particular wavelength λ or the averaged value, with wavelength probability distribution $P(\lambda)$. The

wavelength-dependent parameters can be determined with the path-integral model described in 1.3.1, but the averaged terms must be calculated via the integrals in Eqn. (1.43). For wavelength and time-independent potentials, the average phase and contrast in Eqn. (1.43) can be calculated by taking the *circular mean* of the wavelength-dependent phase shifts [77], giving us

$$\Delta\phi_{\text{avg}} = \tan^{-1}\left(\frac{\int_0^\infty P(\lambda)\mathcal{C}_\lambda \sin\left(\Delta\phi_\lambda\right)}{\int_0^\infty P(\lambda)\mathcal{C}_\lambda \cos\left(\Delta\phi_\lambda\right)}\right) \tag{1.44}$$

$$\mathcal{C}_{\text{avg}} = \sqrt{\left[\int_0^\infty P(\lambda)\mathcal{C}_\lambda \sin\left(\Delta\phi_\lambda\right)\right]^2 + \left[\int_0^\infty P(\lambda)\mathcal{C}_\lambda \cos\left(\Delta\phi_\lambda\right)\right]^2}, \tag{1.45}$$

which allows us to compute the expected phase shift due to any external potential. In the case of measuring the electric polarizability of sodium atoms in, the averaged phase shift, $\Delta\bar{\phi}_{\text{Stark}}$ is measured and used to extract the wavelength dependent phase shift [76]. This same procedure can be applied to a neutron 3-PGMI, taking advantage of the full fluence of a polychromatic neutron beam and enabling precision measurements with neutron interferometry. Of particular interest in this thesis is the application of this procedure to the measurement of the gravitational potential induced by a laboratory-scale source mass.

1.4.3 Modeling neutron phase grating interferometers

In [36], Eqn. (1.42) was used to compute the intensity measured by the camera in those experiments using the grating transmission functions. A rectangular grating with a phase height, ϕ, has the transmission function,

$$T(x) = exp\left[-i\frac{\phi}{2}G(x)\right],$$

where $G(x)$ is a square wave that alternates between 1 and -1. This transmission function can be written as a Fourier series,

$$T(x) = \cos\left(\frac{\phi}{2}\right) - i\sin\left(\frac{\phi}{2}\right)\sum_{n=1,3,5,\ldots}^{\infty}\frac{4}{\pi n}\cos\left(\frac{n\pi}{P_g}x\right), \tag{1.46}$$

where P_g is the grating period. Taking the Fourier transform of this transmission function, with respect to the spatial coordinate x, is

$$\mathcal{F}\left[T(x)\right] = \cos\left(\frac{\phi}{2}\right)\delta(k_x) + \sin\left(\frac{\phi}{2}\right)\sum_{\substack{n,odd \\ n=-\infty}}^{\infty}\frac{2}{\pi n}\delta\left(k_x - \frac{n\pi}{P_g}\right). \tag{1.47}$$

These diffraction orders are the classically allowed trajectories we will integrate along in the model expanded upon in Chapter 4. The Fourier transform of the grating transmission function gives us the complex amplitude that each of these diffracted paths acquires following the phase grating. The interference pattern seen at the camera can be modeled by computing the phase accumulated along all neutron paths created by the diffraction orders in Eqn. (1.47) from all three gratings in the 3-PGMI. Neutron paths at the camera detected by the same pixel interfere, producing a pattern at the camera location. With this, a Monte Carlo simulation of the 3-PGMI can reproduce the interference pattern at the camera, where the phase along classical neutron trajectories is calculated with Eqn. (1.22). The neutron angle, wavelength, and position will be varied in this Monte Carlo model based on experimental parameters. We can also use Eqn. (1.47) to compute the expected phase shift arising from translating each grating (G_i) by a displacement Δx_{G_i},

$$\Delta\phi_G = \frac{2\pi}{P_g}(\Delta x_{G1} - 2\Delta x_{G2} + \Delta x_{G3}), \tag{1.48}$$

which was verified experimentally [38].

1.5 Measuring the Gravitational Constant

The fundamental motivation to develop a neutron interferometer capable of measuring phase shifts induced by source masses on the order of 1 tonne is the persistent discrepancies between state-of-the-art measurements of G. In the two centuries since Henry Cavendish first performed the precision measurement of G, uncertainty in its measured value has only reduced by two orders of magnitude [78]. That experiment used a torsion balance to measure the attractive force from two source masses [79], an experimental design that has been refined and enhanced significantly. These experiments can be classified into

- Torsion Balance
- Suspended Body
- Beam Balance

- Atom Interferometry

which will each be outlined here. The torsion balance is by far the most common method of measuring G, with 11 of the 16 measurements in CODATA 2022 using some variation of this method [80]. All of these torsion balances, including that of Cavendish, consist of a test mass suspended by either a fiber or a strip. These balances then measure a change in either the position or motion of the test mass. In the case of measuring G, this change is induced by the introduction of source masses, which are positioned to create a restoring force. Depending on the operating mode of the torsion balance, this change in the test mass may be in the form of an altered oscillation frequency, as the test mass twists [81], or the angular acceleration may be *compensated* by an additional turntable that negates anelastic fiber properties [82]. Other experiments use the *suspended-body* method, where each reflector of a Fabry-Perot cavity is suspended, allowing source masses to alter the cavity distance [83, 84]. The 2 experiments in CODATA that do not fit in the above categories are UZur-06 and LENS-14, as labeled in [80]. For UZur-06, a beam balance was used to measure the force applied to two suspended test masses by two tanks of mercury, acting as source masses [85]. The LENS-14 experiment used two laser-cooled atom clouds to measure the gravitational phase shift induced by source masses in two configurations [74].

Of the 16 measured values of G in the 2022 CODATA publication, 15 rely on some form of pendulum. The persistent disagreement between these values points to an unknown systematic effect affecting most of these measurements, but this cannot be truly ascertained without new experiments that possess independent sources of uncertainty. To that end, this thesis will build toward an experimental design to use a three-grating neutron PGMI to measure G. As we progress towards that result, there are several applications of the techniques and analogies that have been highlighted so far that can be leveraged to develop novel structured wave devices with both light and neutron optics.

Chapter 2

Applications of Prism Potentials

2.1 Triangular Arrays of Refractive Prisms

In Section 1.2, we discussed some of the limitations of neutron optics, namely the low neutron flux produced by modern sources compared to what is available in X-ray or electron beams. This problem is exacerbated by the near unity index of refraction for neutron interactions with all measured materials, preventing high-efficiency lenses from being manufactured as they are in light optics. These challenges motivated the development of a neutron Fresnel prism, enabled by high-aspect ratio prisms machined from aluminum via a diamond turning machine.

The contents of this chapter were published on March 13, 2023 as "High-Transmission Neutron Optical Devices Utilizing Micro-Machined Structures" [1]. Author contributions are summarized below.

- **IT, DP** Conceived the device
- **IT** Fabricated the device
- **DP, MB, MEH, MGH** performed the experiment
- **CK, BH, DP, MGH** Analyzed the data
- **CK** wrote the first draft
- **All authors** edited and contributed to the final draft

2.1.1 Introduction

Neutrons possess the unique ability to deeply penetrate materials due to their zero charge, making them unparalleled probes of bulk material. In particular, neutron optics has established itself as an indispensable tool for measuring material properties and probing internal magnetic and phonon interactions [8, 9]. In Small-Angle Neutron-Scattering (SANS) experiments, a compound refractive lens (CRL) is often used to focus an incident neutron beam. CRL devices use a series of lenses, in some cases up to 30 individual elements [86, 87, 88]. These devices, while effective, require large amounts of material to construct, resulting in a significant amount of beam attenuation. Alternatives to neutron CRL devices which circumvent these limitations include lenses that utilize magnetic fields [89, 90, 91, 92, 93, 94, 95, 96], focusing capillaries [97, 98], Wolter mirrors [99], and Fresnel lenses [100]. Recent work attempts to overcome the limited range of refractive indices available to neutrons by leveraging magnetic fields, structuring neutron wavefronts through the spin degree-of-freedom [101, 102, 5]. Other research has generated structured neutron wavefronts by applying nano-scale gratings to generate orbital angular momentum states [103].

In addition to SANS methods, neutron optics has expanded to include a wealth of techniques from polarized neutron experiments [104, 105, 106], single-crystal interferometers [107, 108, 109, 110, 111], and grating-based neutron interferometers [38, 37, 112, 113]. The first neutron interferometer was built with two prisms that caused Fresnel interference by means of wave front division [16]. With this device, a path separation of only 60 µm was obtained, which was later improved to a few centimeters with a perfect crystal Mach–Zehnder interferometer relying on Bragg diffraction [114]. The perfect crystal interferometer allowed for a number of investigations on neutron properties and interactions with unprecedented precision [115, 46, 64, 27, 116] but suffered some important drawbacks, including a acceptance and difficulty of fabrication [117, 118, 119, 120].

Utilizing a diamond turning machine, we have fabricated a high aspect ratio structure of refractive prisms that deflects a neutron beam. In this work, we demonstrate a functioning triangular array refractive prism (TARP) with neutrons at the BT-5 Ultra-Small-Angle Neutron-Scattering (USANS) instrument located at the National Institute for Standards and Technology (NIST) Center for Neutron Research (NCNR) facility [121]. Experimental results are compared to theoretical predictions based on Snell's Law. The effects of

manufacturing imperfections are simulated and compared to experimental USANS results. The TARP functions as a Fresnel prism and enables prism-based neutron interferometers to create path separations larger than previously possible. The micro-prisms used in this TARP device also enable the construction of next-generation neutron-focusing devices.

2.1.2 Materials and Methods

Micro-Prism Fabrication

High-aspect ratio prisms can now be manufactured due to the availability of an ultra-high-precision machining center (Moore Nanotech 350FG [122]) which features C-axis control and live tooling. The individual prisms were fabricated from a 5052-O aluminum ring of 38 mm outer diameter (OD), 25 mm inner diameter (ID), and thickness of 250 µm that is held on an aluminum chuck. The full aluminum ring is shown, after machining was complete, in Figure 2.1a. This accommodates mounting by a wax (Crystal bond 509-3), allowing the aluminum ring to be dismounted via either heating or dissolving the wax in acetone. The choice of material, fully annealed 5052-O aluminum, was dictated by its strength and formability, coupled with the material's heat resistance, allowing the aforementioned wax to be heated without damaging the finished aluminum prisms. First, the backside of the ring is turned using diamond tooling to create a flat surface with a surface finish of 20 nm roughness average (Ra). The now flat reference face is remounted to the chuck to ensure a seating of better than 3 µm parallelism with the chuck face. The remounted ring is then segmented radially by an auxiliary milling spindle into pieces 5.4 mm wide at their base and 8.5 mm wide at the prism apex, the segmented ring is shown in Figure 2.1b. The finishing operation involves diamond turning a flat face with a 140 µm target thickness from 25 mm ID to 29 mm OD transitioning into a conical face, starting at 29 mm OD and tapering to zero thickness at 37 mm OD.

The 2° angle of the radial cross-section of each segment has an uncertainty of 0.02° arising from two sources. The first uncertainty is due to the parallelism of the front and back faces, which was measured by the maximum variation in thickness (3 µm) at the OD of 38 mm after facing a ring without conical features, resulting in an uncertainty of 0.005°. The second, and more significant source, of uncertainty arises from the fact that the angled prism segment is machined radially, as shown by black dashed lines in Figure 2.1b which indicate the 2° surface. This causes the prism surface at the edge of each prism to be a hyperbolic curve, as opposed to the uniformly angled surface which would be expected of a prism. This curved surface, when fit to a straight line, will have a surface angle of 1.98°, as opposed to the 2.00° flat surface in the middle of each prism segment. Therefore,

the maximum angle deviation due to the conical shape of each segment is determined to be 0.02° at the region furthest from the center line. The most unpredictable error in the deviation from a perfect prism is due to the extremely thin apex of the prisms, which deforms at the slightest pressure. Heating the chuck to release the segments showed severe buckling of all apices likely attributed to uneven rates of thermal expansion. Therefore, the piece was unmounted by dissolving the mounting wax in acetone instead of raising the temperature. After releasing the segments and gently cleaning, without agitation, the segments were assembled into the TARP device. The base of each prism (shown in Figure 2.1b with a base length of 5.4 mm) was placed in an aluminum vice, stacking subsequent prisms on this flat base segment. A fine pitch screw was then used to squeeze these flat regions at the base of the prism together, resulting in an assembled TARP device.

The manufacturing quality of the TARP was first evaluated using white-light interferometry and optical microscopy. Fitting sampled surface height values along the blue line in Figure 2.1c, we find the surface to be angled at $1.999° \pm 0.001°$, matching the designed surface angle of 2°. The residual of this fit, shown in Figure 2.1d, indicates that, within this region, surface form is straight to within $\pm 0.1\,\mu m$. Once this annulus is cut and assembled, the alignment and spacing of prisms in the TARP can be measured by comparing the separation of the prism apices at different locations on the optical microscope image. Figure 2.2a shows red points where the prism peak is detected along each vertical slice of pixels. Each series of red points corresponding to a single prism are then linearly fit to extract a series of slopes, m_i, and intercepts, b_i. Figure 2.2b shows these y-intercepts, b_i, which are again linearly fit to determine that the spacing between prism peaks is $141\,\mu m \pm 3\,\mu m$. The slopes, m_i, show a variation in the alignment of these prisms with a standard deviation of $\pm 0.3°$. A histogram of these slope values can be seen in Figure 2.2c. The high aspect ratio, 14.3, suggests that the TARP prototype would be capable of deviating a neutron beam equivalent to a single prism that is 3 mm wide and 85.9 mm in height.

The refractive characteristics of the TARP were tested using cold neutrons at the BT-5 USANS instrument located at the NCNR facility [121]. The experimental arrangement is shown in Figure 2.3a.

Device Modelling

The neutron ray deflection was calculated by propagating rays across material boundaries using Snell's Law. Taylor-expanding the resulting equations about $n = 1$, we can obtain the well-known approximation for prism deflection [123]. Applying this to each side of the first and second prism that a neutron encounters, we find deflection angles, $\Delta\theta_{a,i}$, where

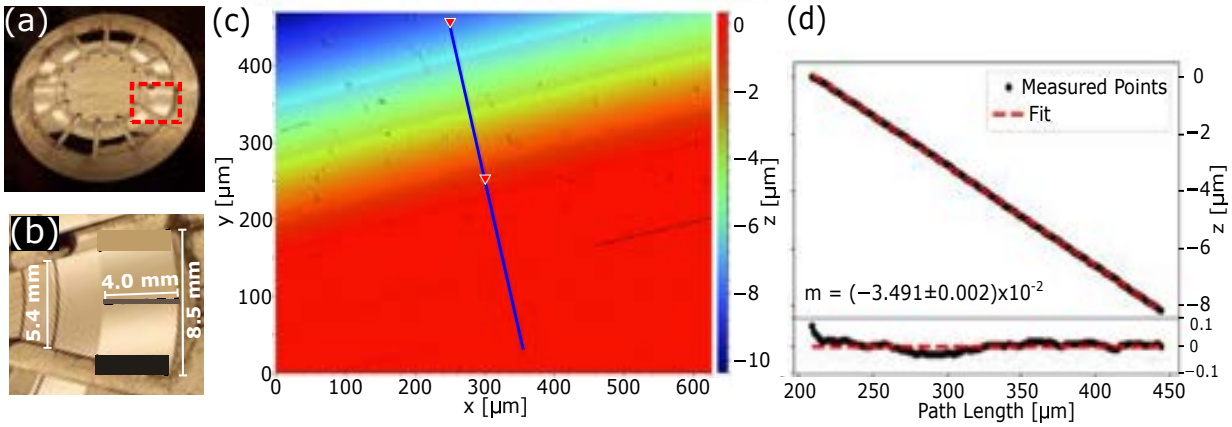


Figure 2.1: (**a**) Micro-prisms before assembly into the TARP. Here, the angled faces of each prism can be seen tapering radially, and each prism has been segmented into equal pieces. These pieces are then assembled with the non-angled section at the base of each prism. A single prism element, expanded in (**d**), is shown within a red box. (**b**) Enlarged image of a single prism segment whose angled surfaces, indicated with black dashed lines, are machined to 2°. Labels indicate prism base width, peak width, and prism height. Note that these width dimensions are the cord length of segmented rings which form the base and apex of the prism. (**c**) White light interferometry data showing the machined surface of the prism segment. Density plot colour shows surface height, where the flat base of the prisms is shown in red and the sloped face can be seen with varying colours. Surface imperfections can be observed which correspond to a surface finish of 20 nm roughness average (Ra). Points along the blue line were sampled to measure the angle of this surface. (**d**) These points show an angle of $1.999° \pm 0.001°$. This angle matches the designed surface angle of 2°. The residual plot shown below indicates that within this region, the surface form is straight to within $\pm 0.1\,\mu m$. Figure reproduced from [1].

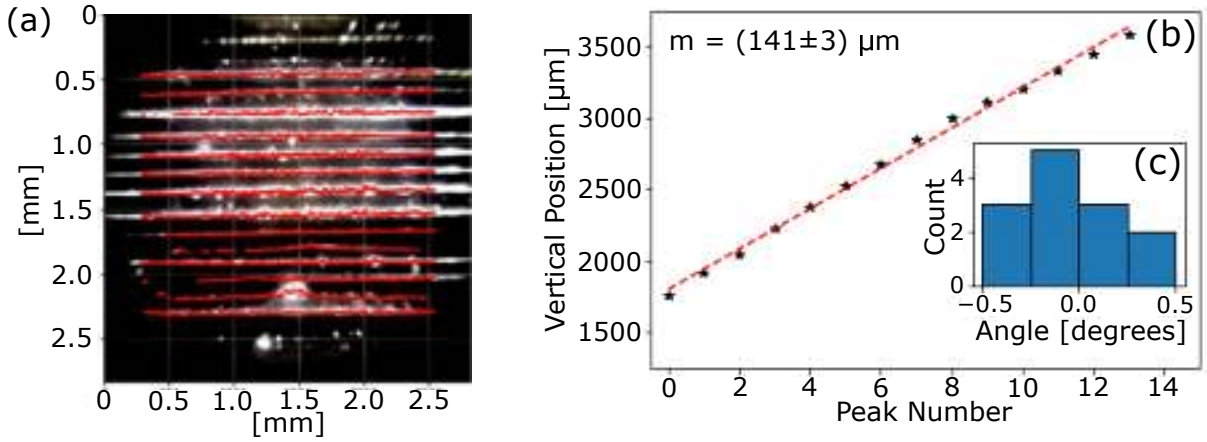


Figure 2.2: (**a**) Microscope image of assembled TARP device with peak locations labelled with red dots. Peaks are detected along each vertical slice of pixels. Peak locations along a single horizontal prism are fit to a line which is then used to determine prism spacing and alignment. (**b**) The y-intercepts of each linear fit from (**a**) are plotted and fit to a line. The slope of this line corresponds to the average spacing of the prism peaks. The y-intercept of this line indicates the position of the first prism peak relative to the top of the camera and therefore is not shown in this plot. (**c**) Histogram of the slope of fit lines from (**a**). This shows that prism alignment has a standard deviation of $\pm 0.3°$. Figure reproduced from [1].

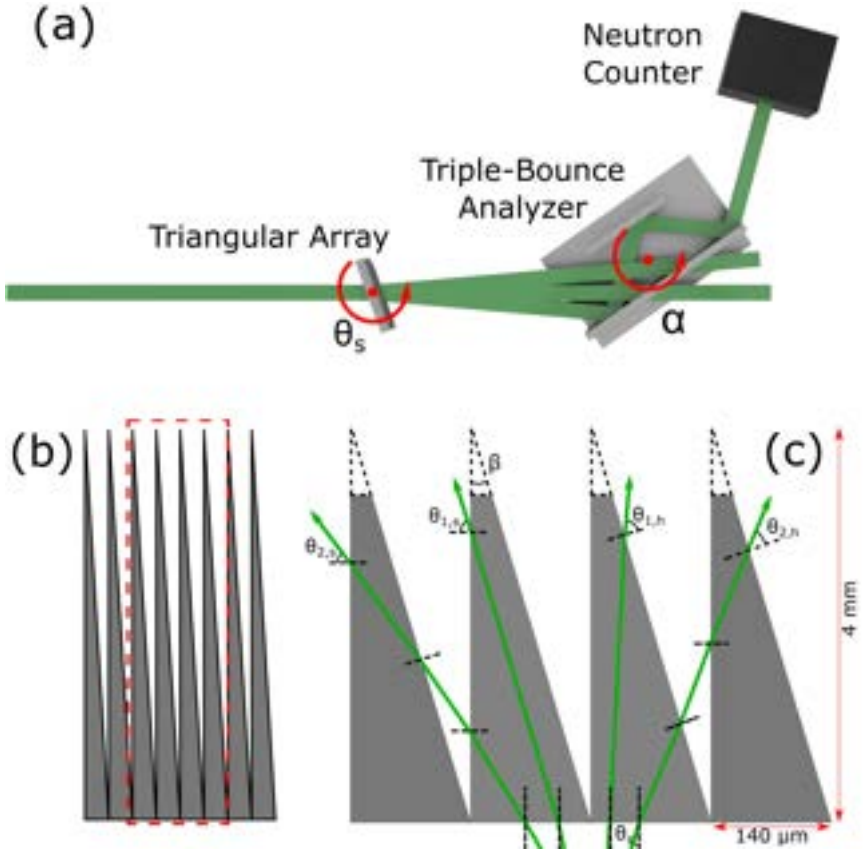


Figure 2.3: (**a**) Experimental apparatus used to measure beam deviation from the TARP. Small angle deviations are measured by utilizing a crystal applying Bragg diffraction to select a particular deviation angle caused by the sample. The neutron beam had a wavelength of $2.38\,\text{Å} \pm 0.05\,\text{Å}$, accounting for the reduction in wavelength at the sample due to Bragg refraction off the monochromator and the slit placed before the TARP device. The angles α and θ_s correspond to the analyzer angle and sample angles, respectively. (**b**) Scaled schematic of TARP, where the red dashed box indicates the region which is magnified and shown with an exaggerated scale in (**c**). The aspect ratio shown here (>14) is correct for the prototype TARP. (**c**) Schematic of the TARP showing the arrangement and length scale of each prism. The neutron path and corresponding outgoing angle of the four possibilities modelled in Equations (2.1) to (2.4) are indicated as green lines. Imperfect prism apices are modelled as flat tops, shown here, with dashed lines indicating the ideal prism apex. Figure reproduced from [1].

the subscript a indicates which prism side a neutron exits, and subscript i denotes the number of prisms a neutron has encountered.

$$\Delta\theta_{h,1} \approx (1-n)[\tan(\pi/2-\beta-\theta)+\tan(\theta)], \tag{2.1}$$
$$\Delta\theta_{s,1} \approx (1-n)[\tan(\pi/2-\theta)+\tan(\theta)], \tag{2.2}$$
$$\Delta\theta_{h,2} \approx (1-n)[\tan(\beta-\pi/2-\theta-\Delta\theta_{h,1})+\tan(\pi/2+\theta+\Delta\theta_{h,1})], \tag{2.3}$$
$$\Delta\theta_{s,2} \approx (1-n)[\tan(-\pi/2+\theta+\Delta\theta_{s,1})+\tan(\pi/2-\theta-\Delta\theta_{s,1}+\beta)], \tag{2.4}$$

for rays incident at an angle, θ, to a prism of angle β. Imperfections in the prism manufacturing will result in flat prism apices, as shown in Figure 2.3c, the effect of which can be modelled by applying Snell's Law directly to neutrons which encounter these flat apex regions.

Using these approximations, we can model the TARP with neutron rays in a Monte Carlo simulation. These rays have a wavelength and initial angle that is drawn from two Gaussian distributions, corresponding to the BT-5 instrument's wavelength range and the Darwin width of the monochromator, respectively [121]. Neutron rays possess an additional angle, correlated to its wavelength, labelled θ_D, caused by a monochromator which functions via the Bragg diffraction. From here, the rays are propagated across each prism boundary, with Snell's Law dictating the angular deflection. Prisms in this model have flat prism apices, as opposed to perfectly sharp peaks. This effect can be seen in Figure 2.3c, where the outline of a perfect prism apex is shown with a dotted line. The flat apex of these prisms models the effect of buckling at the thinnest region of the prisms. Neutrons may also encounter adjacent prisms after exiting the first prism. The resulting beam deviation is then the difference between the final propagation angle of each ray and the incident ray angle. As the analyzing crystal also operates via Bragg diffraction, the angle θ_D is subtracted from the final angle of each ray. This procedure is repeated at each sample angle with the Gaussian distribution of initial ray angles shifted by the sample angle.

2.1.3 Results

At the BT-5 instrument, three sets of USANS data were taken, each consisting of a series of rocking curves at different ranges and step sizes of both sample and analyzer angles. In total, 46 sample angle positions were measured with 213 analyzer angles. These three datasets were then combined by linearly interpolating the lower resolution scans such that

all three datasets had resolutions of $(1 \cdot 10^{-4})^\circ$ in the analyzer angle and 0.1° in the sample angle. With equal resolutions, these three datasets can then be combined by averaging regions where multiple datasets overlap, producing the density plot shown in Figure 2.4a. In order to extract meaningful values from a fit of the approximate deviation in Equations (2.1) to (2.4), the sample angle axis of the experimental data must be aligned with $\theta_s = 0^\circ$, as defined by the device. This can be achieved by comparing experimental plots of a constant sample angle, θ_s, to the simulation. At $\theta = -1^\circ$ for $\beta = 2^\circ$, the primary scattering peaks are of equal magnitude and this feature can be used to align the sample. The comparison of simulation to the experiment shown in Figure 2.4b allows us to specify this point in the experiment as $\theta_s = -1^\circ \pm 0.12^\circ$. Furthermore, the Lorentzian-like tails of the scattered peaks arise due to misalignment of individual prisms in the TARP, as well as variance in the neutron wavelength and incident angle at the device. The effective wavelength distribution and divergence angle of the instrument, including apertures used in the experiment, can be measured by fitting the peak shape at $\theta_s = -1^\circ$, assuming a Gaussian distribution for both values. This results in a wavelength range of $2.38\,\text{Å} \pm 0.05\,\text{Å}$ and initial ray angle of $\pm(0.38 \cdot 10^{-3})^\circ$. The central peak seen in experimental data can be modelled by accounting for neutrons which exit a prism through the flat apex shown in Figure 2.3c. Using a least-squares fit, the average prism apex width was $w_{apex} = 15.0\,\mu\text{m} \pm 0.5\,\mu\text{m}$.

Figure 2.4a shows a false-colour representation of the neutron intensity from the single-pixel detector at each sample angle, θ_s, and Bragg analyzer angle, α. From the data, a central peak along $\alpha = 0^\circ$ can be seen at each sample angle, with two roughly symmetric peaks diverging toward either positive or negative analyzer angles, α. Four peaks can be observed in total, with the two primary peaks nearest to $\theta_s = -1^\circ$ arising due to refraction from a single prism, while the secondary peaks arise from neutron rays that exit the initial prism and refract within the adjacent prism.

Agreement between theory and experiment can be demonstrated by comparing the theoretical material index of refraction to the value obtained by fitting Equations (2.1) to (2.4) with a free parameter $(1 - n)$. The data were fit as shown in Figure 2.4a, and the resulting material index value is $n = 1 - (1.95 \pm 0.09) \cdot 10^{-6}$, which is within 95 % confidence agreement with the expected value of $1 - n = 1.93 \cdot 10^{-6}$ for the aluminum alloy used in these prisms.

The simulated beam deviation is shown overlaying the experimental data in Figure 2.4b. From this, we can see qualitative agreement between the simulated prisms and our experiment using the theoretical material index. The undeviated central peak seen in the USANS measurement is accounted for by a prism with a flat apex 15 µm in width. We can define the relative efficiency of this manufactured TARP as the ratio between the expected beam

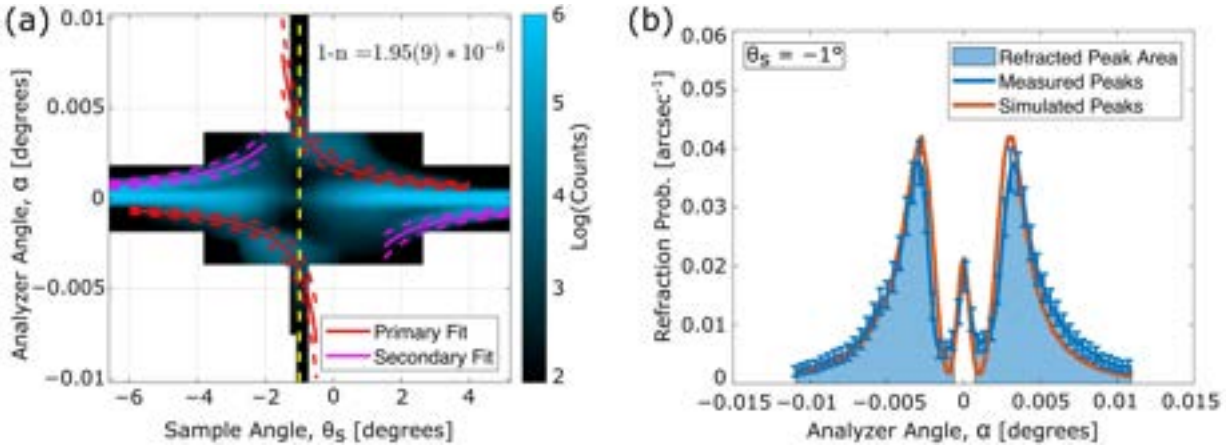


Figure 2.4: (**a**) Ultra-small-angle neutron-scattering (USANS) results from the TARP where a false colour corresponds to the logarithm of counts. Scattering peaks have been fit to a Gaussian to extract the peak maximum. Red and pink lines correspond to first- and second-order theoretical scattering curves, respectively, fit to these peaks. Curves are calculated via Equations (2.1) to (2.4), accounting for the BT-5 wavelength distribution, and fit with a free-fit parameter for material index. Dashed lines show the 95 % confidence interval of this fit. This fit returns a material index of $n = 1-(1.95\pm0.09)\cdot10^{-6}$. The dashed yellow line indicates a sample angle of $\theta_s = -1°$. (**b**) Comparison of the TARP USANS measurements (blue) with Monte Carlo simulation (red) taken at $\theta = -1°$. The shaded area in blue denotes the region where beam deviation is expected from the simulation of an ideal TARP, with perfect apices. Uncertainty on neutron counts is shown for a subset of analyzer measurement angles. Neutron ray deviations from USANS experiments with the TARP show qualitative agreement with simulations. Figure reproduced from [1].

deviation area for an ideal TARP (shaded area in Figure 2.4b) and the total area of the measured refraction peak. Therefore, we find that at $\theta_s = -1°$ our device has a relative efficiency of $\eta_{-1°} = 93.2\,\%$. Two other sample angles of interest are when $\theta_s = \beta$, which has $\eta_{-2°} = 71.5\,\%$, and when the sample is perpendicular to the beam, $\eta_{0°} = 62.9\,\%$.

2.1.4 Discussion

We have designed and fabricated a neutron optical device which utilizes an array of high-aspect ratio micro-prisms to deviate a neutron beam with high efficiency. The TARP has been modelled with Snell's Law and experimental data have been fit to measure material

index of refraction, which agrees with the accepted value for aluminum 5052-O. The fabrication methods described here can be applied to a refractive prism neutron interferometer or to construct a Fresnel lens with micro-prisms. To compare the TARP with current state-of-the-art neutron optical devices, we plot a quality-factor, similar to the figure-of-merit in the Ref. [124], which will quantify the total beam deviation normalized to the attenuation caused by each neutron prism design.

There are two obvious methods of combining the beam deviation, $\Delta\theta$, and transmission fraction, T, first these two values can be multiplied, $Q_1 = \Delta\theta \cdot T$, and the second by dividing beam deviation by the absorption fraction, $Q_2 = \frac{\Delta\theta}{1-T}$. We will calculate beam attenuation using the penetration depth, δ, and the average length of material a neutron propagates through, t, thus, $T = e^{-t/\delta}$. Assuming a constant prism base width, w, for every design, the average thickness a neutron penetrates will be given by $t = \frac{w}{2\tan\beta}$. Figure 2.5a illustrates the significant increase in prism quality-factor, Q_1, as the prism angle decreases. Different materials are considered, and plotted as red lines of different styles (i.e., dotted, dashed). Prism angles utilized in other neutron prism experiments are shown in solid vertical lines, with the TARP shown in black. The prisms of the Ref. [125] are shown in red, and both prisms described in the Ref. [124] are shown in dark and light blue.

Our analysis thus far has considered neutrons incident to the base of a prism as in the TARP design, but there is a second case that is of interest. To describe the deviation of a neutron in the first case, as shown in Figure 2.5b, we can use Equation (2.1) to estimate a beam deviation,

$$\Delta\theta_1 \approx \frac{1-n}{\beta}, \tag{2.5}$$

where the prism angle, β is again in radians. For the second case, consider a neutron incident to the side of an isosceles prism as shown in Figure 2.5c, where the neutron deviation is given by

$$\Delta\theta_2 \approx 2(1-n)\tan\left(\frac{\xi}{2}\right), \tag{2.6}$$

where the prism angle, ξ is in radians.

Equation (2.5) describes a neutron deflected by a prism in the same orientation as the TARP, therefore the prism angle, $\beta \sim 1°$. Equation (2.6) applies to neutron prisms similar in design to the Ref. [124, 125], and therefore has a $\xi \sim 90°$. Plotted in Figure 2.5d is a comparison of the neutron deviation from these designs, both as a function of prism angle, ξ, as labelled in Figure 2.5b,c. This plot clearly shows the significantly increased neutron deviation which can be achieved using a TARP design with small prism angles.

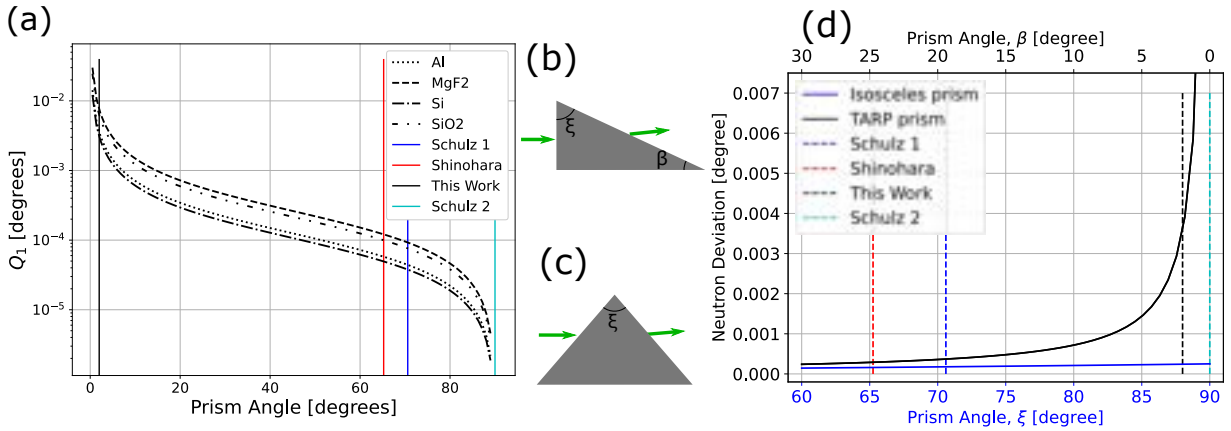


Figure 2.5: (**a**) Quality-factor, Q_1, for a neutron prism, calculated using beam deviation and neutron transmission fraction, $Q_1 = \Delta\theta \cdot T$, as a function of prism angle. Here, it is clear that smaller prism angles provide a significant increase in prism quality-factor. Note that this plot is shown in logarithmic y-scale. Different materials are considered, and as black lines of different style (i.e., dotted, dashed). Prism angles utilized in other neutron prism experiments are shown in solid lines, with the TARP shown in black, the prisms of the Ref. [125] shown in red, and both prisms described in the Ref. [124] shown in dark and light blue. (**b**) Schematic of prism orientation used in the TARP device, with both the prism angle β and complementary angle, ξ, labelled. (**c**) Schematic of prism orientation used in the Ref. [125, 124] with prism angle, ξ, and neutron ray shown as a green arrow. (**d**) Comparison of neutron deviation from prism orientations shown in (**b**,**c**) plotted in blue and black, respectively. Figure reproduced from [1].

The beam fraction deviated by the triangular array, seen in Figure 2.4c, indicates that this device can effectively deviate 93.2 % of the transmitted beam intensity. This demonstrates a significant increase in efficiency compared to previous neutron optical devices, such as the CRL device, whose absorption and scattering from manganese alone reduces the neutron beam down to 84.7 % transmission.

The beam deviation offered by the TARP can be used to construct a neutron interferometer. Early experiments in neutron interferometry made use of refractive prisms to coherently separate 4.4 Å neutrons by 60 µm over a 10 m flight path [16]. Utilizing the TARP examined in this work, a separation of 870 µm is achievable with the 2.38 Å neutrons used to test the sample, implying that a separation of 3 mm is realizable with 4.4 Å neutrons over 10 m. While the coherence properties of beams refracted by the TARP have not been studied, a neutron interferometer with a beam separation of 60 µm could be achieved with a beam-line of less than 1 m using two TARP devices similar to what was shown here.

The fabrication methods described here can also be applied to construct a Fresnel lens of micro-prisms to achieve shorter focal lengths than what is currently accessible through neutron lenses, with an intensity gain significantly larger than existing lenses. The reduction in material thickness also significantly lowers neutron losses due to absorption and scattering, while also allowing the possibility of working with expensive materials such as Nickel isotopes or magnetic materials.

2.1.5 Applications

The above manuscript, published in Quantum Beam Science, briefly mentioned a TARP-style devices applied to create a Fresnel lens. Here, we will show these designs and quantify the expected gain of such a device, and outline how a TARP can be used as a monochromator or neutron spectrum analyzer.

Neutron Fresnel Lens

Advancing the fabrication techniques in [1] will allow for prisms of smaller angle. With that, a neutron Fresnel lens can be constructed with prisms of varying angles, down to

Figure 2.6: Schematic of neutron Fresnel lens using a series of variable angle triangles made with a high index material. Deflection of neutrons is given by $\theta = \pi/2 - \alpha - sin^{-1}(n(1-\alpha^2))$ for neutrons traveling perpendicular to the device. Variations from perpendicular change the neutron deflection angle by a negligible amount for $\theta_i = 1^\circ$

1°, assembled around a flat central region, as shown in Figure 2.6. A collimated neutron beam, incident on this Fresnel lens, could then be focused to a spot sized equal in area to that central region.

A neutron normally incident to these triangles will have an outgoing angle of $\theta = \pi/2 - \alpha - sin^{-1}(n(1-\alpha^2))$. For example a triangle with $\alpha = 1^\circ$ of MgF_2 would deflect a neutron beam by 0.26°. With those prisms at the outer edge of the Fresnel lens, subsequent prisms within the device must be fabricated with angle

$$\tan\theta_n = \frac{R - t \times n}{R} \tan\theta_0, \tag{2.7}$$

where t is the thickness the prisms (equal in this design), R is the radius of the fully assembled lens, n is an index that starts at the outer most prism (equal to zero) and increments toward the center, and θ_0 is the deviation angle of the outermost prism. A series of 60 prism, assembled about a flat region 1 mm wide creates a Fresnel lens that focuses a 10 mm wide beam to a spot size of 1 mm, with a focal distance of 1.1 m.

TARP Monochromator

Following the publication of [1], a correspondence with Dr. Robert Cubitt raised the possibility of applying the TARP to create a monochromator or spectrum analyzer that could

replace costly chopper spectral analyzer systems [126]. Dr. Cubitt's work demonstrated that prisms could be applied to neutron refractometry to enable inexpensive wavelength analysis [127, 128]. Using the estimates for the D17 instrument at ILL from [127], a chopper can achieve wavelength resolutions below 1% but at the cost of significantly reduced neutron flux. In chopper systems, the resolution for a particular wavelength, λ is given by

$$\frac{\Delta\lambda}{\lambda} = \frac{\theta_C}{360^\circ}\frac{\lambda_{\max}}{\lambda}, \tag{2.8}$$

where θ_C is the opening angle of the chopper, $\lambda_{\max}$ is the longest wavelength able to pass through the chopper (at a particular setting). Using the same beam collimation and mean wavelength as [1], achieving a 1% resolution in wavelength would require a TARP fabricated from aluminum with a prism angle $\alpha < 0.5^\circ$. In this design, a neutron beam incident on the TARP as shown in Figure 2.5(c) is refracted by an angle proportional to wavelength. The wavelength spread of the beam can then be set by the width of and distance to a slit placed down beam of the TARP, which transmits $\approx 94\%$ of the incoming neutron beam. While the fabrication of these prisms would be extremely challenging, the gain in neutron intensity over a chopper would be on the order 100, as the chopper at D17 uses an opening angle of 3°, reducing neutron flux by a factor of $3^\circ/360^\circ$. A Fresnel prism device for neutron spectrum analysis also offsets a significant reliability issue with chopper devices. As a chopper is effectively a massive flywheel with an angular slice removed, they are subject to extreme forces caused by the misalignment between the center of mass and the rotation axis of the device. The solid-state and stationary nature of the TARP eliminates these challenges.

2.2 Spin-based collimator

Just as traditional prisms resulted in significant attenuation to a neutron beam, neutron collimators result in similarly undesirable neutron loss. Many neutron systems use Soller slit collimators, where a series of parallel, equally spaced absorbing plates are stacked, restricting the range of angles at the output of the device [129]. As these plates have finite thickness, there is a fraction of the neutron beam which is completely blocked at the input of the collimator. While the peak transmission of modern collimators is often quoted at 95%, this applies to collimators that are up to 3 m in length and drops off rapidly for non-zero divergence angle settings [130]. Once constructed, modifying the collimation angle of these designs is difficult. This both restricts the available settings of neutron collimators

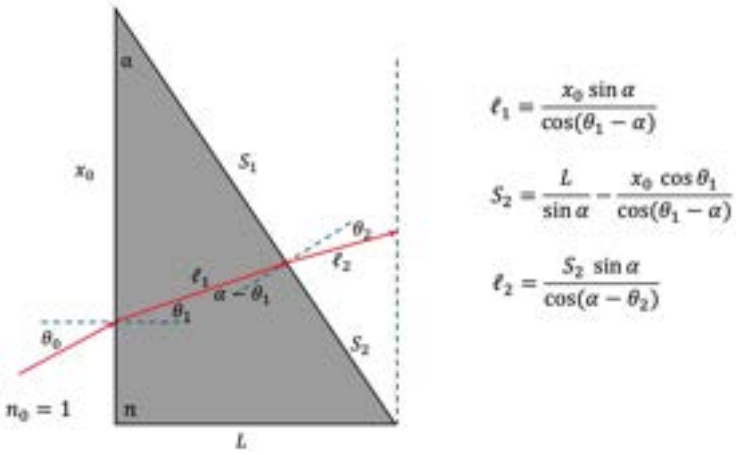


Figure 2.7: Angle and path labels for a neutron trajectory incident on a triangular prism potential region with index of refraction n. A vertical dotted line shows the detection plane where where the accumulated phase of a neutron along the red-line trajectory is of interest.

and requires neutron facilities or experimenters to source a variety of collimators with different designed collimation angles.

We can leverage neutron polarizers and prism potentials containing magnetic fields to design a new neutron collimation device [131]. To do so, we will compute the phase difference $\Delta\gamma$ between neutron polarization states beam incident on a series triangular-shaped magnetic potential regions.

2.2.1 Prism Potential Phase

As we discussed in Chapter 1, Snell's law shows that neutron spin states will take different trajectories through a magnetic potential region. Figure 2.7 shows the trajectory of one polarization state, passing through a triangular potential region with index n. As polarization states have different indices of refraction, we can use these equations to find the trajectory for each. Before the prism, each spin state acquires the same phase. For the first path segment in the prism, ℓ_1, the phase difference is due to both the difference in path lengths (as a result of the different angles given by Snell's Law) and the different index of refraction for each polarization state,

$$\Delta\gamma_{\mathrm{I}} = k_0(n_{\uparrow\uparrow}\ell_{1,\uparrow} - n_{\downarrow\uparrow}\ell_{1,\downarrow}), \tag{2.9}$$

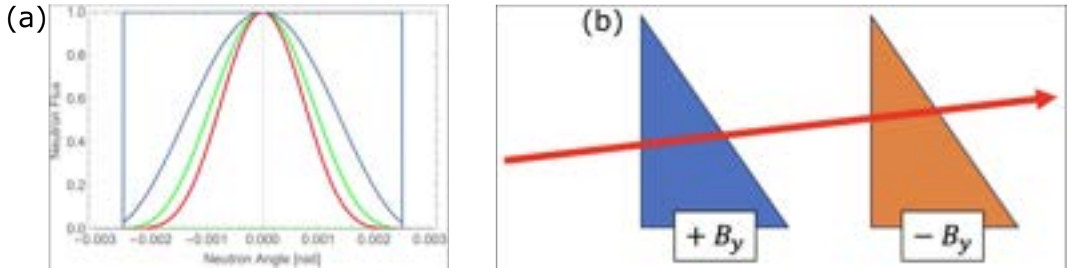


Figure 2.8: (a) Neutron flux for two prism arrangement of spin polarizing collimator. Rectangular region denotes the input neutron angle to the collimating device. Blue, green, and red curves show neutron flux after one, two, and three collimating elements in series. Collimating elements includes two magnetic prisms with opposite field directions and a polarizer. (b) Schematic of two prism arrangements. An example polarized neutron path is shown as a red arrow. Magnetic field direction is denoted by labels and prism coloring.

where the path length is,

$$\ell_{1,\uparrow/\downarrow} = \frac{x_0 \sin\alpha}{\cos(\theta_{1,\uparrow/\downarrow} - \alpha)}. \tag{2.10}$$

The path segment after the prism has a phase difference, $\Delta\gamma_{\mathrm{III}}$ given by the difference in propagation length between the states shown in Figure 2.7 and the vertical detection plane.

Continuing to propagate this path across two prisms, in the arrangement shown in Figure 2.8(b), the only modification that is needed is to compute the position that each path enters the second prism. The phase difference accumulated within the second prism is also given by Eqn. (2.9), where the path length within the prism is now

$$\ell_{2,\uparrow/\downarrow} = \frac{x_2 \sin\alpha}{\cos(\theta_{2,\uparrow/\downarrow} - 2\alpha)}, \tag{2.11}$$

where x_2 is the position from the prism top that a neutron trajectory enters the prism. Starting from x_0, the position both trajectories enter the first prism, we can compute the position that a path exits the first prism

$$x_1 = x_0 - \ell_1 \sin\theta_1, \tag{2.12}$$

and continue to the position that the path enters the second prism

$$x_2 = x_1 - (L + D - \ell_1 \cos\theta_1)\tan(\theta_2 - \alpha), \tag{2.13}$$

where L is the bottom side-length of the prism and D is the spacing between prisms. This allows us to calculate the total phase difference, including the phase difference accumulated between the prisms.

2.2.2 Neutron Approximation

The energy of neutrons we are interested in is somewhere between 1 meV and 100 meV, while the energy of magnetic field potential is $38\,\mathrm{peV\,G^{-1}}$. Therefore, even for magnetic fields $1T$ in strength, the index of refraction differs from unity by 10^{-6}. Therefore, the index of refraction within this potential can be approximated as,

$$\begin{aligned} n &\approx 1 - \frac{mV_{mag}}{\hbar^2 k_0^2} \\ &\approx 1 - \frac{m\gamma|B|}{2\hbar k_0^2}. \end{aligned} \tag{2.14}$$

Therefore, with $\Delta n \equiv 1 - n$

$$\sin\theta_1 = \frac{\sin\theta_0}{n_1} \implies \sin\theta_1 \approx \sin\theta_0(1 + \Delta n), \tag{2.15}$$

with the approximation $\theta_{i,\uparrow} \approx \theta_{i,\downarrow} \approx \theta$, the phase difference between polarization states is,

$$\Delta\gamma_{\mathrm{I}} \approx k_0(n_{\uparrow\uparrow} - n_{\downarrow\uparrow})\ell_1 = 2k_0\Delta n\ell_1 \tag{2.16}$$

$$\Delta\gamma_{\mathrm{II}} \approx k_0(n_{\uparrow\downarrow} - n_{\downarrow\downarrow})\ell_2 = -2k_0\Delta n\ell_2. \tag{2.17}$$

Applying this approximation to the path lengths,

$$\begin{aligned} x_2 &\approx x_0 - \ell_1\sin\theta - (L + D - \ell_1\cos\theta)\tan\theta \\ &\approx x_0 - (L + D)\tan\theta. \end{aligned} \tag{2.18}$$

Computing the total phase difference between polarization states,

$$\Delta\gamma \approx 2k_0\Delta n(\ell_1 - \ell_2) \tag{2.19}$$

$$\approx 2k_0\Delta n\frac{(L+D)\tan\theta\sin\alpha}{\cos(\theta-\alpha)}, \tag{2.20}$$

where the intensity measured, as a function of incident neutron angle, is given by,

$$I(\theta) = |\langle\psi_{x+}| e^{-i\mathcal{H}t/\hbar} |\psi_{x+}\rangle|^2 \tag{2.21}$$

$$= |\langle\psi_{x+}| e^{-i\sigma_x\Delta\gamma} |\psi_{x+}\rangle|^2 \tag{2.22}$$

$$= \cos^2(\Delta\gamma) \tag{2.23}$$

This intensity is plotted in Figure 2.8(a), where two prisms of size 6 cm in height, with an angle $\alpha = 30°$, containing a field of strength 100 G are placed between two neutron polarizers in the z-directions. Adding additional collimating devices and polarizers narrows the achievable collimation angle, shown as distinct lines in Figure 2.8(a). An neutron beam time at the NCNR polarized neutron reflectometry instrument was scheduled to test this device, but reactor shut-downs due to COVID-19 and the subsequent reactor malfunction have postponed that experiment. We can use light to experimentally demonstrate the efficacy of this polarization collimator, with some modification to the above analysis.

2.2.3 Light Approximation

Following the notation of the previous section, the index of refraction for one polarization state in birefringent quartz is $n_\uparrow = \bar{n} + \Delta n/2$, while the other is, $n_\downarrow = \bar{n} - \Delta n/2$. Therefore, the angle within the first prism is,

$$\sin\theta_1 = \frac{\sin\theta_0}{\bar{n} \pm \Delta n/2} \implies \sin\theta_1 \approx \frac{\sin\theta_0}{\bar{n}}\left(1 \pm \frac{\Delta n}{2\bar{n}}\right). \tag{2.24}$$

With the approximation $\Delta n/2\bar{n} << 1$, we can assume that the path lengths within each prism are equal, where,

$$\ell_1 = \frac{x_0\sin\alpha}{\cos(\theta_1-\alpha)}, \qquad \text{and} \qquad \ell_2 = \frac{x_2\sin\alpha}{\cos(\theta_2-2\alpha)}. \tag{2.25}$$

With Snell's Law we can compute the angle coming out of the first prism and can the position that this path hits the second prism,

$$x_2 = x_0 - \ell_1 \sin\theta_1 - (L + D - \ell_1 \cos\theta_1) \tan(\theta_2 + \alpha), \tag{2.26}$$

This allows us to simulate the effect of two birefringent prisms with opposite birefringence axes. Experimentally, identical prisms were used for both the first and second elements, and the opposing rotation axis was achieved with a half-waveplate.

2.2.4 Experiment

Using 642 nm wavelength laser and 25.4 mm diameter quartz prisms, of angle 2°, where the fast-axis of the quartz is aligned to the prism gradient, several measurements of the collimating effect of this design were tested. Figure 2.9 shows both the unpolarized and polarized results with increasing distance between the prisms.

Normalizing the intensity measured with a polarizer at the output by the unpolarized image, we can directly compare the above approximation for light with these measured results. Figure 2.10 compares the normalized intensity of the polarization collimator to theory for three distances between the prisms, showing good agreement between our approximation and experiment. When applied to the neutron case, the variable magnetic field strength of our triangular coils allows for instant changes in collimation angle limited only by power supply current and thermal limits of the coil material.

2.3 Next Steps

Demonstrating this effect with neutrons is a clear next step, with triangular prism coils already assembled and demonstrated at NCNR (see Chapter 3). Beyond this, there is another prism arrangement that produces a symmetric collimation profile about $\theta = 0$. This arrangement is shown in Figure 2.11, requiring four prisms containing equal strength magnetic fields of alternating direction. We can analyze this arrangement with the tools already developed here. In this arrangement, all neutron paths have a total path length within the prisms of $2L$. Continuing with the neutron approximations, the phase difference between polarization states after the first two prisms is

$$\Delta\gamma_{\mathrm{I}} = 2k_0\Delta n(\ell_1 - [L/\cos\theta - \ell_1]), \tag{2.27}$$

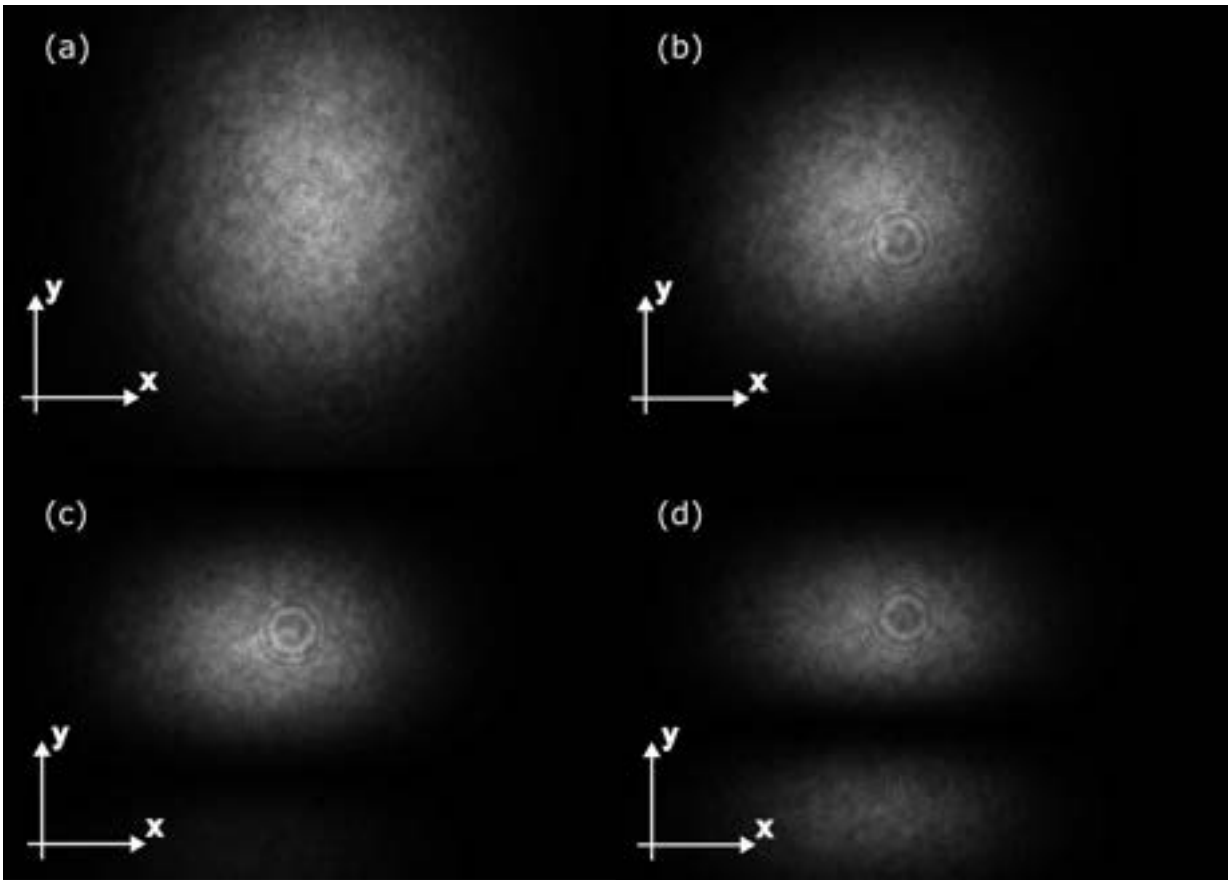


Figure 2.9: (a) Measured intensity for red light experiment without polarization filtering. (b) Measured intensity for red light experiment with polarizer after two prism arrangements shown in Figure 2.8 with prism separation of 10 cm. (c) Measured intensity for red light experiment with polarizer after two prism arrangements shown in Figure 2.8 with prism separation of 16 cm. (d) Measured intensity for red light experiment with polarizer after two prism arrangements shown in Figure 2.8 with prism separation of 19 cm. At this distance between prisms, oscillations in intensity can be observed within the infrared beam.

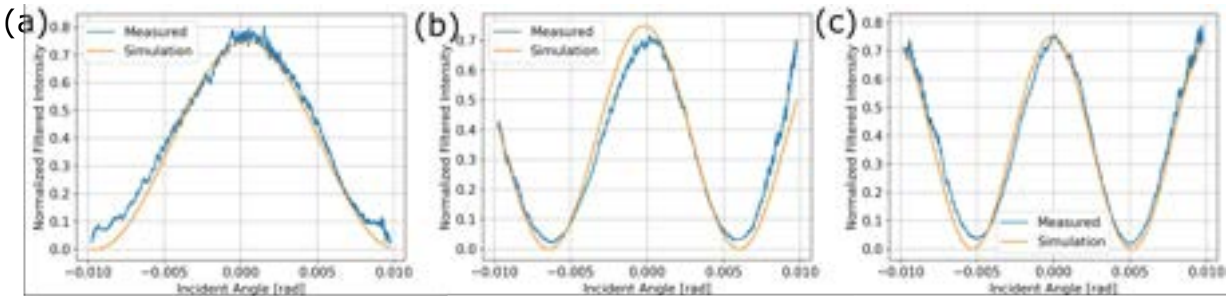


Figure 2.10: Normalized intensity measured in polarization collimator experiments with light and quartz prisms. Distance between each prism in each image is (a) $L = 10.2\,\text{cm}$, (b) $L = 16.3\,\text{cm}$, (c) $L = 19.5\,\text{cm}$. Measured intensity is compared to theory using the approximation for light in Section 2.2.3.

which can be seen by noting that path lengths $\ell_1 + \ell_2 = \frac{L}{\cos\theta}$. The same equation describes the phase difference accumulated by passing through the second pair of prisms, with an initial height given by $x_1 = x_0 - L\tan\theta$.

Figure 2.11(a) shows that this arrangement generates a symmetric collimation of the incident neutron beam, while Figure 2.11(b) illustrates the arrangement described above. The advantage of the four-prism arrangement is that the phase shift, $\Delta\gamma$ is symmetric about $\theta_0 = 0$, while the two-prism is only approximately symmetric.

With either arrangement, this polarization collimator could also be used to improve the contrast of a neutron phase-grating interferometer. In the demonstrations of the very cold neutron (VCN) interferometer by Gruber et al., slits placed between phase gratings in the interferometer selected a single pair of interfering neutron paths [34]. These slits can be replaced by polarizing collimators, selecting only these interfering orders while allowing for a wider wavelength distribution with the VCN interferometer design.

Simulating a phase grating interferometer, with grating period $2\,\mu\text{m}$ and polarization collimators between adjacent gratings, using the path integral model in Chapter 1, we can compute the expected contrast as a function of wavelength distribution. Distances from the slit to grating 1, grating 1 to grating 2, etc. were set to $[4.704, 0.046, 0.046, 4.004]\text{m}$, with grating heights $[17.2, 34.5, 17.2]\mu\text{m}$. Wavelengths in the simulation are Gaussian distributed with a mean of $\bar{\lambda} = 4.4\,\text{Å}$, and standard deviation $\Delta\lambda = [0\,\text{Å}, 2.2\,\text{Å}]$. An integrating detector after the final grating was simulated, and contrast computed by phase stepping the first grating [38]. The resulting contrast curve is shown in Figure 2.12. Without slits to select a single interfering path as in [34], the contrast from this configuration is zero. The addition of magnetic prism collimators to select the interfering path pair

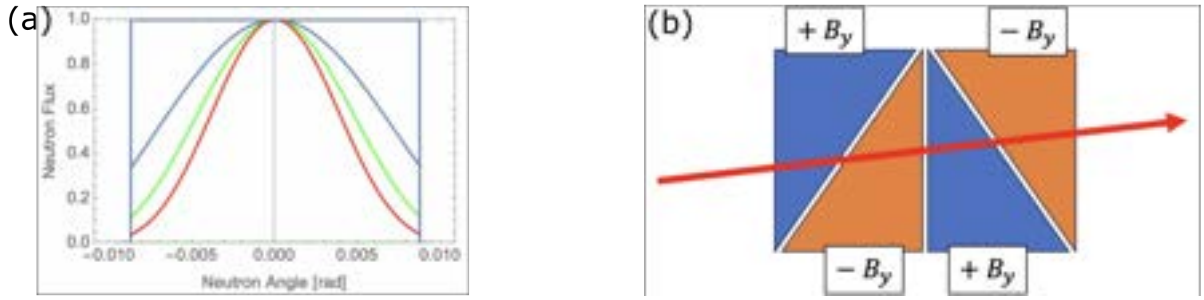


Figure 2.11: (a) Neutron flux for four prism arrangement of spin polarizing collimator. Rectangular region denotes the input neutron angle to the collimating device. Blue, green, and red curves show neutron flux after one, two, and three collimating elements in series. Collimating element includes four magnetic prisms of alternating field direction and a polarizer. (b) Schematic of four prism arrangement. Example polarized neutron path shown as red arrow. Magnetic field direction is denoted by labels and prism coloring.

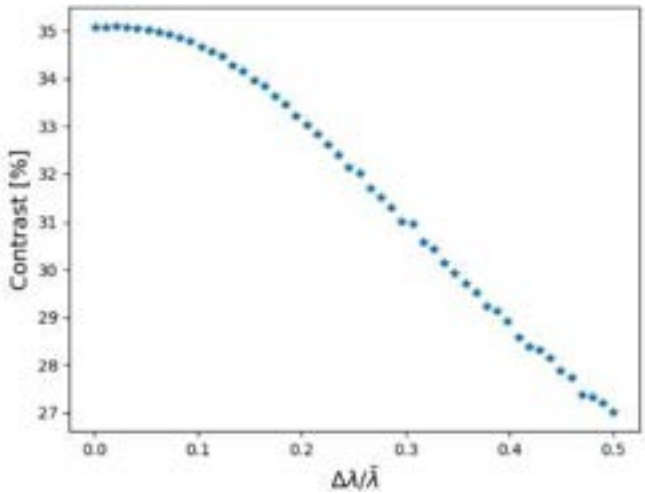


Figure 2.12: Simulated contrast of very cold neutron interferometer as a function of wavelength spread, for a Gaussian distribution with mean $\bar{\lambda} = 4.4\,\text{Å}$ and standard deviation $\Delta\lambda$. The use of polarization collimators between each grating selects only the diffraction orders of interest, labelled in Figure 3 of [35].

illustrated in Figure 4 of [35], results in contrast comparable to the three phase grating moiré interferometer for wide wavelength distributions. Replacing the slits from previous VCN interferometers enables the use of higher fluence cold neutrons, previously unusable due to the reduction in diffraction angle compared to very cold neutrons. The applications for magnetic prism potentials above are made accessible by the successful demonstration of triangular coils used to generate spin-orbit states for neutrons, as will be shown in Chapter 3.

Chapter 3

Orbital Angular Momentum States

The dramatically increased flux, availability of bench top sources, and plethora of off-the-shelf components are all excellent motivations to develop devices and techniques with light optics, before working with neutrons. Experiments demonstrating the use of birefringent quartz crystals to generate a lattice of optical vortex states were originally designed for neutron experiments, but were first demonstrated with laser light for those very reasons [60]. The long history of structured states in optics also provides fertile ground to explore techniques that have not been applied to neutron optics. From that first demonstration of the "lattice of optical vortex" (LOV) prisms, several experiments applied quantum information techniques to demonstrate remote state preparation of single-photon OAM lattices [132], and the Talbot effect with single-photons [133]. States of light possessing orbital angular momentum (OAM) coupled to the polarization degree of freedom, also called structured states, are commonly referred to in literature as "classically entangled" [134, 135]. Before discussing a series of optical experiments with OAM states, let us first discuss the definition of "classical entanglement" and how structured states differ from entangled states.

3.1 Non-Separable States

We established in Chapter 1 that OAM, in the context of light and matter waves, is simply a property of the momentum of the beam; however, OAM in the context of experiment typically refers to "OAM beams", which are paraxial beams possessing the phase profile $e^{i\ell\phi}$ [136]. The earliest experimentally reported OAM beams are the Laguerre-Gaussian

(LG) modes [62], which are characterized by an OAM number ℓ, and radial number p, with beam profile

$$LG_p^{\ell}(\rho,\varphi,z) = C_{lp}^{LG}\frac{1}{w(z)}\left(\frac{\rho\sqrt{2}}{w(z)}\right)^{|l|}\exp\left(-\frac{\rho^2}{w^2(z)}\right)L_p^{|l|}\left(\frac{2\rho^2}{w^2(z)}\right) \times \exp\left(-ik\frac{\rho^2}{2R(z)}\right)\exp(-il\varphi)\exp(i\psi(z)), \tag{3.1}$$

where $C_{lp}^{LG} = \sqrt{\frac{2p!}{\pi(p+|l|)!}}$ is a normalization constant, $\psi(z) = (|\ell| + 2p + 1)\tan^{-1}(z/z_R)$ is the Gouy phase, z_R is the Rayleigh distance, $w(z)$ is the radius of the beam, $L_p^{|l|}$ is the associated Laguerre polynomial, and the beam waist is $w(z = 0)$. Nearly all OAM states of interest in this work are LG beams with $p = 0$. In the language of quantum mechanics, these states are eigenstates of the OAM operator, $\hat{L}_Z$, with eigenvalue ℓ. This can be combined with neutron spin to describe a polarized neutron with OAM, or indeed a neutron that has OAM on only one polarization state. In the bra-ket formalism, we can write a spin-orbit state, $|\psi\rangle$, with OAM $\ell = 5$ on the spin-up state as

$$|\psi\rangle = LG_{p=0}^{\ell=5}(\rho,\varphi,z)\,|\uparrow\rangle + LG_{p=0}^{\ell=0}(\rho,\varphi,z)\,|\downarrow\rangle \tag{3.2}$$

$$= |\uparrow,5\rangle + |\downarrow,0\rangle\,. \tag{3.3}$$

As this state cannot be written as a product of pure states of the OAM and spin degrees of freedom, the state $|\psi\rangle$ appears to show entanglement [137]. We can verify that it is non-separable by taking advantage of the orthonormality of the LG modes [138] to calculate the Schmidt decomposition of our spin-orbit beam

$$|\psi\rangle = \frac{LG_{p_1}^{l_1}(\rho)\,|\uparrow\rangle + LG_{p_2}^{l_2}(\rho)\,|\downarrow\rangle}{\sqrt{2}} = \sum_{i=1}^{2}(\lambda_i)^{1/2}f_i(\rho)\,|e_i\rangle\,,$$

with $\lambda_1 = \lambda_2 = 1/2$, $f_1 = LG_{p_1}^{l_1}$, $f_2 = LG_{p_2}^{l_2}$, $|e_1\rangle = |\uparrow\rangle$, $|e_2\rangle = |\downarrow\rangle$. This yields a Schmidt Rank of $K = \left(\sum_{i=1}^{2}\lambda_i^2\right)^{-1} = 2$. As a state is separable if and only if the Schmidt Rank is

$K = 1$, we conclude that spin-orbit states of this form are non-separable [139]. The above treatment applies to single particles, but what about OAM generated from laser light?

A spin-orbit state can be written as a combination of LG modes and polarization vectors or, equivalently, a combination of Hermite-Gauss (HG) modes and polarization. All first-order polarization vortices can be written as a superposition of first-order HG modes and polarization vectors

$$\Psi(\rho) = A_{x\uparrow}\psi_x(\rho)\left|\uparrow\right\rangle + A_{x\downarrow}\psi_x(\rho)\left|\downarrow\right\rangle + A_{y\uparrow}\psi_y(\rho)\left|\uparrow\right\rangle + A_{y\downarrow}\psi_y(\rho)\left|\downarrow\right\rangle,$$

with basis states $\{\psi_\mu(\rho)\left|\nu\right\rangle\}$ for first-order HG modes oriented in the $\mu = x, y$, and polarized in the $\nu = \uparrow, \downarrow$ directions in the Hilbert space $\mathcal{H}_S \otimes \mathcal{H}_P$. Higher order polarization vortices can be created by similar combinations of higher-order HG modes, where each ψ_μ contains multiple HG modes [140]. The classical HG modes can be written quantum mechanically as Heisenberg operators for the positive frequency component of the electric field

$$\hat{A}^{(+)}(\rho, t) = e^{i(kz-\omega t)} \sum_{\mu,\nu} \hat{a}_{\mu\nu}\psi_\mu(\rho)\left|\nu\right\rangle,$$

where the operator $\hat{a}_{\mu\nu}$ annihilates a photon in the $\psi_\mu(\rho)\left|\nu\right\rangle$ mode. To determine the separability of a coherent spin-orbit state, let us construct a basis of spin-orbit states as

$$\begin{aligned} \Psi_\pm(\rho) =& \frac{\psi_x(\rho)\left|\uparrow\right\rangle \pm \psi_y(\rho)\left|\downarrow\right\rangle}{\sqrt{2}}, \qquad \Phi_\pm(\rho) = \frac{\psi_x(\rho)\left|\downarrow\right\rangle \pm \psi_y(\rho)\left|\uparrow\right\rangle}{\sqrt{2}} \\ \implies \hat{a}_{\Psi_\pm} =& \frac{\hat{a}_{x\uparrow} \pm \hat{a}_{y\downarrow}}{\sqrt{2}}, \qquad \hat{a}_{\Phi\pm} = \frac{\hat{a}_{x\downarrow} \pm \hat{a}_{y\uparrow}}{\sqrt{2}}. \end{aligned} \tag{3.4}$$

Using Eqn. (3.4), we can construct a Fock state in spatial mode and polarization, corresponding to N photons on mode Ψ_+ and 0 photons on Ψ_-

$$
\begin{aligned}
|N\rangle_{\Psi_+}|0\rangle_{\Psi_-} &= \frac{(\hat{a}^\dagger_{\Psi_+})^N}{\sqrt{N!}}|0\rangle_{\Psi_+}|0\rangle_{\Psi_-} \\
&= \sum_{n=0}^{N}\frac{\sqrt{N!}(\hat{a}^\dagger_{x\uparrow})^n(\hat{a}^\dagger_{y\downarrow})^{N-n}}{2^{N/2}n!(N-n)!}|0\rangle_{x\uparrow}|0\rangle_{y\downarrow} \\
&= \sum_{n=0}^{N}\sqrt{\frac{N!}{2^N n!(N-n)!}}|n\rangle_{x\uparrow}|N-n\rangle_{y\downarrow}\,.
\end{aligned}
$$

A single photon in a spin-orbit state can then be written as a non-separable state of spatial mode and polarization

$$
|1\rangle_{\Psi_+}|0\rangle_{\Psi_-} = \frac{|1\rangle_{x\uparrow}|0\rangle_{y\downarrow}+|0\rangle_{x\uparrow}|1\rangle_{y\downarrow}}{\sqrt{2}}, \tag{3.5}
$$

note that the right hand side of Eqn. (3.5) is non-separable. While the left hand side appears separable, each ket on the left represents a composition of basis states and is neither an individual basis state in the Hilbert space $\mathcal{H}_S\otimes\mathcal{H}_P$, nor the Hilbert space of an individual degree of freedom [141]. Let us now consider a two-mode coherent state,

$$
\begin{aligned}
|\alpha,\alpha\rangle &= e^{-|\alpha|^2}\sum_{n,m=0}^{\infty}\frac{\alpha^{n+m}}{\sqrt{n!m!}}|n,m\rangle \\
&= e^{-|\alpha|^2}\sum_{N=0}^{\infty}\sum_{m=0}^{N}\frac{\alpha^N}{\sqrt{(N-m)!m!}}|N-m,m\rangle\,.
\end{aligned} \tag{3.6}
$$

Using the operator $\hat{a}^\dagger_{\Psi_+}$ that generates a non-separable state, defined in Eqn. (3.4), we can put our two mode coherent state given by Eqn. (3.6) in the form

$$
\begin{aligned}
|\alpha,\alpha\rangle &= e^{-|\alpha|^2}\sum_{n=0}^{\infty}\frac{\left(\sqrt{2}\alpha\right)^n\left(\hat{a}^\dagger_{\Psi_+}\right)^n}{n!}|0\rangle \\
&= |\sqrt{2}\alpha\rangle_{MNS}\,.
\end{aligned}
$$

Thus, a coherent spin-orbit state is also a coherent state in the maximally non-separable (MNS) mode of Eqn. (3.5) [142]. Another way to create a coherent state, is by acting on vacuum with a displacement operator,

$$\begin{aligned} D_{\Psi_+}(\alpha) &= \exp(\alpha \hat{a}^\dagger_{\Psi_+} - \alpha^\star \hat{a}_{\Psi_+}) \\ &= D_{x\uparrow}(\alpha/\sqrt{2}) D_{y\downarrow}(\alpha/\sqrt{2}) \\ \implies |\alpha\rangle_{\Psi_+} |0\rangle_{\Psi_-} &= |\alpha/\sqrt{2}\rangle_{x\uparrow} |\alpha/\sqrt{2}\rangle_{y\downarrow} . \end{aligned} \tag{3.7}$$

This appears to suggest that a spin-orbit state generated from a coherent source like a laser is separable; however, one must again consider the difference between a state which is separable in a local basis of the Hilbert space, and one which has a separable *mode partition*. Eqn. (3.7), describes a *mode partition* of a coherent spin-orbit state, but this is not written in a local basis for the Hilbert space $\mathcal{H}_S \otimes \mathcal{H}_P$. Thus, it does not imply that a coherent spin-orbit state is non-separable. Again, this analysis can be generalized to higher-order spin-orbit states by writing basis spatial modes that are combinations of higher-order HG or LG modes.

Therefore, a spin-orbit state is indeed non-separable for both single particles, like neutrons and single photons, and coherent states like those of a laser beam. While non-separability is commonly described in introductory texts as the hallmark of entanglement [137, 143, 144], this definition does not fully capture the conditions commonly called "entanglement". States, such as those in Eqn. (3.7), that are non-separable in the degrees of freedom of a single particle do not demonstrate the non-local behavior of two separated systems that originally concerned Einstein, Podolsky, and Rosen [145]. This distinction gave rise to alternative descriptions of non-separable degrees of freedom of a single particle, including "classical entanglement", "non-separable states", and "single-particle entanglement" [146, 147, 148]. The calculations above demonstrate that these states are non-separable, and this is the feature that distinguishes "single-particle entanglement" from states that are described as "entangled" in quantum information research. Regardless of the "entanglement" content of structured states of light, there are a litany of applications for these beams from optical trapping [149], to edge-enhanced microscopy [150], and quantum communication [151]. Of particular interest in this work are a series of experiments that projected structured states onto the human retina to create visible patterns in a person's vision [152].

3.2 Human Discrimination of Spin-Orbit states

The foundation of this work was the observation by Wilhelm Karl Haidinger that polarized light, scattered from the atmosphere, created "two faint yellow, connected cloud-like spots of about 2° in apparent size" [153]. This phenomenon, later called Haidinger's Brush, is an entoptic pattern, meaning it occurs within the eye instead of from an external light source [154]. In 1850, James Clerk Maxwell conducted several experiments investigating the cause of Haidinger's Brush within the eye; his conclusion was that a "polarizing structure lies within the boundary of the foramen centrale (macula)" that was radially oriented [155]. Nearly 100 years later, interest in Haidinger's brush was renewed by optometrists and ophthalmologists who suggested that there could be a clinical application of polarization perception as a screening test for the integrity of the macula [156, 157, 158, 159]. Later work found that continuously rotating linearly polarized light would produce a clear and continuously visible entoptic pattern, subtending 3.75° of visual angle [160]. The spin-orbit states generated by the LOV prisms are, fundamentally, a spatially varying polarization structure, it was therefore hypothesized that a subject could use Haidinger's brush to distinguish between spin-orbit states. The first experiment exploring entoptic phenomena with structured states directed subjects to distinguish between a spin-orbit state with OAM $\ell = 1$ and $\ell = -1$.

That work was published on February 28, 2022 in Scientific Reports as "Human psychophysical discrimination of spatially dependant Pancharatnam–Berry phases in optical spin-orbit states" [2]. Author contributions are summarized below.

- D.S., C.K., A.E.S., D.G.C., B.T., and D.A.P. designed this research;
- D.S., C.K., and A.E.S. performed the experiment;
- D.S., C.K., and A.E.S. analyzed the data;
- D.S., C.K., A.E.S., D.G.C., and D.A.P. wrote the paper.

3.2.1 Introduction

The phase that is acquired during cyclic evolution governed by a slow change of parameters is known as the geometric phase [161]. The Aharonov-Bohm phase in quantum mechanics [162] and the Pancharatnam-Berry phase in optics [163, 164] are the two of the most well-known examples of phase shifts with geometrical origin, and they have had a profound impact on a wide range of areas in physics [165, 166, 167, 168]. Unlike typical phase shifts that arise from optical path differences, the Pancharatnam-Berry phase is induced when the polarization state traces out a geodesic triangle on the Poincaré sphere [163, 164]. It has led to the development of optical components that enable polarization dependant wavefront shaping and novel methods of inducing polarization coupled OAM through spin-orbit coupling [169, 170, 171, 172, 102, 5]. Optical waves carrying OAM possess a helical wavefront and are described by the phase term $e^{i\ell\phi}$, where ϕ is the azimuthal coordinate and ℓ is the OAM value [173]. Beams with polarization coupled OAM, also known as "vector vortex beams" or "spin-orbit" beams, may be prepared to be non-separable in polarization and spatial modes [174, 175] and manifest dynamic 2D polarization topologies [176, 177, 178, 179]. A variety of methods exist to generate spin-orbit beams using spatial light modulators [180, 181], sub-wavelength gratings [182], and inter-cavity interference within a laser source [183, 184].

Due to their unique propagation properties spin-orbit beams have found numerous applications in high-resolution imaging, communication protocols, and optical metrology [185, 186, 187] and a wealth of characterization techniques based on Stokes polarimetry have been developed [188, 189, 190]. Ref. [3] extended the applications to visual science which sees a growing interest in integrating human detectors with recent technological advances [191, 192, 193, 194, 195]. It was shown that humans are able to perceive and discriminate spin-orbit states through entoptic images that arise from the interaction between the 2D polarization topologies of these beams and the radially symmetric dichroic elements in the macula of the human eye [3]. As shown in Fig. 3.1a, when looking in the vicinity of the center of a spin-orbit beam composed of a superposition of right and left circular polarization coupled to two different OAM values (ℓ_1 and ℓ_2), the observer may perceive an entoptic profile composed of $N = |(\ell_1 - \ell_2) - 2|$ azimuthal fringes. Note that this is a measurement of the OAM difference between the two polarization states, rather than the absolute value of each OAM component. Ref. [3] employed refractive elements to generate OAM=7 and couple it to different polarization states to induce $N = 5$ and $N = 9$ azimuthal fringes. Here we consider spin-orbit states prepared through devices that manipulate geometric phases. This enables a robust study of discriminating between beams with different OAM values.

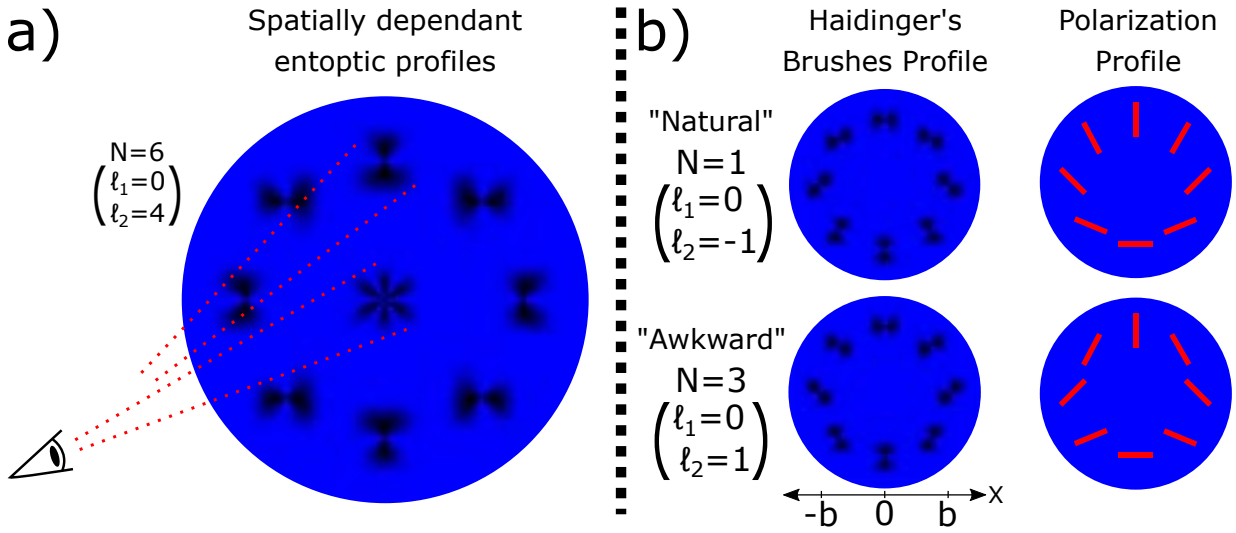


Figure 3.1: a) Pictorial representation of the spatially dependant entoptic profiles that a human observer would perceive when directly viewing different regions of a spin-orbit beam described by Eq. 3.8 where $\ell_1 = 0$ and $\ell_2 = 4$. If the observer looks at the polarization gradient in the center they will perceive $|(\ell_1 - \ell_2) - 2| = 6$ azimuthal fringes. If the observer looks at a region away from the center where the polarization is roughly uniform in the field of vision, they will observe specifically oriented Haidinger's brushes. b) In this study the strong polarization gradients in the central region of the beam were reduced by preparing spin-orbit states with radially dependent terms, as described by Eq. 3.9. The distance at which there is an equal amount of the two circular polarization states is denoted by b, and in our particular setup b was approximately 1.5 cm. The beam state was not varied with time, and the participants were asked to move their gaze around the perimeter of the beam while observing and discriminating the elicited Haidinger's brush profile, labelled either the "awkward" or "natural" profile depending on whether the entoptic brush appeared to rotate along or against the observer's eye movement. In order to minimize visual adaptation to optical polarization the suggested speed for the self-generated circular eye motion was 1 Hz. Figure reproduced from [2].

The detection of optical polarization by humans is enabled by a series of radially symmetric dichroic elements centred on the foveola in the human eye [153, 196, 197, 198, 199]. An observer directly viewing polarized light would perceive a bowtie-like shape, known as "Haidinger's brush", in the central point of their visual field. These entoptic profiles can be observed, on average, in light with more than approximately 56% polarization [200], with peak clarity occurring for blue light of approximately 460 nm wavelength [201]. However, observation of Haidinger's brush in everyday life is hindered by visual adaptation which causes the entoptic images to disappear after a few seconds. Experiments show that a rotating polarization source at approximately 1 Hz allows Haidinger's brush to be observed continuously with clarity [160].

Typical studies with human detectors of optical polarization require the observer to keep their gaze on a fixed point while the beam is time modulated to overcome visual adaptation. Correspondingly, in Ref. [3] an induced phase shift caused the entoptic profile to rotate. In the presented study we consider an alternative method of observation utilizing stationary beams. Rather than fixing their gaze at the center of the beam, the participants made self-generated eye movements to view different parts of the beam and determine the presented state based on the rotational symmetry of the Haidinger's brushes (see Fig. 3.1b).

The transverse wavefunction of a spin-orbit state travelling along the z-direction can be written as:

$$|\Psi\rangle = \frac{1}{\sqrt{2}}\left[C_1(\ell_1, r, z)e^{i\ell_1\phi}\,|R\rangle + C_2(\ell_2, r, z)e^{i\ell_2\phi}\,|L\rangle\right], \tag{3.8}$$

where we have used the bra-ket notation for convenience, $|L\rangle = \begin{pmatrix}0\\1\end{pmatrix}$ and $|R\rangle = \begin{pmatrix}1\\0\end{pmatrix}$ denote the left and right circular polarization, and (r, ϕ) are the cylindrical coordinates. The radial terms $C_1(\ell_1, r, z)$ and $C_2(\ell_2, r, z)$ depend on the preparation method [173, 202].

In our setup the spin-orbit states were prepared via Lattice of Optical Vortices (LOV) prism pairs which induce highly uniform phase gradients and minimize distortions in the beam's intensity profile [60, 133, 101]. Furthermore, they introduce a radial dependence which can be used to prepare a cue that helps participants learn the proper eye movement. In the study we specifically prepare and differentiate between the following two states:

$$|\Psi_\pm\rangle \approx \cos\left(\frac{\pi r}{4b}\right)|R\rangle \pm i\sin\left(\frac{\pi r}{4b}\right)e^{\pm i\phi}\,|L\rangle\,, \tag{3.9}$$

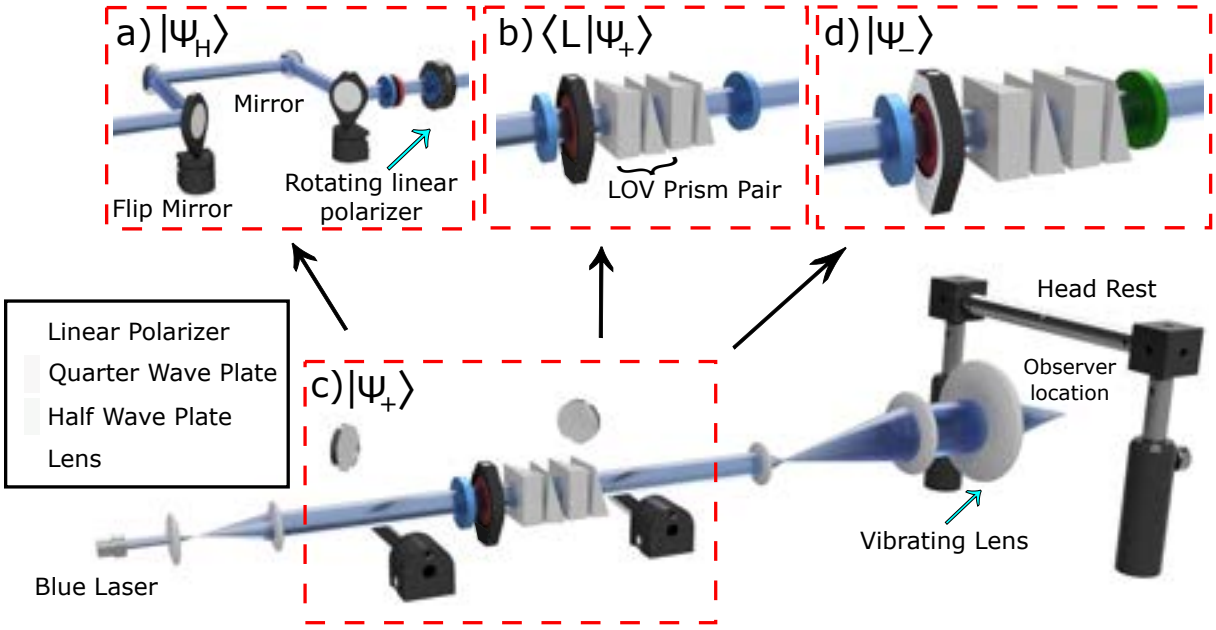


Figure 3.2: Schematic of the experimental setup with four different configurations for directing structured light onto the retina of the observer. a) The first configuration prepares linearly polarized light with an orientation that rotates with a speed of approximately 1 Hz. This setup was used in the pre-study to determine if the participants were able to perceive Haidinger's brushes when gazing at a fixed point. b) The second configuration uses a polarization filter to prepare a doughnut shaped intensity profile. This configuration was used to familiarize the participant with the optimal eye movement during a familiarization period on the first day. The last two configurations, c) and d), prepare the two states of Eq. 3.9 which possess uniform intensity profiles and were used during the main experiment. Figure reproduced from [2].

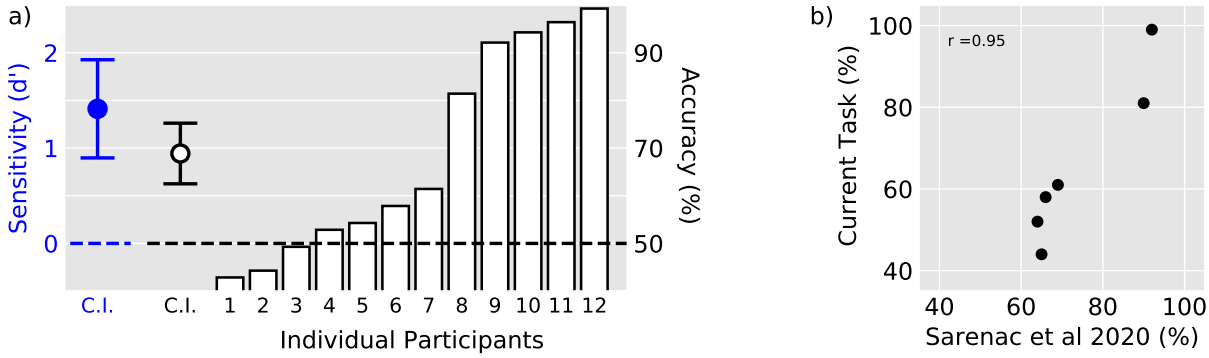


Figure 3.3: Group and individual-participant data. a) Sensitivity and accuracy for the discrimination task. Each participant performed 140 trials over four days. The dashed lines indicate chance performance. The open bars illustrate individual rank-ordered performance, and the circular symbols illustrate group mean sensitivity (blue: left ordinate) and accuracy (black: right ordinate). The error bars are 95 % confidence intervals. Generally, participants either performed very well or at chance levels. b) Relationship between performance of common participants between Ref. [3] and the current study. Performance in the previous study was strongly predictive of performance in the current study. Figure reproduced from [2].

where b is the distance at which there is an equal amount of the two circular polarization states. The helical phase denoting the OAM is induced via the Pancharatnam-Berry phases. It follows from Eq. 3.9 that the left circular polarization state of $|\Psi_+\rangle$ carries an OAM of $+1$ and that of $|\Psi_-\rangle$ carries an OAM of -1. Polarization directions, and the orientations of the corresponding Haidinger's brushes, are shown in Fig. 3.1b for several regions centered on $r = b$. Viewing slightly different radii would result in the same rotational symmetry but with reduced contrast. Note that the polarization topologies of $|\Psi_+\rangle$ and $|\Psi_-\rangle$ depict the "star" and "lemon" Poincaré beams [176, 177, 178, 179].

The OAM dynamics were negligible and the beams possessed highly uniform intensity profiles in our setup. As a result, a speckle pattern arose which greatly hindered the observation of entoptic images. Therefore, we employed a vibrating lens, which is a common method of removing speckle patterns [203].

In typical operation two sets of LOV prism pairs take as input a circularly polarized state and output a lattice of spin-orbit states. The parameters in the experiment were such that one unit cell covered the entire beam, and the state in each unit cell of the lattice depended on the polarization of the input state as follows:

$$|R\rangle \rightarrow \cos\left(\frac{\pi r}{4b}\right)|R\rangle + i\sin\left(\frac{\pi r}{4b}\right)e^{i\phi}|L\rangle \tag{3.10}$$

$$|L\rangle \rightarrow \cos\left(\frac{\pi r}{4b}\right)|L\rangle + i\sin\left(\frac{\pi r}{4b}\right)e^{-i\phi}|R\rangle \tag{3.11}$$

It follows that $|\Psi_+\rangle$ may be obtained by passing $|R\rangle$ through two sets of LOV prism pairs, while to obtain $|\Psi_-\rangle$ we start with an input of $|L\rangle$ and add a half wave plate at the end.

Our setup allowed for the robust and quick access to four different configurations, as shown in Fig. 3.2. For a detailed description of the setup see Supplementary Material A and B, including the polarization analysis of the beam profile using the Stokes parameters [204] and the laser safety considerations [205]. The first configuration, Fig. 3.2a, prepares a uniform intensity beam with a varying linear polarization direction:

$$|\Psi_{\mathrm{H}}\rangle \approx |R\rangle + e^{i\theta(t)}|L\rangle\,, \tag{3.12}$$

where $\theta(t)$ was set by the rotation stage onto which a polarizer was mounted. This configuration was used in the study for pre-screening of the participants. The second configuration prepares the $|\Psi_+\rangle$ state (described by Eq. 3.9) filtered on $|L\rangle$. The resulting intensity possesses a doughnut profile that is described by $\sin^2(\pi r/4b)$. The outer boundary of the central dark region provides an aligning aid for participants, outlining the optimal locations for saccadic eye movements when discriminating the spin-orbit states. This configuration was used during an initial familiarization and training period. The third and fourth configurations are the $|\Psi_+\rangle$ and $|\Psi_-\rangle$ spin-orbit states as described in Eq. 3.9. These two configurations possess uniform intensity profiles and were used during all experimental trials.

Seventeen participants were recruited in this study and provided informed written consent to voluntarily participate. All participants were treated in accordance with the Declaration of Helsinki, and all research activities received approval from the University of Waterloo Office of Research Ethics.

Before the main discrimination task, each participant performed an initial screening procedure in which a linearly polarized light beam was presented, whose polarization orientation rotated either clockwise or counterclockwise. Participants were presented with 10 testing trials and were asked to verbally discriminate the direction of rotation through the perception of rotating Haidinger's brushes. Twelve participants achieved >70% accuracy

and moved on to the main study. Participants performed the main discrimination task over four days, each containing thirty-five trials. Participants verbally discriminated between $|\Psi_+\rangle$ and $|\Psi_-\rangle$ configurations, and one randomly-selected configuration was presented per trial. All trials of the same type were identical to one another. See Supplementary Material C and D for full participation and psychophysical details, respectively.

3.2.2 Results

Participant performance was strikingly non-normal, and therefore non-parametric statistical tests were employed. No significant effect was found when subjecting the accuracy data from the 9 participants who scored less than 90% on the first day of the experimental task to a Friedman test with day as the repeated measure, $X^2(3) = 4.5$, $p = 0.22$. Therefore, the data from all days were collapsed for the main analysis. Sensitivity (d') and response bias (c) were calculated for each individual participant [206]. Accuracy (% correct) and sensitivity were analyzed using a one-tailed one-sample Wilcoxon signed rank test to determine whether group performance was significantly better than chance. Response bias was analyzed using a two-tailed one-sample Wilcoxon signed rank test to determine whether either response was systematically favored. Participants performed significantly better than chance: Median Accuracy = 60%, Median Sensitivity $d' = 0.5$, $W = 68$, $p = 0.01$ for both measures of performance. No significant response bias was observed: Median $c = 0$, $W = 42$, $p = 0.85$. Fig. 3.3 illustrates group and single-subject data.

3.2.3 Discussion

Despite successful completion of our initial screening procedures from all participants (See Supplementary Material D for details), inspection of Fig. 3.3a reveals an evident bimodal distribution of task performance with subjects 1 to 7 performing at chance levels and subjects 8 to 12 performing at ceiling. One explanation for this pattern of results is that seven participants were unable to perform the relatively complex psychophysical task that required the combination of self-generated eye movements with judgements of Haidinger's brush orientation patterns. However, it is also possible that the bimodal distribution reflects individual differences in macular pigment structure [207, 208, 209]. Initial support for this intriguing possibility can be found in Ref. [3] where the same bimodal task performance distribution was observed for a much easier psychophysical task that employed a rotating beam and did not require self-generated eye movements. Fig. 3.3b provides a visual comparison of both datasets for the six participants that completed both studies and

confirms the robust nature of the bimodal performance distribution, demonstrating that performance in Ref. [3] was strongly predictive of performance in the current study. It is important to note that in both studies, each participant was initially required to demonstrate a strong ability to perceive Haidinger's brushes when viewing uniformly polarized light. Therefore, the stimuli and tasks employed by both studies are highly selective probes of sensitivity to the entoptic phenomenon. Our future studies will aim to gain further insights into the functional properties of individual macular pigment variations by examining the relationship between psychophysical performance and retinal images.

While the task employed in Ref. [3] may provide high resolution for capturing the full spectrum of spin-coupled OAM sensitivity, the current task appears exceedingly effective at identifying high and low spin-coupled OAM discrimination performers, such that anybody unable to achieve ceiling performance will invariably perform near chance. Although both of these works have examined human perception of structured light that possess correlations between two degrees of freedom, protocols exist for the preparation of more complex spatial modes [210] and higher dimensional non-separable states [135]. An interesting future experiment to consider is the measurement of the classical GHZ state correlations using human detectors as per the polarization-based Bell-state projection measurements outlined in Ref. [135]. Furthermore, future work should apply these structured light discrimination tasks to measure properties of the macular pigment, allowing meaningful applications for diseases affecting the macular pigment such as macular degeneration [159, 211, 212].

3.2.4 Supplementary Material

Structured Light and preparation of spin-orbit states

The core idea behind preparation of custom light fields known as "structured light" is the tailoring of the transverse phase profiles. By manipulating the wavefront it is possible to induce special properties including "OAM", "self-healing", and "non-diffraction", among many others [185]. In this work we are particularly interested in OAM beams and their coupling with polarization.

Consider a very simple example of a well-defined monochromatic beam travelling along the z-direction and passing through an optical prism. One way to calculate the behaviour of the beam is through the application of Snell's law, but we can also consider the spatial phase shift that the beam acquires after the prism. The phase shift will be proportional to the thickness of the prism which varies along a direction that is perpendicular to the propagation direction of the beam, for example the x-direction. Hence the wave function

of the beam will acquire a term $e^{ik_x x}$ where k_x is determined by the prism's incline angle and index of refraction. The result is that the propagation direction of the beam has been altered due to the addition of the linear momentum along the x-direction. Now instead of a prism (gradient along a particular Cartesian direction) let us consider a spiral phase plate (SPP) which is a gradient along the azimuthal direction ϕ. Analogous to how the prism introduces linear momentum, the SPP introduces orbital angular momentum and the wave function of the beam acquires a term $e^{iq\phi}$ where q is known as the topological charge of the SPP and is similarly set by the slope of the SPP gradient and the material's index of refraction. The trajectory of the OAM beam is modified accordingly with the addition of the momentum along the ϕ direction resulting in a doughnut intensity profile as the beam propagates.

Numerous methods have been developed to prepare orbital angular momentum states that include the use of: optical elements such as transmission and reflection spiral phase plates, computer-generated holograms that are transferred onto holographic plates through lithography techniques, and the use of liquid crystal-based Spatial Light Modulators (SLMs) [180, 181, 182, 183, 184]. The SLM is particularly versatile as it enables real-time wavefront shaping. The field of structured light is currently extremely vibrant and many extensions and sophisticated methods have been analyzed and demonstrated. Likewise, there are many ways to detect and characterize OAM beams [188, 189, 190]. The two direct methods involve characterizing the phase profile $e^{iq\phi}$ through an interferometric measurement, and determining the momentum distribution by allowing the beam to propagate into the far field where the intensity profile is set by the momentum distribution.

"Vector vortex beams" or "spin-orbit beams" arise when the polarization degree of freedom is correlated with OAM [174, 175]. For example, we may prepare a coherent superposition of right-circularly polarized light with no OAM and left-circularly polarized light with OAM. The superposition of the two circular polarization states results in a linear polarization state, where the OAM term $e^{iq\phi}$ specifies the orientation of the linearly polarized state at each location ϕ. Therefore it is possible to obtain many variations of rich polarization topologies across the beam [176, 177, 178, 179]. In this work we consider the human perception and quantification of such beams.

In our study to prepare the spin-orbit states we used Lattice of Optical Vortices (LOV) prisms [60]. The LOV prisms induce OAM through the Pancharatnam-Berry phase, and thus enable the preparation of the positive and negative OAM states through polarization control; providing an advantage over the SPP used in Ref. [3]. Unlike typical phase shifts that arise from optical path differences, the Pancharatnam-Berry phase is induced when the polarization state traces out a geodesic triangle on the Poincaré sphere [163, 164]. To see how the LOV prisms work we can consider the two spin-orbit states that we desire for

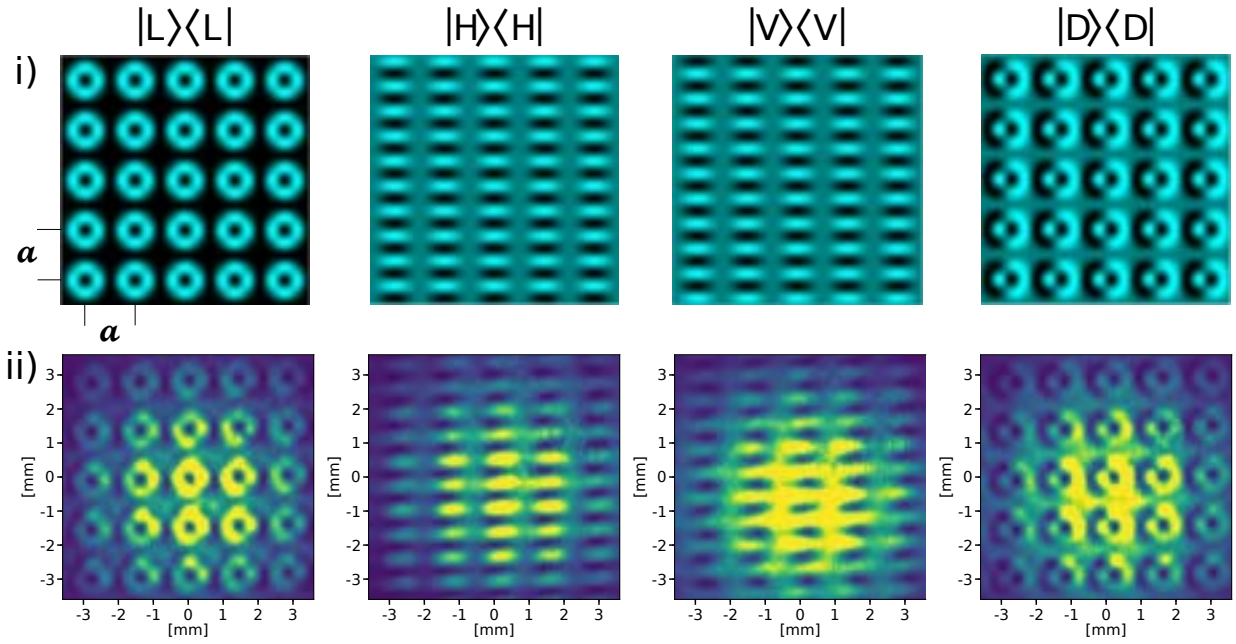


Figure 3.4: LOV prisms prepare a lattice of spin-orbit states where in each lattice cell there is a superposition between the OAM and the polarization degree of freedom. The state in each lattice cell is described by Eq. 3.13 and here we examine the $|\Psi_+\rangle$ state. (a) Simulated intensity profiles after the corresponding (left, horizontal, vertical, diagonal) polarizers. b) Intensity profiles measured with the setup of Fig. 3.2 by putting the corresponding polarizer followed by a camera after the LOV prism pairs (before beam expansion). The presented images are raw data with the colormap chosen for visual clarity over the default blue-black colormap (the participants viewed blue light). The lattice period is given by Eq. 3.16 and with $\lambda = 455$ nm, quartz birefringence of 0.0091, and prism angles of 2° we expect a period of $a = 1.4$ mm, which is in good agreement with the observation. Figure reproduced from [2].

the given study:

$$|\Psi_{\pm}\rangle \approx \cos\left(\frac{\pi r}{4b}\right)|R\rangle \pm i\sin\left(\frac{\pi r}{4b}\right)e^{\pm i\phi}|L\rangle\,, \tag{3.13}$$

where r and ϕ are the cylindrical coordinates, $r = b$ specifies the radial location with equal superposition of the two circularly-polarized states $|R\rangle$ and $|L\rangle$, and we have neglected the transverse beam profile (typically Gaussian) for clarity. The spin-orbit operator that acts on the right-circularly polarized state of light to prepare the $|\Psi_{+}\rangle$ state of Eq. 3.13 has the following form:

$$\hat{U} = e^{i\frac{\pi r}{4b}[\cos(\phi)\hat{\sigma}_x + \sin(\phi)\hat{\sigma}_y]} \tag{3.14}$$

The motivation for LOV prisms comes from taking the Suzuki-Trotter expansion of the operator as follows:

$$e^{i\frac{\pi}{4b}(x\hat{\sigma}_x + y\hat{\sigma}_y)} = \lim_{N\to\infty}(e^{i\frac{\pi}{4b}x\hat{\sigma}_x/N}e^{i\frac{\pi}{4b}y\hat{\sigma}_y/N})^N, \tag{3.15}$$

where $x = r\cos(\phi)$ and $y = r\sin(\phi)$. The right hand side of this relation can be interpreted as N pairs of linear birefringent gradients that are orthogonal to each other. The gradients can be achieved via optical prisms, where one prism possesses an optical axis along the prism incline and the second prism with an optical axis offset by 45°. It was shown in Ref. [60] that two pairs of LOV prisms generate a lattice of spin-orbit states as described by Eq. 3.13, and where the lattice period is given by:

$$a = 8b = \frac{\lambda}{\Delta n\tan(\theta)} \tag{3.16}$$

where Δn and θ are the birefringence and the incline angle of the prisms. The location in the setup of the two LOV prism pairs is depicted on Fig. 3.2. The preparation of the $|\Psi_{-}\rangle$ state of Eq. 3.13 is achieved through polarization control: we start with the other circularly polarized state and add a half wave plate at the output.

Fig. 3.4 shows the simulated and measured intensity profiles after passing the beam through various polarizers. Here we analyze the beam right after the LOV prisms (before

beam expansion) in Fig. 3.2. We can see that passing the beam through a left circular polarizer results in a lattice of doughnuts defined by the *sine* amplitude term of Eq. 3.13. The lattice period is given by Eq. 3.16 and with $\lambda = 455$ nm, quartz birefringence of 0.0091, and prism angles of 2° we expect a period of $a = 1.4$ mm, which is in good agreement with the observation.

In the current study we are interested in one of the lattice cells, and hence the beam was magnified approximately 85 times so that the region of interest would be displayed on the 5.08 cm diameter user lens. With this magnification the value of b (distance of most linearly polarized light as specified in Fig. 3.1) is roughly 1.5 cm. Moving the analyzer and the camera to the user location the beam is characterized as shown in Fig. 3.5, where a $f = 50$ mm lens was placed before the camera and thus the size of the beam was reduced three times for imaging. The shown intensity profiles correspond to the region of one cell as shown in Fig. 3.4. Note that the participants in the study viewed a beam without the aid of a polarizer. Hence there was no intensity structure across the profile as shown in Fig. 3.5. The profiles without a polarizer are shown in Fig. 3.6.

We can take the four polarization projections to reconstruct the state at each location of the beam as shown in Fig. 3.6. Here the polarization state of the beam is indicated with directional ellipses at various points. This polarization plot was constructed by first taking polarized images with the analyzer set to the $\{H, V, D, R\}$ polarization states and determining the Stokes parameters. The four Stokes parameters $\{S_0, S_1, S_2, S_3\}$ represent the intensity, coordinates along the horizontal/vertical, diagonal/anti-diagonal, and right/left axis of the Poincaré sphere, respectively. These parameters can be reconstructed for each pixel using the relations $\{S_0, S_1, S_2, S_3\} = \{I_H + I_V, I_H - I_V, 2I_D - S_0, S_0 - 2I_R\}$ [204]. The Stokes parameters were then used to determine the handedness and eccentricity of the polarization ellipses plotted in Fig. 3.6.

Setup and Stimuli

The setup used a laser of wavelength 455 nm and the beam was attenuated to <1 μW/mm^2 at the location of the observer in order to conform to the guidelines for laser exposure time outlined by the International Commission on Non-Ionizing Radiation [205]. The beam was passed through a single mode fiber followed by two lenses which expanded the beam to a diameter of approximately 2 cm.

There are four different configurations in the setup. The common parts that are present in each configuration are the mentioned fiber, attenuators, and lenses at the first stage of the setup, and then also the parts in the last stage of the setup that include the lenses

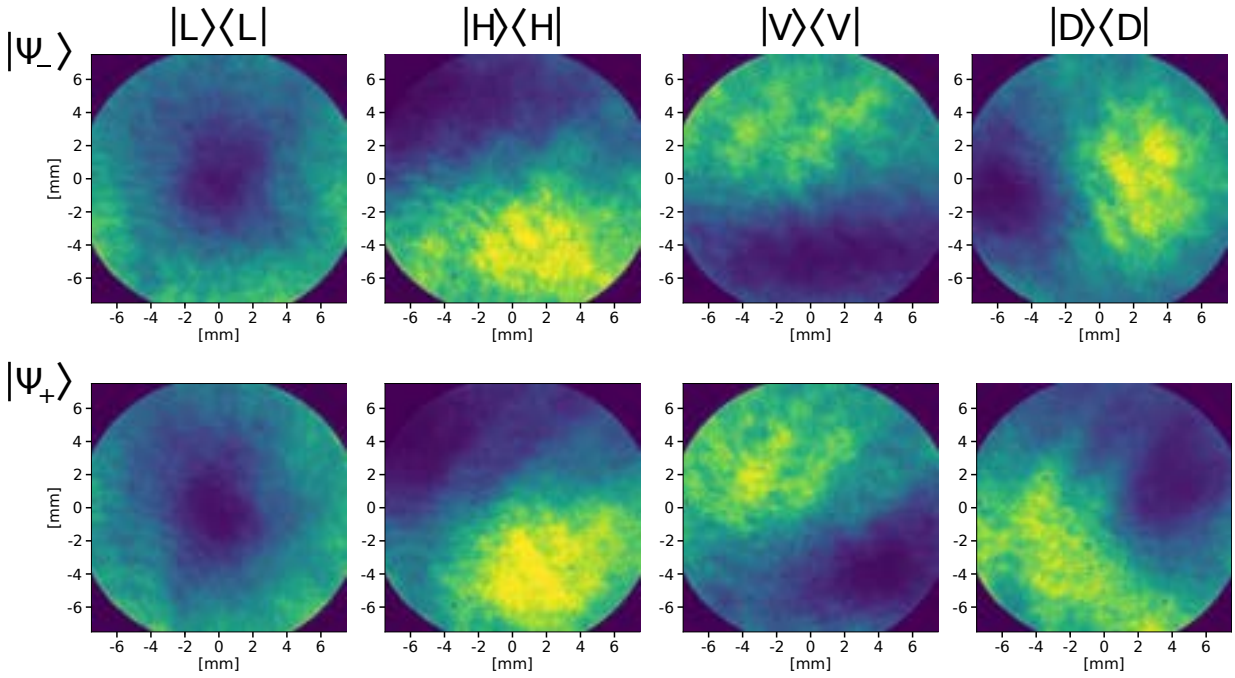


Figure 3.5: For the study we are interested in the profile topology of one lattice cell. Hence in the setup of Fig. 3.2 after the LOV prisms we magnify the beam approximately 85 times so that the region of interest would fill up the 5.08 cm diameter lens and be easily observable by the participants. The lens of the human eye then focuses the light towards the retina. Here we place a lens with $f = 50$ mm after the final user lens with $f = 150$ mm (see Fig. 3.2) to image the beam with a camera. Putting the appropriate analyzer before the mentioned $f = 50$ mm lens we obtain the shown profiles for the (top) Ψ_- state and the (bottom) Ψ_+ state of Eq. 3.13. The shown images are raw data and the intensity profiles correspond to the region of one cell as shown in Fig. 3.4. The observed diameter of the beam on the camera should be $\approx 50.8\,\text{mm}(50\,\text{mm}/150\,\text{mm}) = 16.9$ mm. Note that the beam profiles and the polarization topologies that the participants viewed in the study are shown in Fig. 3.6. Figure reproduced from [2].

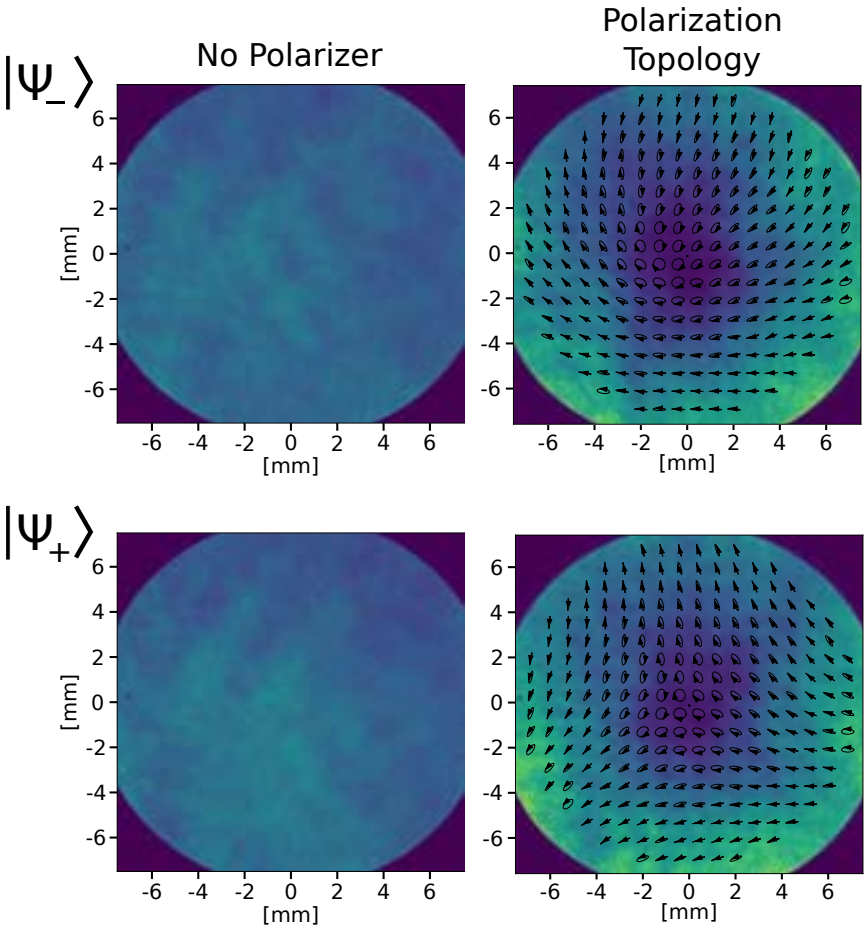


Figure 3.6: The profiles shown in Fig. 3.5 represent the four polarization measurements needed to determine the four Stoke's parameters and characterize the polarization profiles of the beams. Here we use the data of Fig. 3.5 and plot the resulting spatially dependant polarization across the beam for (top) Ψ_- state and (bottom) Ψ_+ state. The topology is in good agreement with Fig. 3.1b). The specified value of "$b = 1.5$ cm" in Fig. 3.1 corresponds to a radius of $r = 1.5\,\text{cm}(50\,\text{mm}/150\,\text{mm}) = 0.5$ cm away from the origin in the images shown here. Furthermore, note that although the respective intensity profiles from Fig. 3.5 are displayed here in the background for visual clarity, in the study the participants viewed the beam without the post-selection on polarization. The intensity profiles at the camera without a polarizer is shown for (top) Ψ_- state and (bottom) Ψ_+ state. The exposure time was lowered compared to Fig. 3.5 to avoid saturation, and the shown images are raw data. Figure reproduced from [2].

used to expand the beam to a diameter of approximately 5 cm and the user lens ($f = 150$ mm) that directed the beam onto the retina of the observer. To remove the speckle pattern the user lens was vibrated via push-pull motor that operated at 60 Hz with a stroke of 5 mm along the direction perpendicular to the beam propagation axis. Finally, a headrest, that included a chin rest with a variable height and a forehead rest bar, was placed at the end of the setup. The location of the headrest was optimized for each participant. The participants covered their non-viewing eye with an eye patch.

The first configuration of the setup (see Fig. 3.2a) uses mirrors to redirect the beam around the main optical components. A linear polarizer, quarter wave plate, and a rotating polarizer are then used to generate light whose polarization direction rotates in time.

The next three configurations use two sets of LOV prisms to generate the desired spin-orbit beams. The LOV prism pairs were circular quartz wedges with a wedge angle of 2°, a diameter of 2.54 cm, and for one wedge the optical axis was aligned with wedge angle while for the other wedge the optical axis was aligned 45° to wedge angle. Their characteristics are described in detail in Ref. [60] and Ref. [133].

The participants were tasked with discriminating between $|\Psi_-\rangle$ and $|\Psi_+\rangle$ based on the rotational symmetry of the Haidinger's brushes along the circle of radius b. Because the direction of rotation of the Haidinger's brushes of $|\Psi_-\rangle$ ($|\Psi_+\rangle$) is the same (opposite) relative to the direction of the eye movement, this trial type was given the label "natural" ("awkward").

Participants

Experimental participants were recruited from the Institute for Quantum Computing and the School of Optometry and Vision Science at the University of Waterloo. The complete study was run over a five day period. All research procedures received approval from the University of Waterloo Office of Research Ethics and all participants were treated in accordance with the Declaration of Helsinki.

A total of 17 participants, two of which are authors on the current study, were recruited. Participation was entirely voluntary and all participants, aside from the authors, received $15 CAD per day in appreciation for their time. Out of the 17 participants, 5 participants were unable to pass the screening on the second day and their participation was terminated. Of the 5 who did not complete the study, 4 were unable to achieve adequate performance with the setup in the first configuration (See Fig. 2a), and 1 was unable to perform the physical task without head movement. Therefore, a total of 12 participants completed the experiment.

Psychophysical Procedure

Participants were trained and tested on a psychophysical discrimination task over five days. During the first day the participants were familiarized with the study and presented with the first configuration of the setup (see Fig. 3.2a). The polarization of the light rotated either clockwise or counterclockwise, and participants were asked to fixate at the center of the beam and indicate the direction of rotation of the Haidinger's brush. The second and third configurations of the setup (see Fig. 3.2b&c) were then presented to the participant, and they were trained to execute the correct eye movement - eye movements along the indicated circle within the beam while keeping the head still - while observing the spin-orbit beam.

During the second day of the study, participants completed an assessment before beginning the main task. They were again exposed to the the first configuration of the setup (see Fig. 3.2a) and performed ten trials of the orientation discrimination task. The second configuration of the setup (see Fig. 3.2b) was then presented and the ability to perform the correct oculomotor action was assessed. Participants were excluded from further testing if they could not identify the direction of the Haidinger's brush with a >70% probability or if they produced visually noticeable head movement while viewing the beam from the second configuration and attempting the self directed eye motion. Participants who successfully completed the assessment were then able to perform the main task.

Participants performed the main psychophysical task during days 2, 3, 4, and 5, following an identical procedure. During testing, all participants observed the beam with their preferred eye and the other eye was occluded. Each testing day was composed of five blocks. At the start of each block, participants observed two alternating presentations of "awkward" and "natural" stimuli, and participants observed the stimuli by freely generating the correct eye movement for 15 seconds. After this free-viewing period, the actual discrimination task began. Seven trials were presented per block, each trial presenting either an "awkward" or a "natural" stimulus for 45 seconds, and the participant verbally indicated the perceived trial type. All trials of the same type were identical to one another. Real-time corrective feedback was given. Each block contained 7 trials, and each participant completed 5 total blocks per testing day. In total, 35 trials were completed per testing day and each participant completed a total of 140 trials across 4 days. Participants were given a 1 minute break in between blocks.

3.3 Human Discrimination of Structured States

The difficulty reported by participants of creating consistent circles with their gaze motivated the development of an alternate procedure, where the spin-orbit state itself would be manipulated to generate a moving entoptic pattern. This re-designed experiment was published on June 16, 2020 as "Direct discrimination of structured light by humans" [3]. Author contributions are summarized below.

- D.S., C.K., A.E.S., D.G.C., B.T., and D.A.P. designed the experiment;
- D.S., C.K., A.E.S., and D.A.P. performed the experiment;
- I.T. developed the spiral phase plate;
- D.S., C.K., A.E.S., D.G.C., B.T., and D.A.P. analyzed data;
- D.S., C.K., A.E.S., D.G.C., I.T., B.T., and D.A.P. wrote the paper.

3.3.1 Introduction

Custom light fields, also known as "structured light", can be engineered to achieve nontrivial propagation properties such as orbital angular momentum (OAM), nondiffraction, self-healing, and self-imaging [213, 214, 215, 216, 217, 214, 218]. In particular, the emergence of helical waves carrying OAM [173] These so called "spin-orbit states" or "vector vortex beams" possess space-varying polarization profiles and they have found applications in high-resolution imaging and optical metrology [185, 186, 187].

In this work we consider the physiology of human vision and optical spin-orbit states. We experimentally verify an entoptic phenomenon through which humans can perceive and discriminate between different spin-orbit states when directly viewing them. Direct discrimination is possible through the perception of distinct entoptic images that are induced by space-varying polarization. The behaviour and form of the 2D polarization topologies that arise when there is a superposition of polarization states coupled to different OAM

values has been thoroughly studied in the literature [176, 177, 178, 179, 5]. A pictorial representation of our experiment is shown in Fig. 3.7a, where optical states composed of a coherent superposition of differently polarized planar and helical waves carrying OAM were directed onto the retina of the observers. These spin-orbit states are non-separable in polarization and spatial modes [174, 175]. When considering light (as in the case of our experiment) this terminology refers to the way in which the scalar and vector aspects of light are combined in the optical beams: non-separable in a product basis of scalar (particularly azimuthal phase) and vector (polarization) states. Note that the same terminology is used in quantum optics, to describe the same optical states, but in the context of experiments involving correlations between individual photons.

The ability to perceive space varying polarization may be derived from an entoptic phenomenon through which humans can perceive the polarization state of light [153, 196, 197, 198]. When viewing polarized light, a bowtie-like shape (known as "Haidinger's brush") appears in the central point of the visual field. Although the exact physiological origin of the Haidinger's brushes is not fully understood, the prominent theory suggests that the perception of Haidinger's brushes depends on the presence of radially symmetric dichroic elements that are centered on the foveola [199]. This has led to studies where Haidinger's brushes are used to assess central visual field dysfunction and age-related macular degeneration [159, 211], measure macular pigment density [212], and determine the location of the fovea [219].

The orientation of the Haidinger's brush depends on the polarization state of light. Linearly polarized light induces a brush oriented perpendicular to the polarization direction [153], while the brush appears rotated $\approx 45^\circ$ clockwise (counter-clockwise) when viewing left (right) circularly polarized light [220]. However, retinal adaptation causes Haidinger's brushes to disappear after a few seconds if the polarization direction relative to the eye does not change. It has been found that stable perception of the brushes is achieved when the linear-polarization source is rotated at ≈ 1 Hz [160]. One may observe the behaviour of Haidinger's brushes by looking at the light scattered in the clear sky $\approx 90^\circ$ from the sun [221]. With some practice, a brush may be observed that points towards the sun.

Here we consider spin-orbit states that are composed of a coherent superposition of differently polarized planar and helical waves. The techniques explored in this work bring the vast toolbox of structured light, OAM states, and spin-orbit states to visual science applications. The wavefunction of a spin-orbit state travelling along the z-direction can be written as:

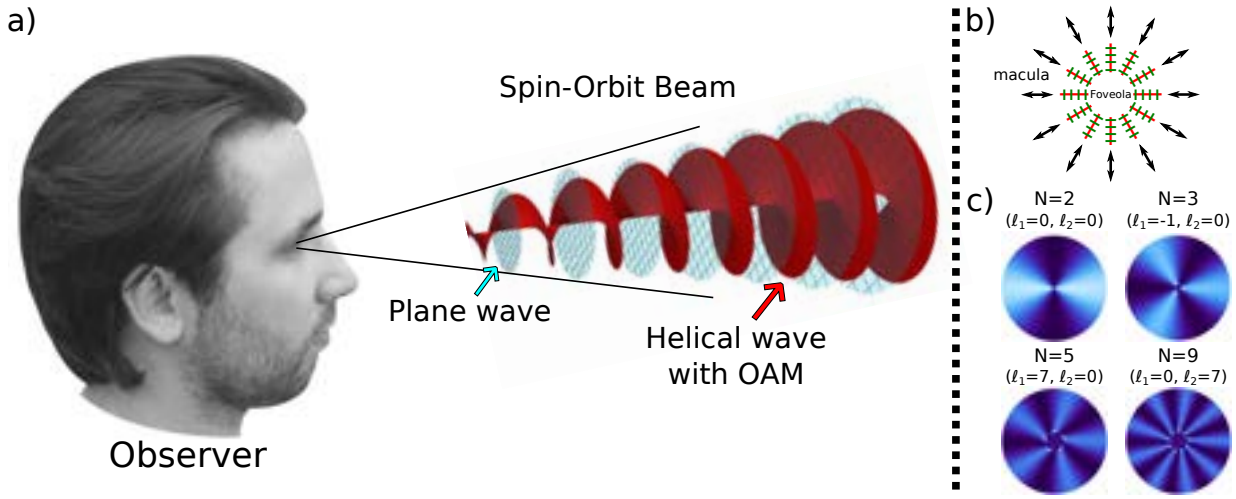


Figure 3.7: a) Pictorial representation of a spin-orbit beam, composed of a coherent superposition of a planar right-circularly polarized state and a helical left-circularly polarized state, being directed onto the retina of an observer. The helical state carries orbital angular momentum (OAM) and its phase varies along the azimuthal coordinate ϕ. The depicted example corresponds to Eq. 3.17 with $\ell_1 = 0$ and $\ell_2 = -1$. b) In the macula of the human eye the macular pigment molecules (green) are bound to the radially oriented Henle fibers (red) that surround the foveola. The radial symmetry of these dichroic elements (polarization filter direction as a function of the azimuthal coordinate is shown by black arrows) coincides with the symmetry of the polarization coupled OAM beams shown in a). c) The number of azimuthal fringes that a human sees when viewing the spin-orbit beams is equal to the number of radial lines (N) in the corresponding polarization profile of the beam, where $N = |(\ell_1 - \ell_2) - 2|$. Shown are the examples for $N = 2$ where $\ell_1 = \ell_2 = 0$; $N = 3$ where $\ell_1 = -1, \ell_2 = 0$; $N = 5$ where $\ell_1 = 7, \ell_2 = 0$; and $N = 9$ where $\ell_1 = 0, \ell_2 = 7$. The size of the central region increases with propagation. The N=2 case depicts the Haidinger's brush profile when horizontally polarized light is observed. Figure reproduced from [3].

$$|\Psi\rangle = \frac{1}{\sqrt{2}}\left[C_1(\ell_1, r, z)e^{i\ell_1\phi}\,|R\rangle + C_2(\ell_2, r, z)e^{i\ell_2\phi}\,|L\rangle\right], \tag{3.17}$$

where we have used the bra-ket notation for convenience, $|L\rangle = \begin{pmatrix}0\\1\end{pmatrix}$ and $|R\rangle = \begin{pmatrix}1\\0\end{pmatrix}$ denote the left and right circular polarization, and (r, ϕ) are the cylindrical coordinates. The form of the radial and propagation contributions, $C_1(\ell_1, r, z)$ and $C_2(\ell_2, r, z)$, depends on the method used to prepare the OAM beams. Exact forms have been shown for the Laguerre Gauss modes [173] and beams reflected from a spiral phase plate (SPP) [202].

As shown in Fig. 3.7b, the macular pigment molecules (green) in the human macula are bound to the radially oriented Henle fibers (red) that surround the foveola [199]. The accepted model for the action of the macula on the incoming light is to treat it as a radial polarization filter [222, 223, 224], a concept dating back to Maxwell and Helmholtz [225, 226]. The operator of the macula can therefore be expressed as:

$$|M\rangle\langle M| = \frac{1}{2}\begin{pmatrix}1 & e^{-i2\phi}\\ e^{i2\phi} & 1\end{pmatrix} \tag{3.18}$$

Several theories have been put forward in order to account for the human perception of circularly polarized light. Good agreement is found when accounting for corneal birefringence that is uniformly along the visual axis [227, 228, 222]. The corresponding operator is given by:

$$U_m = e^{i\frac{\alpha}{2}\hat{\sigma}_x} \tag{3.19}$$

where $\hat{\sigma}_x$ is the Pauli operator. The clarity of the brush when viewing circularly polarized light is determined by the total amount of phase (α) that the ocular birefringence induces, which is subject to individual variation [227, 228, 222]. The two operators of Eq. 3.18 & 3.19 acting on a polarized light beam reproduce with good agreement the reported descriptions of the Haidinger's brushes and polarization gradients [196, 197, 198, 153].

It follows that the profile that a person would perceive when viewing a spin-orbit beam is given by:

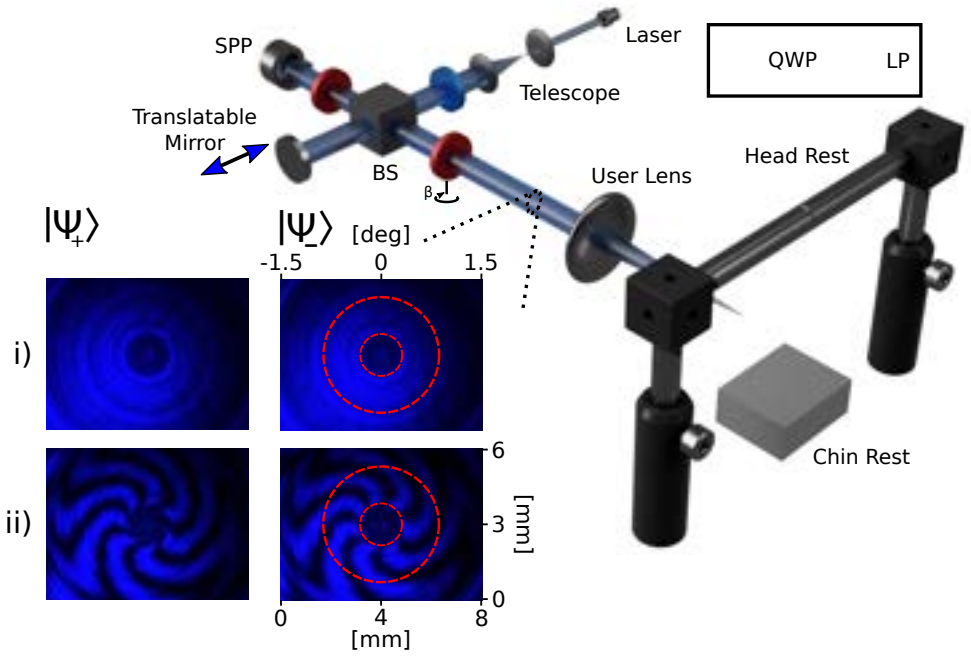


Figure 3.8: Schematic of the experimental setup where a Michelson interferometer along with a spiral phase plate (SPP) and standard polarization optics components are used to prepare the spin-orbit states that are directed onto the retina of the participants in the study. For a complete description of the setup see Materials and Methods A. Translating the mirror along the beam path direction varies $\theta(t)$ in Eq. 3.21, while the two orientations of the outer quarter wave plate (QWP), $\beta \in [0, 180°]$ around the vertical axis, correspond to the two states ($|\Psi_+\rangle$ and $|\Psi_-\rangle$) of Eq. 3.21. i) The images observed by a CMOS camera placed before the user lens, for both $|\Psi_+\rangle$ and $|\Psi_-\rangle$. It can be noted that azimuthal fringes are not present. The ring features are artifacts from SPP machining and they are equally present in both images. ii) The images observed by a CMOS camera placed before the user lens when a linear polarizer (LP) is placed in front of the camera. The seven azimuthal fringes correspond to the helical (OAM=7) phase structure of $|\Psi_+\rangle$ and $|\Psi_-\rangle$, the only notable difference being the 180° azimuthal phase shift. The attenuators were removed to obtain the images shown in i) and ii) and the camera gain was correspondingly optimized. In the study the participants only observed beams shown in i), and the red circles bound the area ($\approx 2°$ of field of vision) with good intensity and high quality phase structure that the participants were instructed to observe. The two simulated profiles of what the participants were expected to observe are shown in Fig. 3.7c under the labels "N=5" for $|\Psi_+\rangle$ and "N=9" for $|\Psi_-\rangle$. Note that the characteristic spherical phase of a Michelson interferometer caused the azimuthal fringes to wind. Figure reproduced from [3].

$$I = |\langle M| U_m |\Psi\rangle|^2 \tag{3.20}$$

where $|\Psi\rangle$ is given by Eq. 3.17. The radial symmetry of the macula in the human eye coincides with the symmetry of polarization coupled OAM states. The eye operator in Eq. 3.18 possesses an $e^{i2\phi}$ term, whereas OAM states are associated with a helical phase front which is described by the factor $e^{i\ell\phi}$ in the wave function, where ϕ is the azimuthal coordinate and ℓ is the OAM value.

The schematic of the experimental setup is shown in Fig. 3.8. The laser light was attenuated to $< 1\ \mu\text{W/mm}^2$ at the location of the observer in order to conform to the guidelines for laser exposure time outlined by the International Commission on Non-Ionizing Radiation [205]. An SPP [229] was placed in one arm of a Michelson interferometer along with standard polarization components. The SPP in reflection mode induced OAM of $\ell = 7$ for $\lambda = 450$ nm light. The setup thus allowed us to prepare and switch between the following two spin-orbit states:

$$\begin{aligned} |\Psi_+\rangle &= \frac{1}{\sqrt{2}}\left[C_1(7,r,z)e^{i7\phi}|R\rangle + C_2(0,r,z)e^{i\theta(t)}|L\rangle\right], \\ |\Psi_-\rangle &= \frac{1}{\sqrt{2}}\left[C_2(0,r,z)e^{i\theta(t)}|R\rangle + C_1(7,r,z)e^{i7\phi}|L\rangle\right], \end{aligned} \tag{3.21}$$

where $\theta(t)$ is a phase that varies linearly in time and acts to rotate the polarization profile of the beam, analogous to rotating the polarization direction of a beam to induce high clarity Haidinger's brush [160]. By translating the mirror along the beam propagation direction we varied $\theta(t)$ with a speed of $\approx 2\pi$ rad/s. For a complete description of the parameters in the setup see Materials and Methods A.

For the two states of Eq. 3.21 we can determine the profiles that a person would observe using Eq. 3.20. The two simulated profiles are shown in Fig. 3.7c under the labels "N=5" for $|\Psi_+\rangle$ and "N=9" for $|\Psi_-\rangle$. Therefore a person may discriminate between the two states of Eq. 3.21 by observing the number of azimuthal fringes: $|\Psi_+\rangle$ state manifests 5 azimuthal fringes and $|\Psi_-\rangle$ state manifests 9 azimuthal fringes. Furthermore, it can be noted that the number of azimuthal fringes that a human sees when viewing the spin-orbit beams is equal to the number of radial lines (N) in the corresponding polarization profile of the beam, where $N = |(\ell_1 - \ell_2) - 2|$ [176, 177, 178, 179]. The observable is proportional to the difference in the OAM values which manifests itself as a number of

entoptic azimuthal fringes. In order to determine the OAM value of the helical beam, an observer would be required to know the polarization state of the reference beam, as both ($\ell_1 = 0$, $\ell_2 = 7$) and ($\ell_1 = -7$, $\ell_2 = 0$) induce 9 azimuthal fringes: $N = |(0-7)-2| = 9$ and $N = |(-7-0)-2| = 9$. Or, if the setup enabled the perception of the azimuthal fringes in the first diffraction ring, then as shown in Fig. 3.7c, the OAM value can be determined by observing the number of azimuthal fringes along with their winding direction in the first ring.

To test the hypothesis that human observers can discriminate between the two states of Eq. 3.21, a psychophysical study was conducted where randomly selected states (either $|\Psi_+\rangle$ or $|\Psi_-\rangle$) were presented and participants discriminated between the two states based on the number of azimuthal fringes that they observed. Several factors helped ensure that the number of azimuthal fringes was the only cue for discriminating the beams. The setup used the orientation of the outer QWP to change between $|\Psi_+\rangle$ and $|\Psi_-\rangle$ while keeping the same SPP configuration. This ensured that the ring features noticeable in Fig. 3.8i were equally present in both cases. The studies were done without any ambient light and there was a screen (with a 1 inch diameter hole for the laser light to travel through) before the user lens which blocked the view of the setup by the participant. Furthermore, the QWP whose orientation determined which state was being observed was motorized to make an equal amount of motion between each trial. For a complete description of the psychophysical procedure see Materials and Methods C.

After a brief familiarization period, the participants performed 100 random trials with structured light over two sessions on separate days. After viewing the stimulus, participants responded in one of two ways, responding "many" if they observed 9 rotating azimuthal fringes or responding "fewer" if they observed 5 rotating azimuthal fringes. Fig. 3.9 shows the results for the ten participants who completed the study. There was no statistical difference between the results of session 1 and session 2, and therefore the data from both sessions were collapsed for the main analysis.

Sensitivity d' and response bias c were calculated for each participant. Percent correct is influenced by both a participant's ability to perform the task and the participant's response bias. However, d' is independent of response bias and is therefore a more accurate measure of performance when response bias is present [206]. Data was analyzed using two-tailed, one-sample t-tests with 9 degrees of freedom against the null value of 0.

All participants achieved performance that is numerically above chance, and collectively they achieved good discrimination sensitivity, $d' = 1.7$, $t(9) = 5.9$, p-value: $p = 2 \times 10^{-4}$, corresponding to a mean accuracy of 77.6 % correct. A significant response bias was also observed, $c = -0.2$, $t(9) = 3.0$, $p = .02$, as participants responded "many" more often

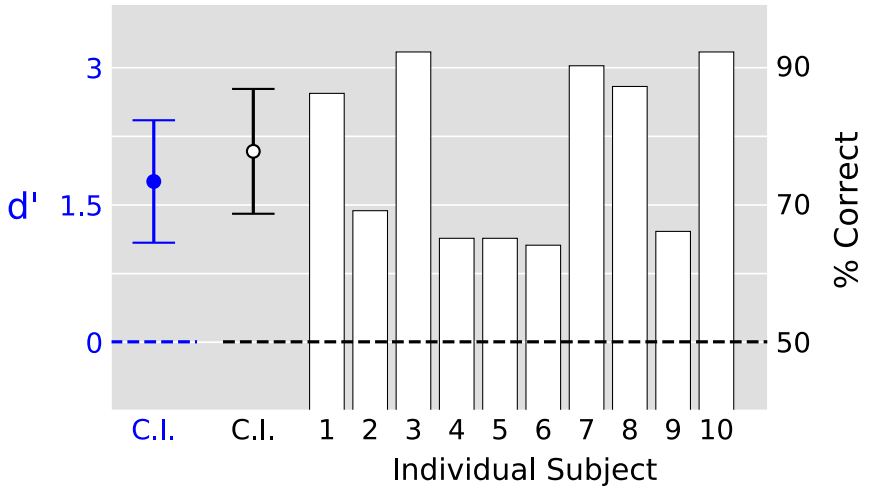


Figure 3.9: Sensitivity and accuracy for the discrimination task. Each participant performed 100 trials over two sessions. The dashed line indicates chance performance. Open bars show individual participant performance. Circular symbols show group mean sensitivity (blue: left ordinate) and accuracy (black: right ordinate). Error bars show 95% confidence intervals. Participants were highly sensitive to the difference between both trial types, performing significantly better than chance. Figure reproduced from [3].

than "fewer". Fig. 3.9 also suggests a bimodal distribution, where half of the participants achieved near-ceiling performance and the other half exhibited lower scores but remained above chance. There are no apparent explanations for this subdivision in terms of gender, age, or vision. We speculate that task performance is related to the various degrees of sensitivity that results from individual differences in the amount of ocular birefringence and the organizational structure of the macula.

To the best of our knowledge these experiments provide the first exploration and confirmation of humans directly perceiving and discriminating optical spin-orbit states and structured light with non-separable modes. Many follow up experiments are enabled given the recent advances in the control and manipulation of structured light. The setup in Fig. 3.8 can be advanced by incorporating a spatial light modulator (SLM) in place of the SPP. This would allow us to prepare arbitrary polarization gradients and test the psychophysical thresholds of human perception of polarization: the sensitivity distribution to a range of OAM values, individual differences in discrimination ability, and human sensitivity to other forms of structured light and polarization gradient patterns. Furthermore, optimizing the subjective clarity of the observed image allows us to determine the exact forms of Eq. 3.18 & 3.19 for a particular person. The exact form of the operators is currently subject to debate [199, 222, 223, 224].

Our follow up studies will also explore clinical applications of structured light perception. We speculate that structured light can be a highly sensitive probe of central visual field dysfunctions and age-related macular degeneration. The new techniques could provide a novel basis for the rapid, objective, and accurate assessment of macular pigment structure. Current clinical assessment techniques such as Optical Coherence Tomography (OCT) and the subjective report of visual field distortions are only sensitive to the presence of ocular disease after irreversible retinal damage has occurred [230]. Macular pigment assessment may be clinically useful in disease screening settings because macular pigment changes have been associated with a number of retinal diseases including macular degeneration. Similar to fundus imaging with polarized light [209, 219] we can devise objective photographic tests with structured light.

Lastly, we can contribute to the research that integrates human detectors with recent technological advances [191, 192, 193, 194]. Given the non-separability of Eq. 3.21 an experiment can be conducted where the correlations between the two degrees of freedom (DOF), polarization and OAM, are confirmed with the human eye as the detector. The rotation of the profile that would be observed in the following two cases should be identical: phase shift on the OAM DOF (induced by rotating the SPP) and the phase shift on the polarization DOF (induced by a properly aligned birefringent material).

3.3.2 Setup and Stimuli

In order to perform a valid human experiment, we are required to use a setup where the two beams that are presented to the observers do not have any differing intensity variations. Otherwise an observer has the possibility to distinguish different spin-orbit beams by noticing a number of other features such as radially dependant intensity profiles as well as the intensity variations throughout the beam due to diffraction and/or OAM dynamics.

Consider the spin-orbit states shown in Fig. 3.10 that are generated with our setup employing an SLM in place of the SPP. The topological charge of the fork dislocation pattern on the SLM sets the OAM value of the diffraction orders. Imaged is the intensity between the first diffraction order and the reference beam. Several important things can be noted: 1. The spin-orbit beams manifest radial intensity variations as they propagate. 2. Helical beams carrying different OAM values manifest unique dark regions in the center, and recognizable radial intensity variations. 3. The negative and positive OAM values also have differing features as the azimuthal fringes wind in opposite directions. Furthermore artifacts and imperfections in the setup manifest differently for the two cases. Therefore, in order to ensure a valid experiment, we use two beams with the same OAM values but coupled to opposite polarization states. In this scenario the intensity variations and the diffraction related effects are identical for both presented beams and could not be used as a cue.

The schematic of the setup is shown in Fig. 3.8. For this experiment we adhere to the guidelines for laser exposure time outlined by the International Commission on Non-Ionizing Radiation Protection which state that the maximum permissible exposure for a human eye for blue wavelengths is 1 μW/mm^2 [205]. Attenuators of ND=3.5 were placed after the laser in the setup and the intensity of light was $\approx$ 2.9 nW before the user lens. It was confirmed that the power density of light near the focal spot (near the eye location) was well below the stated limit. The apparatus was approved for use with human participants by the University of Waterloo Ethical Review Board following an assessment by the University of Waterloo Safety Office.

As the clarity of the Haidinger's brushes peaks for blue light of $\approx$ 460 nm wavelength, we used a diode laser with a central wavelength of 450 nm. A single mode optical fiber was used to clean the beam which was then expanded to 1.25 cm diameter via a 2 lens telescope system (f_1 = 25 mm and f_2 = 150 mm). The beam was then passed through a vertical polarizer. A Michelson interferometer was used to prepare the states of Eq. 3.21. The first beamsplitter creates a coherent superposition of two paths. One of the paths is reflected by a mirror and the other path is reflected by a spiral phase plate (SPP). The SPP was

generated out of 4N purity aluminum in an ultra precision machining center using custom diamond tooling. Temperature control was kept within 1°C and form accuracy was limited by the thermal expansion of the aluminum due to any thermal drift. The SPP used in the experiment was originally designed for experiments with $\lambda = 532$ nm. The actual step height of the SPP is 1596 nm, and over a 25 mm aperture the form accuracy is ± 0.5 μm, and the finish is ± 15 nm.

A quarter wave plate (QWP) was placed in front of the SPP in order to induce a polarization flip. Finally a QWP was placed at the output of the Michelson interferometer in order to prepare the two states of Eq. 3.21. The orientation of the QWP determined which output state was being prepared. The two orientations, $\beta \in [0, 180°]$, correspond to the two states ($|\Psi_+\rangle$ and $|\Psi_-\rangle$) of Eq. 3.21. Note that the QWP is oriented along 45° and 135° in the two cases since β is the angle around the vertical axis. Hence this QWP was placed on a rotation stage. A lens with f = 150 mm was used to direct the beam onto the retina of the participants. Several lenses (f= 75, 100, 150, 200, 250, 400, 500 mm) were tested by authors D. S. and C. K. who determined based on their subjective perceptions of the structured light that f=150 mm was the optimal choice.

The mirror was placed on a translation stage in order to induce a controlled phase shift and hence effectively rotate the polarization profile. By translating the mirror along the beam propagation direction we varied $\theta(t)$ with a speed of $\approx 2\pi$ rad/s. This is analogous to rotating the polarization direction of a beam to induce high clarity Haidinger's brush [160].

The participants covered their non-viewing eye with an eye patch. The headrest included a chin rest with a variable height and a forehead rest bar. The location of the user lens was optimized for each participant.

Fig. 3.8i shows the camera imaged intensity profiles that were observed. The $|\Psi_-\rangle$ state inducing 9 fringes was termed "many" while the $|\Psi_+\rangle$ state inducing 5 fringes was termed "fewer". In the study the participants only observed beams shown in Fig. 3.8i, and the red circles bound the area ($\approx 2°$ in field of vision) with good intensity and high quality phase structure that the participants were instructed to observe.

3.3.3 Participants

Experimental participants were recruited from the Institute for Quantum Computing and the School of Optometry and Vision Science at the University of Waterloo. The complete study involved two experimental sessions. Participation required written informed consent and all participants received CAD$15 per session in appreciation for their time. All research

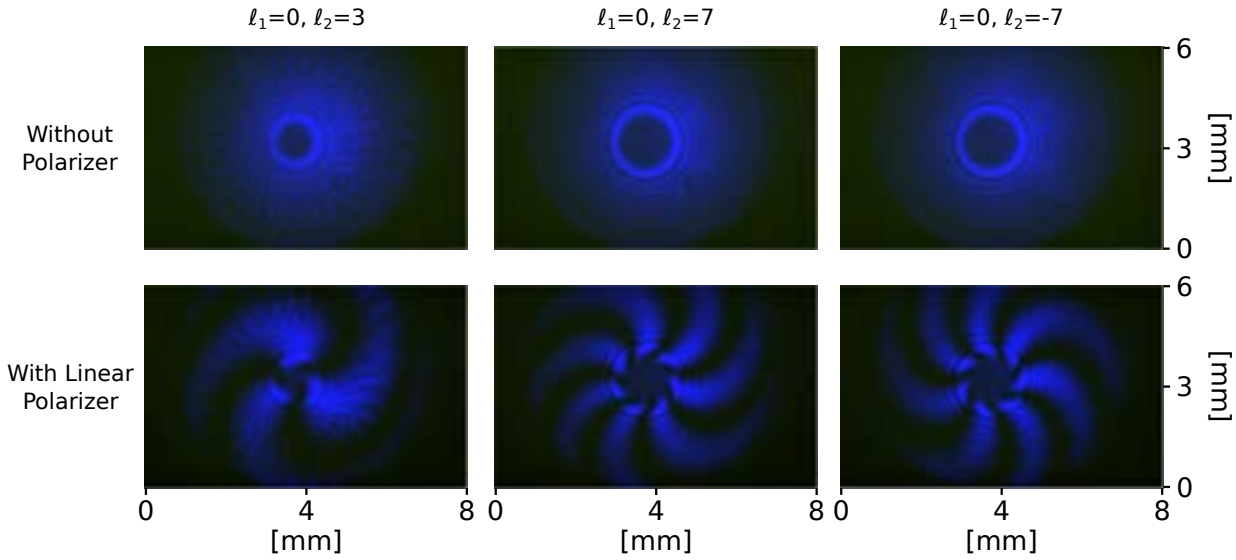


Figure 3.10: Comparison of spin-orbit states generated with the setup of Fig. 3.8 employing a Spatial Light Modulator (SLM) in place of the SPP. The topological charge of the fork dislocation pattern on the SLM sets the OAM value of the diffraction orders. Imaged is the intensity between the first diffraction order and the reference beam (top row) without a linear polarizer before the camera (bottom row) with a linear polarizer before the camera. Shown are the examples for $\ell_1 = 0, \ell_2 = 3$; $\ell_1 = 0, \ell_2 = 7$; and $\ell_1 = 0, \ell_2 = -7$. Note that only the stimuli shown in Fig. 3.8 were presented to the observers during the study. Figure reproduced from [3].

procedures received approval from the University of Waterloo Office of Research Ethics and all participants were treated in accordance with the Declaration of Helsinki.

A total of 12 participants were recruited. Of these, 2 participants did not complete the study. One participant voluntarily withdrew after reporting that they saw many floating features which obscured the stimulus during the familiarization period. The second participant reported discomfort and so they were immediately removed from the study. Therefore, 10 participants completed the experiment.

3.3.4 Psychophysical Procedure

Participants were tested on a psychophysical discrimination task over two experimental sessions. A familiarization period occurred during Session 1 whereby the participants viewed the "many" beam while the mirror in the setup was translated, inducing a rotation of the pattern either clockwise or counterclockwise. Participants were asked to observe the region bounded by the red circles in Fig. 3.8i and indicate the direction of rotation. Participants began the main experiment after five consecutive correct answers in the familiarization task.

After familiarization, participants performed the main psychophysical task. A 5 min dark adaptation period occurred at the start of each session. All participants observed the beam with their preferred eye and the other eye was patched. Each session was composed of 5 blocks with 10 trials each. The trials were separated by ≈ 5 sec, and no break occurred between blocks. At the start of a block, participants observed two alternating presentations of the "many" and "fewer" beams, each lasting up to 10 seconds. The correct label for each beam was told to the participants. After completing the alternating presentations, participants performed the discrimination task. For each trial a Python 3.6 random number generator was used to determine which state the participant would view. Each trial was presented for no more than 15 seconds (excluding the instances where the participant wished to adjust their position), and the participant verbally indicated the perceived trial type. C. K. was in charge of initializing the QWP orientation via the motorized stage, and he provided the real-time corrective feedback to the participant after each trial. D. S., who did not know the orientation of the QWP in the trials, was present to answer any questions that the participant might have during the study. In total, each participant completed 100 trials across 2 testing sessions (5 blocks $\times$ 10 trials per block $\times$ 2 sessions).

3.4 Measuring the visual angle of entoptic phenomena

This design was further improved with the introduction of spatial light modulator (SLM) to generate arbitrary phase profiles, in place of the SPP used previously. That enhanced experiment was published on February 1, 2024 as "Measuring the visual angle of polarization-related entoptic phenomena using structured light" [4]. © 2024 Optica Publishing Group under the terms of the Open Access Publishing Agreement Author contributions are summarized below.

- C.K., A.E.S., D.G.C., D.A.P., B.T., and D.S. designed the experiment;
- C.K. built the apparatus and wrote the control software
- C.K., M.K., M.A.M., and T.S. performed the experiment;
- C.K., A.E.S., and D.A.P. analyzed data;
- C.K., A.E.S., D.G.C., D.A.P., B.T., and D.S. wrote the paper.

3.4.1 Introduction

The human perception of polarized light has long been an area of active research, dating back to the identification of the Haidinger's Brush phenomenon in 1844 [231], continuing with the Maxwell and Helmholtz models of human polarization perception [225, 232], to modern investigations, motivated by the observation that human polarization perception is inhibited in patients with early-stage age-related macular degeneration (AMD) [233, 234, 235]. Despite this research interest, current clinical diagnosis of AMD does not utilize polarization perception, in part because existing polarization perception diagnostic tests show significant false-positive AMD detection, that is, healthy participants are not always able to perceive these polarization patterns [236, 237]. AMD remains the leading cause of blindness in people over the age of 60 in the developed world [238], and a significant number of people over 60 show symptoms of AMD that are not detected in standard vision care [239].

Over the past five decades, the term "structured light" has evolved from referring to the generation of intensity patterns at a particular camera plane by diffractive optics to a wide variety of techniques for creating non-trivial phase patterns in coherent beams of light and other non-optical waves [185, 240, 241]. Recently, the field of structured light has become associated with orbital angular momentum (OAM) states which possess an azimuthal phase-ramp from 0 to some multiple (also called the OAM number) of 2π. The development of numerous components capable of generating the phase vortex indicative of OAM states has led to applications in information transmission, matter manipulating, and material science [216, 242, 67, 66, 243, 244, 60, 133]. Furthermore, advancements in the generation of structured states of light have bridged the gap between structured light research and biological material characterization, including the study of biological tissue [245], and the study of human polarization perception [3, 2, 246, 247].

Structured light tools enable the generation of polarization states which elicit entoptic profiles inaccessible with traditional forms of light [3, 2]. Here, we present the first direct measurement of the visual angle of entoptic patterns through a psychophysical perception task coupled with retinal imaging of structured light profiles. The extent of the entoptic pattern generated by polarization-coupled OAM states with OAM value $\ell = 13$ was measured by obstructing the central region of the structured light state, with a variable diameter obstruction. A forced-choice 2-up/1-down staircase was used to vary the size of the obstruction to determine the apparent size of the entoptic pattern. This diameter could then be converted to degrees of visual angle with reference to retinal images taken with an imaging device using structured light illumination. By projecting the polarization-coupled state directly onto the retina, we remove the propagation effects seen in [3] and enable the use of variable obstructions. Furthermore, we enable the generation of entoptic patterns selectively on particular regions of the retina. Leveraging these advantages, we report that the perceived entoptic pattern generated by an $\ell = 13$ OAM state is $9.5° \pm 0.9°$ in diameter, while Haidinger's Brush extends 3.75° [160]. This increase in apparent entoptic pattern size and clarity suggests that structured states may provide significantly increased utility as a diagnostic tool over polarization perception methods utilizing Haidinger's Brush.

3.4.2 Theory

While several physiological mechanisms through which humans perceive polarized light have been proposed [248], recent consensus is that axons located in Henle's fiber layer of the retina cause this effect [200, 196]. These axons contain pigment molecules, such as lutein, with an average orientation radial to the central axis of the fiber [249]. Within the macula, these axons lie parallel to the surface of the retina and are oriented radially [250].

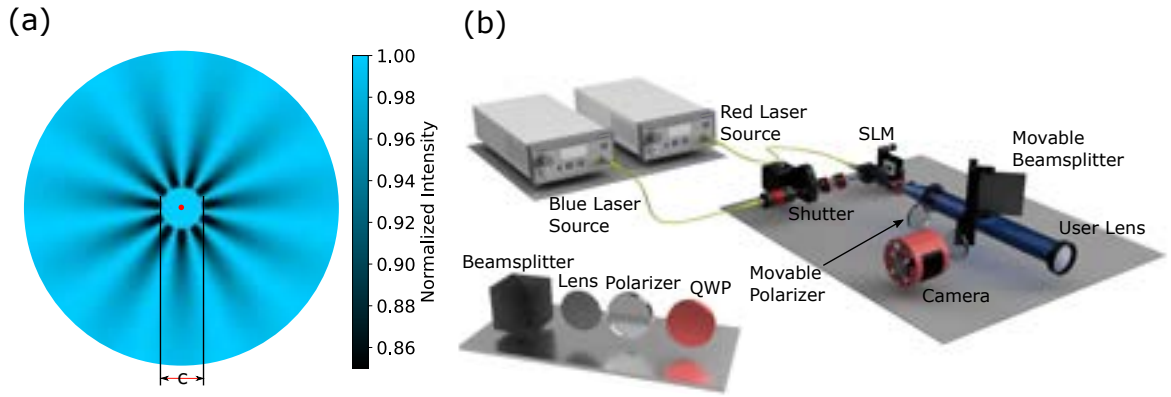


Figure 3.11: (a) Simulation of the entoptic pattern generated by a $\ell = 13$ spin-coupled OAM state, as shown in Equation 3.23. The intensity of this entoptic pattern was generated using the macular pigment optical density (MPOD) model shown in Equation 3.22. The state viewed by participants has a red guide light at the center of the orbital angular momentum state. The size of the central circular obstruction is shown here as c. (b) Monochromatic light from a 450 nm diode laser is prepared in a circularly polarized state, followed by a polarizer and quarter waveplate, each mounted on separate rotation stages. Following this, the beam is prepared in a polarization state which is orthogonal to the optic axis of the spatial light modulator (SLM). Light can then be prepared in the polarization-coupled OAM state described in Equation 3.23. A two-lens imaging system is used to expand the beam for viewing through a Volk 20D Binocular Indirect Ophthalmoscopy lens. Retinal imaging is enabled by the translation stage mounted plate beamsplitter placed before the Volk lens. When placed in the beam, this plate beamsplitter directs reflected light from the retina through a linear polarizer to the camera-lens imaging system. The structured light imaging microscope enables the measurement of structured light pattern dimensions directly on a participant's retina. Figure reproduced from [4].

The dichroic properties of lutein lead to Henle's fiber layer acting as a radially oriented dichroic optical element in the region of the retina where these fibers lie parallel to the retinal surface [251]. A model for the macular pigment optical density (MPOD) [252], is

$$D(r) = A_1 10^{-\rho_1 r} + A_2 10^{-\rho_2 (r-\alpha_2)^2}, \tag{3.22}$$

where these parameters have been measured to be $A_1 = 0.31 \pm 0.12$, $A_2 = 0.11 \pm 0.08$, $\rho_1 = 0.32° \pm 0.24°$, $\rho_2 = 1.2(°)^{-2} \pm 1.1(°)^{-2}$, and $\alpha_2 = 0.70° \pm 0.66°$ [252]. A state with OAM value $\ell = 13$ was chosen because this state produced a significant number of azimuthal fringes without reaching the spatial resolution limit of our spatial light modulator (SLM). The structured state generated by the SLM is a polarization-coupled OAM state described by,

$$\frac{1}{\sqrt{2}}(1 - \Pi[r/c])(e^{i(13\phi + 2\theta t)} |R\rangle + |L\rangle), \tag{3.23}$$

where we have used bra-ket notation for the right, $|R\rangle = \binom{1}{0}$, and left, $|L\rangle = \binom{0}{1}$, circular polarization states, (r, ϕ) for the cylindrical coordinate system, $\Pi[r/c]$ is the unit pulse function that sets the size (c in Fig. 3.11(a)) of the central obstruction area, and $2\theta t$ is a time-varying phase-shift. The polarization state after each element in the device is described in the Appendix. The macula can be modeled by a partially polarizing optical element of the form,

$$\hat{U}_M = \frac{D(r)}{2} \begin{pmatrix} 1 & e^{-i2\phi} \\ e^{i2\phi} & 1 \end{pmatrix} + (1 - D(r))\mathbf{1}, \tag{3.24}$$

where $D(r)$ is the MPOD, and $\mathbf{1}$ is the identity operator. The combination of this polarizing filter in the macula with a structured light state will produce a number of azimuthally varying fringes, where the number of fringes is given by $N = |\ell - 2|$ [3]. The time-varying phase-shift, $2\theta t$, causes these entoptic fringes to rotate, either clockwise or counter-clockwise.

The entoptic pattern created by this structured state and the macula model in Equations 3.22, 3.23, 3.24 is shown in Figure 3.11(a), using the mean parameter values measured by [252]. The human cornea has been shown to possess birefringence, oriented about a roughly horizontal axis [253]. In the special case of a uniformly polarized beam, $\ell = 0$, the two azimuthal fringes of Haidinger's Brush are visible, but the rotation direction of the pattern is reversed for large corneal birefringence values. With the $\ell = 13$ OAM

state, the perceived rotation direction of the entoptic phenomenon is insensitive to corneal birefringence, see the Appendix for a detailed derivation.

It has been observed that the visibility of stationary entoptic patterns created by polarized light structures will reduce over time due to visual adaptation. Therefore, any polarization pattern projected onto the retina must vary with time. This can be accomplished using a rotating linear polarizer that will modify the phase, θ in Equation 3.23, and cause the polarization-coupled OAM state to rotate. Using the ability to control the polarization structure projected on the retina, limited only by the resolution of the SLM, we can measure the apparent size of this entoptic phenomenon through a perception task.

A schematic of the device used in this experiment is shown in Figure 3.11(b). The polarization-coupled OAM-state is created with a 450 nm wavelength fiber-coupled diode laser, attenuated to 150 nW at the location of the pupil. After exiting the coupler, the light is prepared in a circularly polarized state, followed by a rotating polarizer and quarter waveplate combination which allows for any polarization state orthogonal to the horizontal axis to be prepared at equal intensity. This light is then reflected from an SLM, whose optical axis is aligned horizontally. The SLM is placed at one output of a beamsplitter, while a red laser and pinhole, creating a fixation target light for participants, are placed at the other output port. Both the SLM screen and pinhole are then imaged and expanded by a $4f$-imaging system. A 20D Volk lens is then used to map the image created by the $4f$-imaging system directly onto a participant's retina. This direct projection of the polarization-coupled OAM state onto the retina removes the effects of state propagation seen in [3] and enables the use of a variable obstruction on the SLM screen. Real-time in-vivo imaging is enabled by an 80R/20T plate beamsplitter and a linear polarizer, both of which can be moved into the beam via translation stages. Light reflected off a participant's retina then passes through an analyzer, anti-aligned to the movable polarizer placed before the beamsplitter, which eliminates corneal reflections from the image. Finally, the retina is imaged with the ZWO camera shown in Figure 3.11(b).

The high refresh-rate SLM used to generate this state allows for the real-time control of an arbitrary polarization pattern that illuminates a participant's retina directly. Therefore, we can obstruct the central region of a structured light state to determine the spatial extent of the entoptic pattern generated by said profile, as can be seen in Figure 3.11(a). To ensure that participants are not able to distinguish the motion of the entoptic pattern from any other motion, the rotating polarizer used to generate rapid motion in the polarization profile is set to always rotate in the same direction. Distinct motion in the entoptic stimulus can be generated by changing the orientation of the quarter waveplate following the rotating polarizer. Note that this quarter waveplate remains stationary during a trial.

3.4.3 Empirical Experiment

Twenty-four participants were recruited to perform the discrimination task. All participants provided informed consent and were treated in accordance with the Declaration of Helsinki. All research procedures received approval from the University of Waterloo Office of Research Ethics.

The retina of each participant was illuminated with a structured light state, where an OAM number of $\ell = 13$ was prepared on the right-circular polarization state, resulting in $N = 11$ fringes when filtered with the polarizer described in Equation 3.24. Aligned to the center of this OAM state was a 50 µm pinhole illuminated by a red laser, creating a $\approx 1^\circ$ visual angle guide light for participants to fixate on. Each trial consisted of 500 ms of an OAM state, which produced 11 azimuthal fringes, rotating either clockwise (CW) or counterclockwise (CCW). After the 500 ms presentation, the structured light pattern was blocked by a shutter, while the fixation target remained on, and the participant indicated the direction of pattern rotation. Each new trial began with the presentation of a stationary structured light state pattern to allow the participant to verify visibility, and the onset of the task rotation was participant-controlled.

In order to measure the eccentric extent of polarization sensitivity, a circular obstruction was centered on the fixation point, and the diameter was varied following the 2-up/1-down staircase method [254]. Two consecutive correct answers resulted in an increase in the diameter of the circular obstruction placed at the center of the structured light state, while one incorrect response resulted in a decrease in the diameter of the central obstruction. This procedure enables the calculation of an obstruction threshold corresponding to 70.7% performance accuracy, where a larger threshold indicates a larger eccentric range of polarization sensitivity.

The staircase terminated after 14 reversals (that is, a change in hole-size progression from increasing to decreasing or vice versa) or after 90 total trials. The initial obstruction was 20 pixels in diameter, equal to the diameter of the red fixation point. The initial step size of the change in central obstruction visual angle was 2.70°, became 1.80° after three reversals, then became 0.90° after six reversals, and finally became 0.45° after nine reversals. Each person's eccentric obstruction threshold is calculated by taking the arithmetic mean of the final six reversal points. If the participant completed 90 trials, then the final point was treated as a reversal point. Example staircases and thresholds are shown in Figure 3.12. Before performing the thresholding task, all participants performed an initial familiarization task. The initial obstruction size (0.90°) was presented for several seconds 10 times, and all participants achieved at least 70% discrimination accuracy. Participants whose staircase results show more than 3 reversal points at the minimum

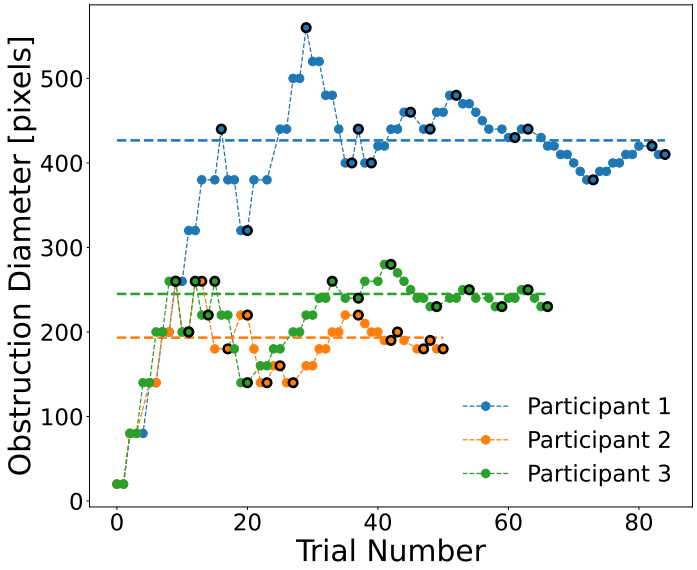


Figure 3.12: Select examples of participant staircase results. The final six reversal points, labeled as black dots, are averaged to determine the diameter at which the structured light stimulus is perceivable at 70.7% correct. Three example staircases are shown. Figure reproduced from [4].

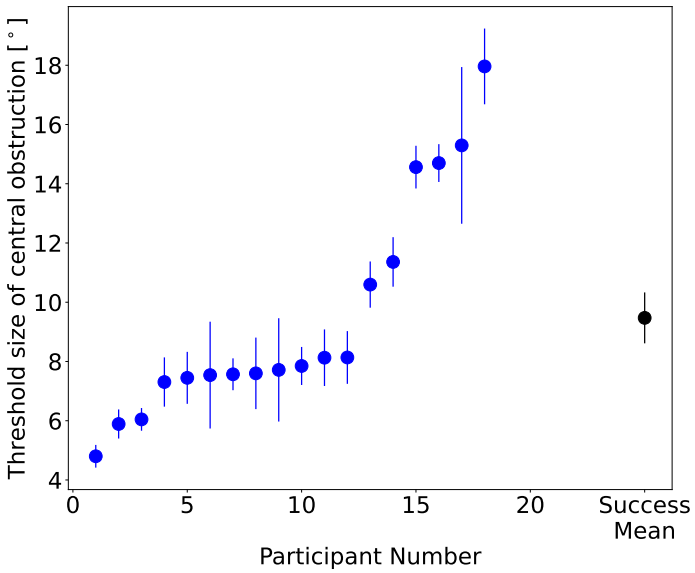


Figure 3.13: Threshold results from all participants who successfully complete the perception task, shown as blue points. The threshold value was measured by averaging the final six reversal points from each participant's staircase, with the standard deviation of the reversal points indicated as error bars. The threshold was converted to degrees of visual angle impinging on the retina by coregistering a structured light image of the retina with a commercial fundus image and calculating the size of landmarks. The average threshold visual angle was $9.5° \pm 0.9°$. Figure reproduced from [4].

obstruction diameter are considered to have "failed" the perception task. Altogether, 18 out of 24 total participants successfully completed the task with a valid threshold. While these "failed" participants correctly perceived the entoptic phenomenon rotation direction when presented for no less than 2 seconds, the stimulus presentation time of 500 ms inhibited these participants' ability to discern a rotation direction. One participant produced a threshold visual angle that was 3.3 standard deviations beyond the mean value and was removed on the assumption of improper fixation.

3.4.4 Results

From each participant's perception threshold in SLM pixel units, it is possible to calculate the threshold in degrees of visual angle. To achieve this, retinal images are taken using the

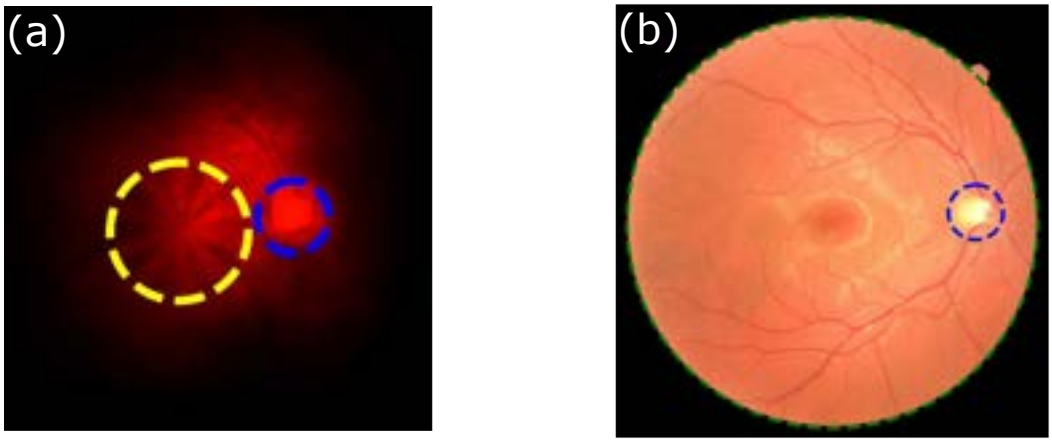


Figure 3.14: Two example retinal images from a single participant. (a) Retinal image taken with the structured light imaging device. The incident light is passed through a polarizer in order to display the radial pattern of the structured light state. By displaying structured light states limited to a set diameter (dotted yellow line), we can measure the size of these patterns relative to features on each participant's retina. (b) Retinal image captured by a Nidek MP-3 fundus camera. The size of features in the optic nerve head (dotted blue lines) can be used to relate the size of various structured light patterns. These two images allow us to verify the detection threshold diameter in degrees of visual angle, accounting for differences on an individual level. Figure reproduced from [4].

described structured light device to determine the spatial extent of the central field obstruction on the retina through an image that shows both the optic disk and the structured light pattern. As a confirmation, retinal images are also taken using a Nidek MP-3 fundus camera and the size of the optic disk in degrees of visual angle can be compared between these two photos. An example of the image captured by the structured light imaging device can be seen in Figure 3.14(a) and the corresponding image produced by the commercial retinal camera can be seen in Figure 3.14(b).

The results for each participant, converted from pixel units into degrees of vision, are shown in Figure 3.13, where the mean value is determined by the average of the final six reversal points and the error bars are given by the standard deviation of these reversal points. As can be seen in Figure 3.13, the average threshold was $9.5° \pm 0.9°$ with a 95% confidence interval of [5.83°, 13.12°]. These results show that all participants observe an entoptic pattern that is larger than the mean size of Haidinger's Brush measured in [160].

3.4.5 Discussion

In this work, we have directly mapped a polarization-coupled OAM state onto the human retina. This negates propagation effects seen in [3], enabling the use of a variable obstruction on the SLM screen itself. Using this variable obstruction, we have directly measured the extent of the entoptic phenomenon created by a polarization-coupled OAM state. This, combined with structured light retinal imaging has allowed for the measurement of these entoptic phenomena in degrees of visual angle. Between participants, there is significant variation in the visual angle this entoptic pattern subtends. Patient history, refractive error, fundus images, and optical coherence tomography data were gathered on each patient during this study. No significant correlation is observed between perceived entoptic pattern size and refractive error, including spherical, cylindrical, and spherical equivalent refractive errors. One possible source of the variation between patient thresholds is individual differences in macular pigment density.

The resulting mean apparent size of the entoptic pattern with 11 azimuthal fringes, $9.5° \pm 0.9°$, exceeds measurements of the apparent size of Haidinger's Brush, 3.75° [160]. The diagnostic potential of Haidinger's Brush perception tasks has previously been established [223, 212]. The significant increase in the apparent size and clarity of entoptic phenomenon produced by polarization-coupled OAM stimuli suggests a greater utility of structured light stimuli as a perception test to evaluate macular health. These advancements open new avenues of research whereby the extent of patterns created by structured light stimuli can be used to measure properties of the macula and spatially map changes in the macula through polarized light perception. Future studies will relate direct measurements of spatially-dependent changes in polarization perception to AMD and other retinal disorders.

3.4.6 Appendix

Coordinate System

Here we quantize the polarization state along the circular polarization axis. The real-space coordinate system is defined with z following beam propagation, x on the horizontal, and y on the vertical with positive y pointing 'up'. In this system, the diagonal state $|D\rangle$ is pointed in the positive x and y quadrant. Up to a normalization factor, these states are given by,

$$
\begin{aligned}
|R\rangle = \left(\begin{smallmatrix}1\\0\end{smallmatrix}\right), |L\rangle = \left(\begin{smallmatrix}0\\1\end{smallmatrix}\right),\\
|H\rangle = \left(\begin{smallmatrix}1\\1\end{smallmatrix}\right), |V\rangle = \left(\begin{smallmatrix}1\\-1\end{smallmatrix}\right),\\
|D\rangle = \left(\begin{smallmatrix}1\\i\end{smallmatrix}\right), |A\rangle = \left(\begin{smallmatrix}1\\-i\end{smallmatrix}\right).
\end{aligned}
$$

Polarization State in the Apparatus

Incident to the rotating polarizer, the laser is prepared in $|\psi_0\rangle = |R\rangle$ state. Following the rotating polarizer, the state is described by,

$$
|\psi_1\rangle = |R\rangle + e^{i2\theta} |L\rangle ,
$$

where the angle θ is defined relative to the horizontal axis in real space. Following the rotating polarizer, a rotating quarter-waveplate is set to either the diagonal or anti-diagonal axis. This produces one of two states,

$$
\begin{aligned}
|\psi_{2,D}\rangle &= |H\rangle + e^{i2\theta} |V\rangle ,\\
&= cos(\theta) |R\rangle - sin(\theta) |L\rangle ,\\
|\psi_{2,A}\rangle &= |V\rangle + e^{i2\theta} |H\rangle ,\\
&= cos(\theta) |R\rangle + sin(\theta) |L\rangle ,
\end{aligned}
$$

where the waveplate setting has been denoted with the subscript D or A. The spatial light modulator will then write a spatially dependent phase on the horizontal polarization state, for example, we will choose an orbital angular momentum (OAM) state with OAM number ℓ,

$$
\begin{aligned}
|\psi_{3,D}\rangle &= e^{-i\ell\phi} |H\rangle + e^{i2\theta} |V\rangle ,\\
|\psi_{3,A}\rangle &= e^{-i\ell\phi} e^{i2\theta} |H\rangle + |V\rangle .
\end{aligned}
$$

The spatial light modulator is followed by a fixed quarter waveplate which is set to diagonal, mapping the states $|H\rangle \mapsto |L\rangle$ and $|V\rangle \mapsto |R\rangle$. This produces one of two states,

$$|\psi_{4,D}\rangle = e^{i2\theta}\,|R\rangle + e^{-i\ell\phi}\,|L\rangle\,,$$
$$|\psi_{4,A}\rangle = |R\rangle + e^{-i\ell\phi}e^{i2\theta}\,|L\rangle\,.$$

Entoptic Pattern, Without Corneal Birefringence

The pattern perceived by a test subject can be modeled using a radial polarization filter, given by Equation 3.24. Assuming the macula perfectly polarizes, ie. $D(r) = 1$, this filter produces an intensity pattern, given by,

$$\begin{aligned} I_D &= \frac{1}{4}\begin{pmatrix} e^{-i2\theta} & e^{i\ell\phi}\end{pmatrix}\begin{pmatrix} 1 & e^{-i2\theta} \\ e^{i2\theta} & 1\end{pmatrix}\begin{pmatrix} e^{i2\theta} \\ e^{-i\ell\phi}\end{pmatrix}, \\ I_D &= \frac{1}{4}(2 + e^{-i2\theta}e^{-i(\ell+2)\phi} + e^{i2\theta}e^{i(\ell+2)\phi}), \\ &= \cos^2\left(\frac{\ell+2}{2}\phi + \theta\right), \end{aligned}$$

$$\begin{aligned} I_A &= \frac{1}{4}\begin{pmatrix} 1 & e^{-i2\theta}e^{i\ell\phi}\end{pmatrix}\begin{pmatrix} 1 & e^{-i2\theta} \\ e^{i2\theta} & 1\end{pmatrix}\begin{pmatrix} 1 \\ e^{-i\ell\phi}e^{i2\theta}\end{pmatrix}, \\ I_A &= \frac{1}{4}(2 + e^{i2\theta}e^{-i(\ell+2)\phi} + e^{-i2\theta}e^{i(\ell+2)\phi}), \\ &= \cos^2\left(\frac{\ell+2}{2}\phi - \theta\right). \end{aligned}$$

The above shows that, for any ℓ value, this state produces azimuthal fringes which rotate clockwise or counter-clockwise depending on the rotation waveplate setting. The effect of corneal birefringence can be considered by adding another waveplate element before the macular polarizer. Consider the strongest possible corneal effect, namely a half-waveplate oriented horizontally. The effect of this element is to map the states $|R\rangle \mapsto |L\rangle$ and $|L\rangle \mapsto |R\rangle$.

$$
\begin{aligned}
I'_D &= \frac{1}{4}\begin{pmatrix} e^{i\ell\phi} & e^{-i2\theta} \end{pmatrix}\begin{pmatrix} 1 & e^{-i2\theta} \\ e^{i2\theta} & 1 \end{pmatrix}\begin{pmatrix} e^{-i\ell\phi} \\ e^{i2\theta} \end{pmatrix}, \\
I'_D &= \frac{1}{4}(2 + e^{i2\theta}e^{i(\ell-2)\phi} + e^{-i2\theta}e^{-i(\ell+2)\phi}), \\
&= \sin^2\left(\frac{\ell-2}{2}\phi + \theta\right),
\end{aligned}
$$

$$
\begin{aligned}
I'_A &= \frac{1}{4}\begin{pmatrix} e^{i2\theta}e^{i\ell\phi} & 1 \end{pmatrix}\begin{pmatrix} 1 & e^{-i2\theta} \\ e^{-i2\theta} & 1 \end{pmatrix}\begin{pmatrix} e^{-i\ell\phi}e^{i2\theta} \\ 1 \end{pmatrix}, \\
I'_A &= \frac{1}{4}(2 + e^{-i2\theta}e^{i(\ell-2)\phi} + e^{i2\theta}e^{-i(\ell+2)\phi}), \\
&= \sin^2\left(\frac{\ell-2}{2}\phi - \theta\right).
\end{aligned}
$$

Comparing these two cases with $\ell = 5$, a participant with a corneal birefringence of $\gamma_{cornea} = 180°$ will see 3 azimuthal fringes while a participant with no corneal birefringence will see 7 lines. Critically, both participants will observe rotation clockwise or counter-clockwise at the same waveplate setting. In the case of a uniform polarization state, producing a Haidinger's brush entoptic pattern, the participants will observe,

$$
\begin{aligned}
I_D = \cos^2(\phi + \theta),\ I_A = \cos^2(\phi - \theta), \\
I'_D = \cos^2(\phi - \theta),\ I'_A = \cos^2(\phi + \theta),
\end{aligned}
$$

thus for the same waveplate setting, each participant will observe an opposite rotation direction.

Entoptic Pattern, With Corneal Birefringence

Assuming a horizontal orientation for the birefringence inherent in the cornea, we can generalize the above result for any rotation about the horizontal polarization by an angle, β. The effect of the cornea is given by the operation,

$$
\hat{U}_C = \begin{bmatrix} \cos\left(\frac{\beta}{2}\right) & -i\sin\left(\frac{\beta}{2}\right) \\ \sin\left(\frac{\beta}{2}\right) & \cos\left(\frac{\beta}{2}\right). \end{bmatrix}
$$

The state after the cornea is given by,

$$\begin{aligned}
|\psi_{5,D}\rangle &= \hat{U}_C\,|\psi_{4,D}\rangle\,, \\
&= \left(e^{i2\theta}\cos\left(\beta/2\right) - ie^{-i\ell\phi}\sin\left(\beta/2\right)\right)|R\rangle \\
&+ \left(ie^{i2\theta}\sin\left(\beta/2\right) - e^{-i\ell\phi}\cos\left(\beta/2\right)\right)|L\rangle\,, \\
|\psi_{5,A}\rangle &= \hat{U}_C\,|\psi_{4,A}\rangle\,, \\
&= \left(\cos\left(\beta/2\right) - ie^{i2\theta}e^{-i\ell\phi}\sin\left(\beta/2\right)\right)|R\rangle \\
&+ \left(i\sin\left(\beta/2\right) + e^{i2\theta}e^{-i\ell\phi}\cos\left(\beta/2\right)\right)|L\rangle\,.
\end{aligned}$$

We can calculate the intensity profile for this generalized case using this state $|\psi_{5,D}\rangle$ or $|\psi_{5,A}\rangle$,

$$\begin{aligned}
I_D &= |\langle M|\,|\psi_{5,D}\rangle|^2 \\
&= 1/2 + 1/2\cos([\ell+2]\phi + 2\theta)\cos^2(\beta/2) \\
&\quad - 1/2\sin(\beta/2)\cos(\beta/2)\sin(\ell\phi + 2\theta) \\
&\quad - 1/2\sin(\beta/2)\cos(\beta/2)\sin(2\phi) \\
&\quad - 1/2\cos([\ell-2]\phi + 2\theta)\sin^2(\beta/2),
\end{aligned}$$

$$\begin{aligned}
I_A &= |\langle M|\,|\psi_{5,A}\rangle|^2 \\
&= 1/2 + 1/2\cos([\ell+2]\phi - 2\theta)\cos^2(\beta/2) \\
&\quad - 1/2\sin(\beta/2)\cos(\beta/2)\sin(\ell\phi - 2\theta) \\
&\quad - 1/2\sin(\beta/2)\cos(\beta/2)\sin(2\phi) \\
&\quad - 1/2\cos([\ell-2]\phi - 2\theta)\sin^2(\beta/2).
\end{aligned}$$

While these patterns do not have a well-defined number of equal contrast fringes, the phenomenon seen in the previous case holds. That is, for OAM states with $\ell \neq 0$, the entoptic pattern caused by the macula appears to rotate clockwise/counter-clockwise for every participant regardless of their corneal birefringence value. For the case of $\ell = 0$, there exists a second birefringence value of interest, $\beta = 90°$, where no continuous motion of Haidinger's brush is apparent.

3.5 Outlook on Biological Applications of Structured States

The series of experiments above, culminating in a measurement of the enhanced entoptic pattern size of structured states compared to Hadiginer's brush was expanded to explore human perception of radially varying patterns [255]. The combination of these perception tasks was later analyzed with a spatiotemporal energy model, predicting the perceived pattern size based on macular pigment density [256]. These works illustrate the enhancements that structured states can achieve in the measurement of biological tissues. Looking beyond studies of the human visual system, spin-orbit states could enhance signals from tissues with birefringent properties, like those with amyloid fibrils, without the need for chemical treatment [257]. Recent work has shown that structured states offer improved tissue penetration characteristics, demonstrated in mouse brain tissue [134, 258] and chicken breast tissue [245]. This suggests that technologies, like X-ray imaging and tomography, could reduce patient dosage by imaging with OAM states. The wealth of applications for structured states with light suggests that neutron structured states may find similarly impactful use-cases.

3.6 Neutron OAM States

The first demonstration of an OAM state with neutrons used a spiral phase plate (SPP) to generate the azimuthal phase profile and a single-crystal interferometer to show the OAM phase profile [64]. Following that work, a proposal to apply quadrupole magnetic fields to generate OAM states led to the discovery that a series of magnetic field gradients generates a lattice of states with OAM coupled to polarization [101, 259]. While a linear magnetic field gradient is difficult to generate experimentally across a neutron beam, a series of triangular prisms containing uniform magnetic fields was found to also generated OAM states, first shown with birefringent crystals and light [260]. Therefore, a series of triangular coils were constructed and their magnetic properties were tested. One critical difference between the magnetic field LOV prisms and the birefringent optical prisms is the presence of non-zero magnetic fields throughout the beam path. In neutron polarization experiments, a uniform guide field is generated throughout the beamline to prevent Earth's magnetic field from causing unwanted spin rotation [261]. Stray fields outside the magnetic prisms further complicate this experiment, creating additional spin-rotations that vary across the neutron beam. Figure 3.15 shows the magnetic field strength measured (b) inside the coil, at half-depth, and (c) on the prism surface.

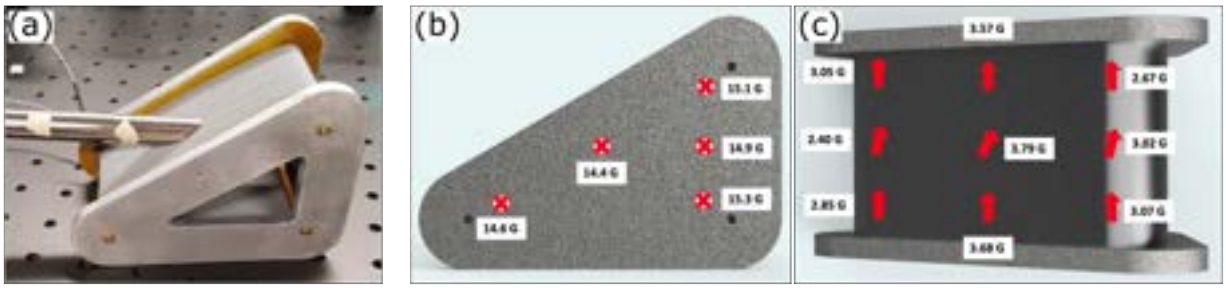


Figure 3.15: (a) Photo of assembled triangular coil. Aluminum wire was used to allow neutrons to transmit with minimal inelastic scattering. (b) Magnetic field strength and direction, measured with hand-held magnetometer, inside the magnetic prisms at half-depth. (c) Magnetic field strength and direction, measured with hand-held magnetometer, at surface of magnetic prisms.

Field strength within the prism was 14.9 G, and varied at most by 6%. At the surface of the coil, stray fields of 3.12 G were consistently present, roughly aligned with the interior coil field. These stray fields will rotate the neutron polarization as it propagates between prisms. If the propagation time between prisms was constant, this uniform phase shift would not distort the LOV prism effect. A simple solution is to orient the prisms such that the flat surfaces of prism pairs face each other, as is shown in Figure 3.17; however, this leaves two inclined prism faces, between prism 2 and 3, oriented in perpendicular directions and facing each other. In the event that those stray fields destroy the LOV states generated by the prisms, a shielding tube was constructed from μ-metal that could be placed between the second and third grating. Figure 3.16 shows the interior and surface magnetic fields with the μ-metal tube in place.

These magnetic LOV prisms were then tested at the NG-7 Polarized ^{3}He and Detector Experiment Station (PHADES) beamline in Gaithersburg. The results of this experiment were published in PNAS as "Generation and detection of spin-orbit coupled neutron beams" [5]. Author contributions are summarized below.

- D.S., D.G.C., and D.A.P. designed the research;
- C.K., W.C., M.G.H., and K.Z. performed the research;
- D.S., C.K., and D.A.P. analyzed data;
- D.S., C.K., W.C., C.W.C., D.G.C., M.G.H., I.T., K.Z., and D.A.P. wrote the paper;

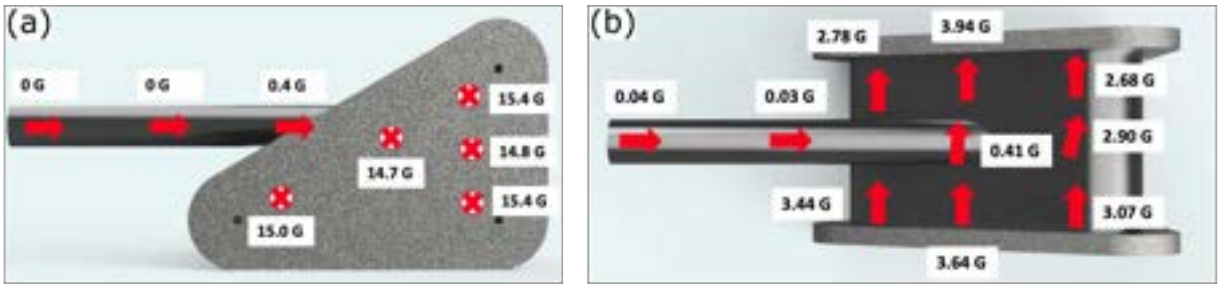


Figure 3.16: (a) Magnetic field strength and direction, measured with hand-held magnetometer, inside the magnetic prisms at half-depth with a μ-metal tube shielding the neutron beam region. (b) Magnetic field strength and direction, measured with hand-held magnetometer, at surface of magnetic prisms.

- D.S., C.K., I.T., K.Z., and D.A.P. designed and built the triangular coils.

3.6.1 Introduction

Studies of optical orbital angular momentum (OAM) have blossomed since the early 1990's and are now encompassed in a larger framework of structured waves of light and matter [185, 216]. OAM has been induced in beams of light [173], electrons [262, 263, 63], and neutrons [264]. Photonic OAM has demonstrated usefulness in edge-detection microscopy, quantum information processing protocols, encoding and multiplexing of communications, and optical manipulation of matter [242, 67, 69, 65, 66, 243, 244, 68]. Electron OAM beams have found applications in the characterization of nanoscale magnetic fields in materials [265] and exploration of magnetic monopoles [266]. Neutron OAM has shown promise in the detection of buried interfaces [108]. Furthermore, it has been theorized that neutron OAM can modify Schwinger scattering of neutrons on nuclei [267], and might also enable studies of neutron's internal structure [268].

A related set of techniques have been developed for preparing and characterizing beams in which the spin and OAM are correlated. In the case of photons, these "spin-orbit" beams possess correlations between polarization and the OAM [269, 270], whereas for electrons

and neutrons the correlations are between the spin and the OAM [271, 102]. Photonic spin-orbit beams have been demonstrated and they have enriched the application range of OAM beams by increasing the number of accessible degrees of freedom [187, 186, 272, 273]. Although analogous preparation methods have been proposed for electrons [271, 274, 275, 276] they have yet to be implemented in the laboratory.

In this paper we demonstrate not only the first preparation and characterization of spin-orbit beams using neutrons, but also neutron beams with a lattice of spin-orbit correlations. Our technique, which we previously demonstrated with light [60], involves the preparation of a spin-orbit textured "lattice of vortices" wavefront. A variety of textures can be generated by this method [101], including skyrmion-like geometries analogous to those recently observed in evanescent electromagnetic fields [277]. We expect the techniques shown here to pave the way for neutron OAM and spin-orbit applications in material characterization and fundamental physics.

3.6.2 Methods

The experiment was carried out the on the Polarized ^{3}He And Detector Experiment Station (PHADES) [278] at the National Institute for Standards and Technology Center for Neutron Research (NCNR). A monochromatic beam of neutrons with wavelength $\lambda = 0.41$ ($\Delta\lambda/\lambda \approx 2\%$) nm was directed into the setup, as shown in Fig. 3.17. The beam divergence was $\approx 1^\circ$ in both x and y directions. The setup is composed of a slit, two ^{3}He neutron spin filters, guide field coils, two pairs of specifically orientated triangular coils, a permalloy tube, and a neutron camera. The neutron camera has a 25 mm diameter active area, a spatial resolution of 100 μm, and a quantum efficiency of $\approx 38\%$ [279].

A 1×1 mm^2 slit was placed at the start of the setup. The slit sets the lower limit on the transverse coherence length at the first triangular coil to:

$$\sigma = \frac{\lambda L_1}{s} \approx 0.4\ \mu\text{m} \tag{3.25}$$

where $L_1 = 0.965$ m is the distance from the slit to the first triangular coil and s is the slit width. Although it might be desirable for some specific applications to reduce the slit width to the point that the transverse coherence length extends over the beam diameter, it is not practical in this experiment as the neutron peak count rate was $\approx 15\ s^{-1}$ at the camera.

Two ^{3}He cells were used as the spin polarizer and the spin analyzer due to their spatially homogeneous neutron polarization [280]. The cells were polarized in an off-line lab

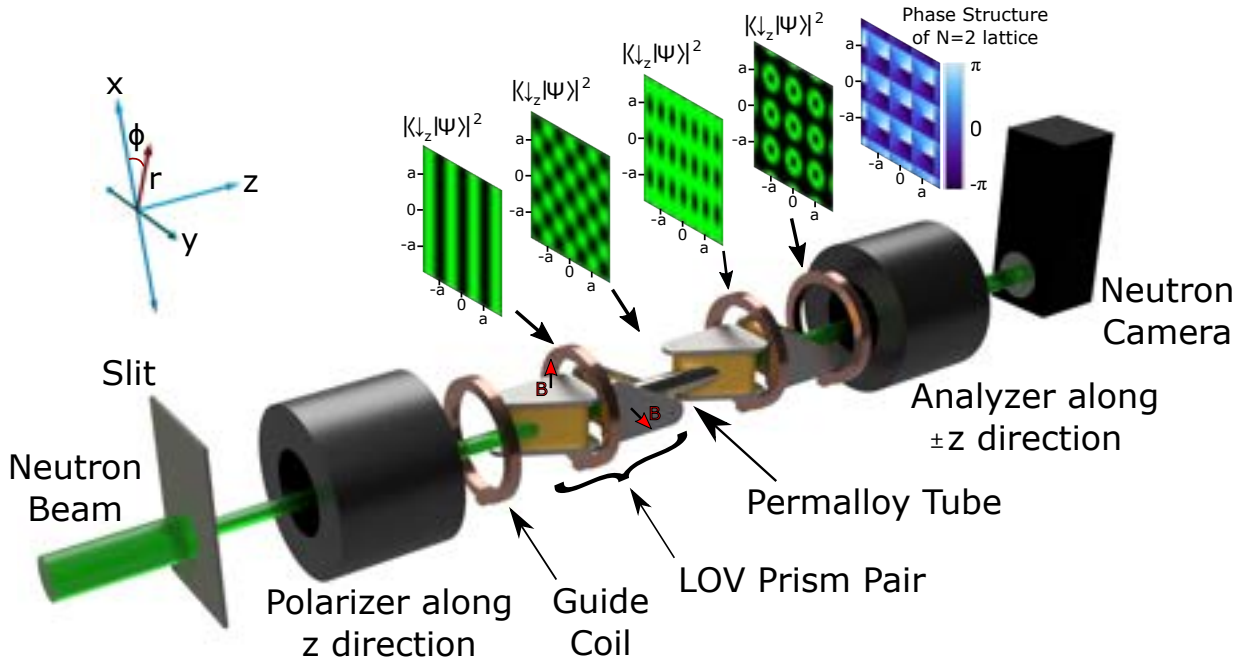


Figure 3.17: Schematic diagram of the experimental setup which consists of a slit, a ^{3}He spin polarizer and analyzer, guide field coils, two pairs of specifically oriented triangular coils that act as LOV prism pairs, a permalloy tube, and a neutron camera. The triangular coils induce perpendicular magnetic phase gradients onto the neutron wavefunction. LOV prism pairs prepare beams with a lattice of spin-orbit correlations where in each lattice cell the phase between the two spin states varies azimuthally. The simulated spin dependant intensity profile after each triangular coil is shown in green, and the profile of the phase difference between the two spin states, given by $\left(\arg[\langle\downarrow_z|\Psi^{N=2}_{\mathrm{LOV}}\rangle] - \arg[\langle\uparrow_z|\Psi^{N=2}_{\mathrm{LOV}}\rangle]\right)$, is shown in blue. Figure reproduced from [5].

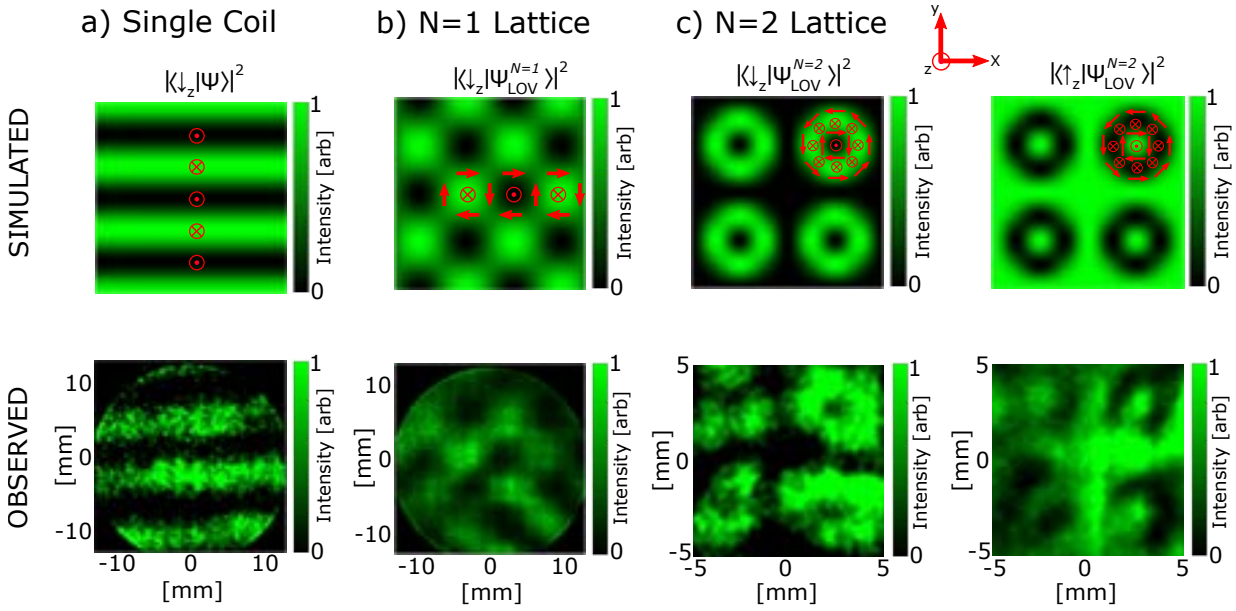


Figure 3.18: The simulated and observed spin-dependant intensity profiles. A Gaussian filter as well as an intensity gradient was added to each observed image, to highlight the features of interest. The currents on the (1^{st}, 2^{nd}, 3^{rd}, 4^{th}) triangular coil were set to (0, 0, 0, 2.5 A) for a), (2.5, 2.5, 0, 0 A) for b), and (5, 5, 5, 4 A) for c). The spatially varying spin direction (before the spin filtering) is overlaid on the simulated intensity profiles via the red arrows. The N=1 lattice exhibits a vortex anti-vortex structure and its spin dependant intensity profile resembles a checkerboard pattern. The N=2 lattice appears as a lattice of doughnut/ring shapes. Agreement is shown between the simulated and observed intensity profiles. Figure reproduced from [5].

using spin-exchange optical pumping [281], and they were changed three times during the experiment. Their initial ^{3}He polarization at the beamline was measured to be between 73 % and 82 %, while their relaxation time was measured to be between 365 h and 516 h. The polarization of the neutron beam would reduce from $\approx$ 94 % to $\approx$ 90 % during a 2-3 day time period. The spin filter direction could be aligned with the $\pm z-$axis at the beamline using the adiabatic fast passage nuclear magnetic resonance method [282].

To prepare neutron beams with lattices of spin-orbit correlations we used specifically orientated triangular coils that acted as "Lattice of Optical Vortices" (LOV) prism pairs [60, 101]. They were arranged to induce magnetic phase gradients perpendicular to each other as well as to the incoming neutron beam. Therefore the coil arrangement differs from the Wollaston arrangement where two triangular coils with anti-parallel fields are placed

with their inclined sides facing each other [283, 284]. The triangular coils have side lengths of 8.5 cm, 12 cm, and 14.7 cm with an overall height of 7.3 cm. At an applied 10 A current their inner magnetic field was $\approx$ 0.014 T which provided a magnetic phase gradient of $\approx 1.5\pi$ rad/mm. The triangular coils were run between 2.5 A and 10 A throughout the experiment, and in every configuration the current in each coil was optimized to compensate for beam divergence.

As shown in Fig. 3.17 there is a spatially dependant path difference between the 2$^{\text{nd}}$ and the 3$^{\text{rd}}$ triangular coils due to their inclined sides. Therefore it is necessary to minimize the magnetic field in this region to avoid an unwanted phase gradient across the beam. In our setup this was accomplished via a permalloy tube. The permalloy tube was built from 15 layers of a 500 μm thick nickel-iron soft ferromagnetic sheets. The sheets were wrapped around a thin-walled aluminum pipe with an inner diameter of 3.18 cm and whose ends were cut to match the angled prism faces. Guide coils were placed between other triangular coils to provide a uniform magnetic field along the spin quantization axis.

3.6.3 Results and Discussion

The first ^{3}He polarizer filters the neutrons with spin along the beam propagation axis, thereby setting the neutron wavefunction to

$$|\Psi_{\text{in}}\rangle = |\uparrow_z\rangle\,. \tag{3.26}$$

The triangular coils induce perpendicular phase gradients along the directions that are also perpendicular to the direction of the incoming spin state. Pairs of triangular coils then effectively act as LOV prism pairs, as described in Ref. [101]. In this particular case their individual operators are given by:

$$\hat{U}_y = e^{-i\frac{\pi}{a}y\hat{\sigma}_x} \qquad \hat{U}_x = e^{-i\frac{\pi}{a}x\hat{\sigma}_y} \tag{3.27}$$

where $\hat{\sigma}_y$ and $\hat{\sigma}_x$ are the Pauli spin operators, and a is the spatial spin oscillation period. For the case of no beam divergence:

$$a = \frac{2\pi v_z}{\gamma_{\text{n}}|B|\tan(\theta)} \tag{3.28}$$

where $|B|$ is the magnetic field inside the triangular coils, v_z is the neutron velocity, γ_n is the neutron gyromagnetic ratio [285], and θ is the incline angle of the triangle coils. For example, for a field of $|B| = 0.005$ T inside the triangular coils the corresponding period of a non-diverging beam would be $a = 3.8$ mm.

A pair of specifically orientated triangular coils, or a LOV prism pair, approximates the action of a quadrupole magnetic field [60]. The state induced by a quadrupole acting on $|\Psi_{in}\rangle = |\uparrow_z\rangle$ has the following form [102]:

$$|\Psi_Q\rangle \approx \left[\cos\left(\frac{2\pi r}{a}\right)|\uparrow_z\rangle + ie^{-i\phi}\sin\left(\frac{2\pi r}{a}\right)|\downarrow_z\rangle\right], \tag{3.29}$$

where (r, ϕ) are the cylindrical coordinates. It follows from Eq. 3.29 that two spin states possess a differing spatial amplitude profile and that there is an azimuthal phase difference between the two spin states which indicates the OAM difference between the two spin states of $\Delta\ell = \ell_\uparrow - \ell_\downarrow = 1$.

In addition to approximating the quadrupole operator, LOV prism pairs possess a periodic structure which induces a 2D lattice structure in the output state [60]. The state after N sets of LOV prism pairs is given by:

$$|\Psi^N_{LOV}\rangle = (\hat{U}_x\hat{U}_y)^N|\Psi_{in}\rangle\,. \tag{3.30}$$

The small transverse coherence length given by Eq. 3.25 indicates that we do not have a single eigenstate of OAM in the incoming beam but rather a distribution of OAM states. Therefore, for each lattice cell, if we assume symmetry in the incoming transverse momentum distribution, filtering $|\uparrow_z\rangle$ neutrons would result in an OAM distribution with a mean value of 0, while filtering $|\downarrow_z\rangle$ neutrons would result in an OAM distribution with mean value 1.

After passing through one of the triangular coils the spin state varies sinusoidally along the direction of the coil incline. Therefore the intensity profile post-selected on one spin state exhibits linear fringes with period a, as shown in Fig. 3.18a. After passing through a pair of perpendicular triangular coils, or a LOV prism pair, an N=1 lattice of spin-orbit correlations is prepared. The intensity profile post-selected on $|\downarrow_z\rangle$ is shown in Fig. 3.18b, and it resembles a checkerboard pattern. The spin direction before the post-selection, is overlaid on the intensity profile via the red arrows and it elucidates why the N=1 lattice is is composed of a vortex anti-vortex structure.

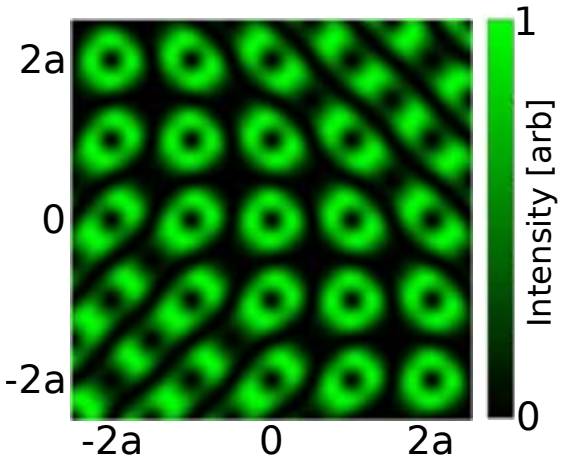


Figure 3.19: The simulated distortions when including a $B_z = 6 \times 10^{-4}$ T magnetic field besides the inclined sides of the second and third triangular coil. The magnetic field results in a gradient along the negative y-direction after the second triangular coil followed by a gradient along the negative x-direction before the third triangular coil. It can be observed that gradients are a possible cause of the distortions that are observed in Fig. 3.18c. Figure reproduced from [5].

Passing a polarized neutron beam through two pairs of LOV prisms pairs prepares a beam with a lattice of spin-orbit correlations as described by Eq. 3.29. The spin dependant intensity profile has the doughnut/ring structure as shown in Fig. 3.18c. This is a consequence of the cosine/sine amplitude terms in Eq. 3.29. The major features can be seen between the simulated and observed profiles in Fig. 3.18c. Note that the spin analyzer sets the spin filter direction, and the two profiles in Fig. 3.18c are from two separate setup configurations.

The slight differences between the simulated and observed profiles shown in Fig. 3.18a and Fig. 3.18b can be attributed to the interface region between the longitudinal field of the guide coils and the transverse field of the triangular coils. However, when triangular coils 2 and 3 are used to prepare the N=1 lattice the observed profile is significantly more distorted, indicating that the permalloy tube is not sufficiently removing the field between the triangular coils. A non-zero magnetic field in the permalloy tube results in a path gradient due to the inclined sides of the triangular coils. Fig. 3.19 shows the distortions that arise when a uniform $B_z = 6 \times 10^{-4}$ T magnetic field is present besides the inclined sides of the second and third triangular coil. It can be observed that the doughnut profiles become stretched, and that therefore gradients are a possible cause of the distortions that are observed in Fig. 3.18c.

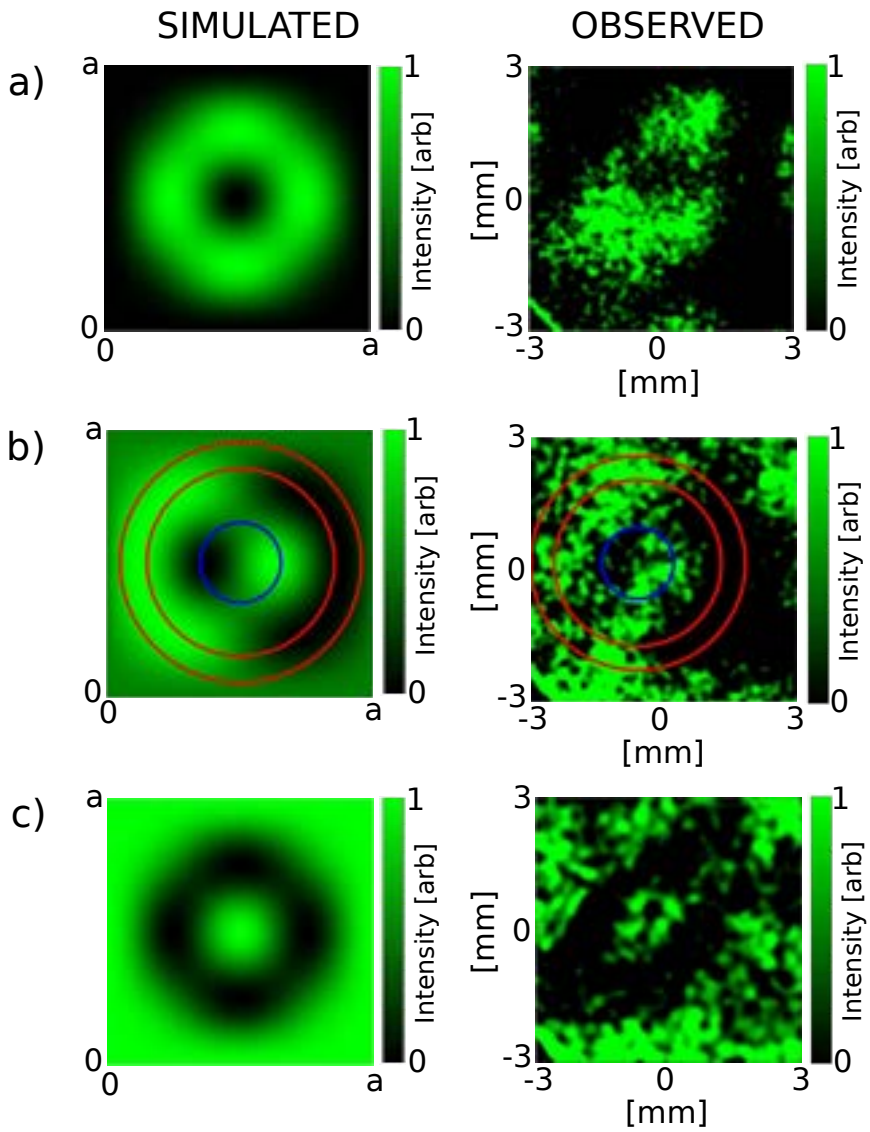


Figure 3.20: The simulated and observed spin dependant intensity profile, after two sets of LOV prism pairs, as the first coil in the setup is translated along the y-direction, see Fig. 3.17, for a) 0 mm b) 3 mm c) 6 mm. The profiles of a) and c) correspond to the spin-up and spin-down intensity profiles of a single cell of the N=2 lattice, as shown in Fig. 3.18. The profile in b) corresponds to the intensity profile after mixing the two spin states. It can be seen that the intensity varies azimuthally, indicating the phase structure of a single cell in the N=2 lattice, as shown in Fig. 3.17. Figure reproduced from [5].

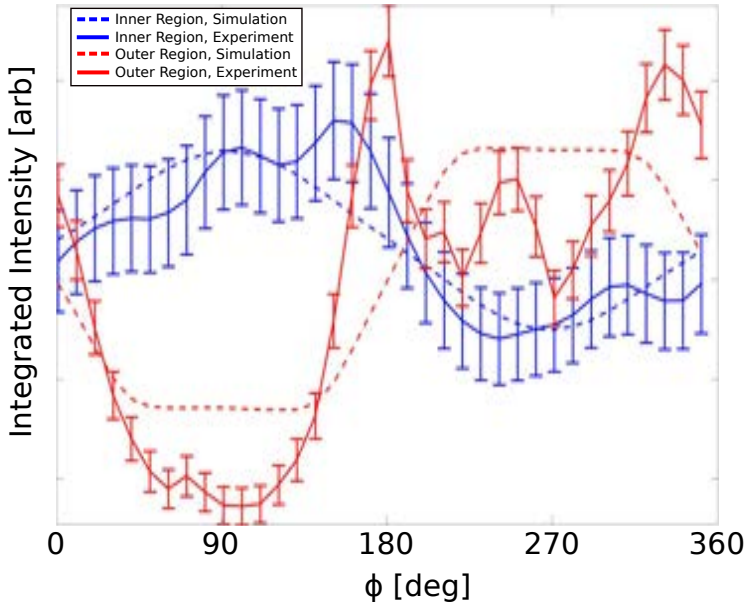


Figure 3.21: The azimuthal variations in the integrated intensities of the observed image in Fig. 3.20b. The two regions of interest, the inner region and the outer region, are pictorially bounded by the red and blue circles in Fig. 3.20b. The fits (dashed lines) were computed from the simulated image of Fig. 3.20b. The one sinusoidal period is a signature of the OAM = 1 phase structure. Figure reproduced from [5].

The phase difference between the two spin states of the N=2 lattice is shown in Fig. 3.17. This phase structure can be mapped via the spin-dependant intensity profile after mixing the two spin states. That is, we require to post-select the spin along a direction that is perpendicular to the spin quantization axis, which in our case would be the x and y directions.

It can be noted that translating one of the triangular coils along its incline direction induces an additional uniform phase shift. This provides a convenient method of obtaining the $|\downarrow_{x,y}\rangle$ dependant intensity profiles without changing the ^{3}He polarization direction [101]. Fig. 3.20 shows the simulated and observed spin dependant intensity profile as the first coil in the setup is translated along the y-direction. Fig. 3.20a and Fig. 3.20c correspond to the spin-up and spin-down intensity profiles of a single cell of the N=2 lattice, as shown in Fig. 3.18. Fig. 3.20b corresponds to the intensity profile after mixing the two spin states.

To quantify the data shown in Fig. 3.20b we can consider the two regions pictorially bounded by the red and blue circles that manifest out-of-phase azimuthal variation. The inner (outer) region in the simulation profile where the azimuthal variation is found to be the most pronounced is bound by $r = 0$ and $r = 0.15a$ ($r = 0.35a$ and $r = 0.45a$). On the experimental data the origin was picked to be at the center of the intensity transition, and the period is set to $a = 5.29$ mm. Fig. 3.21 shows the azimuthal variations in the integrated intensities of the observed image in Fig. 3.20b. The intensity curves were normalized w.r.t. the area under the curves, and they were constructed by integrating over the radial direction and 10 degree increments in the azimuthal direction. The fits (dashed lines) were computed from the simulated image of Fig. 3.20b. The one sinusoidal period is a signature of the the OAM = 1 phase structure. Longer data acquisition times would be required to increase the signal to noise ratio.

3.6.4 Conclusion

Photon spin-orbit coupling arises naturally in nano-optics, photonics, plasmonics and optical metamaterials [286, 287] and is a core construct of chiral quantum optics [288] and topological photonics [289]. Here we show spin-orbit coupling in the context of freely-propagating beams in which spin and OAM degrees of freedom are correlated. We have prepared and characterized neutron beams with lattices of spin-orbit correlations in which the OAM of one spin state is different from the OAM of the other spin state. This was achieved via sets of specifically oriented triangular coils which acted as LOV prism pairs. The beams were characterized via their spin dependant intensity profiles.

The triangular coils induced good quality magnetic phase gradients, as can be observed

in Fig. 3.18a and Fig. 3.18b. However, in our experiment the permalloy tube did not sufficiently remove the magnetic field between the two sets of triangular coils. This resulted in distortions when all four coils were on simultaneously. For more pronounced results a better mechanism of removing the field is required.

We expect the described techniques to be the forerunners of neutron OAM applications in material characterization and fundamental physics. Superconducting triangular coils with higher fields may be employed to prepare lattices with smaller periods. The next set of experiments will focus on the preparation of spin-orbit correlations over the coherence length of neutron wave packets and the characterization of these spin-orbit states via the correlations between spin and projected linear momentum.

3.7 Outlook on Structured Neutron States

Following the demonstration of neutron OAM states with the magnetic LOV prisms, it was shown theoretically that a series of magnetic Wollaston prisms with superconducting films could also be used to generate structured states [290]. Advancements in nano-fabrication techniques have also made gratings with periods on the order of 100 nm accessible, enabling the generation of structured states via diffraction from a series of microscopic gratings. When patterned as a fork grating, these designs produce OAM states in the diffraction orders, which can be measured by SANS [103]. Beyond OAM states, these patterned gratings can also be used to generate other structured waves like Airy beams that show self-acceleration [291]. Combinations of nano-period gratings were then used to show interference properties between neutron states with different OAM numbers [292]. These advancements in the generation of structured neutron waves allow for the integration of structured neutron states with other neutron optics methods, like polarimetry or holography, to enhance signals from topological materials like skyrmions [293, 13, 294].

Chapter 4

Phase Grating Interferometry

In Chapter 1, we described the first experiments with visible light and X-rays that showed the universal moiré effect, on which the phase grating moiré interferometer (PGMI) is based [36]. As was the case in Chapter 3, we can make use of optics to test the ability of a PGMI to measure potential gradients, like those produced by gravitational fields with neutrons.

4.1 Modeling neutron PGMI with light

For the neutron PGMI, demonstrated in [295, 37, 38], silicon gratings were used to create an interference pattern at the camera. Silicon is ideal for this purpose as it has a small incoherent scattering length and can be fabricated into high-aspect ratio gratings that maximize contrast in a PGMI. These phase gratings show similar properties with near infra-red wavelength light (NIR) [296]. We can therefore use silicon gratings, of a larger period than what is optimal for neutrons, to investigate experimental design and effects that would be expected when using a neutron PGMI to measure gravitational forces. Figure 4.1(a) shows three silicon gratings mounted in the NIR beamline constructed to model the neutron PGMI that will be used to measure gravitational forces.

To model the effect of a linear potential gradient, similar to the effect of local gravitational acceleration, we used a silicon wafer whose faces were imperfectly parallel. This wedge-shaped silicon sample produces a potential gradient that should, as in the case of local acceleration and co-rotating gratings, produce a phase shift in the interference fringes [35]. As was shown with the neutron 3-PGMI, we can also measure changes in fringe contrast and period as the distance between gratings is changed, allowing us to demonstrate

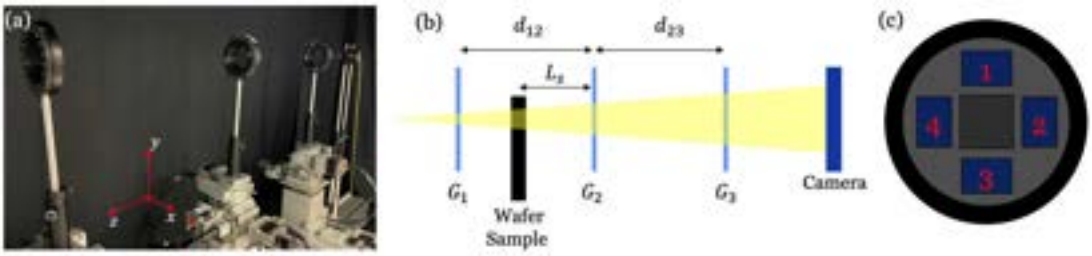


Figure 4.1: (a) Near infrared beamline used to test PGMI designs and modeling, with three silicon gratings mounted. (b) Schematic of the 3-PGMI experiment measuring the gradient in a silicon wafer. The top region of the wafer is placed between gratings 1 and 2, shown as a black rectangle. (c) Schematic of the wafer sample, with the central patterned area show as a darker inset. The regions of interest, labeled 1-4, highlighted in blue are positioned in the beam between gratings 1 and 2.

that this optical model of local acceleration produces a constant phase shift. Figure 4.2(a) shows interference fringes measured from the vertically integrated image of the near-IR camera and the fringe carpet generated by stacking interference fringe images from different grating separations. Unlike the interference fringes shown in [38] or [37], high-frequency fringes are visible in the integrated intensity images.

These fringes arise from the Talbot effect, causing interference fringes of varying contrast created by the periodic structure of the phase gratings. As the grating period used in neutron PGMI experiments is on the order of 1 µm, these Talbot fringes were not resolvable to the neutron camera used in those experiments. In the NIR case, the grating period of $P_g = 180\,\mu\text{m}$ can be resolved by the camera. Gaussian filtering the integrated intensity produces the pattern shown as a dotted orange line in Figure 4.2, which matches the period and contrast resulting from directly fitting the integrated intensity. To correctly model the effect of a potential gradient induced by a wedge-shaped silicon wafer, we must first characterize the profile of our sample.

Between grating 1 and grating 2 of the PGMI, we will be placing the top edge of a silicon wafer into the beam, as shown in Figure 4.1(b). Therefore, we can measure the effect on the PGMI of different edges of this sample; specifically, we have chosen to measure the edge of a previously patterned wafer at four positions, shown in Figure 4.1(c). The patterned area of this wafer is only visible at the edge of our scanned area. We will first characterize the profile of these regions by scanning the wafer across a collimated Gaussian beam, directly imaging displacements in the beam. Figure 4.3(a) shows an example of the deflected beam from the wafer, with the center of intensity highlight with a red dot

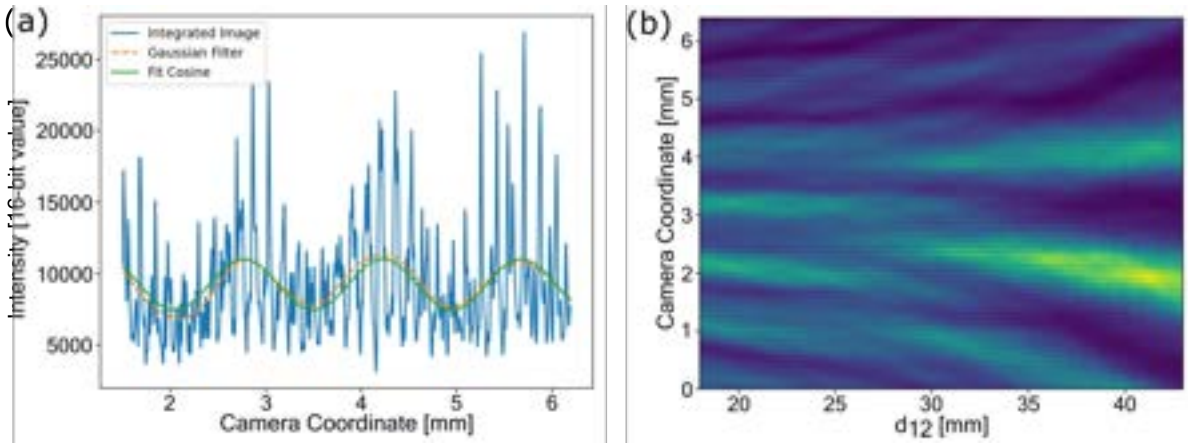


Figure 4.2: (a) Vertically integrated NIR intensity taken from NIR camera. Interference pattern primarily shows two periodic signals. The high-frequency oscillations arise from the Talbot effect and have a period equal to the grating period $P_g = 180\,\mu\text{m}$. Low frequency oscillations have a period given by the fringe period, P_f, in and arise from the universal moiré effect [36]. Curves overlaid on the integrated intensity show the result of a Gaussian filter on the image and sinusoidal curve fit, showing the expected contrast and frequency from a neutron experiment. (b) Fringe carpet for the NIR 3-PGMI, showing changes in fringe contrast and period with varying distance from grating 1 to grating 2.

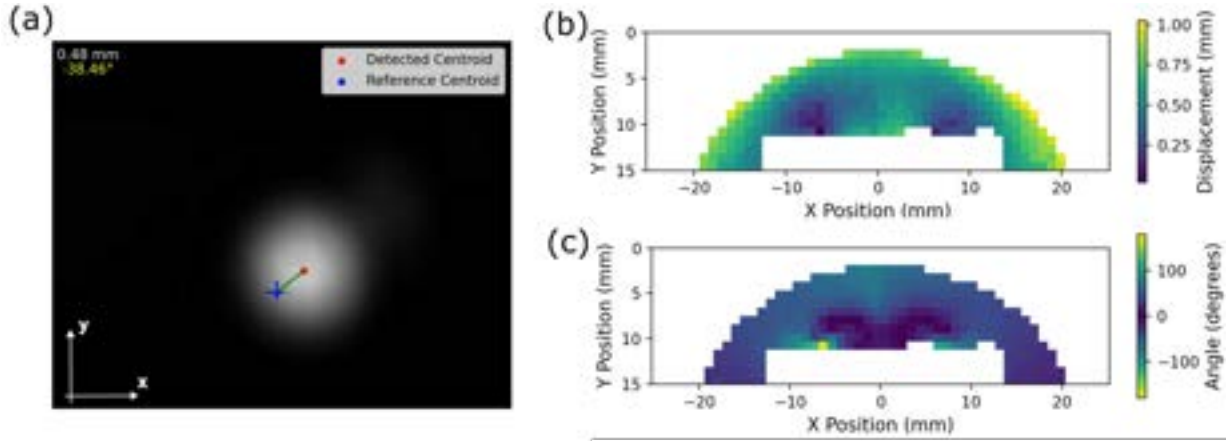


Figure 4.3: (a) Example of beam deflection measured by the NIR camera. Centroid of deflected beam is indicated with a red dot, with the reference centroid measured without a sample is indicated with a blue cross. The magnitude and angle (with the positive x-axis as the right pointing horizontal) of this deflection are shown in the top left of the image. (b) Map of beam deflection magnitude across the scanned area of the wafer. Images that did not produce a Gaussian beam profile were omitted, leading to the edge and patterned area of the wafer being visible as blank regions. (c) Map of deflection angles, measured from the right pointing horizontal from the camera perspective.

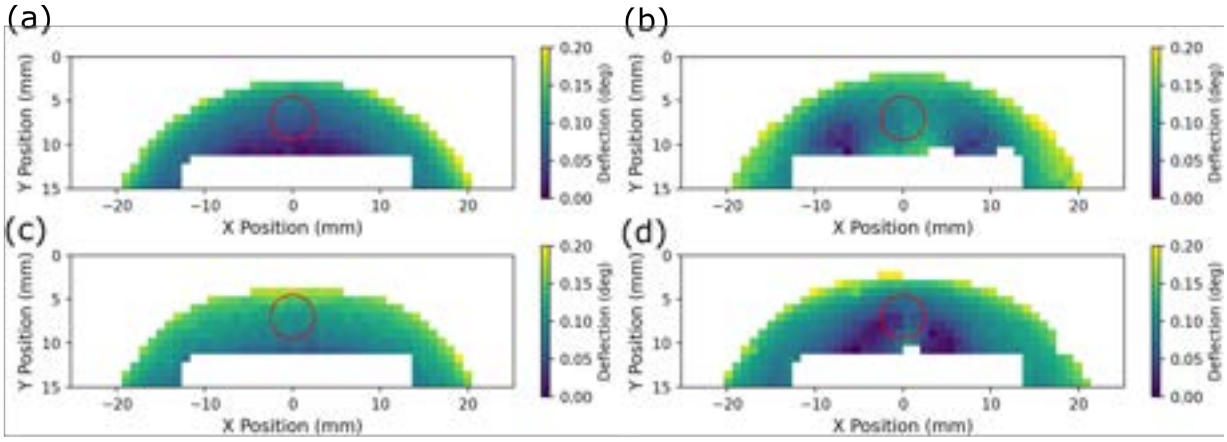


Figure 4.4: Beam deflection calculated from displacement imaged by the NIR camera for each orientation of the wafer sample. The wafer was rotated by 90° between orientations, with the angle of the sample as measured by the rotation mount listed as (a) 8°, (b) 98°, (c) 188°, (d) 287°. A red circle indicated the area exposed to the NIR beam during the 3-PGMI experiment and is the area that is averaged to determine the beam deflection value.

and the center of intensity of the direct beam marked with a blue cross. We can map this deflection angle, calculated using the distance from the sample to the camera, across the wafer. Figure 4.3(b) shows the deflection angle across the wafer, while (c) shows the orientation of this deflection, with zero angle as a "rightward" horizontal deflection as seen by (a). In the 3-PGMI, phase shifts in the interference pattern arise due to changes or gradients in the potential perpendicular to the grating lines; therefore, we are only interested in the beam deflection projected on the horizontal direction. Figure 4.4(a-d) shows the horizontal projection of the beam deflection mapped across each position of the wafer. The position of the diverging cone beam in the NIR 3-PGMI is denoted on those maps with a red circle, allowing us to calculate the average beam deflection when this sample is placed in the 3-PGMI. The resulting beam deflection for each wafer position is shown in Table 4.1.

When placed between grating 1 and grating 2, this wafer will similarly deflect the beam, causing a beam translation that is equivalent to translating subsequent gratings. Translating each grating by a distance Δx_i results in a phase shift of

$$\Delta\phi = \frac{2\pi}{P_g}(\Delta x_1 - 2\Delta x_2 + \Delta x_3). \tag{4.1}$$

Sample Orientation	Direct Deflection	PGMI Computed Deflection
98°	17″	18″ ± 4″
188°	1′21″	1′20″ ± 3″
278°	1′30″	1′29″ ± 3″
368°	1′25″	1′26″ ± 4″

Table 4.1: Beam deflection measurements for different sample orientations, measured from the direct beam and phase grating moiré interferometer.

When the sample is placed a distance L_S, ahead of grating 2, with a distance L_{23} between grating 2 and 3, this phase shift reduces to

$$\Delta\phi = \frac{2\pi}{P_g}(L_{23} - L_S)\tan\theta. \tag{4.2}$$

Phase values will be extracted from interference fringes over grating separation values ranging from $d_{23} - d_{12} = [60\,\text{mm}, 80\,\text{mm}]$. The resulting phase fit values and beam deflection values computed with Eqn. (4.2). Averaging these results yields the deflection values shown alongside the direct deflection measurements in Table 4.1.

While this experiment is not precision metrology, demonstrates that our models of the PGMI are sufficient to predict the phase shift from a potential gradient.

4.2 Modeling the PGMI

We established in Chapter 1 that we can model a neutron interferometer by integrating along a neutron trajectory to the detector; however, in Section 4.1, we also modeled the PGMI by computing the beam deflection caused by a potential and treated this deflection as equivalent to translating each phase grating. A natural question is, "should both the phase accumulated along the neutron's trajectory and any beam deflection (corresponding to grating translation) be included in the model?" We can look to the first experiment measuring gravitational forces with a phase grating neutron interferometer to answer this.

4.2.1 Modeling Gravitational Potentials

In 2000, van der Zouw et al. measured the phase shift induced by Earth's local gravitational field by co-rotating the three phase gratings of their very-cold neutron (VCN)

interferometer [35]. That work models the expected intensity in their experiment with

$$I(\alpha) = \langle 1 + \mathcal{C}\cos(\Delta\phi_\lambda(\alpha))\rangle_\lambda, \tag{4.3}$$

where $\mathcal{C}$ is contrast, $\Delta\phi_\lambda(\alpha)$ is the wavelength-dependent phase shift as a function of grating rotation, α, and $\langle\cdot\rangle_\lambda$ is an average over the beam's wavelength distribution. Noting that the interferometer area is $A = L^2\tan(\lambda/P_g)$, the above phase shift is

$$\Delta\phi_\lambda(\alpha) \approx \frac{2\pi m_N^2}{h^2}\frac{L^2\lambda^2}{P_g}g\sin\alpha \equiv q_0\frac{L^2\lambda^2}{P_g}g\sin\alpha. \tag{4.4}$$

where m_N denotes the neutron mass, h is Plank's Constant, L is the distance between subsequent gratings, λ is the neutron wavelength, P_g is the grating period, g is the gravitational acceleration, and α is the rotation angle of the PGMI.

While this is the total description given by [35], there is an additional factor in Eqn. (4.3). This can be seen as integral over wavelength is an average over even functions, yet produces an odd function. This missing factor is the effect of grating translation, also called phase stepping. As shown in Figure 4.5, this grating translation will produce a cosine intensity pattern. Therefore, there is an additional phase, $\Delta\phi_{PS}$, which is due to the alignment of the gratings during the experiment.

Averaging over the wavelength distribution measured at this instrument, Zeilinger et al. fit for the quantity, $q_{0,exp.}$, which is defined by known constants. The measured value of q_0 was found to agree within uncertainty with the value calculated from known quantities, $q_0 = \frac{2\pi m_N^2}{h^2} = 4.014\,763\,681(98)\times 10^{13}\,\mathrm{rad}^2/\mathrm{m}^4$. This would seem to suggest that there is no additional phase caused by the neutron "falling" in this gravitational potential. Nevertheless, we can calculate the distance a neutron falls and therefore, compute the phase shift expected from that effect. The displacement of a neutron in Earth's gravity, as a function of grating rotation, is,

$$\Delta x_{G2} = \frac{g}{2}\sin(\alpha)\left(\frac{L}{v_N}\right)^2$$
$$\Delta x_{G3} = \frac{g}{2}\sin(\alpha)\left(\frac{2L}{v_N}\right)^2 = 4\Delta x_{G2},$$

or in terms of the De Broglie wavelength,

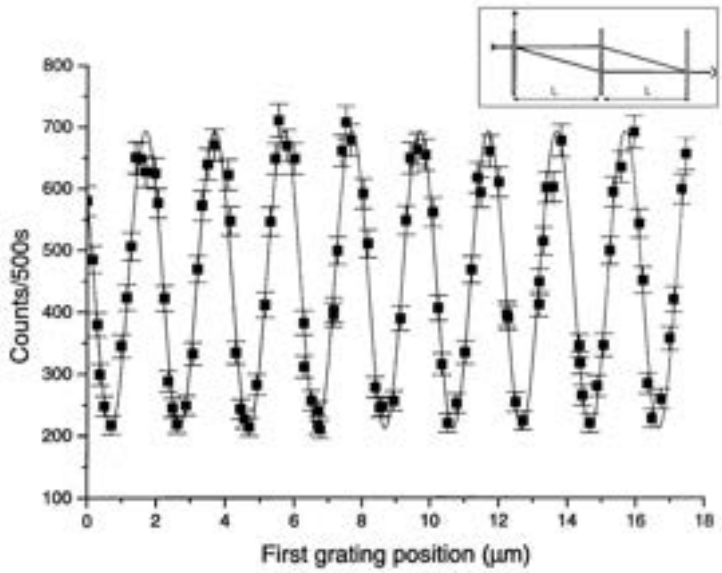


Figure 4.5: Neutron count measurements as a function of the first grating translation along the grating vector. These results show that neutron count is periodic over 2 µm, which is equal to the grating period itself. Figure reproduced from [35].

$$\Delta x_{G2} = \frac{g}{2}\sin(\alpha)\left(\frac{L\lambda m_N}{h}\right)^2. \tag{4.5}$$

Applying these to Eqn. (4.1),

$$\begin{aligned}\Delta\phi_{PS} &= \frac{4\pi}{P_g}\Delta x_{G2} \\ &= \frac{2\pi}{P_g} g\sin\alpha\left(\frac{L\lambda m_N}{h}\right)^2.\end{aligned} \tag{4.6}$$

Comparing Eqn. (4.4) and Eqn. (4.6), the phase shift calculated by calculating the distance a neutron "falls" in the x-direction is equal to the phase shift calculated by integrating along the classically allowed trajectory. This tells us that we do not need to add any effect of "grating translation" to our path-integral model, and is also a demonstration of the assumption that underlies Einstein's equivalence principal, described in 1907 as the assumption of "complete physical equivalence of a gravitational field and a corresponding

acceleration of the reference system" [297]. With that context, the calculation in Eqn. (4.6) makes use of the equivalence between gravitational and inertial mass to replace the effect of Earth's local gravitational field with an accelerating laboratory reference frame that causes a motion in the gratings.

4.3 Measuring the Gravitational Constant with a neutron PGMI

With the above question answered, we can apply the model outline in Section 1.3.1 to quantify the precision with which the gravitational constant (G) can be measured with a neutron 3-PGMI. The advantage of this method over the single crystal interferometer and the VCN interferometer discussed in Section 1.2.1 is the dramatically increased neutron count rate at the detector. Single crystal interferometer experiments report count rates on the order of $1\,\mathrm{s}^{-1}$ - $10\,\mathrm{s}^{-1}$ [33, 64, 120], while the VCN reported a detector count rate of $1\,\mathrm{s}^{-1}$ from an incident beam flux of $200\,\mathrm{cm}^{-2}\,\mathrm{s}^{-1}$ [35]. The first demonstration of a 3-PGMI with neutrons, though limited by low-contrast interference fringes and a detector efficiency of 40%, reported a count rate at the detector of $3 \times 10^{7}\,\mathrm{s}^{-1}$.

The contents of this chapter are under review as "Design and Monte Carlo simulation of a phase grating moiré neutron interferometer to measure the gravitational constant" A pre-print is available at [298]. Author contributions are summarized below.

- **DS, BH, DGC, MGH, DAP** Conceptualized the experiment
- **CK, DS, RS, MGH DAP** Developed the PGMI model
- **CK** wrote the first draft
- **All authors** edited and contributed to the final draft

4.4 Introduction

Performing a precision measurement of the Newtonian constant of gravitation is a long-standing challenge, evident when comparing the relative uncertainty to which other fundamental constants of nature are known. The recommended value for the G, $6.674\,30(15) \times 10^{-11}\,\mathrm{m^3\,kg^{-1}\,s^{-2}}$, is listed with a relative uncertainty of $2.2 \cdot 10^{-5}$, a significantly larger uncertainty than, for example, the Rydberg Constant, R_∞, listed at $1.1 \cdot 10^{-12}$, and the vacuum electric permittivity, ϵ_0, at $1.6 \cdot 10^{-10}$ [80]. Most measurements of G attempt to measure the gravitational force using a pendulum or force balance with source masses on the order of 10 kg. Examples include the historical Cavendish pendulum [79], the time-of-swing torsion pendulum [299], and the more modern angular acceleration method [300, 301, 302, 303]. Other experiments have used electrostatic and torsion force balances [304, 305, 306], a Fabry-Pérot to measure changes in pendulum frequencies [307, 308], and laser-cooled atom interferometry [309, 74] while a recent measurement utilized resonating beams to extract a dynamic measurement of G [310]. Although the reported uncertainty of modern measurements has been reduced [311], significant discrepancies between measurements used to generate the CODATA estimate of G persist, as shown in Figure 4.6. [80, 312]. In the two centuries since Cavendish's experiment, the relative uncertainty in the gravitational constant has only improved by two orders of magnitude, with disagreement between experiments of 550 parts-per-million (ppm) [78]. This necessitated an expansion factor of 3.9 applied to the uncertainties from each experiment shown in Figure 4.6 when calculating the 2022 CODATA recommended value for G [80]. This underscores the need for experiments to measure G with systematic uncertainties that can be decoupled from existing measurements.

Modern metrology often makes use of matter-wave interferometers where sub-atomic particles [114], atoms [313], and even molecules [314] are split in a quantum superposition. Neutrons are convenient probes of gravity as they are both massive quantum particles and electrically neutral [8, 9]. Neutron interferometry has historically been used in several groundbreaking experiments, such as the first observation of gravitational effects on a quantum particle [315] and the first measurement of the 4π symmetry of spin-$\frac{1}{2}$ particles [115]. Gravitational effects on neutrons were measured by Colella et al. in 1974 with a perfect-crystal neutron interferometer (NI) [315], and by van der Zouw et al. in 2000 using a phase grating NI [35]. However, single-crystal interferometers are limited to monoenergetic neutrons and the phase grating NI of [35] requires very cold, low-flux neutrons. Therefore both interferometers, restricted by low neutron flux, could not generate the statistics required for precision measurements of gravity.

It has been shown that a series of nano-fabricated phase gratings can be used to create

a polychromatic far-field interferometer with x-rays [36] and neutrons [38, 37, 112], called a phase-grating moiré interferometer (PGMI). Of interest here is a PGMI using three phase gratings, with grating heights that produce a phase shift of $\pi/2$, π, and $\pi/2$ at the design wavelength. In a 3-PGMI, a fringe pattern is created by interfering the first and zeroth diffraction orders from the first grating, as described in Ref. [36] and shown in Figure 4.7. The increased wavelength acceptance of the PGMI, coupled with interferometer areas comparable to single-crystal NIs, allows the PGMI to measure significantly weaker forces than previously possible. A PGMI measurement of the gravitational force from a source mass whose density profile can be measured precisely provides a method of measuring the gravitational constant with systematic effects independent of measurements in the most recent CODATA report [80].

We describe an experiment that can measure gravitational effects using the three-grating arrangement of the PGMI and model the expected phase shift induced by a source mass. This model is validated by simulating existing neutron phase grating interferometric experiments [35, 37, 38]. We then apply this model to quantify systematic effects and uncertainty from several significant sources, demonstrating the feasibility of measuring G using a neutron PGMI to a precision of 150 ppm.

4.5 Phase Grating Moiré Interferometer Model

In the model described here, we calculate the phase shift accumulated along each neutron's propagation axis from the first grating to the neutron camera. The motivation to develop a new model describing the PGMI is the inability of other models to simulate non-linear potentials, like those produced by the gravitation of a source mass, efficiently. Several neutron PGMI configurations have been previously simulated using a momentum space model of each grating and propagation effects [73]. Here, we develop a new model of the neutron PGMI that can efficiently compute the effect of neutron propagation through an arbitrary potential.

A phase grating separates a neutron wave-packet into several diffraction orders, which may be further separated by subsequent gratings. The probability of detecting a neutron at a particular pixel is given by the amplitude of each path and the phase accumulated along the trajectories that reach said pixel. For a pixel at coordinate x_p with a single interacting trajectory, the probability of detecting a neutron is given by the product of each diffraction order amplitude, $I(x_p) = |A_l \cdot A'_m \cdot A_n|^2$ where the amplitude, A_n denotes the n-th diffraction order from a grating and the π-height grating is distinguished from the $\pi/2$-height by the prime, A'_m. In this case, any phase terms that arise from the complex

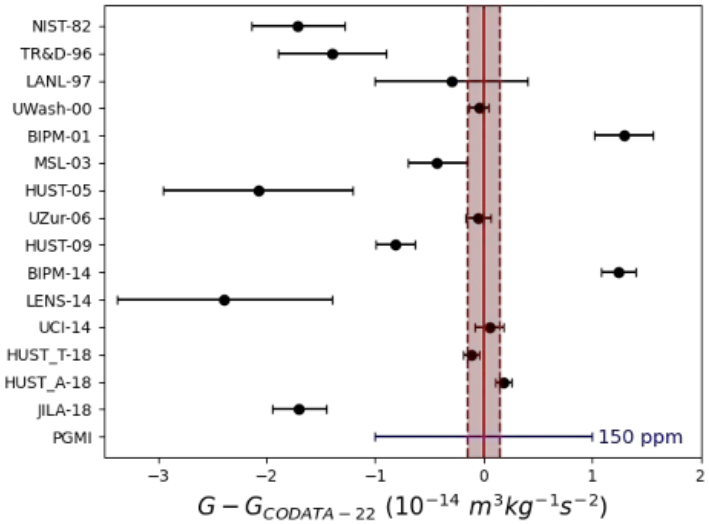


Figure 4.6: Difference between experimental results of G (labeled with acronyms from [80]) and the CODATA 2022 recommended value, $G = 6.674\,30(15) \times 10^{-11}\,\mathrm{m^3\,kg^{-1}\,s^{-2}}$. The shaded red region denotes the uncertainty in the CODATA 2022 value of G. The blue errorbar shows the uncertainty in G from the neutron PGMI experiment proposed in this work. Uncertainties are shown to 1 standard deviation.

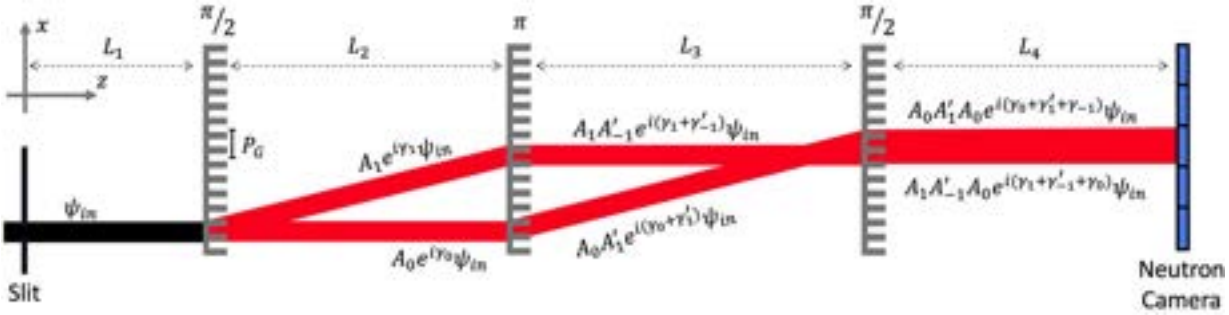


Figure 4.7: Schematic showing interfering paths in a three-grating neutron PGMI as red lines. The source neutron slit is shown in black on the left while the blue rectangle on the right indicates the camera position. In a phase-grating moiré interferometer, a visible fringe is created when grating separations, L_2 and L_3 are unequal, as illustrated [36]. The wavefunctions of paths within the PGMI are shown with each path's amplitude (A_l) and phase (ξ_l) factors. Amplitude and phase factors with a prime (A'_l, ξ'_l) denote values from the transmission function of the π-height grating. The terms shown beside each path segment corresponds to the wavefunction at the next object in the beam (grating/camera) and thus the phase term (γ_i) includes the phase accumulated from propagation.

transmission function of the gratings, or propagation between gratings are omitted as they do not affect the intensity measured at the camera. An example case of multiple trajectories that reach a given pixel is illustrated in Figure 4.7. In that case, the probability of a neutron being detected by a pixel is

$$I(x_p) = \left| \sum_{\{l,m,n\}} A_l A'_m A_n e^{-i(\gamma_l+\gamma'_m+\gamma_n)} \right|^2 , \tag{4.7}$$

where the sum runs over the paths detected by a pixel at x_p, indexed by the triplet of diffraction orders $\{l, m, n\}$ that correspond to a particular path, and terms γ_i include the phase accumulated by propagation which now must be included to compute the detection probability. For convenience, we combine these amplitudes and phases into $A_{lmn} \equiv A_l \cdot A'_m \cdot A_n$, and $\gamma_{lmn} \equiv \gamma_l + \gamma'_m + \gamma_n$. The phase terms in Eqn 4.7 can be computed following the Wentzel–Kramers–Brillouin (WKB) approximation, commonly applied to matter-wave interferometers [8, 76, 316]. Therefore, the phase γ_{lmn} can be computed using a path-integral along the neutron trajectory S_{lmn}

$$\gamma_{lmn} = \int_{S_{lmn}} \mathbf{k}(\mathbf{r}) \cdot d\mathbf{r}, \tag{4.8}$$

where the neutron wave-vector $\mathbf{k}(\mathbf{r})$ depends on the potential at any point in space, and the path S_{lmn} is the classical trajectory including path deviations due to any applied potentials. A Monte Carlo simulation of the 3-PGMI, computing the phases along all possible paths, should reproduce the interference pattern at the camera, where the neutron angle, wavelength, and position at the source slit are varied. Our model has been validated against existing phase grating interferometer experiments, with gravitational potentials and in PGMI arrangements, in Appendix A.

4.6 Measuring G

The Hamiltonian for a neutron propagating between the gratings of a 3-PGMI is

$$\mathcal{H} = \frac{\hbar^2 \mathbf{k}^2}{2m_N} - U_G(\mathbf{r}) - U_S(\mathbf{r}) - U_A(\mathbf{r}) - U_L(\mathbf{r}, t), \tag{4.9}$$

where $\hbar$ is the reduced Plank's constant, m_N is the neutron mass, $\mathbf{r}$ is the neutron position coordinate, U_G is the gravitational potential of the source mass, U_S is the correction to the Hamiltonian due to Earth's rotation, U_A is the nuclear potential of the ambient air, and U_L is the potential induced by lunar tidal forces, and t is the time coordinate. The phase accumulated from the source slit to the camera can then be computed with Eqn. 4.8 along each neutron's propagation axis, with the neutron wavevector

$$\begin{aligned} \mathbf{k} &= \mathbf{k}_0 \sqrt{1 + \frac{2m_N U_{\text{tot}}}{\hbar^2 \mathbf{k}_0^2}} \\ &\approx \mathbf{k}_0 \left(1 + \frac{m_N U_{\text{tot}}}{\hbar^2 \mathbf{k}_0^2} + \mathcal{O}\left[\left(\frac{U_{\text{tot}}}{E_0} \right)^2 \right] \right), \end{aligned} \tag{4.10}$$

where the potentials in Eqn. 4.9 have been collected into U_{tot}, and E_0 is the initial kinetic energy of the neutron. As $U_{\text{tot}} << E_0$, the accumulated neutron phase is

$$\gamma_{lmn} \approx \int_{S_{lmn}} \mathbf{k}_0 \cdot d\mathbf{s} + \frac{m_N}{\hbar^2 \mathbf{k}_0^2} \int_{S_{lmn}} U_{\text{tot}}(s)\ \mathbf{k}_0 \cdot d\mathbf{s}, \tag{4.11}$$

which implies that, to the first order, the phase induced by each of the potentials in Eqn. 4.9 can be written in separate terms, as is done for models of precision atom interferometry experiments [317]. As described in the Appendix of [36], moiré fringes arise from a product of two terms, which correspond to interference between two paths in our model. For two interfering paths, the measured intensity given by Eqn. 4.7 reduces to

$$\begin{aligned} I_G(x_p) &\sim \cos\left(\Delta\gamma_0 + \Delta\gamma_G + \Delta\gamma_S + \Delta\gamma_A + \Delta\gamma_L\right) \\ &\equiv \cos\left[\Delta\Phi_G(x_p)\right], \end{aligned} \tag{4.12}$$

where the phase differences $\Delta\gamma_i$ correspond to the potential fields in Eqn. 4.9. A measurement of the gravitational constant will require isolating the phase difference induced by the gravitational potential of the source mass, $\Delta\gamma_G$, from the other phase factors. This can be achieved by subtracting the measured phase from a null experiment, $\Delta\Phi_N(x_p)$, where the source mass is removed such that its gravitational potential is negligible. The phase shift induced by the gravitational potential can then be extracted:

$$\begin{aligned} \Delta\gamma_G &= (\Delta\Phi_G - \Delta\gamma_S - \Delta\gamma_{A,G} - \Delta\gamma_{L,G}) - (\Delta\Phi_N - \Delta\gamma_S - \Delta\gamma_{A,N} - \Delta\gamma_{L,N}) \\ &\equiv (\Delta\Phi_G - \Delta\gamma_{\mathrm{corr},G}) - (\Delta\Phi_N - \Delta\gamma_{\mathrm{corr},N}), \end{aligned} \tag{4.13}$$

where the subscripts G and N on each phase difference $\Delta\gamma_{i,G/N}$ refer to the source mass and null experiment, respectively. Note that different correction factors are required as ambient atmospheric conditions and tidal forces will vary between null and source mass experiments. The phase difference at the camera coordinate x_p due to the source mass can be written from Eqn. 4.11,

$$\Delta\gamma_G(x_p) = \frac{m_N}{\hbar^2\mathbf{k}_0^2} \oint_{S_{x_p}} G \cdot m_N \left[\iiint \frac{\rho(\mathbf{r}_V)}{\mathbf{s} - \mathbf{r}_V} d^3\mathbf{r}_V\right] \mathbf{k}_0 \cdot d\mathbf{s}, \tag{4.14}$$

where the path integral is over the specific path S_{x_p} that reaches the camera at coordinate x_p, the volume integral is over the source mass-centered coordinate $\mathbf{r}_V$, and the density of the source mass material is described by $\rho(\mathbf{r}_V)$. The gravitational potential term in Eqn. 4.14 can be solved numerically but has been solved analytically for right rectangular prisms, shown in Appendix B [318, 319]. Combining Equations 4.13 and 4.14, the gravitational constant can be measured by computing

$$G = \frac{\hbar^2 \mathbf{k}_0^2}{m_N^2} \frac{(\Delta\Phi_G - \Delta\gamma_{\mathrm{corr},G}) - (\Delta\Phi_N - \Delta\gamma_{\mathrm{corr},N})}{\oint_{S_{x_p}} \left[\iiint \frac{\rho(\mathbf{r}_V)}{\mathbf{s}-\mathbf{r}_V} d^3\mathbf{r}_V \right] \mathbf{k}_0 \cdot d\mathbf{s}}, \tag{4.15}$$

where the phase functions $\Delta\Phi_{G/N}$ are measured from the interference patterns of the source mass/null experiments, and the path integral term is computed for each coordinate across the camera. This result applies to one particular pair of interfering paths (i.e., the $\{0, 1, -1\}$ and $\{1, -1, 0\}$ paths shown in Figure 4.7, where the $\{0, 1, -1\}$ path is generated by the 0-order of grating 1, +1-order of grating 2, and −1-order of grating 3) at one neutron wavelength.

In reality, a neutron 3-PGMI accepts a distribution of neutron wavelengths and intensity at each pixel is an average over interfering path pairs. Therefore, computing a value for G, as in Eqn. 4.15, requires calculating the averaged phase from each potential. A similar procedure is used in atom interferometry for measuring the electric polarizability using atom beams with a velocity distribution [76, 320, 317]. For a polychromatic neutron 3-PGMI, the intensity is the incoherent sum over pairs of interfering paths and the wavelength distribution of the beam. Rewriting Eqn. 4.7:

$$I(x_p) = \sum_{\substack{\{lmn,\\ \tilde{l}\tilde{m}\tilde{n}\}}} \int_0^\infty P(\lambda) \left| A_{lmn} e^{-i\gamma_{lmn}} + A_{\tilde{l}\tilde{m}\tilde{n}} e^{-i\gamma_{\tilde{l}\tilde{m}\tilde{n}}} \right|^2 d\lambda, \tag{4.16}$$

where $\{lmn,\ \tilde{l}\tilde{m}\tilde{n}\}$ denotes a pair of interfering paths, and $P(\lambda)$ is the probability of a neutron having wavelength λ. As interference fringes arise exclusively from pairs of interfering paths of the 3-PGMI, we can simplify the modulus term to

$$\begin{aligned} I(x_p) &= \sum_{\substack{\{lmn,\\ \tilde{l}\tilde{m}\tilde{n}\}}} \left(|A_{lmn}|^2 + |A_{\tilde{l}\tilde{m}\tilde{n}}|^2 \right) \int_0^\infty P(\lambda) \left\{ 1 + \mathcal{C}(\lambda) \cos\left[\Delta\gamma_{0,G/N} + \Delta\gamma_{\mathrm{corr},G/N} \right] \right\} d\lambda \\ &\equiv I_0 \left\{ 1 + \langle \mathcal{C} \rangle \cos\left[\left\langle \Delta\Phi_{G/N}(x_p) \right\rangle \right] \right\}, \end{aligned} \tag{4.17}$$

where the sum is over all interfering path pairs, $\Delta\gamma_0$ is the residual phase of the interferometer without the previously defined correction factors, $\mathcal{C}$ is the wavelength-dependent contrast, I_0 is the average intensity profile across the camera, and $\langle\ \rangle$ denote the averaged values. The equivalence in Eqn. 4.17 arises because averaging over a distribution of cosines

with similar phases results in a cosine; however, the contrast and phase of the averaged intensity are not averages over the wavelength distribution, but the result of solving Eqn. 4.17 numerically [320]. Experimentally, we measure the averaged phase values $\left\langle \Delta\Phi_{G/N}(x_p) \right\rangle$, for the null and source mass configurations. Similar to [320], we can fit for the phase profile $\Delta\gamma_{0,N}(x_p)$ from the null experiment and $\Delta\gamma_{0,G}(x_p, \lambda)$ from the source mass experiment, where wavelength dependence arises from gravitational effects. This then allows us to compute G from the polychromatic measurements with

$$G = \frac{\hbar^2}{m_N^2} \frac{\langle \Delta\gamma_{0,G}(x_p, \lambda) \rangle - \langle \Delta\gamma_{0,N}(x_p) \rangle}{\left\langle \mathbf{k}_0^{-2} \oint_{S_{x_p}} \left[\iiint \frac{\rho(\mathbf{r}_V)}{\mathbf{s}-\mathbf{r}_V} d^3\mathbf{r}_V \right] \mathbf{k}_0 \cdot d\mathbf{s} \right\rangle}, \tag{4.18}$$

where the averages are over all interfering paths that reach a particular pixel and over the wavelength distribution of the neutron beam. The effect of an extended source can be incorporated by convolving the resulting interference pattern over the slit area, though this results only in a drop in contrast and not a change in the measured phase shift.

4.7 Proposed Experiment

Figure 4.8 shows the proposed arrangement of three phase gratings, each mounted on a six-axis motor control stage. The use of vacuum tubes between the gratings is motivated in Section 4.8.1. This design allows an x-ray source to be used when the neutron beam is blocked to monitor changes in grating alignment between null and source mass experiments independent of gravitational effects. As our neutron camera can image both neutrons and x-rays [321], this x-ray source can be used to monitor changes in grating alignment without disturbing the phase gratings or camera. The NG-6U neutron beam line at NCNR, where proof-of-concept experiments will take place, can accommodate a total interferometer length of up to 10 m. A measurement of G with this apparatus will take advantage of a polychromatic beamline, where we can achieve a neutron fluence rate of $10^9\,\mathrm{cm}^{-2}\,\mathrm{s}^{-1}$ [322]. To achieve appropriate coherence over one cycle of 1 µm period gratings, patterned over a large area, we can use a neutron source slit of up to 35 mm × 0.8 mm.

A 10×10^3 kg source mass was chosen for this design to maximize the gravitational potential across the 3-PGMI without requiring specialized equipment to move the mass. The choice of source mass material should be motivated by two factors: high density and precisely measurable density variations. The transparency of $PbWO_4$ ($\rho = 8235\,\mathrm{kg\,m}^{-3}$) has allowed for optical characterizations of the material to a relative density uncertainty

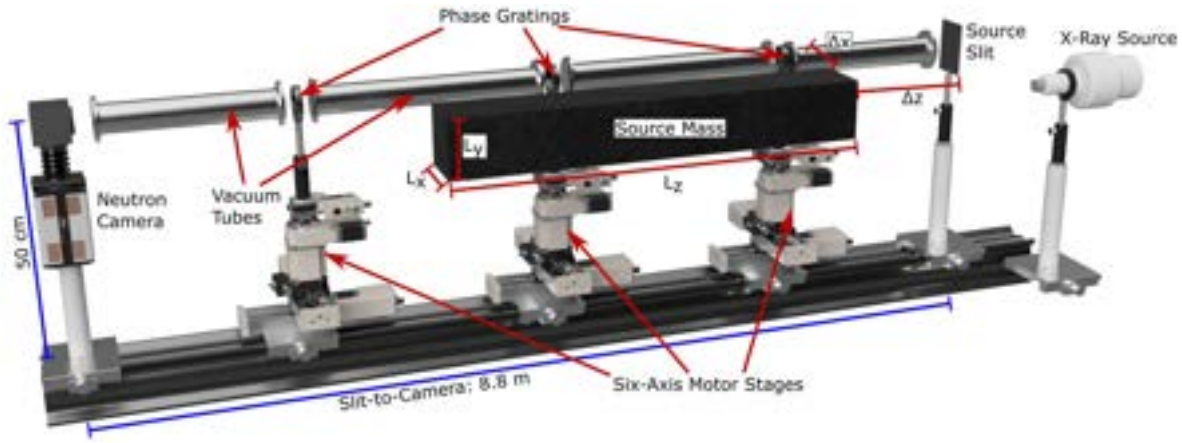


Figure 4.8: Model of the apparatus proposed in this work to measure G using a neutron PGMI, not produced to scale. This design features an x-ray source that can be used when the neutron beam is blocked, allowing for alignment validation independent of gravitational effects. The design of our neutron camera, similar to that shown by LaManna et al. [321], can image both neutrons and x-rays.

of $1.16\,\mu g\,cm^{-3}$ [323]. Solid lead ($\rho = 11\,342\,kg\,m^{-3}$) will create a larger phase shift due to its higher density, albeit with a greater uncertainty in source mass density. Assuming 0.01 % ferromagnetic impurities in the lead sample, modeled as magnetized volume within the block, we can expect at most a 95 nT difference in magnetic field between interfering paths. This results in a phase shift of ± 11.7 mrad for spin-up/down neutrons, resulting in no measurable phase shift in the interferometer for an unpolarized beam. Neutron phase contrast imaging has been used to measure the density distribution of $PbWO_4$, achieving a bound on the density gradient of $\frac{1}{\rho_N}\frac{d\rho_N}{dx} < 0.5 \times 10^{-6}\,cm^{-1}$, where ρ_N is the number density of the material [324]. This uncertainty in the density gradient is 25 times greater than what was achieved with optical characterization, corresponding to an uncertainty in density of $100\,\mu g\,cm^{-3}$ across the source mass width. With these density uncertainty values, the model outlined in Section 4.5 shows that a $PbWO_4$ source mass results in a relative uncertainty in G of 0.13 ppm while a solid lead source mass produces a relative uncertainty of 2 ppm. The increased uncertainty in lead density is a reasonable compromise given the increased gravitational phase shift compared to lead tungstate. It should be noted that these experiments measuring density using optical and neutron methods used samples $2.3\,cm \times 2.3\,cm \times 12\,cm$ in size. Applying these techniques may require a source mass composed of smaller masses arranged to form a larger rectangle. This will likely lead to additional sources of uncertainty based on temperature variation and alignment,

dependent on the exact size and number of masses used.

The location and dimensions of the source mass significantly affects the expected phase shift $\Delta\gamma_G$, and therefore affects the expected beam time for a desired measurement precision. We can apply the path integral model to compute the expected phase shift and contrast from a particular arrangement of the source mass and phase gratings, allowing for a minimization of the expected beam time. The relationship between phase uncertainty, interference fringe contrast, and beam time is described in Appendix C, demonstrating that minimizing beam time is equivalent to maximizing the product of fringe contrast and target phase uncertainty $\mathcal{C} \cdot \sigma_{\Delta\Phi}$. The displacements Δx, Δy, and Δz (listed in Table 4.2) are measured from the surface of the source mass to the center of the source slit. The displacements Δx and Δz are measured to the nearest face of the source mass, while Δy is measured from the top surface to the center of the beam. The result of this optimization is that a source mass of dimensions $\{L_x, L_y, L_z\} = \{13.0\,\text{cm}, 13.0\,\text{cm}, 500\,\text{cm}\}$ should be positioned with $\Delta z = 0$ (see Fig. 4.8) beside a grating interferometer with lengths $\{L_1, L_2, L_3, L_4\} = \{80.0\,\text{cm}, 200.0\,\text{cm}, 200.9\,\text{cm}, 399.1\,\text{cm}\}$. For these simulations, we have assumed perfectly aligned rectangular phase gratings manufactured for ideal phase heights at the mean wavelength of 4 Å. As the divergence of our neutron beam is $< 0.1°$, variation of diffraction order amplitudes with incident neutron angle produce insignificant changes in path amplitude and no change in phase. Extending this model to realistic gratings with imperfect alignment is achievable by computing the Fourier transform of the grating transmission function, with an image of the grating profile itself.

The optimized interferometer parameters result in a contrast of $\mathcal{C} = 22.1\,\%$, both with and without the source mass, and phase shift due to gravity of $\Delta\gamma_G = 13.2\,\mu\text{rad}$. While the 3-PGMI is capable of producing higher interference fringe contrast, the arrangement described here produced the maximum product of $\mathcal{C} \cdot \sigma_{\Delta\Phi}$. The statistical uncertainty as a function of the beam time (for each of the null/source mass experiments) is shown in Figure 4.9, with relative uncertainties of 50 ppm, 100 ppm, 150 ppm, and 200 ppm denoted with dotted lines. A measurement of this phase to 92.7 ppm results in an expected beam time of 120 d and a combined statistical uncertainty for both the null and source mass measurements of 131.1 ppm.

4.8 Uncertainties

The uncertainty in G from Equation 4.18, depends on the uncertainties in the phase correction terms $\Delta\gamma_{\text{corr},G/N}$, the source mass-induced phase $\Delta\gamma_G$, and the measured phase profiles $\Delta\Phi_{G/N}$. The model described here allows us to quantify these uncertainties from

uncertainties in the underlying experimental parameters. The uncertainty in each of these parameters is summarized in Table 4.2. The total uncertainty in G and the relative uncertainty due to each effect are summarized in Table 4.3.

4.8.1 Phase Correction Uncertainty

Atmospheric Phase

As outlined in chapter 3.4.1 of [8], atmospheric corrections depend on pressure, temperature, and humidity. The phase shift due to humidity and air density is

$$\Delta\gamma_A = -\lambda\Delta S\frac{\mathcal{L}P}{RT}\frac{\sum_i N_i b_{c,i}}{\sum_i N_i}, \tag{4.19}$$

where the sums are over each isotope i in the ambient atmosphere, ΔS is the path length difference, N_i and $b_{c,i}$ are the number density and scattering length for a particular isotope, $\mathcal{L}$ is the Loschmidt number, R is the ideal gas constant, P is the ambient pressure, and T is the ambient temperature. At the mean wavelength, the difference in path length for interfering pairs is 23 nm. The difference in phase between vacuum and 1 atmosphere, 20 °C, and 43 % humidity air for the PGMI with 4 Å neutrons is $\Delta\gamma_A = 3.9\,\mu\text{rad}$. Monitoring these parameters to 1 % uncertainty results in a relative uncertainty in G of 129.8 ppm. Placing evacuated cylinders, each at a pressure of 1 Pa, between the source slit, gratings, and camera will reduce the phase due to atmospheric effects to 3.8×10^{-11} rad which, without any correction between the null and source mass experiments, results in a relative uncertainty in G of 2.72 ppm.

Sagnac Phase

Non-inertial effects on neutrons have been well-documented, and the effect of the Earth's rotating reference frame can be computed from elementary mechanics [325, 326, 327, 328]. The phase accumulated by a neutron as the Earth rotates about a vector $\mathbf{\Omega}$ within an interferometer with an area vector $\mathbf{A}$ is

$$\Delta\gamma_S = \frac{2m_N}{\hbar}\mathbf{\Omega}\cdot\mathbf{A}. \tag{4.20}$$

If we assume that the interferometer is pointing perpendicular to the surface of the Earth, this dot product depends only on the latitude angle θ_L. The area of a 3-PGMI is dependent

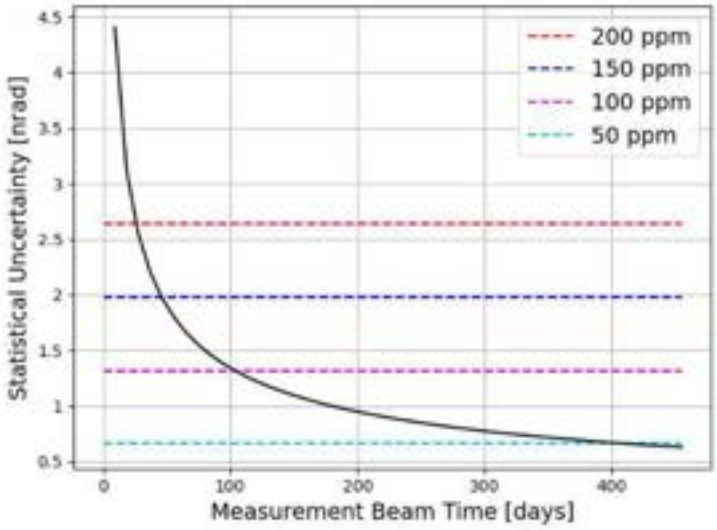


Figure 4.9: Statistical uncertainty in the phase of an interference pattern created in a neutron 3-PGMI with the beam parameters in Table 4.2. Dotted lines show the 50 ppm, 100 ppm, 150 ppm, and 200 ppm relative uncertainties in the measured phase $\Delta\Phi_{G/N}$. Note that the uncertainty in the gravitational constant also includes the effects described in Section 4.8.

on the angle between the first and zeroth diffraction orders of the first grating, therefore the Sagnac phase depends on wavelength as

$$\Delta\gamma_S = \frac{2m_N}{\hbar}|\boldsymbol{\Omega}|\left(\frac{L}{2}\right)^2\left(\frac{\lambda}{P_g}\right)\cos\left(\theta_L\right), \tag{4.21}$$

where L is the total interferometer length, and P_g is the grating period. While the Sagnac effect results in a 19.9 rad phase shift, this is present in both the null and source mass measurements. Therefore, the uncertainty in G due to the Sagnac effect is 10 ppm, arising from uncertainty in the mean wavelength of the neutron beam between experiments.

Lunar Gravitational Phase

The phase induced by tidal forces can be computed by treating the Moon as a point mass and calculating the distance from the laboratory reference frame to the lunar center of mass. Note that these tidal forces are due to changes in the position of the Moon and

not changes in local gravitational acceleration caused by sea level variation. The Earth-Moon distance has been measured to millimeter precision by the Apache Point Observatory Lunar Laser-ranging Operation [329], along with measurements of Earth's obliquity to the ecliptic and the lunar orbital inclination at relative precisions $< 1\,\text{ppm}$ [330, 331]. The remaining parameters used to compute the lunar gravitational phase are the latitude and orientation of the PGMI apparatus, the rotation phase of the Earth, and the orbital phase of the Moon. These parameters allow us to calculate the lunar phase shift by integrating the lunar gravitational potential along each neutron trajectory, as described by Eqn. 4.11. Using commercial GPS and electronic-compass devices, the latitude and orientation relative to Earth's rotation axis can be measured with an uncertainty of $0.14''$ and $0.5°$, respectively [332, 333, 122]. Combining these sources of uncertainty into a Monte Carlo simulation, the relative uncertainty in G from lunar gravitation is 1.7 ppm, for an experiment located in Gaithersburg, Maryland. Applying the same analysis to tidal effects from the Sun result in an uncertainty in G that is $\ll 1\,\text{ppm}$. Additional effects caused by changes in sea level and rainfall have not been account for, but can controlled for with concurrent gravimeter measurements and tidal modeling with software like T-Soft [334, 35, 122].

Precision measurements of local acceleration using atom interferometry have shown that gravity tides produce measurable variations in g on the order of 1 ppm [313]. Despite this, only two of the sixteen experiments contributing to the CODATA 2022 recommended value of Newton's Constant of Gravitation address lunar gravitation [80]. Both [85] and [309] refer to "tidal effects" or "tidal forces", though no value on the uncertainty from these effects is given. To estimate the effect of tidal forces on a torsion pendulum, we can apply our lunar potential simulation to the arrangement in Luther and Towler [81]. For a torsion balance measuring the gravitational force from two source masses, G is calculated with

$$G = \frac{\Delta(\omega^2) I}{k_g}, \tag{4.22}$$

where the torsion pendulum has a momentum of inertia I, twists about an angle θ, and the gravity of the source mass produces a restoring force with a reduced torsion constant k_g. That fictitious torsion constant is calculated by $k_g = G^{-1} d^2 U_T / d\theta^2$, where the source mass potential $U_T = GMm/R$ is integrated over the test-mass volume. The effect of tidal forces can be calculated by adding the potential due to the Moon's gravitation to the term U_T. Using the listed uncertainty in test-mass density, there is a significant torque induced by lunar gravitation, which produces an additional uncertainty in G of 39.5 ppm to the result in Ref. [81].

Parameter	Symbol	Value	Uncertainty
Source-Mass Dimension	L_x, L_y, L_z	13.0 cm, 13.0 cm, 500 cm	5 µm
Mass Density	ρ	11 342 kg/m^3	1.16 µg cm^{-3}
Mass Surface Variation	δL_x, δL_y, δL_z	0	5 µm
Ambient Temperature	T	20 °C	0.1 °C
Ambient Pressure	P	101 kPa	1 kPa
Ambient Humidity	ϵ	43 %	0.5 %
Mass Displacement (Horizontal)	Δx	20 cm	3 µm
Mass Displacement (Vertical)	Δy	6.5 cm	0.5 mm
Mass Displacement (Beam-axis)	Δz	80.0 cm	0.5 mm
Grating Separations	L_1, L_2, L_3, L_4	80.0 cm, 200.0 cm, 200.9 cm, 399.1 cm	3 µm
Mean Grating Period	P_g	700 nm	41 pm
Mean Neutron Wavelength	$\bar{\lambda}$	4 Å	0.0004 Å
Neutron Flux	$\dot{N}$	10^9 cm^{-2} s^{-1}	3×10^4 cm^{-2} s^{-1}
Slit Size	s_w	35 mm × 0.8 mm	1 µm

Table 4.2: Parameters for the experiment proposed in Sec. 4.7 with absolute uncertainties to 1σ (68 % confidence). The distances to each grating from the camera and source slit are each measured with the same absolute uncertainty as the grating separations. Source mass displacements (Δx, Δy, Δz) are given to the surface of the source mass. Parameters are grouped by relevance to subsections in Sec. 4.8.

4.8.2 Source-Mass Phase Uncertainty

The uncertainty of each experimental parameter is shown in Table 4.2. Each of these parameters is varied in a Monte Carlo simulation, and the resulting uncertainty in G is examined here.

Displacements

With an absolute uncertainty of 0.5 mm in beam-axis (vertical) displacements, the uncertainty in G is 11 ppm (3.5 ppm). By lowering the gratings below the neutron beam height, the source mass can be translated into the beam, providing an accurate displacement zero in the horizontal direction. Displacement sensors, like those offered by Attocube [122], can measure the horizontal displacement to an uncertainty of 3 µm, resulting in an uncertainty in G of 11 ppm. The same sensors can be used to measure the distances from the source slit to the first grating, between each grating, and from the third grating to the neutron camera. Uncertainties of 3 µm in each of the distances L_1, L_2, L_3, and L_4, results in a 0.78 ppm relative uncertainty in G.

Parameter	Uncertainty in G (ppm)
Grating Mean Period	58
Neutron Wavelength	40
Source-Mass Displacement (Horizontal)	11
Source-Mass Displacement (Beam-axis)	11
Sagnac Phase	10
Grating Thermal Variation	5.2
Source-Mass Displacement (Vertical)	3.5
Atmospheric Effects	2.7
Source-Mass Density	2.0
Lunar Gravitation	1.7
Grating Separations	0.78
Source-Mass Surface Flatness	0.53
Systematic Uncertainty	73
Statistical Uncertainty (240 d)	130
Total	150

Table 4.3: Uncertainty budget for the 3-PGMI measurement proposed using a rectangular source mass. The methods used to calculate the uncertainty of each parameter are described in Sec. 4.8, with values listed in this table to two significant digits. Statistical uncertainty of 131.1 ppm is the result of 240 d of total experiment time consisting of two 120 d beam time runs for a null and source mass experiment.

Phase Grating Period

Using small-angle x-ray scattering (SAXS) [335], or by imaging the diffracted orders from an x-ray pencil beam, the mean grating period can be measured point-by-point across the gratings to 58 ppm. This uncertainty in the grating period, using the Monte Carlo simulation, leads to an uncertainty in G of 57.7 ppm. Thermal fluctuations during the experiment will cause expansion/contraction of the silicon wafers and therefore change the grating period. Assuming fluctuations of $\pm 2\,^{\circ}\mathrm{C}$, the uncertainty in G introduced by this change in grating period is 5.2 ppm.

Neutron Wavelength

The uncertainty in the effective mean wavelength of a polychromatic beam can be calculated by a Monte Carlo error propagation of uncertainties in the wavelength and neutron count of a neutron spectroscopy experiment. The error in the neutron count of a spectrometer follows Poisson statistics, while the uncertainty in the wavelength measured by a chopper experiment has been analyzed previously [336]. Expanding the chopper spectrometer designed by Ref. [336] to 8 m length and using the parameters for the long spectrometer in that work, the weighted-averaged wavelength can be measured to 98.4 ppm. This results in an uncertainty in the source-mass-induced phase of 40.1 ppm.

4.8.3 Statistical Uncertainty

The final source of uncertainty in determining G from Eqn. 4.18 is in the measured phase values, $\Phi_{G/N}$. Assuming Poissonian distribution for the counts seen at each pixel of the detector, the uncertainty in the resulting least squares fit is

$$(\sigma_\Phi)^2 \propto \frac{1}{\dot{N} T \mathcal{C}^2}, \tag{4.23}$$

where $\dot{N}$ is the count rate at the detector and T is the measurement beam time. A derivation of this result is shown in the Appendix C. The parameters in Table 4.2 results in a statistical uncertainty in the measured phase of 92.7 ppm. Applying this to both the null and source mass measurements, the total statistical uncertainty is 131.1 ppm.

4.9 Conclusion

The significant uncertainty in the CODATA 2022 value for G underscores the necessity that new meteorological devices capable of measuring gravity are designed and new measurements with systematic effects independent of previous experiments are conducted. The mass and electric neutrality of neutrons make them a convenient probe for the relatively weak gravitational potentials created by laboratory-scale source masses. The neutron PGMI, with its wide wavelength acceptance and large interferometer area, has overcome the previous limitations of single-wavelength NIs. Here, we have shown that a neutron 3-PGMI has sufficient sensitivity to measure the phase shift induced by a 1 t source mass and extract the gravitational constant with an uncertainty of 150 ppm [i.e., $G = 6.674(1) \times 10^{-11}\,\mathrm{m^3\,kg^{-1}\,s^{-2}}$] with systematic effects distinct from state-of-the-art experiments. The PGMI and source mass parameters in this proposal result in a gravitationally induced phase shift of $\Delta\gamma_G = 13.2\,\mu\mathrm{rad}$ and a contrast of 22.1 %.

A measurement of G to 100 ppm is possible with this design but would require more than 800 d of experiment time in the current configuration. Neutron beamlines other than those at NCNR offer potential avenues to reduce the statistical uncertainty for equivalent measurement times. The SL-13B beam line at the Oakridge National Lab offers an increase in beam length to 12 m, and potentially a 50 % increase in neutron flux to $\approx 1.48 \times 10^9\,\mathrm{cm^{-2}\,s^{-1}}$ [337]. The PF1B beam line at the Institut Laue-Langevin offers a flux of $2 \times 10^{10}\,\mathrm{cm^{-2}\,s^{-1}}$, with a mean wavelength of 4 Å to 4.5 Å which may also increase the magnitude of the source mass induced phase [338]. The flux from these sources offer a significant increase compared to atom interferometry sources, potentially enabling higher precision measurements compared to those methods [339]. Improvements offering smaller grating periods or different source mass potentials may increase the gravitationally-induced phase shift and therefore improve the achievable precision in G with a neutron PGMI.

Without new methods of measuring gravitational forces, it is difficult to distinguish discrepancies in G caused by systematic effects from new physics [340], variations in Earth's gravitation [341], or relativistic effects [342]. Furthermore, this analysis of the systematic effects in a neutron 3-PGMI suggests that existing experiments measuring G may require a correction factor to account for time-dependent changes in tidal forces. These corrections depend on both the experiment date and location, possibly accounting for some of the variation between experimentally measured values of G. The model introduced here can also be used to design new operational modalities capable of measuring internal magnetic structures, like in skyrmion materials, or fundamental properties, like the neutron electric dipole moment.

4.10 Model Validation

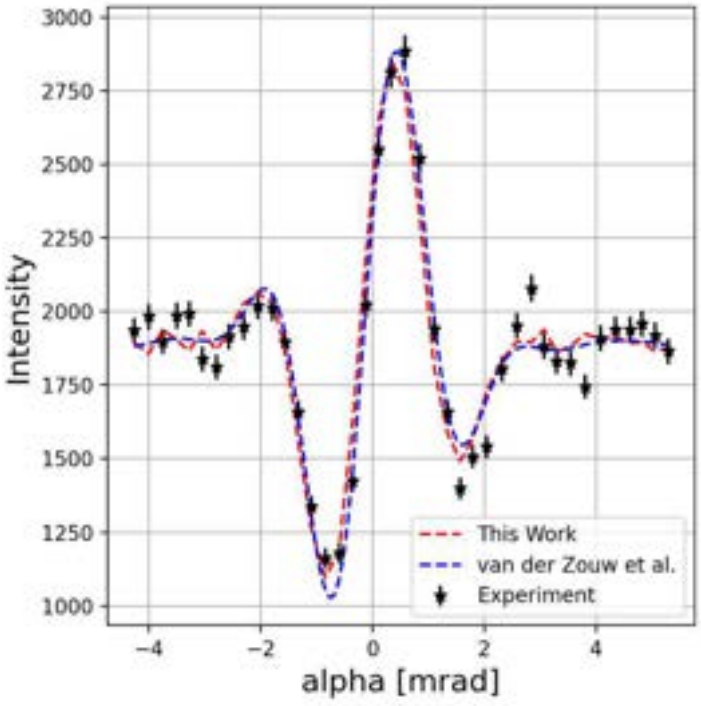


Figure 4.10: Neutron intensity as a function of grating rotation (alpha) from van der Zouw et al. [35]. Experimental neutron counts are shown as black points, with the theoretical curve of Ref. [35] shown as a blue dotted line. Monte Carlo simulation results from this work are shown as a red dotted line.

The Monte Carlo model described in this work, with example scripts used to compare simulation to neutron experiments, can be found at https://git.uwaterloo.ca/c3kapahi/pgmi-big-g-simulation. Several experiments have investigated the interference pattern generated by a series of phase gratings in a neutron beam, some including the effect of gravitational potentials. In 2000, van der Zouw et al. measured the intensity of one path pair in a phase grating NI, namely the interference between the $\{0, 1, -1\}$ and $\{1, -1, 0\}$ orders, where each integer in the set denote the diffraction order from the $\{1^{\text{st}}, 2^{\text{nd}}, 3^{\text{rd}}\}$ grating [35]. The wavevector of a neutron within this interferometer will depend on its position, $\mathbf{r}$, as

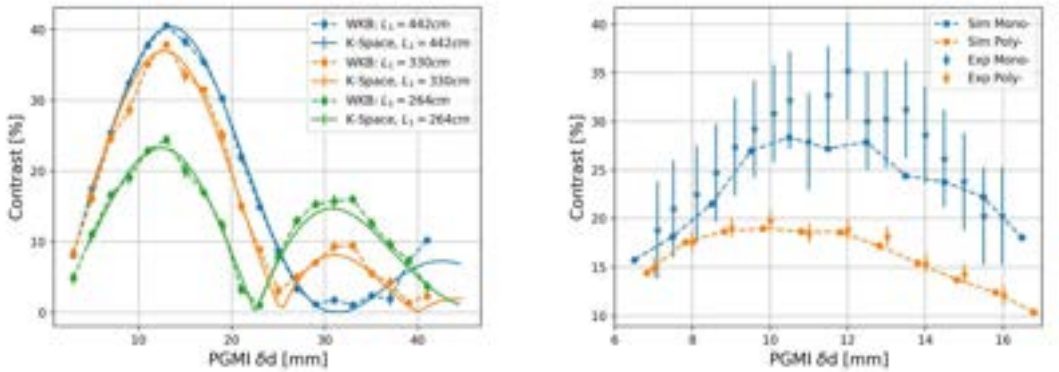


Figure 4.11: (left) Simulated contrast values for two-grating neutron PGMI experiment. Entrance slit to first grating distance, L_1, varies between datasets. Experimental parameters and original data can be found in Ref. [73]. Simulated contrasts with the path integral model described in this work show good agreement with the plane-wave model in Ref. [73]. (right) Simulated and experimental contrast values for two-grating neutron PGMI. Experimental parameters and original data can be found in Ref [37].

$$\mathbf{k}^2 = \mathbf{k}_0^2 + m_N g \mathbf{r} \cdot \hat{\mathbf{y}}, \tag{4.24}$$

where $\mathbf{r} = 0$ is the coordinate of the entrance slit, $\mathbf{k}_0$ is the neutron's initial wavevector, m_N is the neutron mass, and g is the local acceleration due to gravity. The interferometer in Ref. [35] was simulated using the listed total interferometer length of 0.76 m with grating periods of 2 µm and the wavelength distribution shown in Figure 1 of that work. The result of the path integral model of this experiment is shown as a red dotted line in Figure 4.10, with the experimental counts shown as black dots. The path integral model (red) shows good agreement with the theoretical curve (blue), shown in Figure 4.10 of Ref. [35].

Unlike the phase grating interferometer used by van der Zouw, the neutron PGMI generates an interference pattern from a range of incident neutron angles with no restriction on the allowed diffraction orders. Experimental demonstrations of the neutron PGMI have used both two- and three-grating arrangements. Experiments using two gratings have shown high contrast with a variety of neutron spectral distributions [37, 73], while the three-grating arrangement has only been measured with low contrast [38], possibly due to misalignment of the phase gratings [112, 73].

Figure 4.11 shows the contrast of interference patterns generated by a Monte Carlo simulation of Eqn.1 with varying grating separation, δd. Simulations with the WKB model

described in this work are in good agreement with the momentum space model of [73] and with both the monochromatic and polychromatic PGMI experiments of [37].

4.11 Gravitational Potential of a Right Rectangular Prism

The gravitational potential of any source mass can be computed numerically; however, analytic solutions exist for the potential from several simple shapes, including the right rectangular prism [318, 319]. For a rectangular prism source mass of dimension $\{L_x, L_y, L_z\}$, the gravitational potential at a point, (x, y, z), outside the mass volume is

$$U_g(x,y,z) = G\rho \int_{-L_z/2}^{L_z/2}\int_{-L_y/2}^{L_y/2}\int_{-L_x/2}^{L_x/2} \frac{dX\,dY\,dZ}{\sqrt{(x-X)^2+(y-Y)^2+(z-Z)^2}} \tag{4.25}$$

$$\begin{aligned} &= \Bigg|\Bigg|\Bigg| XY\log(Z+|\mathbf{R}|) + YZ\log(X+|\mathbf{R}|) + ZX\log(Y+|\mathbf{R}|) \\ &\quad - \frac{X^2}{2}\tan^{-1}\left(\frac{YZ}{X|\mathbf{R}|}\right) - \frac{Y^2}{2}\tan^{-1}\left(\frac{ZX}{Y|\mathbf{R}|}\right) \\ &\quad - \frac{Z^2}{2}\tan^{-1}\left(\frac{XY}{Z|\mathbf{R}|}\right)\Bigg|_{X=-\frac{L_x}{2}-x}^{\frac{L_x}{2}-x}\Bigg|_{Y=-\frac{L_y}{2}-y}^{\frac{L_y}{2}-y}\Bigg|_{Z=-\frac{L_z}{2}-z}^{\frac{L_z}{2}-z}, \end{aligned} \tag{4.26}$$

where the origin of both coordinates (x, y, z) and (X, Y, Z) are the geometric center of the rectangular prism source mass, the density of the source mass, ρ, is uniform, and $\mathbf{R}$ is the distance from the source mass element at (X, Y, Z) to the point of interest (x, y, z).

4.12 Phase Fit Statistics

This analysis expands on the work in Chapter 4.4 of Ref. [8]. The underlying assumption in this analysis is that the number of counts, N_j, in a detector or single-pixel over some time, T, obeys a Poisson distribution, with a mean count across the experiment of $\bar{N}$, and standard deviation $\sigma_{N_j} = \sqrt{\bar{N}}$. For our interferometer, the expected number of particles per pixel/detector position, N_j, is

$$N_j = \bar{N}\left[1 + \mathcal{C}\cos\left(\frac{2\pi}{P_f}x_j + \Delta\Phi_j\right)\right], \tag{4.27}$$

where $\mathcal{C}$ is the contrast of these interference fringes, P_f if the period of the interference fringes, x_j is the position of pixel j, and $\Delta\Phi_j$ is the phase difference between interfering paths as measured at this detector.

The variances in phase and detector count are related by

$$(\sigma_{N_j})^2 = \left(\frac{\partial N_j}{\partial \Delta\Phi_j}\right)^2 (\sigma_{\Delta\Phi_j})^2, \tag{4.28}$$

where the partial derivative can be computed from Eqn. 4.27,

$$\begin{aligned}\left(\frac{\partial N_j}{\partial \Delta\Phi_j}\right)^2 &= \bar{N}^2\mathcal{C}^2\sin^2\left(\frac{2\pi}{P_f}x_j + \Delta\Phi_j\right) \\ &= \bar{N}^2\mathcal{C}^2 - (N_j - \bar{N})^2 \\ \implies (\sigma_{\Delta\Phi_j})^2 &= \frac{N_j}{\bar{N}^2(\mathcal{C}^2-1) + 2\bar{N}N_j - N_j^2},\end{aligned} \tag{4.29}$$

where the relation, $\sin^2 x + \cos^2 x = 1$, has been used along with Eqn. 4.27. The total uncertainty in $\Delta\Phi$ from fitting all pixels across the detector follows from a χ^2 optimization over M different "detectors" or over M pixels,

$$(\sigma_{\Delta\Phi})^2 = \left[\sum_{j=1}^{M}(\sigma_{\Delta\Phi_j})^{-2}\right]^{-1}. \tag{4.30}$$

The sum over M pixels can be approximated using an integral over a finite number of periods. Choosing to approximate this sum as an integral over one period, P, the sum in Eqn. 4.30 is

$$\begin{aligned}\sum_{j=1}^{M}(\sigma_{\Delta\Phi_j})^{-2} &\approx \frac{1}{2\pi}\int_0^{2\pi}\frac{\bar{N}^2(\mathcal{C}^2-1) + 2\bar{N}N_j - N_j^2}{N_j}dx \\ &\approx \frac{\bar{N}(\mathcal{C}^2-1)}{\sqrt{1-\mathcal{C}^2}} + \bar{N},\end{aligned} \tag{4.31}$$

where the average counts, $\bar{N}$, applies across the range of pixels used in the experiment. Using the relationship, $\bar{N} = \dot{N}T$, where $\dot{N}$ is the count rate at the detector and T is the experiment duration, we can combine Eqn. 4.30 and 4.31 to find

$$(\sigma_{\Delta\Phi})^2 \approx \frac{1}{\dot{N}T\left(1-\sqrt{1-\mathcal{C}^2}\right)}, \tag{4.32}$$

as shown in Section V. We can approximate the square-root term in Eqn. 4.32 with $\mathcal{C}^2 << 1$ and rearrange these terms to estimate the required beam time for a measurement as

$$T \approx \frac{2}{\dot{N}(\sigma_{\Delta\Phi}\cdot\mathcal{C})^2}, \tag{4.33}$$

which suggests that minimizing the required beam time for a measurement is achieved by maximizing the product $(\sigma_{\Delta\Phi}\cdot\mathcal{C})$, as stated in Section IV. For a desired relative uncertainty in the phase $\Delta\Phi$, this is equivalent to maximizing the magnitude of the source mass induced phase shift and contrast.

4.13 Implementation

The experiment outlined in the above publication uses a polychromatic beamline to measure G using a source-mass over the course of 240 d. One consideration of this experiment, omitted due to the focus of the above work on the facilities at the NCNR, is the optimal wavelength and beam characteristics of any implementation of the above proposal. Two elements of any potential beamline for this experiment, most critical for determining the precision of a measurement, are the mean wavelength and wavelength distribution of the beam. In particular, the square of the mean wavelength of the beam is proportional to the induced phase shift of a source mass (see Eqn. (4.15), accounting for the wavelength dependent diffraction angle of a grating), suggesting that colder neutrons (longer wavelength) are optimal for the proposed measurement. As we saw with the VCN, very cold neutrons are produced at relatively low flux by neutron sources. In fact, the parameter we should look to optimize for a precision measurement of G is the relative uncertainty with which

a source-mass induced phase can be measured. Combining the expected phase shift, $\Delta\gamma_G$ from Eqn. (4.15) with the uncertainty in Eqn. (4.23) suggests that the goal of any beamline seeking to measure G with maximum precision is to maximize the product $\sqrt{\dot{N}}\bar{\lambda}^2\mathcal{C}$, equivalently minimizing the relative uncertainty in the source mass induced phase. While this applies to the mean of any beamline used to measure G, an additional effect of a polychromatic beam is to reduced the contrast of the interference pattern generated by the PGMI. The work of Heacock et al [112] showed that the contrast from a monochromatic beam with a 3-PGMI decays from the design wavelength of the gratings, roughly as a Gaussian with FWHM $\Delta\lambda/\bar{\lambda} \approx 0.56$. As the effect of a polychromatic beam is to average over the interference patterns of the constituent wavelengths, the resulting contrast should follow the average value of the contrast function in Figure 5(a) of [112],

$$\mathcal{C} = \frac{1}{2\Delta\lambda}\int_{\bar{\lambda}-\Delta\lambda}^{\bar{\lambda}+\Delta\lambda} \frac{1}{2\sqrt{2\pi}} e^{-\frac{(\lambda-\bar{\lambda})^2}{2\Delta\lambda}} d\lambda \approx \frac{0.3414}{\Delta\lambda}, \tag{4.34}$$

which, with the result from Heacock et al., can be combined with our optimization target above to suggest that the goal of a beamline is to maximize the product

$$\frac{\Delta\gamma_G}{\sigma_\Phi} \propto \sqrt{\dot{N}}\bar{\lambda}. \tag{4.35}$$

Prior to a full-precision measurement of G, there are several experiments which can be conducted over significantly shorter timescales to validate the uncertainty calculations, experimental procedure, and optimal experiment parameters in the above work. First, is a demonstration that significantly higher contrast interference patterns can be generated with the 3-PGMI than what was achieved in [38]. In [73], a cone-beam model of the PGMI was applied to demonstrate that yaw misalignment of the gratings by $\approx 5^\circ$ could have caused a reduction in contrast from 30% to the observed 3%. Coupled with improvements in grating fabrication, resulting in near-perfect square gratings, higher contrast interference patterns should be achievable [343]. The use of an X-ray source with the gratings of the neutron PGMI, or the use of an NIR source and an additional pattern with lower frequency gratings on the same wafer, would allow rapid alignment of the gratings and a demonstration of a full 30% contrast interference pattern.

Next, Earth's local gravitational acceleration can be measured by co-rotating all three gratings as was done in [35]. Computing the local acceleration g with high precision requires quantification of many of the parameters in Table 4.2. This experiment also requires alternating between neutron and X-ray sources, a feature critical to monitoring

for changes in a $> 200\,\mathrm{d}$ experiment, as any misalignment between grating rotation axes will introduce an additional phase shift as gratings rotate. The choice of silicon gratings was motivated by the availability of fabrication techniques to produce sub-micrometer, high-aspect ratio gratings to act as π-gratings in the PGMI. That silicon gratings produce a significant phase shift with x-rays while also being transparent is advantageous for the experiments above, though other materials may offer improvements in grating quality or period. Sapphire in particular possesses a high neutron-optical potential, reducing the required phase grating height for $\lambda = 8.9\,\text{Å}$ from $16\,\mu\mathrm{m}$ for silicon to $6\,\mu\mathrm{m}$. For $10\,\mathrm{keV}$ X-rays, both materials are transparent, with phase heights of $0.86\,\mathrm{rad}$ for silicon and $0.31\,\mathrm{rad}$ for X-rays. Depending on the ability of sapphire precision manufacturing to enable high aspect ratio prisms [344], as are available with silicon, this may prove to be the preferable material for neutron PGMI gratings.

While the experiment proposal in [298] was originally intended for an $8.9\,\text{Å}$ beamline at the NCNR, there are several neutron facilities suitable for this experiment. The Fundamental Neutron Physics Beamline (FNPB), SL-13A at the Oak Ridge National Lab (ORNL) spallation neutron source (SNS) uses a double-crystal monochromator to produce a $8.9\,\text{Å}$ beam and offers up to $20\,\mathrm{m}$ of free neutron flight [337]. This location is ideal for conducting preliminary monochromatic demonstrations of the 3-PGMI and local acceleration measurements. A second beamline, SL-13B, at SNS offers $12\,\mathrm{m}$ of beam line and a polychromatic distribution with a neutron flux of $\approx 1.48 \times 10^9\,\mathrm{cm^{-2}\,s^{-1}}$ at $1.7\,\mathrm{MW}$ of reactor power. This dual offering of monochromatic and polychromatic beamlines is an ideal arrangement to test the precision gravimetry capabilities of the neutron 3-PGMI. Recently, a program review and assessment committee at ORNL recommended that a neutron 3-PGMI be installed at the BL13-A beamline "as soon as the beamline becomes available", to conduct preliminary experiments towards a measurement of G.

The Institut Laue-Langevin (ILL) neutron facility offers two beamlines with desirable qualities to develop the 3-PGMI toward a precision measurement of G. Between 2002 and 2005, a series of experiments at ILL measured discrete energy levels in neutrons generated by the Earth's local gravitational field [345, 346, 347]. A second-generation gravitational neutron spectrometer was designed to take advantage of a new high-flux beamline of $8.9\,\text{Å}$ neutrons [348]. This site not only offers a suitable beamline, but also a wealth of experience in neutron experiments probing gravitational forces. Alternatively, the $4\,\text{Å}$ PF1B beamline houses a large, flexible area for installing a PGMI coupled with an extremely high neutron fluence.

Improving the achievable precision of any neutron 3-PGMI measurement of G can primarily be accomplished through three avenues. First, increasing the phase shift γ_G induced by a source mass improves the relative uncertainty with which this phase can be measured.

To achieve this, alternative source mass geometries should be investigated with the modeling tools developed here, including "c-shaped" source masses, which may wrap around the neutron beamline to move the center of mass closer to the neutron beam. Second, Eqn. (4.23) shows that an increase in interference pattern contrast leads to an improvement in achievable phase uncertainty. The predicted maximum contrast for a neutron 3-PGMI, from both this model and the cone-beam model [73], is $\approx 32\%$. Contrast enhancement beyond this can be achieved by filtering non-interfering diffraction orders, similar to the proposed application of the spin-collimator in Chapter 2 for the VCN interferometer. In particular, filtering orders other than interfering pairs like, those shown in Figure 4.7, will significantly reduce background intensity and improve contrast.

Even before these improvements manifest, the addition of polarization control into the PGMI enable the exploration of spin-dependent neutron interactions, expanding on work that explores physics beyond the Standard Model [349]. Such work can leverage polarized incident neutrons to measure variations in interaction potentials with neutron spin. An additional degree-of-freedom, a second spatial dimension, also enables measurements that produce interference fringes in two dimensions using 2D grating patterns [350]. Such experiments may provide a simultaneous control measurement for future gravitational experiments with neutron phase grating interferometers.

Chapter 5

Outlook

This thesis highlights several theoretical tools and experimental results that have emerged from neutron optics research, advancing the goal of measuring the gravitational constant with a neutron interferometer to high precision. Throughout the preceding chapters, potential applications of light and matter wave states have been described. Here, these potential applications will be expanded upon, and relevant developments from literature will be highlighted.

5.1 Structured States of Light

The field of structured light is so broad, with ongoing research in numerous fields, that we will focus here on areas particularly relevant to the work described. In particular, applications of structured states of light to the characterization of biological tissue and to quantum information transmission will be discussed.

5.1.1 Biological Applications

Modern pathology regularly uses polarization analysis to aid in identifying and classifying of potentially diseased tissue samples [351, 352, 353]. Edge-enhanced microscopy techniques already employ orbital angular momentum (OAM) states to improve the contrast of different tissues and cell types, without the need for chemical modification of samples, like dye staining [150]. Looking beyond studies of the human visual system from Chapter 3, spin-orbit states could enhance signals from tissues with birefringent properties, like those

with amyloid fibrils, without the need for chemical treatment [257]. Recent work has shown that structured states offer improved tissue penetration characteristics, demonstrated in mouse brain tissue [134, 258] and chicken breast tissue [245]. This suggests that imaging technologies, like X-ray imaging and tomography, could reduce patient dosage by imaging with OAM states. The wealth of applications for structured states with light suggests that neutron structured states may find similarly impactful use-cases.

5.1.2 Quantum Information Transmission

The OAM degree of freedom has regularly been investigated as a potential carrier of classical and quantum information due to the wealth of methods to generate OAM states and the infinite-dimensional Hilbert space they occupy [354, 355, 67]. Of particular interest has been the application of OAM states to free-space communication and, therefore, the susceptibility of OAM states to atmospheric turbulence [356, 357]. Encoding information into OAM states allows for information storage greater than 1 bit per photon [67], and has been shown resilient to free-space propagation over 100 km [358]. These discoveries suggest that OAM states may be an ideal carrier of information through turbulent media, including underwater applications [359, 360, 361]. Recent work has applied quantum information techniques that leverage high-dimensional states to beams with OAM, experimentally demonstrating 11-dimension secret sharing between 10 parties [362] and designing single-qudit gates for OAM states [363]. Together, this body of work shows that OAM states are likely to play a pivotal role in the coming transformation of classical communication systems, both by offering higher classical information density carriers and as robust quantum information basis states.

5.2 Neutrons as probes

We have shown in this work that neutrons have a long history at the forefront of the study of quantum particles. Modern neutron facilities are highly sought-after for material characterization, the study of chemical or biological processes, and fundamental physics [13, 364, 365]. The experiments described in this work open new avenues to probe materials with structured neutron states, and perform interferometric measurements with previously unachievable precision. Many of these applications have been alluded to in previous chapters, but here we will describe potential extensions of this work into new experiments.

5.2.1 Structured Neutron States

In 2022, gratings with periods on the order of 100 nm and a fork profile were fabricated and tested [103]. Since then, multiple fork gratings have been combined to show interference between neutron OAM states [292], and accelerating Airy beams [291] have been demonstrated with similarly fabricated gratings. These methods of reliably generating structured neutron states enable the development of material characterization techniques, similar to those described in Chapter 3 with the neutron lattice of optical vortex (LOV) prisms. Unlike the LOV prisms, these new grating methods generate an OAM state with a vortex within the coherence volume of a single neutron [103]. Neutron scattering has already shown utility in characterizing the internal magnetic structure of skyrmion states [366, 367, 13]. The addition of a neutron polarization pattern that matches the topological structure of a sample may enable enhanced characterization of skyrmions and other magnetic structures within materials.

5.2.2 Next Generation Neutron Interferometers

In Chapter 4, an experiment to measure the gravitational constant with a neutron phase grating moiré interferometer (PGMI) was described in detail, and the achievable uncertainty was quantified. Future developments of the design were also described in that chapter, highlighting potential avenues through which the achievable precision in G can be enhanced. Two key parameters determining the performance of a neutron PGMI are the grating profile and period. With silicon gratings, grating height is constrained by the interferometer contrast, which peaks for gratings with a phase height of $\pi/2$ and π. Constructing high-quality (i.e. near-perfect square gratings) of the appropriate phase height is challenging, but this could be mitigated if the material index could be enhanced. Instead of using the material index to generate our diffraction gratings, applying a more readily controllable potential could enable the fabrication of higher-frequency diffraction gratings, or other grating profiles that suppress unwanted higher diffraction orders. In 1979, both a μ-metal prism and custom electromagnet were used to generate magnetic field prisms of $\approx 1\,\mathrm{T}$ and split an incident neutron beam into polarized components [368]. This design was later refined to realize a 99.998% polarized neutron beam using a free-space magnetic field of $\approx 2\,\mathrm{T}$ [369].

Realizing a square or sinusoidal standing wave with magnetic fields, with a period that allows magnetic field diffraction gratings to compete with the sub-micrometer silicon gratings currently fabricated, is challenging. Advances in nano-wire fabrication have enabled

the creation of 221 nm period magnetic gratings [370]. While these gratings are not designed to generate magnetic fields on the order of 1 T, their fabrication and application at electron lasers suggest that magnetic gratings for neutron optics may be feasible. Alternatively, the magnetic fields from conducting wires has been shown to control neutral atoms [371] and magnetic multilayer structures are already widely applied in neutron optics as polarizing mirrors [372, 373]. These techniques may be the future of neutron phase gratings, overcoming the technical challenges of fabricating high-quality, high-aspect ratio gratings and enabling grating periods < 500 nm with diffraction efficiencies that generate high-contrast interference patterns in a PGMI. All of these advancements will benefit future measurements of gravitational forces with a neutron 3-PGMI, but will also further the study of quantum materials [374], improving limits on exotic spin-gravity couplings beyond the Standard Model [349], and probe the nature of dark matter and dark energy [375].

References

[1] C. Kapahi, D. Sarenac, M. Bleuel, D. G. Cory, B. Heacock, M. E. Henderson, M. G. Huber, I. Taminiau, and D. Pushin, "High-Transmission Neutron Optical Devices Utilizing Micro-Machined Structures," *Quantum Beam Science 2023, Vol. 7, Page 10*, vol. 7, p. 10, 3 2023.

[2] D. Sarenac, A. E. Silva, C. Kapahi, D. Cory, B. Thompson, and D. A. Pushin, "Human psychophysical discrimination of spatially dependant pancharatnam–berry phases in optical spin-orbit states," *Scientific reports*, vol. 12, no. 1, pp. 1–6, 2022.

[3] D. Sarenac, C. Kapahi, A. E. Silva, D. G. Cory, I. Taminiau, B. Thompson, and D. A. Pushin, "Direct discrimination of structured light by humans," *Proceedings of the National Academy of Sciences*, vol. 117, no. 26, pp. 14682–14687, 2020.

[4] C. Kapahi, A. E. Silva, D. G. Cory, M. Kulmaganbetov, M. Mungalsingh, D. A. Pushin, T. Singh, B. Thompson, and D. Sarenac, "Measuring the visual angle of polarization-related entoptic phenomena using structured light," *Biomedical Optics Express*, vol. 15, no. 2, pp. 1278–1287, 2024.

[5] D. Sarenac, C. Kapahi, W. Chen, C. W. Clark, D. G. Cory, M. G. Huber, I. Taminiau, K. Zhernenkov, and D. A. Pushin, "Generation and detection of spin-orbit coupled neutron beams," *Proceedings of the National Academy of Sciences*, vol. 116, no. 41, pp. 20328–20332, 2019.

[6] D. Sarenac, *Structured Beams as Quantum Probes*. PhD thesis, University of Waterloo, 2018.

[7] B. J. Heacock, *Neutron Dynamical Diffraction: Interferometer Improvement and Precision Structure Factor Measurements*. PhD thesis, North Carolina State University, 2019.

[8] H. R. Werner and S, "Neutron Interferometry: Lessons in Experimental Quantum Mechanics," *Measurement Science and Technology*, vol. 12, pp. 355–355, 3 2001.

[9] A. D. Cronin, J. Schmiedmayer, and D. E. Pritchard, "Optics and interferometry with atoms and molecules," *Reviews of Modern Physics*, vol. 81, pp. 1051–1129, 8 2009.

[10] X.-L. Wang, K. An, L. Cai, Z. Feng, S. E. Nagler, C. Daniel, K. J. Rhodes, A. D. Stoica, H. D. Skorpenske, C. Liang, *et al.*, "Visualizing the chemistry and structure dynamics in lithium-ion batteries by in-situ neutron diffraction," *Scientific Reports*, vol. 2, no. 1, p. 747, 2012.

[11] F. Salvemini, F. Grazzi, S. Peetermans, F. Civita, R. Franci, S. Hartmann, E. Lehmann, and M. Zoppi, "Quantitative characterization of japanese ancient swords through energy-resolved neutron imaging," *Journal of Analytical Atomic Spectrometry*, vol. 27, no. 9, pp. 1494–1501, 2012.

[12] H. Isaksson, S. Le Cann, C. Perdikouri, M. J. Turunen, A. Kaestner, M. Tägil, S. A. Hall, and E. Tudisco, "Neutron tomographic imaging of bone-implant interface: comparison with x-ray tomography," *Bone*, vol. 103, pp. 295–301, 2017.

[13] M. Henderson, B. Heacock, M. Bleuel, D. Cory, C. Heikes, M. G. Huber, J. Krzywon, O. Nahman-Levesqué, G. Luke, M. Pula, *et al.*, "Three-dimensional neutron far-field tomography of a bulk skyrmion lattice," *Nature physics*, vol. 19, no. 11, pp. 1617–1623, 2023.

[14] A. A. Michelson and E. W. Morley, "On the relative motion of the earth and the luminiferous ether," *American journal of science*, vol. 3, no. 203, pp. 333–345, 1887.

[15] A. A. Michelson, *Light waves and their uses*, vol. 2. University of Chicago Press, 1903.

[16] H. Maier-Leibnitz and T. Springer, "Ein interferometer für langsame neutronen," *Zeitschrift für Physik*, vol. 167, no. 4, pp. 386–402, 1962.

[17] F. J. Landkammer, "Beugungsversuche mit langsamen neutronen," *Zeitschrift für Physik*, vol. 189, no. 2, pp. 113–137, 1966.

[18] H. Rauch, W. Treimer, and U. Bonse, "Test of a single crystal neutron interferometer," *Physics Letters A*, vol. 47, no. 5, pp. 369–371, 1974.

[19] J. Nsofini, K. Ghofrani, D. Sarenac, D. G. Cory, and D. A. Pushin, "Quantum-information approach to dynamical diffraction theory," *Physical review A*, vol. 94, no. 6, p. 062311, 2016.

[20] J. Nsofini, D. Sarenac, K. Ghofrani, M. G. Huber, M. Arif, D. G. Cory, and D. A. Pushin, "Noise refocusing in a five-blade neutron interferometer," *Journal of applied physics*, vol. 122, no. 5, 2017.

[21] J. Nsofini, D. Sarenac, D. Cory, and D. Pushin, "Coherence optimization in neutron interferometry through defocusing," *Physical review A*, vol. 99, no. 4, p. 043614, 2019.

[22] O. Nahman-Lévesque, D. Sarenac, D. Cory, B. Heacock, M. Huber, and D. Pushin, "Generalizing the quantum information model for dynamic diffraction," *Physical review A*, vol. 105, no. 2, p. 022403, 2022.

[23] O. Nahman-Lévesque, D. Sarenac, O. Lailey, D. G. Cory, M. G. Huber, and D. A. Pushin, "Quantum information approach to the implementation of a neutron cavity," *New Journal of Physics*, vol. 25, no. 7, p. 073016, 2023.

[24] R. Colella, A. W. Overhauser, and S. A. Werner, "Observation of gravitationally induced quantum interference," *Physical Review Letters*, vol. 34, no. 23, p. 1472, 1975.

[25] H. Rauch, A. Zeilinger, G. Badurek, A. Wilfing, W. Bauspiess, and U. Bonse, "Verification of coherent spinor rotation of fermions," *Physics Letters A*, vol. 54, no. 6, pp. 425–427, 1975.

[26] B. Heacock, M. Arif, D. G. Cory, T. Gnaeupel-Herold, R. Haun, M. G. Huber, M. E. Jamer, J. Nsofini, D. A. Pushin, D. Sarenac, *et al.*, "Increased interference fringe visibility from the post-fabrication heat treatment of a perfect crystal silicon neutron interferometer," *Review of Scientific Instruments*, vol. 89, no. 2, 2018.

[27] K. Li, M. Arif, D. G. Cory, R. Haun, B. Heacock, M. G. Huber, J. Nsofini, D. A. Pushin, P. Saggu, D. Sarenac, *et al.*, "Neutron limit on the strongly-coupled chameleon field," *Physical Review D*, vol. 93, no. 6, p. 062001, 2016.

[28] J. Rocha and F. Dahia, "Neutron interferometry and tests of short-range modifications of gravity," *Physical Review D*, vol. 103, no. 12, p. 124014, 2021.

[29] Y. Liu, B. Sowerby, and J. Tickner, "Comparison of neutron and high-energy x-ray dual-beam radiography for air cargo inspection," *Applied Radiation and Isotopes*, vol. 66, no. 4, pp. 463–473, 2008.

[30] C. Glinka, J. Barker, B. Hammouda, S. Krueger, J. Moyer, and W. Orts, "The 30 m small-angle neutron scattering instruments at the national institute of standards and technology," *Applied Crystallography*, vol. 31, no. 3, pp. 430–445, 1998.

[31] D. S. Hussey, M. Abir, J. C. Cook, D. L. Jacobson, J. LaManna, K. Kilaru, B. Ramsey, and B. Khaykovich, "Design of a neutron microscope based on wolter mirrors," *Nuclear Instruments and Methods in Physics Research Section A: Accelerators, Spectrometers, Detectors and Associated Equipment*, vol. 987, p. 164813, 2021.

[32] M. G. Huber, S. F. Hoogerheide, M. Arif, R. W. Haun, F. E. Wietfeldt, T. C. Black, C. B. Shahi, B. Heacock, A. R. Young, I. A. Taminiau, *et al.*, "Overview of neutron interferometry at nist," in *EPJ Web of Conferences*, vol. 219, p. 06001, EDP Sciences, 2019.

[33] M. Huber, B. Heacock, I. Taminiau, D. Cory, D. Sarenac, R. Valdillez, and D. Pushin, "Achieving a near-ideal silicon crystal neutron interferometer using submicrometer fabrication techniques," *Physical Review Research*, vol. 6, no. 4, p. 043079, 2024.

[34] M. Gruber, K. Eder, A. Zeilinger, R. Gähler, and W. Mampe, "A phase-grating interferometer for very cold neutrons," *Physics Letters A*, vol. 140, no. 7-8, pp. 363–367, 1989.

[35] G. van der Zouw, M. Weber, J. Felber, R. Gähler, P. Geltenbort, and A. Zeilinger, "Aharonov–Bohm and gravity experiments with the very-cold-neutron interferometer," *Nuclear Instruments and Methods in Physics Research Section A: Accelerators, Spectrometers, Detectors and Associated Equipment*, vol. 440, pp. 568–574, 2 2000.

[36] H. Miao, A. Panna, A. A. Gomella, E. E. Bennett, S. Znati, L. Chen, and H. Wen, "A universal moiré effect and application in x-ray phase-contrast imaging," *Nature physics*, vol. 12, no. 9, pp. 830–834, 2016.

[37] D. A. Pushin, D. Sarenac, D. S. Hussey, H. Miao, M. Arif, D. G. Cory, M. G. Huber, D. L. Jacobson, J. M. LaManna, J. D. Parker, *et al.*, "Far-field interference of a neutron white beam and the applications to noninvasive phase-contrast imaging," *Physical review A*, vol. 95, no. 4, p. 043637, 2017.

[38] D. Sarenac, D. A. Pushin, M. G. Huber, D. S. Hussey, H. Miao, M. Arif, D. G. Cory, A. D. Cronin, B. Heacock, D. L. Jacobson, *et al.*, "Three phase-grating moiré neutron interferometer for large interferometer area applications," *Physical review letters*, vol. 120, no. 11, p. 113201, 2018.

[39] J. Chadwick, "The existence of a neutron," *Proceedings of the Royal Society of London. Series A, Containing Papers of a Mathematical and Physical Character*, vol. 136, no. 830, pp. 692–708, 1932.

[40] W. Elsasser, "Sur la diffraction des neutrons lents par les substances cristallines," *CR Acad. Sci*, vol. 202, p. 1029, 1936.

[41] H. D. Smyth, "Atomic energy for military purposes," *Reviews of Modern Physics*, vol. 17, no. 4, p. 351, 1945.

[42] L. De Broglie, *Recherches sur la théorie des quanta*. PhD thesis, Migration-université en cours d'affectation, 1924.

[43] V. Sears, "Fundamental aspects of neutron optics," *Physics Reports*, vol. 82, pp. 1–29, 2 1982.

[44] B. Zwiebach, "Quantum physics iii chapter 3: Semiclassical approximation," February 2018.

[45] J. J. Sakurai and J. Napolitano, *Modern quantum mechanics*. Cambridge University Press, 2020.

[46] S. Werner, H. Kaiser, M. Arif, and R. Clothier, "Neutron interference induced by gravity: new results and interpretations," *Physica B+ C*, vol. 151, no. 1-2, pp. 22–35, 1988.

[47] M. Arif, M. S. Dewey, G. Greene, D. Jacobson, and S. Werner, "X-ray determination of the elastic deformation of a perfect crystal neutron interferometer: implications for gravitational phase shift experiments," *Physics Letters A*, vol. 184, no. 2, pp. 154–158, 1994.

[48] B. Heacock, M. Arif, R. Haun, M. G. Huber, D. A. Pushin, and A. R. Young, "Neutron interferometer crystallographic imperfections and gravitationally induced quantum interference measurements," *Physical Review A*, vol. 95, no. 1, p. 013840, 2017.

[49] V. F. Sears, *Neutron Optics: An Introduction to the Theory of Neutron Optical Phenomena and Their Applications*. Oxford University Press, 1989.

[50] L. D. Landau and E. M. Lifshitz, *Course of theoretical physics*. Elsevier, 2013.

[51] R. A. Serway, J. W. Jewett, and V. Peroomian, *Physics for scientists and engineers*, vol. 2. Saunders college publishing Philadelphia, 2000.

[52] C. G. Darwin, "Free motion in the wave mechanics," *Proceedings of the Royal Society of London. Series A, Containing Papers of a Mathematical and Physical Character*, vol. 117, no. 776, pp. 258–293, 1927.

[53] H. Kaiser, S. Werner, and E. George, "Direct measurement of the longitudinal coherence length of a thermal neutron beam," *Physical Review Letters*, vol. 50, no. 8, p. 560, 1983.

[54] R. Clothier, H. Kaiser, S. Werner, H. Rauch, and H. Wölwitsch, "Neutron phase echo," *Physical Review A*, vol. 44, no. 9, p. 5357, 1991.

[55] H. Rauch, H. Wölwitsch, R. Clothier, H. Kaiser, and S. Werner, "Time-of-flight neutron interferometry," *Physical Review A*, vol. 46, no. 1, p. 49, 1992.

[56] D. Jacobson, S. Werner, and H. Rauch, "Spectral modulation and squeezing at high-order neutron interferences," *Physical Review A*, vol. 49, no. 5, p. 3196, 1994.

[57] D. Pushin, M. Arif, M. Huber, and D. Cory, "Measurements of the vertical coherence length in neutron interferometry," *Physical review letters*, vol. 100, no. 25, p. 250404, 2008.

[58] H. Rauch, E. Seidl, D. Tuppinger, D. Petrascheck, and R. Scherm, "Nondispersive sample arrangement in neutron interferometry," *Zeitschrift für Physik B Condensed Matter*, vol. 69, no. 2, pp. 313–317, 1987.

[59] A. G. Wagh, S. Abbas, and W. Treimer, "The plain truth about forming a plane wave of neutrons," *Nuclear Instruments and Methods in Physics Research Section A: Accelerators, Spectrometers, Detectors and Associated Equipment*, vol. 634, no. 1, pp. S41–S45, 2011.

[60] D. Sarenac, D. Cory, J. Nsofini, I. Hincks, P. Miguel, M. Arif, C. W. Clark, M. Huber, and D. Pushin, "Generation of a lattice of spin-orbit beams via coherent averaging," *Physical review letters*, vol. 121, no. 18, p. 183602, 2018.

[61] A. Forbes, M. De Oliveira, and M. R. Dennis, "Structured light," *Nature Photonics*, vol. 15, no. 4, pp. 253–262, 2021.

[62] L. Allen, M. W. Beijersbergen, R. Spreeuw, and J. Woerdman, "Orbital angular momentum of light and the transformation of laguerre-gaussian laser modes," *Physical review A*, vol. 45, no. 11, p. 8185, 1992.

[63] B. J. McMorran, A. Agrawal, I. M. Anderson, A. A. Herzing, H. J. Lezec, J. J. McClelland, and J. Unguris, "Electron vortex beams with high quanta of orbital angular momentum," *science*, vol. 331, no. 6014, pp. 192–195, 2011.

[64] C. W. Clark, R. Barankov, M. G. Huber, M. Arif, D. G. Cory, and D. A. Pushin, "Controlling neutron orbital angular momentum," *Nature*, vol. 525, no. 7570, pp. 504–506, 2015.

[65] H. He, M. E. J. Friese, N. R. Heckenberg, and H. Rubinsztein-Dunlop, "Direct observation of transfer of angular momentum to absorptive particles from a laser beam with a phase singularity," *Phys. Rev. Lett.*, vol. 75, pp. 826–829, Jul 1995.

[66] M. E. J. Friese, J. Enger, H. Rubinsztein-Dunlop, and N. R. Heckenberg, "Optical angular-momentum transfer to trapped absorbing particles," *Phys. Rev. A*, vol. 54, pp. 1593–1596, Aug 1996.

[67] J. Wang, J.-Y. Yang, I. M. Fazal, N. Ahmed, Y. Yan, H. Huang, Y. Ren, Y. Yue, S. Dolinar, M. Tur, and A. E. Willner, "Terabit free-space data transmission employing orbital angular momentum multiplexing," *Nature Photonics*, vol. 6, p. 488, jun 2012.

[68] R. Zhang, L. Li, Z. Zhao, G. Xie, G. Milione, H. Song, P. Liao, C. Liu, H. Song, K. Pang, A. N. Willner, B. Lynn, R. Bock, M. Tur, and A. E. Willner, "Coherent optical wireless communication link employing orbital angular momentum multiplexing in a ballistic and diffusive scattering medium," *Opt. Lett.*, vol. 44, pp. 691–694, Feb 2019.

[69] M. F. Andersen, C. Ryu, P. Clade, V. Natarajan, A. Vaziri, K. Helmerson, and W. D. Phillips, "Quantized rotation of atoms from photons with orbital angular momentum," *Phys. Rev. Lett.*, vol. 97, p. 170406, Oct 2006.

[70] M. Erhard, R. Fickler, M. Krenn, and A. Zeilinger, "Twisted photons: new quantum perspectives in high dimensions," *Light: Science &Amp; Applications*, vol. 7, p. 17146, mar 2018.

[71] U. Bonse and M. Hart, "An x-ray interferometer with bragg case beam splitting and beam recombination," *Zeitschrift für Physik*, vol. 194, no. 1, pp. 1–17, 1966.

[72] J. Cowley and A. Moodie, "Fourier images: I-the point source," *Proceedings of the Physical Society. Section B*, vol. 70, no. 5, p. 486, 1957.

[73] D. Sarenac, G. Gorbet, C. Kapahi, C. W. Clark, D. Cory, H. Ekinci, D. Garrad, M. Henderson, M. Huber, D. Hussey, *et al.*, "Cone beam neutron interferometry: from modeling to applications," *Physical Review Research*, vol. 6, no. 2, p. 023260, 2024.

[74] G. Rosi, F. Sorrentino, L. Cacciapuoti, M. Prevedelli, and G. Tino, "Precision measurement of the newtonian gravitational constant using cold atoms," *Nature*, vol. 510, no. 7506, pp. 518–521, 2014.

[75] D. W. Keith, C. R. Ekstrom, Q. A. Turchette, and D. E. Pritchard, "An interferometer for atoms," *Physical review letters*, vol. 66, no. 21, p. 2693, 1991.

[76] C. R. Ekstrom, J. Schmiedmayer, M. S. Chapman, T. D. Hammond, and D. E. Pritchard, "Measurement of the electric polarizability of sodium with an atom interferometer," *Physical Review A*, vol. 51, no. 5, p. 3883, 1995.

[77] F. Ehlotzky, *Fundamentals of Quantum Optics II*. Springer, 1987.

[78] C. Xue, J.-P. Liu, Q. Li, J.-F. Wu, S.-Q. Yang, Q. Liu, C.-G. Shao, L.-C. Tu, Z.-K. Hu, and J. Luo, "Precision measurement of the Newtonian gravitational constant," *National Science Review*, vol. 7, pp. 1803–1817, 07 2020.

[79] C. V. Boys, "I. On the cavendish experiment," *Proceedings of the Royal Society of London*, vol. 46, pp. 253–268, 12 1890.

[80] P. Mohr, D. Newell, B. Taylor, and E. Tiesinga, "Codata recommended values of the fundamental physical constants: 2022," *arXiv preprint arXiv:2409.03787*, 2024.

[81] G. G. Luther and W. R. Towler, "Redetermination of the newtonian gravitational constant G," *Physical Review Letters*, vol. 48, no. 3, p. 121, 1982.

[82] J. Gundlach, E. Adelberger, B. R. Heckel, and H. Swanson, "New technique for measuring newton's constant g," *Physical Review D*, vol. 54, no. 2, p. R1256, 1996.

[83] U. Kleinevoss, H. Meyer, A. Schumacher, and S. Hartmann, "Absolute measurement of the newtonian force and adetermination of g," *Measurement Science and Technology*, vol. 10, no. 6, p. 492, 1999.

[84] H. V. Parks and J. E. Faller, "Simple pendulum determination of the gravitational constant," *Physical review letters*, vol. 105, no. 11, p. 110801, 2010.

[85] S. Schlamminger, E. Holzschuh, W. Kündig, F. Nolting, R. Pixley, J. Schurr, and U. Straumann, "Measurement of newton's gravitational constant," *Physical Review D—Particles, Fields, Gravitation, and Cosmology*, vol. 74, no. 8, p. 082001, 2006.

[86] M. R. Eskildsen, P. L. Gammel, E. D. Isaacs, C. Detlefs, K. Mortensen, and D. J. Bishop, "Compound refractive optics for the imaging and focusing of low-energy neutrons," *Nature*, vol. 391, pp. 563–566, 2 1998.

[87] H. R. Beguiristain, I. S. Anderson, C. D. Dewhurst, M. A. Piestrup, J. T. Cremer, and R. H. Pantell, "A simple neutron microscope using a compound refractive lens," *Applied Physics Letters*, vol. 81, pp. 4290–4292, 11 2002.

[88] C. K. Gary, "Compound Refractive Lenses for Thermal Neutron Applications," tech. rep., Chicago Operations Office, Argonne, IL (United States), 11 2013.

[89] T. Oku and H. M. Shimizu, "Neutron lens and prism," *Physica B: Condensed Matter*, vol. 283, no. 4, pp. 314–317, 2000.

[90] T. Oku, H. Iwase, T. Shinohara, S. Yamada, K. Hirota, S. Koizumi, J. i. Suzuki, T. Hashimoto, and H. M. Shimizu, "A focusing-geometry small-angle neutron scattering instrument with a magnetic neutron lens," *Applied Crystallography*, vol. 40, no. s1, pp. s408–s413, 2007.

[91] H. M. Shimizu, Y. Suda, T. Oku, H. Nakagawa, H. Kato, T. Kamiyama, C. Otani, H. Sato, T. Wakabayashi, and Y. Kiyanagi, "Measurement of cold neutron-beam focusing effect of a permanent sextupole magnet," *Nuclear Instruments and Methods in Physics Research, Section A: Accelerators, Spectrometers, Detectors and Associated Equipment*, vol. 430, pp. 423–434, 7 1999.

[92] H. M. Shimizu, H. Kato, T. Oku, Y. Suda, Y. Ogawa, H. Iwasa, T. Kamiyama, Y. Kiyanagi, and T. Wakabayashi, "Cold neutron beam control using magnetic field gradient," *Physica B: Condensed Matter*, vol. 241-243, pp. 172–174, 12 1997.

[93] H. M. Shimizu, T. Oku, H. Sato, C. Otani, H. Kato, Y. Suda, H. Nakagawa, T. Kamiyama, Y. Kiyanagi, and T. Wakabayashi, "Magnetic neutron lens," *Physica B: Condensed Matter*, vol. 276-278, pp. 63–64, 3 2000.

[94] H. M. Shimizu, "Development of neutron optical devices," *Applied Physics A: Materials Science and Processing*, vol. 74, no. SUPPL.I, pp. 123–129, 2002.

[95] J. T. Cremer Jr, H. Filter, J. Klepp, P. Geltenbort, C. Dewhurst, T. Oda, and R. H. Pantell, "Focusing and imaging of cold neutrons with a permanent magnetic lens," *Review of Scientific Instruments*, vol. 91, no. 1, p. 013704, 2020.

[96] K. C. Littrell, S. G. Te Velthuis, G. P. Felcher, S. Park, B. J. Kirby, and M. R. Fitzsimmons, "Magnetic compound refractive lens for focusing and polarizing cold neutron beams," *Review of Scientific Instruments*, vol. 78, p. 035101, 3 2007.

[97] S. S. Arzumanov, L. I. Govor, V. I. Morozov, Y. N. Panin, and A. N. Strepetov, "A convergent neutron lens based on glass capillaries," *Instruments and Experimental Techniques*, vol. 59, pp. 650–652, 9 2016.

[98] M. A. Kumakhov and V. A. Sharov, "A neutron lens," *Nature*, vol. 357, no. 6377, pp. 390–391, 1992.

[99] H. Wu, B. Khaykovich, X. Wang, and D. S. Hussey, "Wolter Mirrors for Neutron Imaging," in *Physics Procedia*, vol. 88, pp. 184–189, Elsevier B.V., 1 2017.

[100] T. Oku, S. Morita, S. Moriyasu, Y. Yamagata, H. Ohmori, Y. Takizawa, H. M. Shimizu, T. Hirota, Y. Kiyanagi, T. Ino, M. Furusaka, and J. Suzuki, "Development of a Fresnel lens for cold neutrons based on neutron refractive optics," *Nuclear Instruments and Methods in Physics Research, Section A: Accelerators, Spectrometers, Detectors and Associated Equipment*, vol. 462, pp. 435–441, 4 2001.

[101] D. Sarenac, J. Nsofini, I. Hincks, M. Arif, C. W. Clark, D. Cory, M. Huber, and D. Pushin, "Methods for preparation and detection of neutron spin-orbit states," *New journal of physics*, vol. 20, no. 10, p. 103012, 2018.

[102] J. Nsofini, D. Sarenac, C. J. Wood, D. G. Cory, M. Arif, C. W. Clark, M. G. Huber, and D. A. Pushin, "Spin-orbit states of neutron wave packets," *Physical Review A*, vol. 94, no. 1, p. 013605, 2016.

[103] D. Sarenac, M. E. Henderson, H. Ekinci, C. W. Clark, D. G. Cory, L. DeBeer-Schmitt, M. G. Huber, C. Kapahi, and D. A. Pushin, "Experimental realization of neutron helical waves," *Science Advances*, vol. 8, no. 46, p. eadd2002, 2022.

[104] N. Kardjilov, I. Manke, M. Strobl, A. Hilger, W. Treimer, M. Meissner, T. Krist, and J. Banhart, "Three-dimensional imaging of magnetic fields with polarized neutrons," *Nature Physics*, vol. 4, pp. 399–403, 3 2008.

[105] E. Jericha, R. Szeywerth, H. Leeb, and G. Badurek, "Reconstruction techniques for tensorial neutron tomography," *Physica B: Condensed Matter*, vol. 397, pp. 159–161, 7 2007.

[106] M. Kageyama, S. Tasaki, M. Hino, T. Ebisawa, D. Yamazaki, H. Hayashida, and Y. Abe, "Development of neutron spin phase contrast imaging," *Physica B: Condensed Matter*, vol. 404, pp. 2615–2619, 9 2009.

[107] D. A. Pushin, M. G. Huber, M. Arif, C. B. Shahi, J. Nsofini, C. J. Wood, D. Sarenac, and D. G. Cory, "Neutron Interferometry at the National Institute of Standards and Technology," *Advances in High Energy Physics*, vol. 2015, pp. 1–7, 3 2015.

[108] D. Sarenac, M. G. Huber, B. Heacock, M. Arif, C. W. Clark, D. G. Cory, C. B. Shahi, and D. A. Pushin, "Holography with a neutron interferometer," *Optics express*, vol. 24, no. 20, pp. 22528–22535, 2016.

[109] H. Lemmel, P. Brax, A. N. Ivanov, T. Jenke, G. Pignol, M. Pitschmann, T. Potocar, M. Wellenzohn, M. Zawisky, and H. Abele, "Neutron interferometry constrains dark energy chameleon fields," *Physics Letters, Section B: Nuclear, Elementary Particle and High-Energy Physics*, vol. 743, pp. 310–314, 4 2015.

[110] Y. Hasegawa, R. Loidl, G. Badurek, M. Baron, and H. Rauch, "Violation of a Bell-like inequality in single-neutron interferometry," *Nature*, vol. 425, pp. 45–48, 9 2003.

[111] H. Bartosik, J. Klepp, C. Schmitzer, S. Sponar, A. Cabello, H. Rauch, and Y. Hasegawa, "Experimental test of quantum contextuality in neutron interferometry," *Physical Review Letters*, vol. 103, p. 040403, 8 2009.

[112] B. Heacock, D. Sarenac, D. G. Cory, M. G. Huber, D. S. Hussey, C. Kapahi, H. Miao, H. Wen, and D. A. Pushin, "Angular alignment and fidelity of neutron phase-gratings for improved interferometer fringe visibility," *AIP Advances*, vol. 9, p. 085115, 8 2019.

[113] F. Pfeiffer, C. Grünzweig, O. Bunk, G. Frei, E. Lehmann, and C. David, "Neutron phase imaging and tomography," *Physical review letters*, vol. 96, no. 21, p. 215505, 2006.

[114] H. Rauch, W. Treimer, and U. Bonse, "Test of a single crystal neutron interferometer," *Physics Letters A*, vol. 47, pp. 369–371, 4 1974.

[115] H. Rauch, A. Zeilinger, G. Badurek, A. Wilfing, W. Bauspiess, and U. Bonse, "Verification of coherent spinor rotation of fermions," *Physics Letters A*, vol. 54, pp. 425–427, 10 1975.

[116] T. Denkmayr, H. Geppert, S. Sponar, H. Lemmel, A. Matzkin, J. Tollaksen, and Y. Hasegawa, "Observation of a quantum cheshire cat in a matter-wave interferometer experiment," *Nature communications*, vol. 5, no. 1, pp. 1–7, 2014.

[117] M. Arif, D. E. Brown, G. L. Greene, R. Clothier, and K. Littrell, "Multistage position-stabilized vibration isolation system for neutron interferometry," in *Vibration Monitoring and Control*, vol. 2264, pp. 20–26, International Society for Optics and Photonics, 1994.

[118] P. Saggu, T. Mineeva, M. Arif, D. G. Cory, R. Haun, B. Heacock, M. G. Huber, K. Li, J. Nsofini, D. Sarenac, *et al.*, "Decoupling of a neutron interferometer from temperature gradients," *Review of Scientific Instruments*, vol. 87, no. 12, p. 123507, 2016.

[119] C. Shahi, M. Arif, D. Cory, T. Mineeva, J. Nsofini, D. Sarenac, C. Williams, M. Huber, and D. Pushin, "A new polarized neutron interferometry facility at the ncnr," *Nuclear Instruments and Methods in Physics Research Section A: Accelerators, Spectrometers, Detectors and Associated Equipment*, vol. 813, pp. 111–122, 2016.

[120] M. Zawisky, J. Springer, R. Farthofer, and U. Kuetgens, "A large-area perfect crystal neutron interferometer optimized for coherent beam-deflection experiments: Preparation and performance," *Nuclear Instruments and Methods in Physics Research Section A: Accelerators, Spectrometers, Detectors and Associated Equipment*, vol. 612, no. 2, pp. 338–344, 2010.

[121] J. G. Barker, C. J. Glinka, J. J. Moyer, M. H. Kim, A. R. Drews, and M. Agamalian, "Design and performance of a thermal-neutron double-crystal diffractometer for USANS at NIST," *Journal of Applied Crystallography*, vol. 38, pp. 1004–1011, 12 2005.

[122] NIST. Certain trade names and company products are mentioned in the text or identified in an illustration in order to adequately specify the experimental procedure and equipment used. In no case does such identification imply recommendation or

endorsement by the National Institute of Standards and Technology, nor does it imply that the products are necessarily the best available for the purpose.

[123] A. G. Wagh and V. C. Rakhecha, "Geometric formula for prism deflection," *Pramana*, vol. 63, no. 2, pp. 381–385, 2004.

[124] J. Schulz, F. Ott, C. Hülsen, and T. Krist, "Neutron energy analysis by silicon prisms," *Nuclear Instruments and Methods in Physics Research Section A: Accelerators, Spectrometers, Detectors and Associated Equipment*, vol. 729, pp. 334–337, 2013.

[125] T. Shinohara, K. Hirota, T. Adachi, K. Ikeda, H. M. Shimizu, J.-i. Suzuki, and T. Oku, "Thermal neutron refraction by material prism," *Physica B: Condensed Matter*, vol. 385, pp. 1232–1235, 2006.

[126] A. J. Jackson and K. Kanaki, "Ess construction proposal loki—a broad-band sans instrument," *ESS: Lund, Sweden*, 2013.

[127] R. Cubitt, J. Segura Ruiz, and W. Jark, "Rainbows: refractive analysis of the incoming neutron beam over the white spectrum. a new fast neutron reflectometry technique exploiting a focusing prism," *Applied Crystallography*, vol. 51, no. 2, pp. 257–263, 2018.

[128] R. Cubitt, H. Shimizu, K. Ikeda, and N. Torikai, "Refraction as a means of encoding wavelength for neutron reflectometry," *Nuclear Instruments and Methods in Physics Research Section A: Accelerators, Spectrometers, Detectors and Associated Equipment*, vol. 558, no. 2, pp. 547–550, 2006.

[129] W. Soller, "A new precision x-ray spectrometer," *Physical Review*, vol. 24, no. 2, p. 158, 1924.

[130] SwissNeutronics, "Neutron collimator catalogue."

[131] D. Sarenac, C. Kapahi, D. A. Pushin, and D. G. Cory, "Collimator system." U.S. Patent, Dec 2021. US Patent 11,199,512 B2.

[132] A. R. Cameron, S. W. Cheng, S. Schwarz, C. Kapahi, D. Sarenac, M. Grabowecky, D. G. Cory, T. Jennewein, D. A. Pushin, and K. J. Resch, "Remote state preparation of single-photon orbital-angular-momentum lattices," *Physical review A*, vol. 104, no. 5, p. L051701, 2021.

[133] S. Schwarz, C. Kapahi, R. Xu, A. R. Cameron, D. Sarenac, J.-P. W. MacLean, K. B. Kuntz, D. G. Cory, T. Jennewein, K. J. Resch, *et al.*, "Talbot effect of orbital angular momentum lattices with single photons," *Physical Review A*, vol. 101, no. 4, p. 043815, 2020.

[134] S. Mamani, L. Shi, T. Ahmed, R. Karnik, A. Rodríguez-Contreras, D. Nolan, and R. Alfano, "Transmission of classically entangled beams through mouse brain tissue," *Journal of Biophotonics*, vol. 11, no. 12, p. e201800096, 2018.

[135] Y. Shen, I. Nape, X. Yang, X. Fu, M. Gong, D. Naidoo, and A. Forbes, "Creation and control of high-dimensional multi-partite classically entangled light," *Light: Science & Applications*, vol. 10, no. 1, pp. 1–10, 2021.

[136] Y. Shen, X. Wang, Z. Xie, C. Min, X. Fu, Q. Liu, M. Gong, and X. Yuan, "Optical vortices 30 years on: Oam manipulation from topological charge to multiple singularities," *Light: Science & Applications*, vol. 8, no. 1, p. 90, 2019.

[137] P. Kaye, R. Laflamme, and M. Mosca, *An introduction to quantum computing*. OUP Oxford, 2006.

[138] Y. Wang, Y. Chen, Y. Zhang, H. Chen, and S. Yu, "Generalised hermite–gaussian beams and mode transformations," *Journal of Optics*, vol. 18, no. 5, p. 055001, 2016.

[139] A. Holleczek, A. Aiello, C. Gabriel, C. Marquardt, and G. Leuchs, "Classical and quantum properties of cylindrically polarized states of light," *Optics Express*, vol. 19, p. 9714, 5 2011.

[140] M. W. Beijersbergen, L. Allen, H. E. van der Veen, and J. P. Woerdman, "Astigmatic laser mode converters and transfer of orbital angular momentum," *Optics Communications*, vol. 96, pp. 123–132, 2 1993.

[141] L. J. Pereira, A. Z. Khoury, and K. Dechoum, "Quantum and classical separability of spin-orbit laser modes," *Physical Review A - Atomic, Molecular, and Optical Physics*, vol. 90, 11 2014.

[142] C. V. Borges, M. Hor-Meyll, J. A. Huguenin, and A. Z. Khoury, "Bell-like inequality for the spin-orbit separability of a laser beam," *Physical Review A - Atomic, Molecular, and Optical Physics*, vol. 82, p. 033833, 9 2010.

[143] E. G. Rieffel and W. H. Polak, *Quantum computing: A gentle introduction*. MIT press, 2011.

[144] D. J. Griffiths and D. F. Schroeter, *Introduction to quantum mechanics*. Cambridge university press, 2018.

[145] A. Einstein, B. Podolsky, and N. Rosen, "Can quantum-mechanical description of physical reality be considered complete?," *Physical review*, vol. 47, no. 10, p. 777, 1935.

[146] R. J. Spreeuw, "A classical analogy of entanglement," *Foundations of physics*, vol. 28, no. 3, pp. 361–374, 1998.

[147] E. Karimi and R. W. Boyd, "Classical entanglement?," *Science*, vol. 350, no. 6265, pp. 1172–1173, 2015.

[148] S. J. van Enk, "Single-particle entanglement," *Physical Review A—Atomic, Molecular, and Optical Physics*, vol. 72, no. 6, p. 064306, 2005.

[149] M. Padgett and R. Bowman, "Tweezers with a twist," *Nature Photonics*, vol. 5, no. 6, pp. 343–348, 2011.

[150] R. Gozali, T.-A. Nguyen, E. Bendau, and R. R. Alfano, "Compact oam microscope for edge enhancement of biomedical and object samples," *Review of Scientific Instruments*, vol. 88, no. 9, 2017.

[151] D. Cozzolino, B. Da Lio, D. Bacco, and L. K. Oxenløwe, "High-dimensional quantum communication: benefits, progress, and future challenges," *Advanced Quantum Technologies*, vol. 2, no. 12, p. 1900038, 2019.

[152] D. Sarenac, C. Kapahi, D. G. Cory, and D. A. Pushin, "Preparing a structured optical beam for human observation." U.S. Patent, Jan 2023. US Patent 11,564,562 B2.

[153] W. Haidinger, "Ueber das directe erkennen des polarisirten lichts und der lage der polarisationsebene," *Annalen der Physik*, vol. 139, no. 9, pp. 29–39, 1844.

[154] B. FRIEDMAN, "Observations on entoptic phenomena," *Archives of Ophthalmology*, vol. 28, no. 2, pp. 285–312, 1942.

[155] J. C. Maxwell, *The Scientific Letters and Papers of James Clerk Maxwell: Volume 1, 1846-1862*, vol. 1. CUP Archive, 1990.

[156] E. J. Gording, "A report on haidinger brushes," *Optometry and Vision Science*, vol. 27, no. 12, pp. 604–610, 1950.

[157] B. S. PRIESTLEY and K. FOREE, "Clinical significance of some ome entoptic ph enomena," *AMA Archives of Ophthalmology*, vol. 53, no. 3, pp. 390–397, 1955.

[158] M. Goldschmidt, "A new test for function of the macula lutea," *Archives of ophthalmology*, vol. 44, no. 1, pp. 129–135, 1950.

[159] H. W. Forster, "The clinical use of the haidinger's brushes phenomenon," *American journal of ophthalmology*, vol. 38, no. 5, pp. 661–665, 1954.

[160] S. Coren, "The use of haidinger's brushes in the study of stabilized retinal images," *Behavior Research Methods & Instrumentation*, vol. 3, no. 6, pp. 295–297, 1971.

[161] E. Cohen, H. Larocque, F. Bouchard, F. Nejadsattari, Y. Gefen, and E. Karimi, "Geometric phase from aharonov–bohm to pancharatnam–berry and beyond," *Nature Reviews Physics*, vol. 1, no. 7, pp. 437–449, 2019.

[162] Y. Aharonov and D. Bohm, "Significance of electromagnetic potentials in the quantum theory," *Physical Review*, vol. 115, no. 3, p. 485, 1959.

[163] S. Pancharatnam, "Generalized theory of interference, and its applications," in *Proceedings of the Indian Academy of Sciences-Section A*, vol. 44, pp. 247–262, Springer, 1956.

[164] M. V. Berry, "The adiabatic phase and pancharatnam's phase for polarized light," *Journal of Modern Optics*, vol. 34, no. 11, pp. 1401–1407, 1987.

[165] F. Wilczek and A. Shapere, *Geometric phases in physics*, vol. 5. World Scientific, 1989.

[166] M. Berry *et al.*, "Anticipations of the geometric phase," *Physics Today*, vol. 43, no. 12, pp. 34–40, 1990.

[167] A. Bachtold, C. Strunk, J.-P. Salvetat, J.-M. Bonard, L. Forró, T. Nussbaumer, and C. Schönenberger, "Aharonov–bohm oscillations in carbon nanotubes," *Nature*, vol. 397, no. 6721, pp. 673–675, 1999.

[168] A. Noguchi, Y. Shikano, K. Toyoda, and S. Urabe, "Aharonov–bohm effect in the tunnelling of a quantum rotor in a linear paul trap," *Nature Communications*, vol. 5, no. 1, pp. 1–6, 2014.

[169] G. Biener, A. Niv, V. Kleiner, and E. Hasman, "Formation of helical beams by use of pancharatnam–berry phase optical elements," *Optics Letters*, vol. 27, no. 21, pp. 1875–1877, 2002.

[170] E. Hasman, V. Kleiner, G. Biener, and A. Niv, "Polarization dependent focusing lens by use of quantized pancharatnam–berry phase diffractive optics," *Applied Physics Letters*, vol. 82, no. 3, pp. 328–330, 2003.

[171] Z. Bomzon, G. Biener, V. Kleiner, and E. Hasman, "Space-variant pancharatnam–berry phase optical elements with computer-generated subwavelength gratings," *Optics Letters*, vol. 27, no. 13, pp. 1141–1143, 2002.

[172] L. Marrucci, C. Manzo, and D. Paparo, "Optical spin-to-orbital angular momentum conversion in inhomogeneous anisotropic media," *Physical review letters*, vol. 96, no. 16, p. 163905, 2006.

[173] L. Allen, M. W. Beijersbergen, R. J. C. Spreeuw, and J. P. Woerdman, "Orbital angular momentum of light and the transformation of laguerre-gaussian laser modes," *Phys. Rev. A*, vol. 45, pp. 8185–8189, Jun 1992.

[174] T. Konrad and A. Forbes, "Quantum mechanics and classical light," *Contemporary Physics*, vol. 60, pp. 1–22, 1 2019.

[175] M. McLaren, T. Konrad, and A. Forbes, "Measuring the nonseparability of vector vortex beams," *Physical Review A*, vol. 92, no. 2, p. 023833, 2015.

[176] Q. Zhan, "Cylindrical vector beams: from mathematical concepts to applications," *Advances in Optics and Photonics*, vol. 1, no. 1, pp. 1–57, 2009.

[177] F. Cardano, E. Karimi, S. Slussarenko, L. Marrucci, C. de Lisio, and E. Santamato, "Polarization pattern of vector vortex beams generated by q-plates with different topological charges," *Applied optics*, vol. 51, no. 10, pp. C1–C6, 2012.

[178] E. J. Galvez, S. Khadka, W. H. Schubert, and S. Nomoto, "Poincaré-beam patterns produced by nonseparable superpositions of laguerre–gauss and polarization modes of light," *Applied optics*, vol. 51, no. 15, pp. 2925–2934, 2012.

[179] C. Rosales-Guzmán, B. Ndagano, and A. Forbes, "A review of complex vector light fields and their applications," *Journal of Optics*, vol. 20, no. 12, p. 123001, 2018.

[180] X.-L. Wang, J. Ding, W.-J. Ni, C.-S. Guo, and H.-T. Wang, "Generation of arbitrary vector beams with a spatial light modulator and a common path interferometric arrangement," *Optics Letters*, vol. 32, no. 24, pp. 3549–3551, 2007.

[181] H. Chen, J. Hao, B.-F. Zhang, J. Xu, J. Ding, and H.-T. Wang, "Generation of vector beam with space-variant distribution of both polarization and phase," *Optics Letters*, vol. 36, no. 16, pp. 3179–3181, 2011.

[182] Z. Bomzon, V. Kleiner, and E. Hasman, "Pancharatnam–berry phase in space-variant polarization-state manipulations with subwavelength gratings," *Optics Letters*, vol. 26, no. 18, pp. 1424–1426, 2001.

[183] A. Forbes, "Controlling light's helicity at the source: orbital angular momentum states from lasers," *Philosophical Transactions of the Royal Society A: Mathematical, Physical and Engineering Sciences*, vol. 375, no. 2087, p. 20150436, 2017.

[184] R. Oron, S. Blit, N. Davidson, A. A. Friesem, Z. Bomzon, and E. Hasman, "The formation of laser beams with pure azimuthal or radial polarization," *Applied Physics Letters*, vol. 77, no. 21, pp. 3322–3324, 2000.

[185] H. Rubinsztein-Dunlop, A. Forbes, M. Berry, M. Dennis, D. L. Andrews, M. Mansuripur, C. Denz, C. Alpmann, P. Banzer, T. Bauer, *et al.*, "Roadmap on structured light," *Journal of Optics*, vol. 19, no. 1, p. 013001, 2016.

[186] G. Milione, M. P. Lavery, H. Huang, Y. Ren, G. Xie, T. A. Nguyen, E. Karimi, L. Marrucci, D. A. Nolan, R. R. Alfano, *et al.*, "4× 20 gbit/s mode division multiplexing over free space using vector modes and a q-plate mode (de) multiplexer," *Optics letters*, vol. 40, no. 9, pp. 1980–1983, 2015.

[187] L. Marrucci, E. Karimi, S. Slussarenko, B. Piccirillo, E. Santamato, E. Nagali, and F. Sciarrino, "Spin-to-orbital conversion of the angular momentum of light and its classical and quantum applications," *Journal of Optics*, vol. 13, no. 6, p. 064001, 2011.

[188] G. Arora, S. Deepa, S. N. Khan, and P. Senthilkumaran, "Detection of degenerate stokes index states," *Scientific Reports*, vol. 10, no. 1, pp. 1–10, 2020.

[189] O. V. Angelsky, I. I. Mokhun, A. I. Mokhun, and M. S. Soskin, "Interferometric methods in diagnostics of polarization singularities," *Physical Review E*, vol. 65, no. 3, p. 036602, 2002.

[190] T. Giordani, A. Suprano, E. Polino, F. Acanfora, L. Innocenti, A. Ferraro, M. Paternostro, N. Spagnolo, and F. Sciarrino, "Machine learning-based classification of vector vortex beams," *Physical Review Letters*, vol. 124, no. 16, p. 160401, 2020.

[191] J. N. Tinsley, M. I. Molodtsov, R. Prevedel, D. Wartmann, J. Espigulé-Pons, M. Lauwers, and A. Vaziri, "Direct detection of a single photon by humans," *Nature communications*, vol. 7, p. 12172, 2016.

[192] M. Loulakis, G. Blatsios, C. Vrettou, and I. Kominis, "Quantum biometrics with retinal photon counting," *Physical Review Applied*, vol. 8, no. 4, p. 044012, 2017.

[193] N. Sim, M. F. Cheng, D. Bessarab, C. M. Jones, and L. A. Krivitsky, "Measurement of photon statistics with live photoreceptor cells," *Physical review letters*, vol. 109, no. 11, p. 113601, 2012.

[194] A. Dodel, A. Mayinda, E. Oudot, A. Martin, P. Sekatski, J.-D. Bancal, and N. Sangouard, "Proposal for witnessing non-classical light with the human eye," *Quantum*, vol. 1, p. 7, 2017.

[195] A. Margaritakis, G. Anyfantaki, K. Mouloudakis, A. Gratsea, and I. Kominis, "Spatially selective and quantum-statistics-limited light stimulus for retina biometrics and pupillometry," *Applied Physics B-Lasers And Optics*, vol. 126, no. 6, 2020.

[196] G. P. Misson, B. H. Timmerman, and P. J. Bryanston-Cross, "Human perception of visual stimuli modulated by direction of linear polarization," *Vision research*, vol. 115, pp. 48–57, 2015.

[197] G. P. Misson and S. J. Anderson, "The spectral, spatial and contrast sensitivity of human polarization pattern perception," *Scientific reports*, vol. 7, no. 1, p. 16571, 2017.

[198] G. P. Misson, S. E. Temple, and S. J. Anderson, "Computational simulation of human perception of spatially dependent patterns modulated by degree and angle of linear polarization," *JOSA A*, vol. 36, no. 4, pp. B65–B70, 2019.

[199] G. Horváth, G. Horváth, and D. Varju, *Polarized light in animal vision: polarization patterns in nature*. Springer Science & Business Media, 2004.

[200] S. E. Temple, J. E. McGregor, C. Miles, L. Graham, J. Miller, J. Buck, N. E. Scott-Samuel, and N. W. Roberts, "Perceiving polarization with the naked eye: characterization of human polarization sensitivity," *Proceedings of the Royal Society B: Biological Sciences*, vol. 282, no. 1811, p. 20150338, 2015.

[201] R. A. Bone, "The role of the macular pigment in the detection of polarized light," *Vision research*, vol. 20, no. 3, pp. 213–220, 1980.

[202] M. Berry, "Optical vortices evolving from helicoidal integer and fractional phase steps," *Journal of Optics A: Pure and Applied Optics*, vol. 6, no. 2, p. 259, 2004.

[203] A. Furukawa, N. Ohse, Y. Sato, D. Imanishi, K. Wakabayashi, S. Ito, K. Tamamura, and S. Hirata, "Effective speckle reduction in laser projection displays," in *Emerging Liquid Crystal Technologies III* (L.-C. Chien, ed.), vol. 6911, pp. 183 – 189, International Society for Optics and Photonics, SPIE, 2008.

[204] B. Schaefer, E. Collett, R. Smyth, D. Barrett, and B. Fraher, "Measuring the stokes polarization parameters," *American Journal of Physics*, vol. 75, no. 2, pp. 163–168, 2007.

[205] I. C. on Non-Ionizing Radiation Protection *et al.*, "Revision of guidelines on limits of exposure to laser radiation of wavelengths between 400 nm and 1.4 μm," *Health Phys*, vol. 79, no. 4, pp. 431–440, 2000.

[206] T. D. Wickens, *Elementary signal detection theory*. Oxford University Press, USA, 2002.

[207] H. De Vries, A. Spoor, and R. Jielof, "Properties of the eye with respect to polarized light," *Physica*, vol. 19, no. 1-12, pp. 419–432, 1953.

[208] P. Liebman, W. Jagger, M. Kaplan, and F. Bargoot, "Membrane structure changes in rod outer segments associated with rhodopsin bleaching," *Nature*, vol. 251, no. 5470, pp. 31–36, 1974.

[209] B. Hochheimer and H. A. Kues, "Retinal polarization effects," *Applied optics*, vol. 21, no. 21, pp. 3811–3818, 1982.

[210] Y. Shen, Z. Wang, X. Fu, D. Naidoo, and A. Forbes, "Su (2) poincaré sphere: A generalized representation for multidimensional structured light," *Physical Review A*, vol. 102, no. 3, p. 031501, 2020.

[211] E. Naylor and A. Stanworth, "The measurement and clinical significance of the haidinger effect.," *Transactions. Ophthalmological Society of the United Kingdom*, vol. 75, p. 67, 1955.

[212] P. L. Müller, S. Müller, M. Gliem, K. Küpper, F. G. Holz, W. M. Harmening, and P. C. Issa, "Perception of haidinger brushes in macular disease depends on macular pigment density and visual acuity," *Investigative ophthalmology & visual science*, vol. 57, no. 3, pp. 1448–1456, 2016.

[213] J. Harris, V. Grillo, E. Mafakheri, G. C. Gazzadi, S. Frabboni, R. W. Boyd, and E. Karimi, "Structured quantum waves," *Nature Physics*, vol. 11, no. 8, pp. 629–634, 2015.

[214] V. Garces-Chavez, D. McGloin, H. Melville, W. Sibbett, and K. Dholakia, "Simultaneous micromanipulation in multiple planes using a self-reconstructing light beam," *Nature*, vol. 419, no. 6903, pp. 145–147, 2002.

[215] G. Siviloglou, J. Broky, A. Dogariu, and D. Christodoulides, "Observation of accelerating airy beams," *Physical Review Letters*, vol. 99, no. 21, p. 213901, 2007.

[216] S. M. Barnett, M. Babiker, and M. J. Padgett, "Optical orbital angular momentum," *Philosophical Transactions of the Royal Society A*, vol. 375, no. 2087, 2017.

[217] G. Molina-Terriza, J. P. Torres, and L. Torner, "Twisted photons," *Nature Physics*, vol. 3, no. 5, pp. 305–310, 2007.

[218] S. Schwarz, C. Kapahi, R. Xu, A. R. Cameron, D. Sarenac, J.-P. W. MacLean, K. B. Kuntz, D. G. Cory, T. Jennewein, K. J. Resch, *et al.*, "Talbot effect of orbital angular momentum lattices with single photons," *arXiv preprint arXiv:1908.01016*, 2019.

[219] D. A. VanNasdale, A. E. Elsner, A. Weber, M. Miura, and B. P. Haggerty, "Determination of foveal location using scanning laser polarimetry," *Journal of vision*, vol. 9, no. 3, pp. 21–21, 2009.

[220] W. A. Shurcliff, "Haidinger's brushes and circularly polarized light," *JOSA*, vol. 45, no. 5, pp. 399–399, 1955.

[221] G. Horváth, P. Takács, B. Kretzer, S. Szilasi, D. Száz, A. Farkas, and A. Barta, "Celestial polarization patterns sufficient for viking navigation with the naked eye: detectability of haidinger's brushes on the sky versus meteorological conditions," *Royal Society Open Science*, vol. 4, no. 2, p. 160688, 2017.

[222] G. P. Misson, "A mueller matrix model of haidinger's brushes," *Ophthalmic and Physiological Optics*, vol. 23, no. 5, pp. 441–447, 2003.

[223] M. Rothmayer, W. Dultz, E. Frins, Q. Zhan, D. Tierney, and H. Schmitzer, "Nonlinearity in the rotational dynamics of haidinger's brushes," *Applied optics*, vol. 46, no. 29, pp. 7244–7251, 2007.

[224] G. P. Misson, S. E. Temple, and S. J. Anderson, "Computational simulation of haidinger's brushes," *JOSA A*, vol. 35, no. 6, pp. 946–952, 2018.

[225] J. Maxwell, "Manuscript on experiments on the cause of haidinger's brushes," *The Scientific Letters and Papers of James Clerk Maxwell*, pp. 199–204, 1850.

[226] H. Von Helmholtz, "Treatise on physiological optics (1867)," *Optical Society of America, Rochester, New York*, 1925.

[227] L. J. Bour, "Polarized light and the eye," *Visual Optics and Instrumentation*, vol. 1, pp. 310–325, 1991.

[228] R. W. Knighton and X.-R. Huang, "Linear birefringence of the central human cornea," *Investigative ophthalmology & visual science*, vol. 43, no. 1, pp. 82–86, 2002.

[229] M. Beijersbergen, R. Coerwinkel, M. Kristensen, and J. Woerdman, "Helical-wavefront laser beams produced with a spiral phaseplate," *Optics Communications*, vol. 112, no. 5-6, pp. 321–327, 1994.

[230] P. S. Bernstein, B. Li, P. P. Vachali, A. Gorusupudi, R. Shyam, B. S. Henriksen, and J. M. Nolan, "Lutein, zeaxanthin, and meso-zeaxanthin: The basic and clinical science underlying carotenoid-based nutritional interventions against ocular disease," *Progress in retinal and eye research*, vol. 50, pp. 34–66, 2016.

[231] W. Haidinger, "Beobachtung der lichtpolarisationsbüschel im geradlinig polarisirten lichte," *Annalen der Physik*, vol. 144, no. 5, pp. 73–87, 1846.

[232] H. von Helmholtz, *Treatise on physiological optics*, vol. 3. Courier Corporation, 2013.

[233] Q. Wang, P. J. Bryanston-Cross, Y. Li, and Z. Liu, "Mathematical and experimental description of spatiotemporal frequency sensitivity for human polarization perception," *Optik*, vol. 251, p. 168376, 2022.

[234] Q. Wang, P. Bryanston-Cross, Y. Li, and Z. Liu, "Mathematical Modeling and Experimental Verification of Aging Human Eyes Polarization Sensitivity," *Journal of the Optical Society of America A*, 12 2022.

[235] G. P. Misson, S. E. Temple, and S. J. Anderson, "Polarization perception in humans: on the origin of and relationship between maxwell's spot and haidinger's brushes," *Scientific Reports*, vol. 10, no. 1, pp. 1–10, 2020.

[236] R. P. O'Shea, G. P. Misson, and S. E. Temple, "Seeing polarization of light with the naked eye," *Current Biology*, vol. 31, no. 4, pp. R178–R179, 2021.

[237] R. M. W. W. Tseng, Y.-C. Tham, T. H. Rim, and C.-Y. Cheng, "Emergence of non-artificial intelligence digital health innovations in ophthalmology: A systematic review," *Clinical & Experimental Ophthalmology*, vol. 49, no. 7, pp. 741–756, 2021.

[238] J. Mottes, D. Ortolan, and G. Ruffato, "Haidinger's brushes: Psychophysical analysis of an entoptic phenomenon," *Vision Research*, vol. 199, p. 108076, 2022.

[239] D. C. Neely, K. J. Bray, C. E. Huisingh, M. E. Clark, G. McGwin, and C. Owsley, "Prevalence of undiagnosed age-related macular degeneration in primary eye care," *JAMA ophthalmology*, vol. 135, no. 6, pp. 570–575, 2017.

[240] K. Y. Bliokh, E. Karimi, M. J. Padgett, M. A. Alonso, M. R. Dennis, A. Dudley, A. Forbes, S. Zahedpour, S. W. Hancock, H. M. Milchberg, *et al.*, "Roadmap on structured waves," *Journal of Optics*, vol. 25, no. 10, p. 103001, 2023.

[241] J. Chen, C. Wan, and Q. Zhan, "Engineering photonic angular momentum with structured light: a review," *Advanced Photonics*, vol. 3, no. 6, pp. 064001–064001, 2021.

[242] A. Mair, A. Vaziri, G. Weihs, and A. Zeilinger, "Entanglement of the orbital angular momentum states of photons," *Nature*, vol. 412, no. 6844, pp. 313–316, 2001.

[243] W. Brullot, M. K. Vanbel, T. Swusten, and T. Verbiest, "Resolving enantiomers using the optical angular momentum of twisted light," *Science advances*, vol. 2, no. 3, p. e1501349, 2016.

[244] N. Simpson, K. Dholakia, L. Allen, and M. Padgett, "Mechanical equivalence of spin and orbital angular momentum of light: an optical spanner," *Optics letters*, vol. 22, no. 1, pp. 52–54, 1997.

[245] N. Biton, J. Kupferman, and S. Arnon, "Oam light propagation through tissue," *Scientific Reports*, vol. 11, no. 1, pp. 1–9, 2021.

[246] L. Gassab, A. Pedram, and Ö. E. Müstecaphoğlu, "Conditions on detecting three-photon entanglement in psychophysical experiments," *arXiv preprint arXiv:2303.07446*, 2023.

[247] I. Kominis, M. Loulakis, and Ö. E. Müstecaphoğlu, "Quantum biometrics," *Recent Advances in Biometrics*, p. 131, 2022.

[248] J. McGregor, S. Temple, and G. Horváth, "Human polarization sensitivity," in *Polarized light and polarization vision in animal sciences*, pp. 303–315, Springer, 2014.

[249] S. E. Temple, N. W. Roberts, and G. P. Misson, "Haidinger's brushes elicited at varying degrees of polarization rapidly and easily assesses total macular pigmentation," *JOSA A*, vol. 36, no. 4, pp. B123–B131, 2019.

[250] B. J. Lujan, A. Roorda, R. W. Knighton, and J. Carroll, "Revealing henle's fiber layer using spectral domain optical coherence tomography," *Investigative ophthalmology & visual science*, vol. 52, no. 3, pp. 1486–1492, 2011.

[251] R. A. Bone and J. T. Landrum, "Macular pigment in henle fiber membranes: a model for haidinger's brushes," *Vision research*, vol. 24, no. 2, pp. 103–108, 1984.

[252] T. T. Berendschot and D. van Norren, "Macular pigment shows ringlike structures," *Investigative ophthalmology & visual science*, vol. 47, no. 2, pp. 709–714, 2006.

[253] G. Van Blokland and S. Verhelst, "Corneal polarization in the living human eye explained with a biaxial model," *JOSA A*, vol. 4, no. 1, pp. 82–90, 1987.

[254] H. Levitt, "Transformed up-down methods in psychoacoustics," *The Journal of the Acoustical society of America*, vol. 49, no. 2B, pp. 467–477, 1971.

[255] D. Pushin, C. Kapahi, A. Silva, D. Cory, M. Kulmaganbetov, M. Mungalsingh, T. Singh, B. Thompson, and D. Sarenac, "Psychophysical discrimination of radially varying polarization-based entoptic phenomena," *Physical Review Applied*, vol. 21, no. 1, p. L011002, 2024.

[256] D. A. Pushin, D. V. Garrad, C. Kapahi, A. E. Silva, P. Chahal, D. G. Cory, M. Kulmaganbetov, I. Salehi, M. A. Mungalsingh, T. Singh, *et al.*, "Characterizing the circularly oriented macular pigment using spatiotemporal sensitivity to structured light entoptic phenomena," *Journal of Vision*, vol. 25, no. 6, pp. 11–11, 2025.

[257] O. Lailey, M. A. Alais, L. Wang, P. Chahal, D. G. Cory, T. Khoo, E. Olkhov-Mitsel, D. Sarenac, D. A. Pushin, and J. Mirkovic, "Quantitative diagnosis of amyloid without congo red staining using polarized light microscopy," *Biomedical Optics Express*, vol. 16, no. 6, pp. 2283–2302, 2025.

[258] L. Shi, L. Lindwasser, W. Wang, R. Alfano, and A. Rodríguez-Contreras, "Propagation of gaussian and laguerre-gaussian vortex beams through mouse brain tissue," *Journal of biophotonics*, vol. 10, no. 12, pp. 1756–1760, 2017.

[259] D. Sarenac, D. G. Cory, D. A. Pushin, J. Nsofini, and I. Hincks, "Generating a lattice of optical spin-orbit beams." U.S. Patent, Sep 2020. US Patent 10,782,464 B1.

[260] D. Sarenac, D. Cory, J. Nsofini, I. Hincks, P. Miguel, M. Arif, C. Clark, M. Huber, and D. Pushin, "Generation of a lattice of spin-orbit beams via coherent averaging," *arXiv preprint arXiv:1710.03169*, 2017.

[261] F. Mezei, "Neutron spin echo: A new concept in polarized thermal neutron techniques," *Zeitschrift für Physik A Hadrons and nuclei*, vol. 255, no. 2, pp. 146–160, 1972.

[262] K. Y. Bliokh, Y. P. Bliokh, S. Savel'Ev, and F. Nori, "Semiclassical dynamics of electron wave packet states with phase vortices," *Physical Review Letters*, vol. 99, no. 19, p. 190404, 2007.

[263] M. Uchida and A. Tonomura, "Generation of electron beams carrying orbital angular momentum," *nature*, vol. 464, no. 7289, p. 737, 2010.

[264] C. W. Clark, R. Barankov, M. G. Huber, D. G. Cory, and D. A. Pushin, "Controlling neutron orbital angular momentum," *Nature*, vol. 525, pp. 504–506, Sep 2015.

[265] V. Grillo, T. R. Harvey, F. Venturi, J. S. Pierce, R. Balboni, F. Bouchard, G. C. Gazzadi, S. Frabboni, A. H. Tavabi, Z.-A. Li, *et al.*, "Observation of nanoscale magnetic fields using twisted electron beams," *Nature communications*, vol. 8, no. 1, p. 689, 2017.

[266] A. Béché, R. Van Boxem, G. Van Tendeloo, and J. Verbeeck, "Magnetic monopole field exposed by electrons," *Nature Physics*, vol. 10, no. 1, p. 26, 2014.

[267] V. A. Afanasev, D. Karlovets, and V. Serbo, "The schwinger scattering of twisted neutrons by nuclei," *arXiv preprint arXiv:1903.12245*, 2019.

[268] H. Larocque, I. Kaminer, V. Grillo, R. W. Boyd, and E. Karimi, "Twisting neutrons may reveal their internal structure," *Nature Physics*, vol. 14, no. 1, p. 1, 2018.

[269] C. Maurer, A. Jesacher, S. Fürhapter, S. Bernet, and M. Ritsch-Marte, "Tailoring of arbitrary optical vector beams," *New Journal of Physics*, vol. 9, no. 3, p. 78, 2007.

[270] L. Marrucci, C. Manzo, and D. Paparo, "Optical spin-to-orbital angular momentum conversion in inhomogeneous anisotropic media," *Phys. Rev. Lett.*, vol. 96, p. 163905, Apr 2006.

[271] E. Karimi, L. Marrucci, V. Grillo, and E. Santamato, "Spin-to-orbital angular momentum conversion and spin-polarization filtering in electron beams," *Physical review letters*, vol. 108, no. 4, p. 044801, 2012.

[272] C. T. Schmiegelow, J. Schulz, H. Kaufmann, T. Ruster, U. G. Poschinger, and F. Schmidt-Kaler, "Transfer of optical orbital angular momentum to a bound electron," *Nature communications*, vol. 7, 2016.

[273] G. Vallone, V. D'Ambrosio, A. Sponselli, S. Slussarenko, L. Marrucci, F. Sciarrino, and P. Villoresi, "Free-space quantum key distribution by rotation-invariant twisted photons," *Phys. Rev. Lett.*, vol. 113, p. 060503, Aug 2014.

[274] E. Karimi, V. Grillo, R. W. Boyd, and E. Santamato, "Generation of a spin-polarized electron beam by multipole magnetic fields," *Ultramicroscopy*, vol. 138, pp. 22–27, 2014.

[275] K. Y. Bliokh, M. R. Dennis, and F. Nori, "Relativistic electron vortex beams: angular momentum and spin-orbit interaction," *Physical review letters*, vol. 107, no. 17, p. 174802, 2011.

[276] K. Y. Bliokh, I. P. Ivanov, G. Guzzinati, L. Clark, R. Van Boxem, A. Béché, R. Juchtmans, M. A. Alonso, P. Schattschneider, F. Nori, *et al.*, "Theory and applications of free-electron vortex states," *Physics Reports*, vol. 690, pp. 1–70, 2017.

[277] S. Tsesses, E. Ostrovsky, K. Cohen, B. Gjonaj, N. H. Lindner, and G. Bartal, "Optical skyrmion lattice in evanescent electromagnetic fields," *Science*, vol. 361, pp. 993–996, Sept. 2018.

[278] S. Watson, Jun 2023.

[279] M. Dietze, J. Felber, K. Raum, and C. Rausch, "Intensified ccds as position sensitive neutron detectors," *Nuclear Instruments and Methods in Physics Research Section A: Accelerators, Spectrometers, Detectors and Associated Equipment*, vol. 377, no. 2-3, pp. 320–324, 1996.

[280] W. Chen, T. R. Gentile, R. Erwin, S. Watson, Q. Ye, K. L. Krycka, and B. B. Maranville, "3he spin filter based polarized neutron capability at the nist center for neutron research," in *Journal of Physics: Conference Series*, vol. 528, p. 012014, IOP Publishing, 2014.

[281] W. Chen, T. Gentile, Q. Ye, T. Walker, and E. Babcock, "On the limits of spin-exchange optical pumping of 3he," *Journal of applied physics*, vol. 116, no. 1, p. 014903, 2014.

[282] A. Abragam and A. Abragam, *The principles of nuclear magnetism*. No. 32 in International Series of Monographs on Physics, Oxford university press, 1961.

[283] F. Li, H. Feng, A. N. Thaler, S. R. Parnell, W. A. Hamilton, L. Crow, W. Yang, A. B. Jones, H. Bai, M. Matsuda, *et al.*, "High resolution neutron larmor diffraction using superconducting magnetic wollaston prisms," *Scientific reports*, vol. 7, no. 1, p. 865, 2017.

[284] W. G. Bouwman, J. Plomp, V. O. De Haan, W. H. Kraan, A. A. van Well, K. Habicht, T. Keller, and M. T. Rekveldt, "Real-space neutron scattering methods," *Nuclear Instruments and Methods in Physics Research Section A: Accelerators, Spectrometers, Detectors and Associated Equipment*, vol. 586, no. 1, pp. 9–14, 2008.

[285] P. J. Mohr, D. B. Newell, and B. N. Taylor, "Codata recommended values of the fundamental physical constants: 2014*," *Rev. Mod. Phys.*, vol. 88, p. 035009, Sep 2016.

[286] K. Y. Bliokh, F. Rodríguez-Fortuño, F. Nori, and A. V. Zayats, "Spin–orbit interactions of light," *Nature Photonics*, vol. 9, no. 12, p. 796, 2015.

[287] T. Stav, A. Faerman, E. Maguid, D. Oren, V. Kleiner, E. Hasman, and M. Segev, "Quantum entanglement of the spin and orbital angular momentum of photons using metamaterials," *Science*, vol. 361, no. 6407, pp. 1101–1104, 2018.

[288] P. Lodahl, S. Mahmoodian, S. Stobbe, A. Rauschenbeutel, P. Schneeweiss, J. Volz, H. Pichler, and P. Zoller, "Chiral quantum optics," *Nature*, vol. 541, no. 7638, p. 473, 2017.

[289] T. Ozawa, H. M. Price, A. Amo, N. Goldman, M. Hafezi, L. Lu, M. C. Rechtsman, D. Schuster, J. Simon, O. Zilberberg, *et al.*, "Topological photonics," *Reviews of Modern Physics*, vol. 91, no. 1, p. 015006, 2019.

[290] Q. Le Thien, S. McKay, R. Pynn, and G. Ortiz, "Spin-textured neutron beams with orbital angular momentum," *Physical review B*, vol. 107, no. 13, p. 134403, 2023.

[291] D. Sarenac, O. Lailey, M. E. Henderson, H. Ekinci, C. W. Clark, D. G. Cory, L. DeBeer-Schmitt, M. G. Huber, J. S. White, K. Zhernenkov, *et al.*, "Generation of neutron airy beams," *Physical Review Letters*, vol. 134, no. 15, p. 153401, 2025.

[292] D. Sarenac, M. E. Henderson, H. Ekinci, C. W. Clark, D. G. Cory, L. DeBeer-Schmitt, M. G. Huber, O. Lailey, J. S. White, K. Zhernenkov, *et al.*, "Small-angle scattering interferometry with neutron orbital angular momentum states," *Nature Communications*, vol. 15, no. 1, p. 10785, 2024.

[293] D. Sarenac, C. W. Clark, D. G. Cory, C. Kapahi, B. Heacock, M. G. Huber, J. Nsofini, C. B. Shahi, and D. A. Pushin, "Structured neutron waves," in *Optical, Opto-Atomic, and Entanglement-Enhanced Precision Metrology*, vol. 10934, pp. 232–240, SPIE, 2019.

[294] D. Sarenac, W. Chen, C. W. Clark, D. G. Cory, C. Kapahi, B. Heacock, M. Henderson, M. Huber, L. DeBeer-Schmitt, K. Zhernenkov, *et al.*, "Novel methods of characterizing topological spin textures with neutron probes," in *Spintronics XVI*, vol. 12656, p. 1265602, SPIE, 2023.

[295] D. S. Hussey, H. Miao, G. Yuan, D. Pushin, D. Sarenac, M. G. Huber, D. L. Jacobson, J. M. LaManna, and H. Wen, "Demonstration of a white beam far-field neutron interferometer for spatially resolved small angle neutron scattering," *arXiv preprint arXiv:1606.03054*, 2016.

[296] V. Y. Mendeleyev, S. Skovorodko, E. Lubnin, and V. Prosvirikov, "Optical constants of silicon in near infrared region," *Applied Physics Letters*, vol. 93, no. 13, 2008.

[297] A. Einstein, "On the relativity principle and the conclusions drawn from it," *Jahrb Radioaktivitat Elektronik*, vol. 4, pp. 411–462, 1907.

[298] C. Kapahi, D. Sarenac, B. Heacock, D. Cory, M. Huber, J. Paster, R. Serrat, and D. Pushin, "Design and monte carlo simulation of a phase grating moir\'e neutron interferometer to measure the gravitational constant," *arXiv preprint arXiv:2505.00170*, 2025.

[299] P. R. Heyl and P. Chrzanowski, *A redetermination of the constant of gravitation.* Bureau of Standards. Physics Department, 1930.

[300] R. D. Rose, H. M. Parker, R. A. Lowry, A. R. Kuhlthau, and J. W. Beams, "Determination of the gravitational constant G," *Physical Review Letters*, vol. 23, pp. 655–658, 9 1969.

[301] J. H. Gundlach, E. G. Adelberger, B. R. Heckel, and H. E. Swanson, "New technique for measuring Newton's constant [Formula presented]," *Physical Review D - Particles, Fields, Gravitation and Cosmology*, vol. 54, pp. R1256–R1259, 7 1996.

[302] J. H. Gundlach, "A rotating torsion balance experiment to measure Newton's constant," *Measurement Science and Technology*, vol. 10, pp. 454–459, 6 1999.

[303] J. H. Gundlach and S. M. Merkowitz, "Measurement of Newton's constant using a torsion balance with angular acceleration feedback," *Physical Review Letters*, vol. 85, pp. 2869–2872, 10 2000.

[304] T. J. Quinn, C. C. Speake, S. J. Richman, R. S. Davis, and A. Picard, "A new determination of G using two methods," *Physical Review Letters*, vol. 87, pp. 111101–111101, 9 2001.

[305] T. Quinn, H. Parks, C. Speake, and R. Davis, "Improved determination of G using two methods," *Physical Review Letters*, vol. 111, p. 101102, 9 2013.

[306] T. Quinn, C. Speake, H. Parks, and R. Davis, "The BIPM measurements of the Newtonian constant of gravitation, G," 10 2014.

[307] J. Schurr, N. Klein, H. Meyer, H. Piel, and H. Walesch, "A new method for testing Newton's gravitational law," *Metrologia*, vol. 28, pp. 397–404, 1 1991.

[308] U. Kleinevoß, H. Meyer, A. Schumacher, and S. Hartmann, "Absolute measurement of the Newtonian force and a determination of G," *Measurement Science and Technology*, vol. 10, pp. 492–494, 6 1999.

[309] M. Prevedelli, L. Cacciapuoti, G. Rosi, F. Sorrentino, and G. M. Tino, "Measuring the Newtonian constant of gravitation G with an atomic interferometer," *Philosophical Transactions of the Royal Society A: Mathematical, Physical and Engineering Sciences*, vol. 372, 10 2014.

[310] T. Brack, B. Zybach, F. Balabdaoui, S. Kaufmann, F. Palmegiano, J.-C. Tomasina, S. Blunier, D. Scheiwiller, J. Fankhauser, and J. Dual, "Dynamic measurement of gravitational coupling between resonating beams in the hertz regime," *Nature Physics*, vol. 18, no. 8, pp. 952–957, 2022.

[311] Q. Li, C. Xue, J. P. Liu, J. F. Wu, S. Q. Yang, C. G. Shao, L. D. Quan, W. H. Tan, L. C. Tu, Q. Liu, H. Xu, L. X. Liu, Q. L. Wang, Z. K. Hu, Z. B. Zhou, P. S. Luo, S. C. Wu, V. Milyukov, and J. Luo, "Measurements of the gravitational constant using two independent methods," *Nature*, vol. 560, pp. 582–588, 8 2018.

[312] NIST, "NSF Ideas Laboratory at NIST: Measuring "Big G" Challenge — NIST."

[313] A. Peters, K. Y. Chung, and S. Chu, "High-precision gravity measurements using atom interferometry," *Metrologia*, vol. 38, no. 1, pp. 25–61, 2001.

[314] B. Brezger, L. Hackermüller, S. Uttenthaler, J. Petschinka, M. Arndt, and A. Zeilinger, "Matter-Wave Interferometer for Large Molecules," *Physical Review Letters*, vol. 88, p. 4, 2 2002.

[315] R. Colella, A. W. Overhauser, and S. A. Werner, "Observation of Gravitationally Induced Quantum Interference," *Physical Review Letters*, vol. 34, pp. 1472–1474, 6 1975.

[316] J. D. Perreault and A. D. Cronin, "Measurement of atomic diffraction phases induced by material gratings," *Physical Review A—Atomic, Molecular, and Optical Physics*, vol. 73, no. 3, p. 033610, 2006.

[317] W. F. Holmgren, M. C. Revelle, V. P. Lonij, and A. D. Cronin, "Absolute and ratio measurements of the polarizability of Na, K, and Rb with an atom interferometer," *Physical Review A—Atomic, Molecular, and Optical Physics*, vol. 81, no. 5, p. 053607, 2010.

[318] D. Nagy, G. Papp, and J. Benedek, "The gravitational potential and its derivatives for the prism," *Journal of Geodesy*, vol. 74, pp. 552–560, 2000.

[319] R. Karcol and R. Pašteka, "On the two different formulas for the 3d rectangular prism effect in gravimetry," *Pure and Applied Geophysics*, vol. 176, pp. 257–263, 2019.

[320] A. Miffre, M. Jacquey, M. Büchner, G. Trénec, and J. Vigué, "Measurement of the electric polarizability of lithium by atom interferometry," *Physical Review A—Atomic, Molecular, and Optical Physics*, vol. 73, no. 1, p. 011603, 2006.

[321] J. M. LaManna, D. S. Hussey, E. Baltic, and D. L. Jacobson, "Neutron and x-ray tomography (next) system for simultaneous, dual modality tomography," *Review of Scientific Instruments*, vol. 88, no. 11, 2017.

[322] D. S. Hussey, C. Brocker, J. Cook, D. Jacobson, T. Gentile, W. Chen, E. Baltic, D. Baxter, J. Doskow, and M. Arif, "A new cold neutron imaging instrument at nist," *Physics Procedia*, vol. 69, pp. 48–54, 2015.

[323] K. Assumin-Gyimah, M. Holt, D. Dutta, and W. Snow, "Imaging of pbwo4 crystals for g experiment test masses using a laser interferometer," *Classical and Quantum Gravity*, vol. 39, no. 16, p. 165001, 2022.

[324] K. Assumin-Gyimah, D. Dutta, D. Hussey, W. Snow, C. Langlois, and V. Lee, "Neutron phase contrast imaging of PbWO4 crystals for G experiment test masses using a talbot-lau neutron interferometer," *Classical and Quantum Gravity*, vol. 39, no. 24, p. 245014, 2022.

[325] J.-L. Staudenmann, S. Werner, R. Colella, and A. Overhauser, "Gravity and inertia in quantum mechanics," *Physical Review A*, vol. 21, no. 5, p. 1419, 1980.

[326] L. A. Page, "Effect of earth's rotation in neutron interferometry," *Physical Review Letters*, vol. 35, no. 8, p. 543, 1975.

[327] S. Werner, J.-L. Staudenmann, and R. Colella, "Effect of earth's rotation on the quantum mechanical phase of the neutron," *Physical Review Letters*, vol. 42, no. 17, p. 1103, 1979.

[328] D. Atwood, M. Horne, C. Shull, and J. Arthur, "Neutron phase shift in a rotating two-crystal interferometer," *Physical Review Letters*, vol. 52, no. 19, p. 1673, 1984.

[329] J. B. Battat, T. Murphy, E. G. Adelberger, B. Gillespie, C. Hoyle, R. McMillan, E. L. Michelsen, K. Nordtvedt, A. E. Orin, C. W. Stubbs, *et al.*, "The apache point observatory lunar laser-ranging operation (APOLLO): Two years of millimeter-precision measurements of the earth-moon range1," *Publications of the Astronomical Society of the Pacific*, vol. 121, no. 875, p. 29, 2009.

[330] B. Luzum, N. Capitaine, A. Fienga, W. Folkner, T. Fukushima, J. Hilton, C. Hohenkerk, G. Krasinsky, G. Petit, E. Pitjeva, *et al.*, "The IAU 2009 system of astronomical constants: the report of the iau working group on numerical standards for fundamental astronomy," *Celestial Mechanics and Dynamical Astronomy*, vol. 110, pp. 293–304, 2011.

[331] R. S. Park, W. M. Folkner, J. G. Williams, and D. H. Boggs, "The JPL planetary and lunar ephemerides de440 and de441," *The Astronomical Journal*, vol. 161, no. 3, p. 105, 2021.

[332] L. Lee, M. Jones, G. S. Ridenour, S. J. Bennett, A. C. Majors, B. L. Melito, and M. J. Wilson, "Comparison of accuracy and precision of gps-enabled mobile devices," in *2016 IEEE International Conference on CIT*, pp. 73–82, IEEE, 2016.

[333] Jewell Instruments, *ECS eCompass Series Datasheet*, 5 2024.

[334] A. Prasad, R. P. Middlemiss, A. Noack, K. Anastasiou, S. G. Bramsiepe, K. Toland, P. R. Utting, D. J. Paul, and G. D. Hammond, "A 19 day earth tide measurement with a mems gravimeter," *Scientific reports*, vol. 12, no. 1, p. 13091, 2022.

[335] T. Hu, R. L. Jones, W.-l. Wu, E. K. Lin, Q. Lin, D. Keane, S. Weigand, and J. Quintana, "Small angle x-ray scattering metrology for sidewall angle and cross section of nanometer scale line gratings," *Journal of Applied Physics*, vol. 96, no. 4, pp. 1983–1987, 2004.

[336] L. Vergara, M. Arai, R. Woracek, M. Olsson, A. Quintanilla, S. Alcock, J. Nilsson, K. Kanaki, P. Kadletz, O. Kirstein, *et al.*, "Evaluation of a method for time-of-flight, wavelength and neutron flight path calibration for neutron scattering instruments by means of a mini-chopper and standard neutron monitors," *Journal of Instrumentation*, vol. 18, no. 04, p. P04012, 2023.

[337] N. Fomin, G. Greene, R. Allen, V. Cianciolo, C. Crawford, T. Tito, P. Huffman, E. Iverson, R. Mahurin, and W. Snow, "Fundamental neutron physics beamline at the spallation neutron source at ornl," *Nuclear Instruments and Methods in Physics Research Section A: Accelerators, Spectrometers, Detectors and Associated Equipment*, vol. 773, pp. 45–51, 2015.

[338] "ILL PF1B Instrument Layout," 2025.

[339] G. Rosi, "Challenging the 'big g'measurement with atoms and light," *Journal of Physics B: Atomic, Molecular and Optical Physics*, vol. 49, no. 20, p. 202002, 2016.

[340] S. Schlamminger, "Gravity measured with record precision," *Nature*, vol. 560, pp. 562+, AUG 30 2018.

[341] J. D. Anderson, G. Schubert, V. Trimble, and M. R. Feldman, "Measurements of newton's gravitational constant and the length of day," *Europhysics Letters*, vol. 110, no. 1, p. 10002, 2015.

[342] J. An, Y. Xue, Z. Cao, X. He, and B. Sun, "The effect of the gravitational constant variation on the propagation of gravitational waves," *Physics Letters B*, vol. 844, p. 138108, 2023.

[343] B. Heacock, D. Sarenac, D. Cory, M. Huber, J. MacLean, H. Miao, H. Wen, and D. Pushin, "Neutron sub-micrometre tomography from scattering data," *IUCrJ*, vol. 7, no. 5, pp. 893–900, 2020.

[344] B. Khanaliloo, H. Jayakumar, A. C. Hryciw, D. P. Lake, H. Kaviani, and P. E. Barclay, "Single-crystal diamond nanobeam waveguide optomechanics," *Physical Review X*, vol. 5, no. 4, p. 041051, 2015.

[345] V. V. Nesvizhevsky, H. G. Börner, A. K. Petukhov, H. Abele, S. Baeßler, F. J. Rueß, T. Stöferle, A. Westphal, A. M. Gagarski, G. A. Petrov, *et al.*, "Quantum states of neutrons in the earth's gravitational field," *Nature*, vol. 415, no. 6869, pp. 297–299, 2002.

[346] V. V. Nesvizhevsky, H. Börner, A. Gagarski, A. Petoukhov, G. Petrov, H. Abele, S. Baeßler, G. Divkovic, F. Rueß, T. Stöferle, *et al.*, "Measurement of quantum states of neutrons in the earth's gravitational field," *Physical Review D*, vol. 67, no. 10, p. 102002, 2003.

[347] V. Nesvizhevsky, A. Petukhov, H. Börner, T. Baranova, A. Gagarski, G. Petrov, K. Protasov, A. Y. Voronin, S. Baeßler, H. Abele, *et al.*, "Study of the neutron quantum states in the gravity field," *The European Physical Journal C-Particles and Fields*, vol. 40, no. 4, pp. 479–491, 2005.

[348] P. Schmidt-Wellenburg, K. Andersen, P. Courtois, M. Kreuz, S. Mironov, V. Nesvizhevsky, G. Pignol, K. Protasov, T. Soldner, F. Vezzu, *et al.*, "Ultracold-neutron infrastructure for the gravitational spectrometer granit," *Nuclear Instruments and Methods in Physics Research Section A: Accelerators, Spectrometers, Detectors and Associated Equipment*, vol. 611, no. 2-3, pp. 267–271, 2009.

[349] S. Parnell, A. Van Well, J. Plomp, R. Dalgliesh, N.-J. Steinke, J. Cooper, N. Geerits, K. Steffen, W. Snow, and V. de Haan, "Search for exotic spin-dependent couplings of the neutron with matter using spin-echo based neutron interferometry," *Physical Review D*, vol. 101, no. 12, p. 122002, 2020.

[350] D. Sarenac, G. Gorbet, C. W. Clark, D. Cory, H. Ekinci, M. Henderson, M. Huber, D. Hussey, C. Kapahi, P. Kienzle, *et al.*, "Phase and contrast moiré signatures in

two-dimensional cone beam interferometry," *Physical Review Research*, vol. 6, no. 3, p. L032054, 2024.

[351] M. Wolman and J. Bubis, "The cause of the green polarization color of amyloid stained with congo red," *Histochemie*, vol. 4, no. 5, pp. 351–356, 1965.

[352] M. Wolman, "Polarized light microscopy as a tool of diagnostic pathology.," *Journal of Histochemistry & Cytochemistry*, vol. 23, no. 1, pp. 21–50, 1975.

[353] S. L. Jacques, J. C. Ramella-Roman, and K. Lee, "Imaging skin pathology with polarized light," *Journal of biomedical optics*, vol. 7, no. 3, pp. 329–340, 2002.

[354] G. Gibson, J. Courtial, M. J. Padgett, M. Vasnetsov, V. Pas'ko, S. M. Barnett, and S. Franke-Arnold, "Free-space information transfer using light beams carrying orbital angular momentum," *Optics express*, vol. 12, no. 22, pp. 5448–5456, 2004.

[355] J. Leach, M. J. Padgett, S. M. Barnett, S. Franke-Arnold, and J. Courtial, "Measuring the orbital angular momentum of a single photon," *Physical review letters*, vol. 88, no. 25, p. 257901, 2002.

[356] C. Paterson, "Atmospheric turbulence and orbital angular momentum¡? format?¿ of single photons for optical communication," *Physical review letters*, vol. 94, no. 15, p. 153901, 2005.

[357] B. Rodenburg, M. P. Lavery, M. Malik, M. N. O'Sullivan, M. Mirhosseini, D. J. Robertson, M. Padgett, and R. W. Boyd, "Influence of atmospheric turbulence on states of¡? a3b2 show [pmg: line-break justify=" yes"/]?¿ light carrying orbital angular momentum," *Optics letters*, vol. 37, no. 17, pp. 3735–3737, 2012.

[358] M. Krenn, J. Handsteiner, M. Fink, R. Fickler, R. Ursin, M. Malik, and A. Zeilinger, "Twisted light transmission over 143 km," *Proceedings of the National Academy of Sciences*, vol. 113, no. 48, pp. 13648–13653, 2016.

[359] L. Zhu, H. Yao, H. Chang, Q. Tian, Q. Zhang, X. Xin, and F. R. Yu, "Adaptive optics for orbital angular momentum-based internet of underwater things applications," *IEEE Internet of Things Journal*, vol. 9, no. 23, pp. 24281–24299, 2022.

[360] A. Wang, L. Zhu, Y. Zhao, S. Li, W. Lv, J. Xu, and J. Wang, "Adaptive water-air-water data information transfer using orbital angular momentum," *Optics express*, vol. 26, no. 7, pp. 8669–8678, 2018.

[361] Y. Chen, W.-G. Shen, Z.-M. Li, C.-Q. Hu, Z.-Q. Yan, Z.-Q. Jiao, J. Gao, M.-M. Cao, K. Sun, and X.-M. Jin, "Underwater transmission of high-dimensional twisted photons over 55 meters," *PhotoniX*, vol. 1, no. 1, p. 5, 2020.

[362] J. Pinnell, I. Nape, M. de Oliveira, N. TabeBordbar, and A. Forbes, "Experimental demonstration of 11-dimensional 10-party quantum secret sharing," *Laser & Photonics Reviews*, vol. 14, no. 9, p. 2000012, 2020.

[363] E. Vashukevich, E. Bashmakova, T. Y. Golubeva, and Y. M. Golubev, "High-fidelity quantum gates for oam single qudits on quantum memory," *Laser Physics Letters*, vol. 19, no. 2, p. 025202, 2022.

[364] R. Ashkar, H. Bilheux, H. Bordallo, R. Briber, D. J. Callaway, X. Cheng, X.-Q. Chu, J. E. Curtis, M. Dadmun, P. Fenimore, *et al.*, "Neutron scattering in the biological sciences: progress and prospects," *Biological Crystallography*, vol. 74, no. 12, pp. 1129–1168, 2018.

[365] M. Andriamirado, A. Balantekin, H. Band, C. Bass, D. Bergeron, D. Berish, N. Bowden, J. Brodsky, C. Bryan, T. Classen, *et al.*, "Improved short-baseline neutrino oscillation search and energy spectrum measurement with the prospect experiment at hfir," *Physical Review D*, vol. 103, no. 3, p. 032001, 2021.

[366] M. E. Henderson, J. Beare, S. Sharma, M. Bleuel, P. Clancy, D. G. Cory, M. G. Huber, C. A. Marjerrison, M. Pula, D. Sarenac, *et al.*, "Characterization of a disordered above room temperature skyrmion material co8zn8mn4," *Materials*, vol. 14, no. 16, p. 4689, 2021.

[367] M. Henderson, M. Bleuel, J. Beare, D. Cory, B. Heacock, M. Huber, G. Luke, M. Pula, D. Sarenac, S. Sharma, *et al.*, "Skyrmion alignment and pinning effects in the disordered multiphase skyrmion material co 8 zn 8 mn 4," *Physical review B*, vol. 106, no. 9, p. 094435, 2022.

[368] G. Badurek, H. Rauch, A. Wilfing, U. Bonse, and W. Graeff, "A perfect-crystal neutron polarizer as an application of magnetic prism refraction," *Applied Crystallography*, vol. 12, no. 2, pp. 186–191, 1979.

[369] W. Treimer and H. Höppner, "Realizing a (nearly) 100% neutron beam polarization," *Measurement Science and Technology*, vol. 31, no. 11, p. 115017, 2020.

[370] D. Weder, C. von Korff Schmising, C. M. Günther, M. Schneider, D. Engel, P. Hessing, C. Strüber, M. Weigand, B. Vodungbo, E. Jal, *et al.*, "Transient magnetic gratings on the nanometer scale," *Structural Dynamics*, vol. 7, no. 5, 2020.

[371] D. Müller, D. Z. Anderson, R. J. Grow, P. D. Schwindt, and E. A. Cornell, "Guiding neutral atoms around curves with lithographically patterned current-carrying wires," *Physical Review Letters*, vol. 83, no. 25, p. 5194, 1999.

[372] T. Kawai, T. Ebisawa, S. Tasaki, Y. Eguchi, M. Hino, and N. Achiwa, "Multilayer neutron polarizing mirrors working under a low external magnetic field less than 100 gausses," *Journal of Neutron Research*, vol. 5, no. 3, pp. 123–132, 1997.

[373] T. Ebisawa, H. Funahashi, S. Tasaki, Y. Otake, T. Kawai, M. Hino, N. Achiwa, and T. Akiyoshi, "Cold neutron interferometry using multilayer mirrors," *Journal of Neutron Research*, vol. 4, no. 1-4, pp. 157–166, 1996.

[374] M. Henderson, D. Cory, D. Sarenac, and D. Pushin, "Quantum advancements in neutron scattering reshape spintronic devices," *arXiv preprint arXiv:2407.10822*, 2024.

[375] S. Sponar, R. I. Sedmik, M. Pitschmann, H. Abele, and Y. Hasegawa, "Tests of fundamental quantum mechanics and dark interactions with low-energy neutrons," *Nature Reviews Physics*, vol. 3, no. 5, pp. 309–327, 2021.